Discover the Fascinating World of Crystal Nucleation: A Cutting-Edge Confocal Microscopy Investigation on Colloidal Hard Sphere Systems

Dissertation
der Mathematisch-Naturwissenschaftlichen Fakultät
der Eberhard Karls Universität Tübingen
zur Erlangung des Grades eines
Doktors der Naturwissenschaften
(Dr. rer. nat.)

vorgelegt von
Sahana Kale
aus Puttur / Indien

Tübingen
2024

Gedruckt mit Genehmigung der Mathematisch-Naturwissenschaftlichen Fakultät der Eberhard Karls Universität Tübingen.

Tag der mündlichen Qualifikation:	02.05.2024
Dekan:	Prof. Dr. Thilo Stehle
1. Berichterstatter/-in:	apl. Prof. Dr. habil. Hans Joachim Schöpe
2. Berichterstatter/-in:	Prof. Dr. Erik Schäffer

Acknowledgments

The success of completing my PhD thesis absolutely deserves acknowledging the guidance and encouragement of many people. I would like to take this opportunity to express my gratitude for the people who were instrumental throughout my thesis at Angewandte Physics, University Tuebingen.

Supervisors can be critically important for research success, and in my case, I am genuinely thankful to my PhD supervisor, Prof. Hans Joachim Schöepe. His vision, continuous spirit of enthusiasm, and tireless efforts motivated me throughout my research. At the time of extreme problems, his continuous support and faith on me meant to me a lot. I equally express my gratitude to my second supervisor, Prof. Martin Oettel, for his unflagging support and advice that allowed me to complete my work.

As the saying goes, "No man is an island," and I am no exception. I owe a debt of gratitude to many individuals who have supported me on my academic journey. My colleagues, Katrin, Nidhi, Eelco, Frank, Miriam, Bernd, Emanual, Nadim, Sam, have been my partners in this endeavor, offering support, and encouragement that have been invaluable. I would like to thank Mrs. Englert for their official help and constant support in administrative issues. I am grateful to DZNE Tubingen for allowing me to work with confocal microscopy. It has been an amazing experience, and I am grateful for the challenge and reward it has brought. Last but not least, I would love to express my cordial gratitude to my family and my friends, who stayed beside me during this endeavor.

In conclusion, as the scientific proverb states, "Science is a collaborative enterprise, spanning the generations." I am grateful to everyone who contributed to my thesis work at Angewandte Physics, University Tuebingen, and I acknowledge their contributions with deep appreciation.

Contents

Abstract

In this thesis, colloidal model systems with different interaction potentials is used. As model systems with hard-sphere interaction, we use poly-hydroxy-stearic acid (PHSA) sterically stabilized plexiglas particles (PMMA) dispersed in organic solvents. Within this work, the PMMA-PHSA colloid particles are prepared in such a way that the physical properties of the system concerning gravity, hydrodynamics, and interparticle interaction are selectively varied. Particles stained with the fluorescent dye $DiIC_{18}$ is very good approximation to an Hard Sphere(HS). The PMMA particles were first comprehensively characterized in size, mass density, and refractive index (RI). We also stress the different behavior of the colloidal system in various solvents by analyzing the structure of the colloidal fluid in the thermodynamic equilibrium (pair distribution function g(r) or static structure factor S(q)). After careful characterization of colloidal particles, nucleation kinetics is studied.

The determination of nucleation kinetics in HS-like colloids is carried out for the first time in an extensive volume fraction range in real space. Confocal microscopy offers a unique opportunity to study the structure and dynamics of the metastable colloidal melt and crystallization kinetics at the particle level. This allows the development of a microscopic picture of the nucleation process. The nucleation rate densities from experimental and theoretical data diverge by several orders of magnitudes, and the curves are qualitatively different. One of our research goals is to find the underlying reason for this discrepancy - if there is any. Direct imaging in three dimensions offers the unique possibility of observing crystal nucleation and growth on the particle level, giving detailed information about the fluid-to-crystal phase transformation. With confocal microscopy, all particle positions as a function of time are observed. These measurements allow us to extract many parameters and determine local structural, order parameters, particle number densities, pair correlation functions, etc., as function of time. The nucleation rate density, the critical nucleus size, and the nucleation barrier height were extracted, all in agreement with other publications from experiments. The results prove the utility of confocal microscopy in quantifying the nucleation rate densities as a function of volume fraction complemental to light scattering experiments. The nucleation kinetics in HS-like colloids under variation of the suspension parameters are also examined systematically using laser scanning confocal microscopy to determine the cause of the significant discrepancy between experiments and simulations.

It can be concluded that the experimental nucleation rate densities in colloidal HS systems are incompatible with nucleation rate densities from simulations. The cause of this finding lies in Classical Nucleation Theory(CNT). No microscopic experiments have been performed on a wide volume fraction range and at the middle of the coexistence range. This is directly comparable to simulations. Furthermore, a fundamental assumption of the classical description of crystal nucleation is untenable. This wealth of information allows a detailed characterization of the physical properties of metastable melt, an analysis of the crystallization process, and a microscopic picture of the nucleation process. In the study of crystallization kinetics, it was found that nearly ordered clusters form as precursors, and these then develop into clusters. Thus, these analysis shed light on the controversy between density or structural changes during nucleation. Our finding concludes that all possible ways can happen during crystallization.

Chapter 1

Introduction

Colloidal systems, i.e., micron-sized particles suspended in liquids, share many properties with atomic systems. In particular, the colloidal particles form crystals and undergo a glass transition at higher volume fractions similar to atomic systems. Therefore, they are often referred to as model systems to address novel concepts in the context of physics in a convenient way. Owing to the brownian motion of such particles, their trajectories can be experimentally studied and allow direct comparison with numerical and theoretical investigations. For the theoretical description of the colloidal system, a coarse-grained viewpoint is used in which the liquid dispersion medium is considered an inert continuum defined by its macroscopic properties. The colloidal particles dispersed in this continuum interact, and their hydrodynamic properties are the same as those of an assembly of atoms. Thus, colloidal particles are used as a model system to study phenomena such as structuring or phase behavior on mesoscopic length scales. The other exciting aspect is that often simple fluid like effective pair potential can describe interactions between the colloidal particles. Furthermore, the interaction potential in colloidal systems is tune-able in several ways, giving more access to various phases. Thus, colloidal particles can be considered macro atoms with inter-particle distances comparable to visible light wavelength and slow relaxation, providing a sound model system of atomic and molecular systems at different time and length scales.

Colloids can reproduce atomic and molecular phenomena with the suspending medium, posing ideal candidates for model systems. Examples of such possibilities are numerous; perhaps the most famous one is the identity between the barometric distribution in an ideal gas and the sedimentation profile of a colloidal suspension discovered by Perrin in 1910 during some experiments to confirm the molecular nature of matter and to measure Avogadro number [151]. Perrin and his co-workers observed monodisperse suspensions of gamboge and mastic in water and applied the equipartition of energy to the colloidal particles. They showed that the absolute temperature determines the energy of the colloidal particles in the same way as for an atom in the solvent. To understand the behavior of complex fluids, fundamental properties of colloidal systems have been identified, and model systems exhibiting these behaviors have been developed. These colloidal systems are of interest for the general understanding of fluids and the knowledge of different classes of colloids. The most important for us is the role played by colloids in shedding light on the phase behavior, particularly crystallization kinetics [161] [213].

1.1 Interaction between colloidal particles

One has to prevent aggregation to exploit colloids as model systems and study the dynamics of single particles. The tendency of aggregating is due to an attractive force (van der Waals) that can be effectively screened by inducing steric or coulomb repulsion. The colloids' dynamics are affected by gravity and random collisions with their surrounding molecules in the dispersion medium. Additionally, several forces are acting on the colloids, some described briefly below.

1.1.1 van der Waals Attraction

Another type of interaction that depends on the dispersion medium is the van der Waals force, called dispersion forces or London forces. The van der Waals interaction originates from quantum fluctuations. The simple picture is that fluctuating dipoles in each atom give rise to an attractive interaction between colloids consisting of many atoms. The exact equation of the van der Waals attraction depends, among others, on the spatial distribution and distance between the interacting dipoles. In the limit of small separations r, the equation for two (colloidal) spheres with radius R is

$$U_{vdw}(r) = -\frac{HR}{12r}, \tag{1.1}$$

where H is Hamaker constant [53]. The Hamaker constant has an energy dimension and is usually of the order of 10 k_BT. The Hamaker constant's value depends on the particles' properties and the solvent, particularly their polarizability. Suppose the suspended particles and medium have the same polarizability, then H=0. It is, therefore, possible to minimize van der Waals attraction by refractive index-matching the solvent with the particles. We can also note that if the particles come close together, their attraction grows as the inverse of their separation distance, and it becomes rapidly larger than the thermal energy k_BT, leading to irreversible aggregation. In order to prevent such aggregation, the particles need to be stabilized and avoid coming into extremely close contact. Stabilization is usually achieved in two ways: charge and steric stabilization. However, in all work described in this thesis, particles are sterically stabilized, and solvent systems are modified to have the refractive index as the colloidal particles. Therefore, the van der Waals interaction is ignored throughout the work.

1.1.2 Steric stabilization

Another way of preventing aggregation is by coating the particles' surface with a layer of polymers. In the case of the particles used in this thesis, the polymers have one end irreversibly attached to the surface of the particles (fig1.1(b)) and, therefore, in contact with the solvent. Thus, it amounts to slightly increasing the adequate size of a colloid. Once two colloids approach each other, such that their stabilizing polymer hairs interpenetrate, the local density of polymer

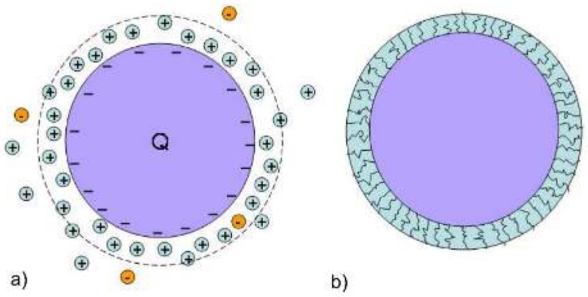

Figure 1.1: a) Schematic representation of a charge-stabilized colloid highlighting the presence of the double layer. b) Schematic representation of a sterically stabilized colloid highlighting the presence of the polymer layer.

hairs increases, leading to entropic repulsion. Depending on how the hairs are arranged, they might bend partially elastic, leading to a repulsion. The chances for a successful steric stabilization are increased under the following conditions: The hairs should completely cover the whole surface of the particle. Also, the polymers should be chemically attached and firmly anchored. The hairs should be soluble in the dispersion medium; in other words, the dispersion medium should be a suitable solvent for the hairs. The Flory-Huggins theory describes the mixing of polymers and solvents [198] [64] [90]. Finally, the hairs should not be more than 75nm to prevent flocculation [198] [211].

The interaction potential can have various contributions. Nevertheless, sterically stabilized PMMA particles act as nearly hard spheres (HS) [161] [168]. The interaction potential of ideal hard spheres is shown in figure1.4 and their pairwise interaction potential is sketched.

1.1.3 Charge stabilization

In some cases, colloidal particles have ionizable groups on their surface, dissociating when the particles are suspended in polar solvents. The dissociated ions partially diffuse away in solution due to Brownian motion but tend to remain near the particle due to Coulomb attraction. The charges on the surface then attract counter ions, forming a double-layer structure and screening the charge. Thus, the double-layer surroundings of the colloidal particles effectively increase the energy barrier for the system to aggregate as the particles approach each other. Therefore, the linear addition of the van der Waals attraction potential to the electrostatic repulsion potential becomes the foundation of the Derjaguin, Landau, Verwey, and Overbeek (DLVO) theory. Combining these two potentials U_{vdW} and U_{Yuk}, as the attraction and repulsion potentials, respectively, produces a total potential U_{DLVO} for the stabilized colloidal particles as given in the equation.

$$U_{DLVO} = U_{vdW} + U_{Yuk} \tag{1.2}$$

We note that by increasing the salt concentration of electrolytes in the solution, e.g., the screening length becomes smaller. Adding salt to charged colloidal suspension is a common way of reducing the range of Coulumbic repulsion. It

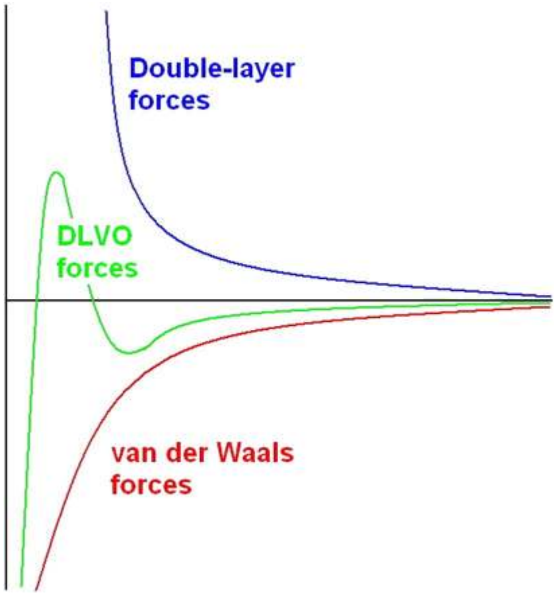

Figure 1.2: Sketch of the DLVO potential (green line), the electrostatic double-layer potential (blue line) and the van der Waals potential (red line) as a function of the interparticle distance 'r' [24].

is frequently used to approximate the hard-sphere limit in charged, polymer-coated colloids.

1.2 PMMA-PHSA as a Hard Sphere and as a Charged Sphere

PMMA is one of the most common materials used for colloids in experiments. These spherical particles are covered with a polymer containing a PMMA stem attached to the particle surface, and the brushes dangling from the stem are polyhydroxy stearic acid (PHSA). These brushes prevent coagulation by steric stabilization, as was mentioned previously. In the case of confocal microscopy studies, fluorophores are used as dyes for these particles. The density of PMMA is 1.19 gcm^{-3} and has a refractive index of about 1.49. To have an index-matched suspension of PMMA, a mixture of solvents is used as a suspension medium. Many of these mixtures consist of two components: one with a low-refractive index like decalin and another with a high-refractive index like cyclohexyl bromide. These mixtures match the refractive index of PMMA and the density, making the particles suspended for a significant time. In this research, PMMA-PHSA spheres used are shown in the figure 1.3

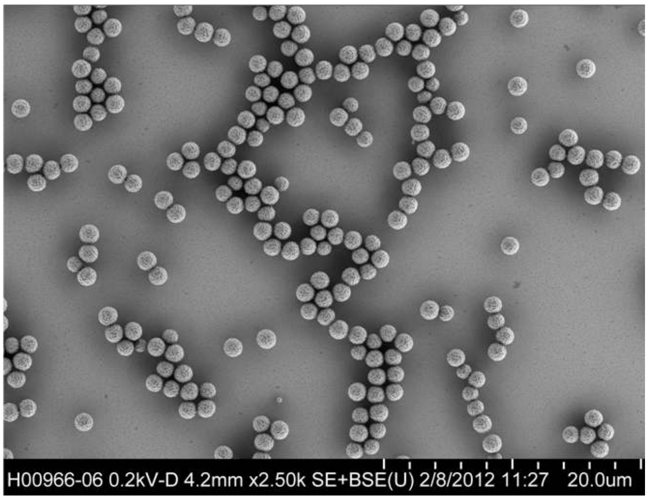

Figure 1.3: An electron microscopy image of the PMMA sphere used in this thesis [114]

1.3 Hard Sphere system (HS)

The Hard-Sphere system is one of the most straightforward systems mimicked by the colloidal suspension. Hard spheres are widely used as model particles in the statistical mechanical theory of fluids and solids. Sterically stabilized colloidal particles have a surface covered by polymer molecules that are chemically bonded or physically adsorbed on the surface. These polymers form an excluded volume, resulting in a repulsive interaction between monomers. In the simplest case, these polymers are alkyl chains. The interaction potential U(r) between two particles is infinitely repulsive at a distance $\leq$ 2R and zero for distances $>$ 2R, as shown in figure 1.1. They are defined simply as impenetrable spheres that cannot overlap in space. The absence of any attraction between the particles governs their phase behavior only by entropy. The freezing of HS is caused by a competition between two contributions to entropy S, associated with the spatial configuration of particles and the free volume available for the local motions of the particles. Freezing occurs at a concentration at which the entropy lost by the system on developing long-ranged spatial order is more than offset by the entropy gained from the larger free volumes to the particles. Thus, the HS phase behavior depends only on a single parameter, its volume fraction ϕ, where $\phi = V_{Sphere}/V_{total}$ relates the volume of all spheres V_{Sphere} to the total volume V_{total}. A disorder-order transition was first predicted by Alder and co-workers [5]. A decade later, computer simulations by Hoover and Ree identified freezing and melting transitions at ϕ_f=0.494 and ϕ_m= 0.545 [89]. This was experimentally confirmed by Pusey and Van Megen [158]. In addition to this, glass transition ϕ_g= 0.565 - 0.57 was also identified(figure 1.5).

Particles used in this work is PMMA-PHSA of diameter 1.4 µm. In this study different combination of solvents are used. Particles are provided with a fluorescent dye. Andrew Schofield synthesized the sterically stabilized PMMA particles (University of Edinburgh) [165]. During the synthesis, the particles were mixed with the entire volume of fluorescent dye $DiIC_{18}$. The particles

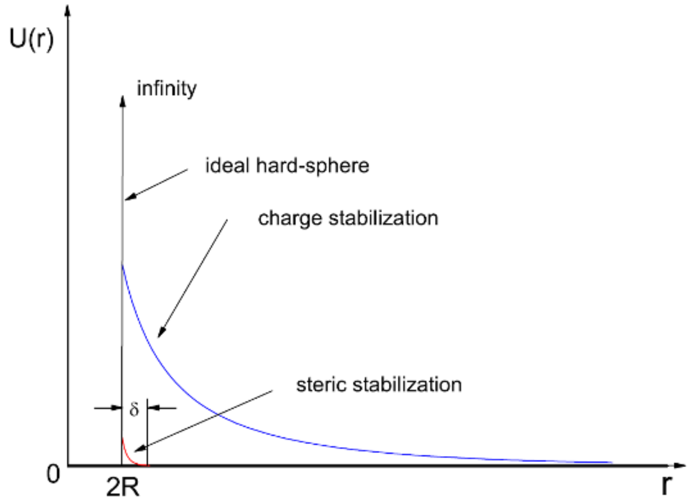

Figure 1.4: Schematic representation of the repulsive part of the interaction potentials for ideal hard spheres, sterically stabilized and charge-stabilized colloids. δ is the thickness of the polymer layer.

were delivered as a decalin stock suspension (mixture of isomers). Detailed information about the particles and solvents used is given in Chapter 2.

1.3.1 HS-Phase diagram

A collection of hard spheres is, arguably, the paradigmatic non-ideal system (either classical or quantum). The particles considered are identical spheres that do not interact except at contact when the repulsion is infinite. Hard spheres are often used as the starting point from which properties of fluids can be calculated by treating any (finite) attractions as perturbations. Theoretically and computationally, hard spheres possess the obvious advantage of not having long-range interactions (which give rise to mathematical complications). Also, as no energy scale is present, altering the temperature makes no difference to the behavior, and the system can be characterized by one parameter, the number density, or more often, the volume fraction

$$\phi = (4/3)\pi R^3 \rho \tag{1.3}$$

where R is the particle radius. In experiments, real spherical particles interact through a short-range van der Waals force caused by the electromagnetic attraction of induced dipoles in nearby particles. This leads to irreversible clustering and aggregation of un-stabilized hard spheres. By chemically grafting a thin layer of polymer hairs to the surface of each particle, the van der Waals attraction can effectively be screened out. When the particles approach one another, the polymer brushes begin to interpenetrate and must pay a very high entropic cost for losing degrees of freedom. Consequently, the interaction between such sterically stabilized particles is an excellent approximation of hard spheres.

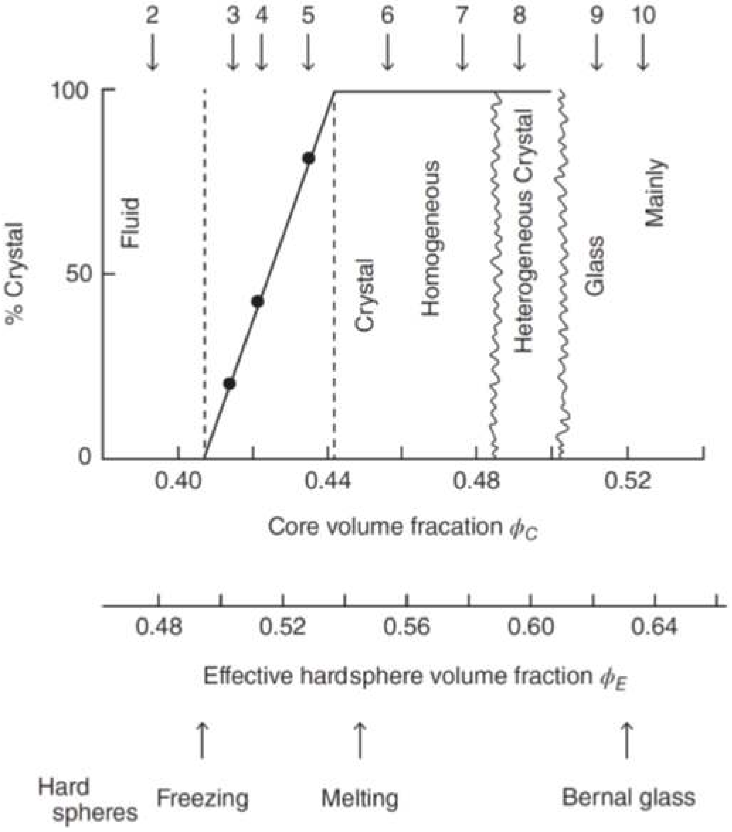

Figure 1.5: Phase diagram for PMMA-PHSA dispersions (614 nm diameter spheres). Arrows at the bottoms indicate volume fractions of hard spheres obtained from computer simulation for freezing, melting, and random close packing (Bernal glass) [158]

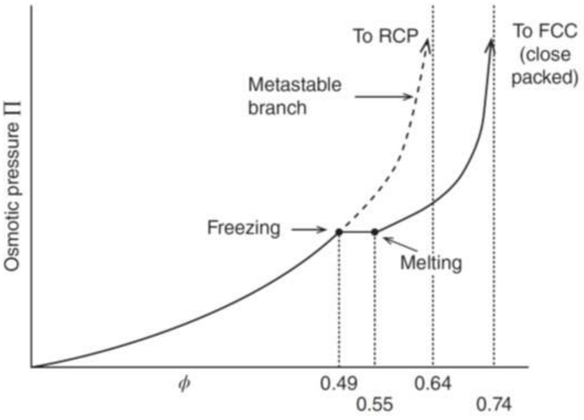

Figure 1.6: The fluid and crystal phases are bridged by the coexistence region located between the freezing and melting points. The metastable state extends the stable fluid phase to the random close packing at $\phi = 0.64$. The crystal phase extends to the face center cubic close packing $\phi = 0.74$ [164].

Almost single-sized hard spheres have been extensively studied experimentally, theoretically, and by computer simulation. The equilibrium phase behavior is very well established. The equation of state is shown in Figure 1.6, calculated using expressions derived by Carnahan and Starling [33] for the fluid portion and by Hall [73] for the solid. Remarkably, these largely phenomenological equations of state agree well with the simulation data of Hoover and Ree [8] and experimental measurements by Phan and colleagues [153]. Coexistence is indicated by the flat portion of the curve during which an increase in ϕ does not increase the osmotic pressure Π as the crystal forms at the same pressure but higher density than the fluid it replaces.

The figure 1.5 shows the complete phase diagram for the hard sphere system. (The percent of crystal present Π is plotted along the y-axis; however, as this is not a true thermodynamic variable, the two-dimensional picture does not constitute a real phase diagram.) At low ϕ, the particles are ergodic and explore the available volume; they are arranged in short-range order, which is lost over long distances. This phase is called a colloidal fluid. At larger volume fractions, the lowest free energy state is the coexistence of colloidal fluid and crystal. Over this range, the volume fraction of the fluid and crystal remain fixed at 0.494 (freezing) and 0.545 (melting), respectively. The overall value of ϕ increases by crystal forming at the expense of fluid. Experimentally, small (<1mm) crystallites are observed to nucleate homogeneously throughout the sample, sediment because of the density difference, and form a polycrystalline phase at the bottom of the container. As crystallinity is increased above the melting point, ϕ>0.545, crystallites alone are observed until the theoretical closest packing for spheres in three dimensions, $\phi_{cp}= \pi\sqrt(2)/6\approx 0.74$ is reached. If the particles are randomly arranged, the closest packing is given by the random close-packed value of $\phi_{rcp}\approx 0.64$. In practice, however, a glass transition is encountered at $\phi=\phi_{gt}= 0.58$, at which homogeneous nucleation of crystals ceases due to the arrest of long-time diffusion.

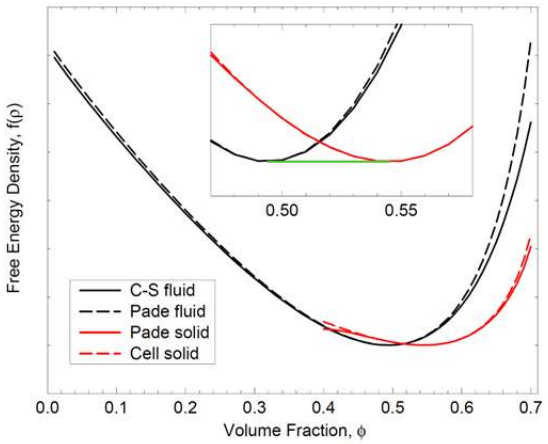

Figure 1.7: Hard sphere free energy curves. The Fluid phase curves (left) come from the Carnahan and Starling (C-S) equation of state [33] and from a Pade approximant [10]. The solid phase curves (right) are from a polynomial fit to simulation data [73] and from a cell theory free energy [12, 13]. The inset shows an enlargement around coexistence and the location of the common tangent. The fluid and solid phases have volume fractions of 0.494 and 0.545, respectively.

For a long time, the existence of a crystal phase in a purely hard sphere system was disputed. Many argued that a crystal phase could not possibly form without attractive interactions. Its stability can be understood by considering the two types of entropy involved: configurational and vibrational. A crystal phase has lower configurational entropy than a fluid, but as in a crystal, the spheres have extra room locally to move; this increase in vibrational entropy more than compensates for the long-range order. The enhanced packing of ordered hard spheres can be seen by comparing the close-packed values quoted above: a randomly ordered phase has maximum packing at $\phi \approx 0.64$, whereas ordered hard spheres at the same ϕ will have space in which to vibrate, as maximum crystalline packing does not occur until $\phi \approx 0.74$.

The hard sphere phase behavior may be predicted by considering the free energies of the two states. Figure1.7 shows plots of calculated free energy curves for the hard-sphere fluid and crystal. The fluid phase free energy has been calculated from the simple Carnahan and Starling (C-S) equation of state [33], which diverges unrealistically at $\phi = 1$. A Pade approximate (the official name for the ratio of two polynomials) calculated by Yuste and co-workers [226], which diverges, more realistically, near the glass transition, is also shown. Other expressions are also available in the literature (e.g., [127]). For the solid, the continuous curve comes from a Pade fit to simulation data by Hall [73] and the dashed curve from a cell theory free energy [27] [184]. Deviations in the solid branch predictions are small, which is encouraging for the relatively straightforward cell theory prediction. The inset in Figure 1.7 shows the common tangent construction between the fluid phase at $\phi = 0.494$ and the crystal at $\phi = 0.545$.

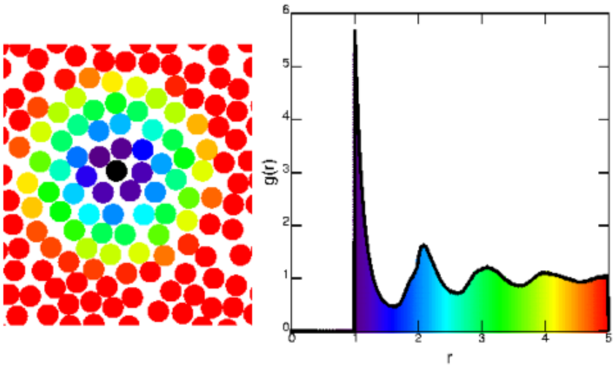

Figure 1.8: Illustration of the procedure for calculating the radial distribution function (right) of an amorphous assembly of discs (left); the color coding of the discs is relative to the distance from the center of the black one. Figure taken from Eric Weeks' web page: http://www.physics.emory.edu/ weeks/idl/gofr.html

1.3.2 The structure in colloidal systems

Colloidal particles dispersed in a fluid move randomly due to collisions with the solvent molecules. Nevertheless, their positions are correlated due to the interparticle interactions; that is, the particles cannot take any arbitrary configuration but only those allowed by the direct interactions, producing, in this way, a local structure of the particles referred to as static structure. The physical quantities describing the static structure, such as the static structure factor and pair correlation function, can be determined by different experimental techniques. They can be directly calculated from their statistical mechanics' expression when the direct interparticle interaction is known. Thus, the precise determination of those interactions is one of the main issues in characterizing a colloidal suspensions since they determine system properties such as stability, phase transitions, and rheology.

A versatile class of liquid state theory methods that theoretically determine the micro structural and thermodynamic properties of atomic and colloidal liquids will be discussed from the knowledge of the particle interactions. These so-called integral equation schemes are based on the Ornstein-Zernike (O.Z.) equation. The quantity of central importance calculated with integral equation schemes is the radial distribution function, g(r), of an isotropic liquid and the associated static structure factor S(q). The latter property is essentially the Fourier transform of g(r) and can be measured using scattering techniques. The radial distribution function (rdf) quantifies the probability of finding a particle at some distance from any other one. Radiation scattering experiments can indirectly measure it whereas, from video microscopy, it can be directly measured.

1.3.3 Pair Distribution function g(r)

Perhaps the most common way of describing the packing structure of spheres is the radial distribution function, also known as the pair distribution function or g(r). Given an assembly of N particles whose coordinates are known, the radial distribution function tells us the probability P(r) of finding another particle at a distance between r and r + dr from any randomly chosen particle. For an isotropic system $P(r)4\pi r^2\text{dr} = \rho_N \text{g(r)} 4\pi r^2\text{dr}$ where ρ_N is the average number density.

If the positions of the particles are entirely uncorrelated, like in an ideal gas, then the probability is independent of r; if the system is arranged into a crystalline lattice, then the probability will be peaked at the lattice positions. There is no long-range order for liquids or amorphous systems like glasses; therefore, g(r) will decay to the ideal gas profile at large distances, but the presence of short-range order will transpire through the presence of peaks at small distances. Figure 1.8 shows how to build two-dimensional radial distribution functions from an amorphous assembly of discs.

The color coding relates the particles in the image on the left to the g(r) on the right. The particles have been colored according to the center-center separation with the black one; the probability of finding another particle at distances smaller than twice the particle radius from the center of the black one is zero due to the excluded volume. We then observe a peak at r = 2R corresponding to direct contact between the black particle and its nearest neighbors. Other peaks are found for the second, the third, and the fourth nearest neighbors, but they are progressively lower and broader, implying a larger distribution of distances. The suspension structure is lost after 3-4 particle diameters from the initial particles. Repeating this procedure for every particle in the image which constructs the system's radial distribution function. More formally, g(r) is obtained by performing the summation:

$$\rho g(r) = \frac{1}{N} \sum_{i=l}^{N} \sum_{j \neq i, j=1}^{N} \delta[r - r_{ij}] \tag{1.4}$$

where δ is the Dirac delta function and r_{ij} is the distance between particles i and j.

In the case of ideal spheres, g(r) is sharply truncated at r = 2R; for data taken from real confocal images, due to inaccuracies in locating the particles' centers and due to polydispersity, a low r tail is always present. Moreover, the position of the first peak of the radial distribution function gives a precise indication of the hard-spheres character of the interaction. For the case of ideal hard spheres, the position of the first peak of g(r) is independent of the suspension's volume fraction; two particles feel each other only when they come in contact, regardless of the presence of other particles. If the colloids are charged, they will be pushed away from each other at distances larger than their diameter, and therefore, the first peak of g(r) will be at a distance r > 2R; when the volume fraction is increased, particles are pushed closer together, and therefore the distance between nearest neighbors will decrease, yielding a shift in the first peak of g(r) towards smaller r.

The radial distribution function plays an essential role in studying liquid systems. This quantity can be determined indirectly by several experimental techniques, for instance, X-ray and neutron scattering (for atomic and molecular fluid), light scattering, and imaging techniques (for colloidal liquids and other complex fluids). From the theoretical point of view, g(r) can be obtained by various approximations and from computer simulations when the interparticle interaction is known. The static structure is also essential in determining physical quantities, such as the dynamic and other transport properties, as well as the thermodynamics of the system.

1.3.4 Ornstein-Zernike Integral equation(OZ)

From the theoretical point of view, the current method employed to compute the static structure of the fluid system is the Ornstein-Zernike integral equation (O.Z.), introduced by Ornstein and Zernike in 1914.

The O.Z. equation of a homogeneous and isotropic system is given by

$$H(r_{12}) = c(r_{12}) + \rho \int dr_3 c(r_{13}) h(r_{23}) \tag{1.5}$$

It introduces the direct correlation function, c(r), as a new function and can be viewed as the definition of c(r) in terms of the total correlation function h(r)=g(r)-1, of two particles a distance r=r_{12} apart. Eq 1.5 can then be recursively solved for h(r_{12}). Once the information is available about c(r) in the form of a closure relation involving potential U(r), the O.Z. equation can be viewed as the closed integral equation for h(r). Thus, given by

$$h(r) = c(r) + \rho \int c(|\vec{r} - \vec{r}\prime|) h(r\prime) d^3 r\prime \tag{1.6}$$

1.3.5 Various closure relations

Closure relations are independent second equations that connect the total correlation h(r) and the direct correlation c(r); the Ornstein-Zernike equation and a second equation are needed in order to solve for two unknowns: the total correlation h(r) and the direct correlation c(r). The word "closure" means that it closes or "completes" the conditions for a unique determination of h(r) and c(r). Diagrammatic and density functional theory methods can obtain these relations and a deeper understanding of the meaning of c(r). Combined with the O.Z. equation, the closures lead to closed integral equations for g(r). Compared with computer simulation results and scattering data, these integral equations are very useful in calculating dense liquids' full r-dependence of g(r) and thermodynamic properties. For a system with a hard-core excluded volume part in U(r), any closure relation should be consistent with the exact condition h(r)

$$h(r < \sigma) = -1, i.e. g(r < \sigma) = 0 \tag{1.7}$$

which states that two spheres of hard-sphere diameter σ cannot interpenetrate, and the asymptotic result

$$c(r) = -\beta u(r) \tag{1.8}$$

for r → ∞ valid for a wide class of pair potentials.

1.3.5.0.1 PY closure relation

The pair distribution function $g(r) = h(r)+1$ of a fluid can be derived recursively from the Ornstein- Zernike integral equation

$$h(r) = c(r) + \rho_N \int_V c|\vec{r} - \vec{r}\prime| h(r\prime) d^3 r\prime \tag{1.9}$$

The integration is carried out over the entire volume V. The Ornstein-Zernike integral equation provides an exact calculation rule and can be solved recursively by h(r_0) in the indirect correlation term is substituted by the entire expression. Therefore however, a final relation is required: The direct correlation function c (r) can be specified for the calculation. There are different approaches for the final relation with which the Ornstein-Zernike Integral equation can be solved. The Percus- Yevick (PY) closing relation especially [102].

$$c_{PY}(r) = g(r)(1 - \exp[\beta U(r)]) \tag{1.10}$$

One can also obtain the PY pair distribution function g_{PY}(r). Furthermore, the structure factor can be calculated analytically using the PY final relation [95]. Various algorithms for calculating the pair distribution function can be found in the literature, and the structure factor of the polydisperse PY fluid [95] [147] [67].

1.3.6 Static structure factor

The last section showed that measuring the pair correlation function requires the simultaneous determination of the position of N particles in a statistically significant portion of the system. The static structure factor S(q) can be derived from the Fourier transform of the local particle number density and is formally related to g(r). In the radially symmetric case, the Fourier transform for q≠0 is given by

$$S(q) = 1 + 4\pi\rho N \int_{r=0}^{\infty} r^2 (g(r) - 1) \frac{\sin qr}{qr} dr \tag{1.11}$$

In Figure 1.9 left, the PY pair distribution functions of the monodisperse fluid are at different volume fractions. The position of the principal maximum of the PY pair distribution function corresponds to the HS diameter. Before that, g(r) is constant zero because the particles are impenetrable. At greater distances, the curve shows a dampened oscillation, which drops to the value of one. With increasing packing density, the peaks' height increases, and the oscillations persist over several periods. While the first maximum position is always at the contact distance d_{HS}, the following peaks with increasing packing density to smaller distances, so particles move together. In Figure 1.9 on the right, the corresponding structural factors are plotted against the scattering vector q. The structure factor rises above the first peak. The further course performs a dampened oscillation; the asymptotic strives towards the value one. The maximum positions correspond to spatial frequencies that are particularly common. The first maximum position corresponds to the most frequently occurring particle distance, the closest neighbor distance via q≈$\frac{2\pi}{d_{NN}}$. With increasing packing density, the maxima become higher and narrower, and the positions of the maxima shift towards larger q values. The shift of the peak positions corresponds to the moving closer together of the particles in the spatial area.

The limit $q \to 0$ structure factor is linked to the isothermal compressibility S(q→0) $=K_T/K_T^0$ [10]. The quantity K_T^0 corresponds to the isothermal compressibility of the ideal gas. The structure factor is smaller than one for small q since the hard-sphere system is less compressible and is more compressible than the ideal gas. The structure factor decreases at higher densities q→0 continues, and the system becomes increasingly incompressible. The validity of the PY theory can be determined by a direct comparison of g(r) or S(q) and can be checked by comparing the equations of state with HS simulation data.

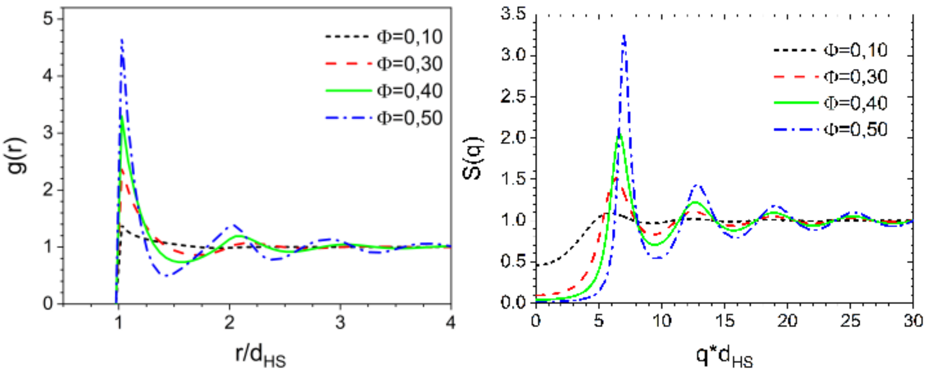

(a) **(b)**

Figure 1.9: (a) PY-g(r) for volume fraction ϕ= 0.1 to 0.5 for hard sphere and corresponding (b) PY-structure factor.

At low packing densities ($\leq$ 0.4), the PY pair distribution functions agree well with the simulations. The PY approximation provides a good description of these areas and the structure of the HS system. At higher packing densities, especially near the freezing volume fraction (ϕ_F = 0.494), systematic discrepancies occur in the pair distribution function between the PY approximation and simulations of hard spheres [209] [107] [106]. The contact value of the PY pair distribution function is lower than in computer simulations of a hard sphere fluid. The oscillations are also slightly out of phase and too weakly damped. The slow decrease in amplitude leads to an excessively high main peak in the structure factor. The peak value in the PY structure factor at the fluid phase boundary $\phi\approx$ 0.49 is 3.05 instead of 2.85, according to Hansen's and Verlet hard spherical fluid simulations . In simulations, it is also just below the melting volume fraction ($\phi>$ 0.45); a splitting of the second peak in g(r) and S(q) was observed [203] [139] [61].

1.4 Diffusion

A characteristic of colloidal suspension is that the colloidal particles are much larger and have a larger mass than the solvent molecules. Therefore, the solvent degree of freedom relaxes on a much shorter time scale than that of colloidal particles. Due to interactions with solvent molecules, the velocity fluctuations of the colloidal particles decay on a time scale over which the particles move only a distance that is a fraction of their size. This results in colloidal particles' diffusive(Brownian) motion [143]. The mean squared displacement$<(\Delta \mathrm{R})^2>$ as a function of time t for a sphere of diameter σ at infinite dilution is given by

$$< (\Delta R)^2 >= 6D_0 t \tag{1.12}$$

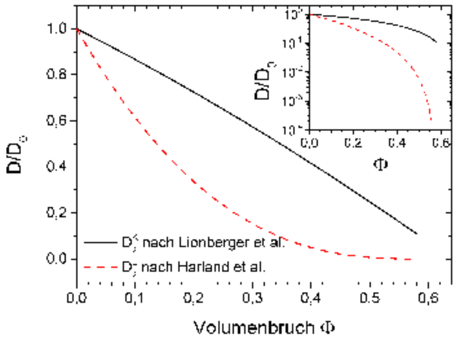

Figure 1.10: The short-term self-diffusion coefficient via equation 1.15 and the long-term self-diffusion coefficient via equation 1.17 as a function of the volume fraction. In the image, the courses are plotted logarithmically [114].

where D_0 is the Stokes-Einstein diffusion coefficient.,

$$D_0 = \frac{k_B T}{3\pi\eta\sigma} \tag{1.13}$$

with k_B Boltzmann's constant, T is the temperature and η the solvent viscosity. Particle interactions that cause crystallization will also influence this diffusion behavior. Here in the thesis, the rate densities are expressed in terms of D_0 and long time diffusion coefficient D_L^s.

1.4.1 Short-time regime

The particles move diffusively in the short-time regime (t$\ll \tau_B$). The distances covered are small compared to the particle radius. In this time range, the system's structure remains almost unchanged, and no structural rearrangement processes must take place to cover the diffusion path. The positions of the nearest neighbors are not affected by such a movement. The short-term self-diffusion is compared to the modified free diffusion. A linearly increasing mean square displacement characterizes the diffusion movement,

$$W(t) = 6D_s^K t \tag{1.14}$$

for $t << \tau_B$.

The proportionality factor D_s^K is referred to as the short-time self-diffusion coefficient. The short-time self-diffusion coefficient is linked to the hydrodynamic function and the structure factor via the equation D_s^K(q) = D_0H(q)/S(q). The formula of Lionberger and Russel can be used to describe the short time diffusion of a hard spherical fluid [121]:

$$D_s^K(\phi) = D_0(1 - \frac{\phi}{0.67})(1 - \frac{\phi}{3.7}) \tag{1.15}$$

1.4.2 Long-time regime

In the long-time regime ($\tau_B \ll$ t), the distances covered by the particles are so great that structural reorganization processes occur. The particles influence each other in addition to the hydrodynamic interaction via direct interaction. Again, the mean square of displacement in the long-time regime can be described as a linear function of time

$$W(t) = 6D_s^L t \tag{1.16}$$

for $t >> \tau_B$. D_s^L is the long-term self-diffusion coefficient. The D_s^L can be derived for the HS system using the semi-empirical formula

$$D_s^L(\phi) = D_0(1 - \frac{\phi}{0.58})^{2.58} \tag{1.17}$$

given by Harland et al. [79].

Figure1.10 shows the self-diffusion coefficients according to equation 1.15 and according to equation 1.17 as a function of the volume fraction. The D_s^L is, in general, smaller than the D_s^K. With a volume fraction of ϕ= 0.3, D_s^K (ϕ= 0.3) is $0.5D_0$, and D_s^L(ϕ= 0.3) is $0.15D_0$. For denser packing (ϕ= 0.5) D_s^K (ϕ= 0.5)is $0.2D_0$ and D_s^L (ϕ= 0.5) is $0.006D_0$. The long-term self-diffusion coefficient decreases dramatically as a function of volume fraction [114].

1.5 The Role of Polydispersity

Experimental hard spheres always have a distribution of particle sizes, which is quantified by the polydispersity. The polydispersity δ is typically defined as the standard deviation of the size distribution divided by the mean $\bar{R} = \frac{1}{N}\sum_{i=1}^{N} R_i$.

For the distribution of N particles with radii R_i, the polydispersity reads

$$\delta = \frac{1}{\bar{R}}\sqrt{\frac{1}{N-1}\sum_{i=1}^{N}(R_i - \bar{R})^2} \tag{1.18}$$

The polydispersity does not contain complete information about the size distribution of the particles. For example, the size distribution might be Gaussian, triangular, flat, or binary. Samples with small polydispersities are expected to behave essentially as hard spheres. For example, the PMMA particles that Pusey and van Megen used to study the equilibrium phase behavior of (nearly) hard spheres have a polydispersity of δ=5%. Rules to map polydisperse hard-sphere mixtures to a monocomponent hard sphere system work well in the fluid and reasonably well in the glass regime [173]. The equilibrium phase diagram changes for polydisperse samples [154] [19] [192] [59] [176] [159]. A possible equilibrium phase diagram for polydisperse hard spheres that also incorporates fractionation [59] [60] is sketched in Figure 1.11. For polydispersities $\delta > 0$, the freezing and melting points shift to higher volume fractions. A single crystal is only stable below a terminal polydispersity δ_t. Reported values of the terminal polydispersity include $\delta_t \approx 5\%$ [227], $\delta_t = 5.7\%$ [104] [25], δ_t≈6% [60] and δ_t≈7% [59]. Crystallization is observed with PMMA spheres having polydispersities of, for example, $\delta = 5\%$ [136] and δ≈ 8% [91]. In 1987, Pusey formulated a criterion for the terminal polydispersity [160], namely

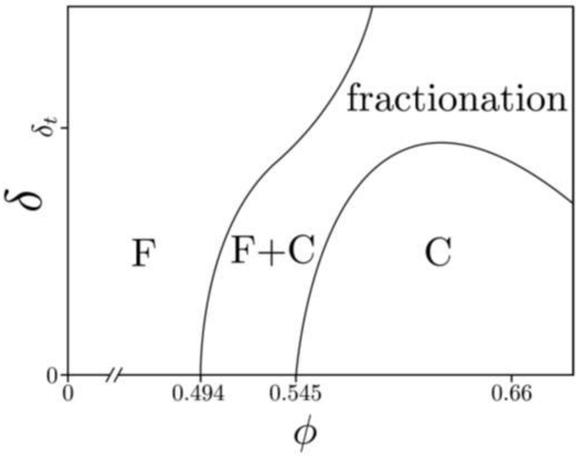

Figure 1.11: Schematic equilibrium phase diagram for hard spheres including polydispersity δ as a function of the volume fractions ϕ, according to Fasolo and Sollich [90, 93]. For $\delta = 0$, the phase diagram reduces to the equilibrium phase diagram for monodisperse hard spheres, as discussed earlier. Crystals (C) are only stable below a terminal polydispersity δ_t. Fractionation includes combinations of multiple crystals with different daughter size distributions and multiple crystals coexisting with a fluid (F).

$$\delta_t = (\frac{0.74}{\phi})^{\frac{1}{3}} - 1 \tag{1.19}$$

His idea is that a crystal becomes unstable once the particle size distribution contains particles whose diameters are more significant than the average particle-particle distance. This idea is similar to Lindemann's melting criterion, and generalized Lindemann measures have been studied with Monte Carlo simulations [100]. As indicated in the schematic phase diagram (figure 1.11) and Pusey's criterion (equation 1.19), the terminal polydispersity depends on the volume fraction.

1.6 Charged spheres (CS)

Charged colloidal particles in liquid electrolytes have vast industrial applications [22]. They can also be used as a model system for metals and alloys [85]. Understanding the stability and phase behavior as a function of colloid concentration and ionic strength is essential. Charged colloids exhibit a variety of order-disorder and structural transitions [35] [190] [118] [41].

This work will also consider charged colloidal systems. Charged colloidal particles can have a long-range repulsive potential and have a different phase behavior from uncharged colloids. Commonly used charged colloids are charge-stabilized particles in aqueous solutions, for example, polystyrene spheres. In the case of these systems, the charge arises due to ionizable groups on the particle surfaces, which mostly dissociate if the particles are dispersed in a polar solvent. It has already been demonstrated that sterically stabilized PMMA colloids carry a charge when suspended in certain organic solvents, such as cyclohexyl bromide

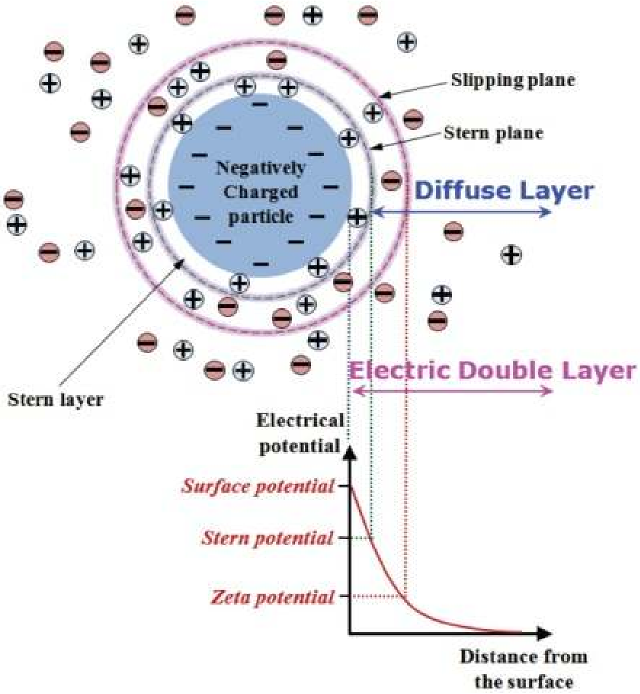

Figure 1.12: Schematic illustration of electrical double layer structure and the electric potential close to a solid surface with a stern and diffuse layer [128].

(CHB). Here, the charging mechanism is unknown. Under certain conditions, globular proteins can also be used as a system in which to study the phase behavior of charged colloids. In a vacuum, electrostatic repulsion between two like-charged particles remains at infinite separation. However, in solution, there are free ions 'i' from the dissociated ion-pairs on the particle surface, molecules of the solvent, and any additional salts. These free ions gather around the oppositely charged particles and create the electrical double layer (Figure 1.12).

The double layer can be modeled in terms of the Gouy-Chapman-Stern model, where it is treated as consisting of two parts. At the particle surface, there is a layer of ions that are specifically adsorbed (temporarily) with a force strong enough to overcome thermal agitation. This is known as the Stern layer. Ions with centers beyond the Stern layer form the diffuse part of the double layer, as illustrated schematically in Figure 1.12. The Debye screening length K^{-1} is the distance over which the potential decreases by an exponential factor, giving a measure of the thickness of the diffuse layer. Thus, the electrical double layer screens the charge on the particle surface so that the electrostatic repulsion decays exponentially, and the Debye screening length K^{-1} measures the length over which the electrostatic repulsion decays.

Figure 1.12 shows the effect of the negatively charged colloid on the positive ions (often called counter-ions) in solution. Initially, attraction from the negative colloid causes some of the positive ions to form a firmly attached layer around the surface of the colloid; this layer of counter-ions is known as the Stern layer. The negative colloid still attracts additional positive ions, but now they are repelled by the Stern layer, and other positive ions are also trying to approach the colloid. This dynamic equilibrium results in the formation of a diffuse layer of counter-ions. They have a high concentration near the surface, gradually decreasing with distance until they reach equilibrium with the solution's counter-ion concentration. In a similar but opposite fashion, there is a lack of negative ions in the neighborhood of the surface because the negative colloid repels them. Negative ions are called co-ions because they have the same charge as the colloid. Their concentration will gradually increase with distance as the positive ions screen out the repulsive forces of the colloid until equilibrium is again reached. The attached counter-ions in the Stern layer and the charged atmosphere in the diffuse layer are what we refer to as the double layer. The thickness of this layer depends upon the type and concentration of ions in the solution. When a colloidal particle moves in the dispersion medium, a layer of the surrounding liquid remains attached to the particle. The boundary of this layer is called the slip plane (shear plane). The slip plane is where the Stern layer and diffuse layer meet, and it is here that the electrical potential is called the zeta potential.

1.6.1 Phase behavior of charged colloids

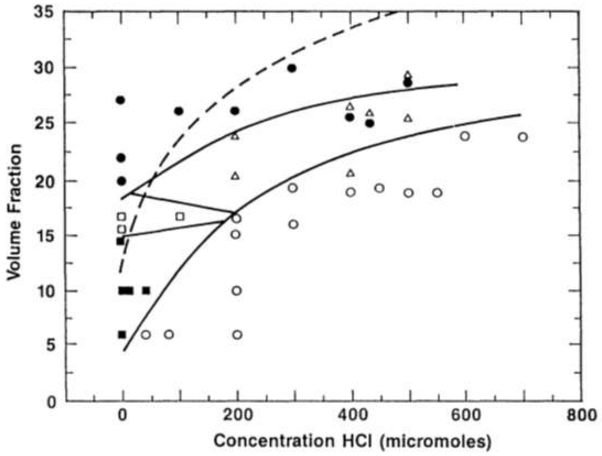

Figure 1.13: Phase diagram for 0.091 polyballs in 0.9-methanol- 0.1-water suspension as a function of concentration ϕ, and electrolyte concentration C_{HCl}. Solid squares, bcc crystal; open triangles, fcc crystal; open squares, fcc+bcc coexistence; closed circles, glass; open circles, liquid. Solid lines are "guide to the eye" phase boundaries. The dashed line is the fcc-liquid theoretical phase boundary for a similar point-charge Yukawa system [190].

At low ionic strengths, the long-range electrostatic repulsion between charged spheres induces a phase transition at a volume fraction as low as 10^{-3} with characteristics similar to that of hard spheres [71] [72]: (i) The order phase can diffract visible light via Bragg scattering showing brilliant opalescence. (ii) The disordered phase can be obtained from the ordered phase by diluting or adding excess electrolytes. (iii) The width of the fluid-coexistence regime is narrow. Such a disorder-order transition can be explained using an effective hard-sphere model [165] [71] [155] [207] [155]. At relatively high ionic strength, the Debye length K^{-1} is much shorter than the interparticle distance.

$$K^{-1} \approx \left(\frac{(ez)^2 n_b}{\epsilon_r \epsilon_0 k_b T}\right)^{(-1/2)} \tag{1.20}$$

If the valence of the positive and negative ions is z=1 and n_b is the concentration of ions. In such a case, each particle is surrounded by its double layer and behaves electrically neutral unless it approaches another particle so that their electric double layers interact (Fig 1.14). Introducing an effective hard-sphere radius $R^* =$ R+K^{-1} and an associated effective volume fraction, $\phi^* =$ n($\frac{4}{3}\pi$)R^{*3} = ϕ(1+$\frac{K^{-1}}{R}$)^3, the crystallization and melting phase transitions take place at ϕ^*_f = 0.494 and ϕ^*_m = 0.545, consistent with the hard-sphere model [8] [71] [155]. The phase diagram produced by Hachisu et al. [71] for aqueous polystyrene (PS) suspensions is the first complete investigation on order disorder transition available before studying PMMA hard spheres.

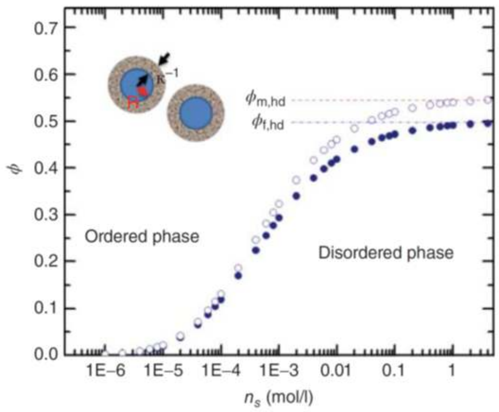

Figure 1.14: Order-disorder phase diagram of charged spheres as predicted by the effective hard-sphere model (suspension of R=50 nm particles in water, B=0.7 nm). The phase transition depends on the solvent's ionic strength and the particles' volume fraction [71].

The apparent weakness of the effective hard-sphere model is that it oversimplifies the interparticle interactions and excludes the possibility of crystallization into other than close-packed structures. Charged colloids crystallize into body-centered-cubic (BCC) crystals at low n_s for highly charged colloids. Figure 1.15 presents the experimental phase diagram of P.S. spheres, diameter 91 nm, suspended in 90% methanol-10% water solution [190]. The particles have a surface charge of 500e. The observed FCC-BCC-fluid triple point is located at an acid concentration of n_s, HCl = 200 µ M, and particle volume fraction of ϕ= 0.17. Monovoukas and Gast obtained an FCC-BCC-fluid triple point for n_s, HCl = 2.65 µ M and ϕ = 0.083 for aqueous suspensions of PS spheres of 66.7 ± 0.5nm in diameter and a surface charge of 1200±40e per particle [133]. The phase diagram for spheres interacting with a hardcore repulsive Yukawa potential has been determined using computer simulations (Fig.1.15) [92]. For sufficiently high contact values of the pair potential (e.g., $\epsilon k_B T > 20$), BCC crystals form in the low salt, weak screening regime ($\frac{1}{K\sigma}$ close to 0.5 in Fig.1.15), while FCC crystals form for high screening. The coexistence of fluid and BCC, BCC, and FCC for volume fraction $\phi < 0.5$ is well described by the phase boundaries of point Yukawa particles. Therefore, similar to the formation of Wigner crystals in the case of electrons [120], charged spheres crystallize and transition from BCC to FCC in the weak screening regime to minimize electrostatic repulsion energy. They constitute an example of enthalpy-driven phase transitions [74] [55]. Figure 1.15 also shows that the hardcore favors the FCC for ϕ>0.5, independent of the screening. This transition, in contrast, is an example of an entropy-driven phase transition. All the phase coexistence regions in the phase diagrams for the hardcore repulsive Yukawa system are very narrow, with only a small density jump for the coexisting phases.

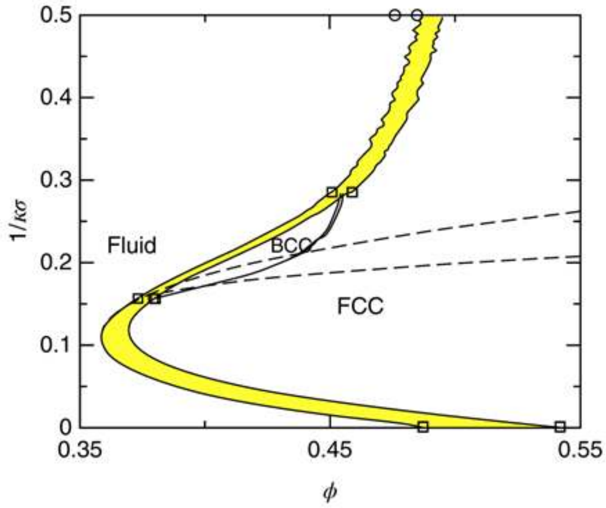

Figure 1.15: Phase diagram of the HS-Yukawa model. The strength of the Yukawa interaction at the contact distance is $U(d_{HS}) = 8k_BT$. The inverse coupling parameter $\lambda^1 = 1/(\kappa\sigma)$ and the volume fraction η are plotted. The HS diameter is referred to here as $\sigma = d_{HS}$. The illustration is taken from [92].

1.6.2 Mean-spherical Approximation (MSA)

The exact asymptotic form of c(r) forms the basis of the so-called mean-spherical approximation, first introduced into liquid state theory by Lebowitz and Percus (1966). In MSA, c(r) is assumed to be given approximately by the closure relation

$$c(r) \approx \beta u(r) \qquad (1.21)$$

for all non overlap distances r $> \sigma$

Together with Eqs.1.7 and 1.21, the O.Z. equation 1.6 becomes a non-linear integral equation determining g(r) for r $> \sigma$ and c(r) for r $< \sigma$. The most attractive feature of the MSA closure, as compared to other ones, is that analytic solutions exist, even in the many-component case, for various pair potential models, namely for the hard and sticky hard-sphere potentials, the square well potential, the Coulomb potential, attractive and repulsive Yukawa-type potentials, and for the dipolar hard-sphere potential. These potentials are particularly interesting for molten salts, electrolyte solutions, and colloid science. No analytic MSA solution exists for the Lennard-Jones potential. While the MSA is well suited for short-range attractive and repulsive potentials, it can predict non-physical negative values for g(r) close to contact distance in the case of dilute systems of strongly repelling particles. At very low density, more precisely, small volume fractions ϕ, the MSA predicts that

$$g(r) = 1 + c(r) + O(\phi) \approx 1 - \beta u(r) + O(\phi), r > \sigma, \tag{1.22}$$

with a negative g(r) for βu(r) > 1.

1.6.3 Rescaled MSA (RMSA) and Penetrating background RMSA (PBRMSA):

For fluids of colloidal particles, where strong and long-range repulsive forces mask the physical hard core, an improved variant of the MSA preserves the positive semi-definiteness of g(r). This variant is the rescaled MSA [76]. It is based on the fact that such systems' g(r) is continuous at all distances r. Moreover, and most importantly, two particles in these systems are virtually never closer to each other than a certain distance $\sigma^{'} > \sigma$, so that g(r) $\approx$ 0 for r $< \sigma^{'}$.

In RMSA, the actual system is replaced by a fictitious system consisting of particles of enlarged diameter $\sigma^{'} > \sigma$, at the same number density ρ and, for r $>\sigma^{'}$, with the same pair potential u(r) as the original one. The (density-dependent) effective diameter, $\sigma^{'}$, is determined from the continuity of g(r) at r $= \sigma^{'}$, by demanding that g(r $= \sigma^{'}$; ρ, $\phi^{'}$) = 0, with g(r) calculated in MSA for a larger rescaled volume fraction $\phi^{'} = \phi(\sigma^{'}/\sigma)^3 > \phi$. The RMSA-g(r) is positive semi-definite since the fictitious system's volume fraction, $\phi^{'}$, is so much larger than ϕ that eq.1.22 no longer applies.

Once Z has been adjusted to fit the peak height, the semi-analytical RMSA solution remarkably predicts the overall g(r) shape. The RMSA has been extended to multi-component systems of mutually repelling Yukawa particles. The rationale behind this idea is that the repulsion between the particles is so strong that the hard sphere part of the potential is negligible anyway so that an increase of the diameter does not really change the interactions but still has an influence on the static correlation functions. A problem of RMSA is that it tends to underestimate the principal peaks of g(r) and S(q) when compared to results from simulations, one has to increase the effective charge Z_{eff} or the coupling parameter artificially to get good quantitative agreement [74]. As a further improvement Snook and Hayter [191] argued that in the derivation of the DLVO pair potential the point-like micro ions (counter ions and salt ions) actually move freely in the whole volume, so that they are actually considered as being able to penetrate the large macro-ions (charged colloids). This leads to an effective decrease of the charge by a factor 1-ϕ that can be compensated with a rescaling to

$$Z^{*}_{eff} = Z_{eff}/(1 - \phi) \tag{1.23}$$

This correction has the name penetrating background RMSA (PB-RMSA), taking into account the penetration abilities of the micro ions. Heinen et al. [82] found that even PB-RMSA still underestimates principal peaks and they argue that the inclusion of a correction for the filling fraction ϕ of the colloids in the computation of the screening parameter κ together with the PB increase of the effective charge (also influencing κ) would be a double correction of κ. To this end they propose to modify κ again as $\kappa_{mod}{=}\kappa\sqrt{1-\phi}$ essentially increasing the screening length, which is proportional to $1/\kappa$. The coupling parameter is also affected as it depends on κ. This modified PBRMSA (MPB-RMSA) scheme performs better compared to the other MSA schemes and is also in quite good agreement with Monte-Carlo simulations. Only compared to the Rogers-Young scheme (RY), which combines both HNC and PY closures and directly imposes thermodynamic consistency, the agreement with simulations is slightly worse in some situations: MPB-RMSA produces a kink at the rescaled diameter $\sigma\prime$ which is smoothed out with the RY scheme and MPB-RMSA slightly underestimates the principal peak of g(r) at high particle densities. On the other hand, also at high densities, the principal peak of S(q) according to MPB-RMSA is sometimes in better agreement with simulations than that computed within the RY scheme [74]. Since the height of the principal peak is particularly important for MCT calculations, MPB-RMSA is thus a good choice for the purpose of this work. Another big advantage is the fact that it is an analytic solution, so the computation is a lot faster than doing a scan for numerical solutions of the RY equations. For this work the author is very grateful having received PB-RMSA software directly from M. Heinen. For more detailed descriptions and performance comparisons the reader is referred to [74].

1.7 Crystal Nucleation

Nucleation processes are ubiquitous in both natural and artificially synthesized systems. However, a nucleation event is often rare and difficult to examine experimentally and theoretically. Phase transitions, such as crystal nucleation from a supercooled fluid, are central to condensed matter physics. As a thermodynamic quantity, such as temperature or pressure changes, phase transitions occur when a fundamental reordering of the material becomes energetically favorable. Thermodynamic quantities are known to change discontinuously at a phase transition. Therefore, transitions are classified as first-order transitions if a first derivative of the free energy shows a discontinuous change and second-order transitions if the first derivatives are continuous. However, a second derivative of the free energy shows a discontinuous behavior.

Colloidal systems are the ideal model systems for studying nucleation phenomena. Nucleation and the proceeding crystallization in such systems often take place on experimentally accessible time scales, and due to the size of the particles, they are accessible to a wide variety of scattering and imaging techniques, such as confocal microscopy [49], holography [115], light and X-ray scattering [206]. Additionally, progress in particle synthesis, solvent manipulation, and the application of external fields allows for significant control over the interparticle interactions, allowing for studying a large variety of nucleation processes. Theoretically, the hard-sphere system is one of the most straightforward systems that can be used to study colloidal and nanoparticle systems and investigate the nucleation process. It is ideal for examining various computational methods for studying nucleation and comparing the results against the experimental data. Such simulation methods include molecular dynamics (M.D.) simulations, umbrella sampling simulations (USS) [201], forward flux sampling (FFS) [7], and transition path sampling (TPS) [45]. The nucleation rates have been measured using light scattering by Harland and van Megen [78] and Sinn et al. [189], in real space experiments, and simulations by Auer and Frenkel [12]. However, the simulations and the experiments do not seem to agree. The reason for this study is to try to understand the discrepancy between simulations and experiments.

1.7.1 Classical Nucleation Theoary(CNT)

Classical nucleation theory (CNT) is the simplest theory to describe nucleation. Small crystal nuclei are continually formed in a fluid due to thermal fluctuations. Most of these small nuclei quickly melt away; however, when the fluid is supersaturated, these nuclei can grow out. CNT assumes that the free energy of making these small nuclei is a surface-free energy cost and a bulk-free energy gain. The Gibbs free energy displays a maximum at the critical size, and when a nucleus is larger than this critical size, the chance of growing out exceeds the chance of melting back into the fluid. With CNT, the nucleation barriers can be predicted and compared with simulations. When the kinetic prefactor is known, nucleation rates can also be obtained from these barriers.

In CNT, it is assumed that the free energy for making a small nucleus is given by a surface free-energy cost proportional to the surface area of the nucleus and a bulk free-energy gain proportional to its volume. More specifically, according to CNT, the Gibbs free-energy difference between a homogeneous bulk fluid and a system containing a spherical nucleus of radius R is given by

$$\Delta G(R) = 4\pi\gamma\ R^2 - \frac{4}{3}|\Delta\mu|\rho_s R^3 \tag{1.24}$$

where $|\Delta\mu|$ is the difference in chemical potential between the fluid and solid phases, ρ_s is the density of the solid, and γ is the interfacial free-energy density of the fluid-solid interface.

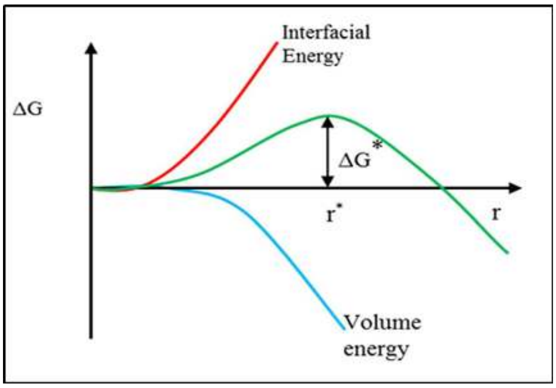

Figure 1.16: Schematic representation showing the dependence of nucleation barrier ΔG(R)* on the radius r according to classical nucleation theory [97].

This free-energy difference is usually referred to as the nucleation barrier. From this expression, the radius of the critical cluster is found to be

$$R^* = 2\gamma/|\Delta\mu|\rho_s \tag{1.25}$$

and the barrier height is

$$\Delta G(R)_{crit} = 16\pi\gamma^3/3\rho_s^2|\Delta\mu|^2 \tag{1.26}$$

1.7.2 Heterogeneous Nucleation

Homogeneous nucleation is often forestalled due to heterogeneous nucleation on seeds, which can be much faster than homogeneous nucleation in the bulk if the free energy barrier is reduced by the presence of the seed. This depends on the surface tensions between seed and fluid, γ_{fs}, and between seed and crystal, γ_{cs} The free energy barrier for heterogeneous nucleation is given by

$$\Delta G(R)_{het} = A_{cs}(\gamma_{cs} - \gamma_{fs}) + A_{cf}\gamma_{cf} - V_c n_c \Delta\mu \tag{1.27}$$

where γ_{cf} is the surface tension between fluid and crystal,A_{cs} denotes the area between crystal and seed, A_{cf} is the area between crystal and fluid, and V_c is the volume of the crystal nucleus. The effect of the seed is determined by the relation of the three surface tension in the above equation.

If γ_{cs}-γ_{fs} $>$ γ_{cf}, the total surface energy is larger than for homogenous crystal nucleation, and consequently, heterogeneous nucleation is slower than homogenous nucleation. In the case , γ_{cs}-γ_{fs} $<$ -γ_{cf} the barrier vanishes with increasing contact area between crystal and seed. Therefore, the crystal wets the seed surface and forms spontaneously. Finally, the intermediate case,
-1$<\frac{\gamma_{cs}-\gamma_{fs}}{\gamma_{cf}}<$1,
leads to partial wetting of the seed with crystal. The surface tensions exert pressure on the contact areas between the phases that tend to reduce these areas. The equilibrium of the forces on the contact of seed, fluid, and crystal defines the contact angle θ. For a flat seed surface, θ is given by

$$cos\theta = \frac{\gamma_{cs} - \gamma_{fs}}{\gamma_{cf}} \tag{1.28}$$

In this case, $\Delta G(R)_{het}$ can be simplified using θ, and it is found to be the same as $\Delta G(R)_{hem}$ up to a factor determined by the contact angle alone:

$$\Delta G(R)_{het} = \Delta G(R)_{hem} f(\theta) \tag{1.29}$$

where $f(\theta)$ = (1/4)(2+$cos\theta$)(1-$cos\theta$)^2. While θ is routinely measured with, e.g., liquid droplets on a surface, a microscopic determination of θ from small crystal nuclei on a seed in a colloidal contact between seed and crystal nucleus is irregular. It does not allow for a determination of θ.

As for the homogenous crystal nucleation outlined above, the formation of critical nuclei in heterogeneous nucleation does not proceed as straightforwardly as expected from CNT; precritical nuclei are not as well defined as assumed. Therefore, studies of heterogeneous crystal nucleation are needed to obtain a complete picture of the formation of critical nuclei.

1.7.3 How to suppress Heterogeneous nucleation

Introducing periodically structured substrates can enhance the nucleation and crystallization scenario's influence. The nucleation of structured substrates cannot be considered within the framework of the CNT. However, structured substrates have been used in several theoretical papers [84] [83] [57] and simulations [223] [51] [30]. In theoretical work and simulations, the wetting behavior of hard spheres was investigated in the presence of periodically structured substrates.

The introduction of structured substrates was found to induce the formation of crystalline layers under the fluid-crystalline phase boundary [83]. When the substrate was structured with the (111) plane of an FCC crystal, a hexagonal layer was formed and the crystalline phase completely wetted the substrate. Different structures like the (100) - or (110)-the FCC crystal and rhombic structures resulted in incomplete wetting [57]. By specifying a crystal structure through a structured substrate, extensive monocrystals are grown [204] [88], and metastable crystal phases for long periods are kept stable [223] [87]. In addition to the crystal structure variation, the lattice spacing of the crystalline layer can be varied. In this case, the ratio between the lattice constant of the substrate lattice g_{Sub} and a coexisting volume crystal g_{FCC} as a dimensionless measure of commensurability is introduced.

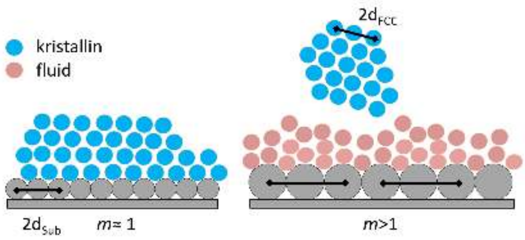

Figure 1.17: Scheme of the different wetting scenarios. Blue particles represent crystalline order configuration, pink particles symbolize fluid-ordered configurations. Left: commensurable Situation. Right: incommensurate situation. Shown is the lattice constant of the substrate and the equilibrium crystal [114]

$$m = \frac{g_{sub}}{g_{FCC}} \tag{1.30}$$

The parameter 'm' is called a mismatch parameter. For the undistorted case (m = 1), a commensurate situation is expected in which the Substrate is thoroughly wetted. Dorosz et al. showed in simulations that an altered crystallization scenario occurs when increasing distortion of the crystal is accompanied by a transition to incomplete wetting [51].

1.8 Crystallization Kinetics

The previous section described the nucleation process as a single event. As a rule, however, several nucleation processes occur in an ensemble. The nucleation rate density (NRD) J is necessary for describing nucleation kinetics. The number of growth-capable nuclei per volume and time unit defines it. The probability of finding critical nuclei is via the Boltzmann statistic associated with free enthalpy:

$$J = J_0 exp(\frac{-\Delta G_{crit}}{K_B T}) \tag{1.31}$$

The kinetic prefactor $J_0{=}\nu\rho_n$Z is a product of particle number density ρ_n, or inhomogeneous nucleation is the number of possible nucleation sites per unit volume and the Zel'dovich factor Z, defining the probability for the nucleus to cross the barrier and growing into a crystal after reaching the top of the free energy barrier. The factor ν is the rate of particles attaching to the critical nucleus, driving its growth. The kinetic prefactor can be calculated using model assumptions. For crystallization in colloidal HS systems with particle radius a, the kinetic prefactor is given by [217]

$$J_0 \propto (2a)^{-5} D_L^s \phi_{crystal}^{-1/3} \phi_{fluid}^{-5/3} \gamma_{fc}^{1/2} \tag{1.32}$$

The dynamics of the system are incorporated via the long-term self-diffusion coefficient D_L^s. It is also considered that the crystal and the fluid can have different packing densities. Dimensionless quantities are used for comparison in literature. With the reduced interfacial tension

$$\gamma^* = \gamma_{fc} \frac{2R^2}{K_B T} \tag{1.33}$$

and the reduced chemical potential

$$\mu^* = \frac{\mu}{K_B T} \tag{1.34}$$

results for the reduced potential barrier

$$\gamma^*_{crit} = \frac{\gamma_{crit}}{K_B T} = \frac{4}{27} \frac{\pi^3 (\gamma^*)^3}{(\phi_{crystal} \Delta\mu^*)^2} \tag{1.35}$$

Likewise, the nucleation rate density can be normalized for comparison:

$$J^* = \frac{J(2R)^5}{D_L^s} \tag{1.36}$$

The reduced sizes are independent of the system-specific particle size and particle dynamics.

1.9 Conclusions and New Direction

Have we understood the nucleation mechanism fully? The answer is a qualified yes for a very simple system, that of monodisperse hard spheres. Computer simulation results for homogeneous nucleation agree with the experiment to within a couple of orders of magnitude [145] [12] [16], which, given the extreme sensitivity of the rate, can be considered quite good agreement. Also, heterogeneous nucleation at a hard wall has been studied [11] and shown to be orders of magnitude faster than homogeneous nucleation. Thus, monodisperse hard spheres in a container with rigid walls should freeze from the outside in. The answer is no in protein solutions, a much more complex system. Even for lysozyme, the most studied protein, there is still debate about whether the nucleation observed is homogeneous or heterogeneous [185] [232] [208] . Thus, the role of impurities is obscure. However, lysozyme dimers have been shown to affect the nucleation rate [28], and disordered porous media have been shown to induce nucleation in solutions where the nucleation barrier would otherwise be so large that no nucleation occurs [36] [37]. This is also true behavior observed by Dogic and Fraden [3] [75] in suspensions of long viral particles with added soluble polymer.

Microscopic methods are exceptionally well suited for studies of crystallization mechanisms and structural details and their distribution. Statistical uncertainty due to the restricted sample volumes studied can be overcome by repeating the experiments after carefully restoring the initial conditions. Therefore, in comparing experimental data to expectations from theory and simulation and vice versa, a crucial aspect is the statistical accuracy in each compared approach. The key advantages of using colloids for crystallization (phase transition) study are accessibility to individual 'particles' by optical methods in space and at convenient timescale in dynamics, adjustability of the morphology of colloids (size, shape, and their distributions), interparticle interactions (by chemical grating, electric, and magnetic fields), and concentration (by gravity, temperature, and temperature gradient). This research field of colloidal crystallization is making progress along several frontiers: (i) Capture the morphology of the nuclei, demanding refinement or new develop in nucleation theory; (ii) quantitatively understand the sensitivity of nucleation rate to the detail of interparticle interactions; especially the softness of near-hard spheres; (iii) incorporate novel techniques to measure the crystallization kinetics, such as droplet microfluidics for emulsion crystallization investigation, and microgravity environment for long-term observation; (iv) bridge to close fields, such as melting, crystal-crystal transformation, phonons, kinetics of defects in crystals and amorphous solids; (v) develop applications of colloidal crystals, such as the fabrication of photonic crystals and chemical sensors.

Future progress will require quantitative experimental studies of nucleation rates, experimental studies in which nuclei are imaged, as Gasser et.al. [69] did, and detailed simulation studies. In the experimental studies, care should be taken to determine whether the nucleation is homogeneous or heterogeneous. For example, if adding impurities or removing them via purification alters the nucleation rate, the nucleation must be heterogeneous. Unfortunately, demonstrating that the nucleation is homogeneous is harder.

1.10 Outline of the thesis

The thesis aims to address various aspects concerning the structure of the HS system in real space and the crystallization kinetics at the particle level. One main aim is to address the real reason for the observed discrepancy in rate density between the experiment and simulation. No microscopic experiment has been done over a wide range of volume fractions on a particle level. The study of this type could be a direct comparison to simulations.

This thesis is organized as follows. First, sample preparation and particle characterization techniques have been introduced in Chapter 2. Detailed information is given about the colloids and solvents used in sample preparation, in particular, preparation of known volume fraction along with density match procedure. The principle of confocal microscopy and using image analysis to get the particle coordinates, along with errors associated with the position, is explained in Chapter 3. The details involving the analysis of data is given in chapter 4. In Chapter 5, the pair correlation function and structure factor as a function of volume fraction for three different colloidal systems have been studied. The main aim is to study the global properties of the hard-sphere system and its comparison to theory. In Chapter 6 details of crystallization study and the method applied to study homogeneous nucleation is given. The method allows the acquisition of large data sets composed of 10^6 particles. Also, temporal evaluation of individual clusters using Visual Molecular Dynamics(VMD) and the type of cluster favorable during nucleation have been studied. It also focuses on explanation of the different methods to get rate density and possible reasons for deviation in rate density has been explained. Also, several methods from various groups are proposed to find the local structure and type of cluster favorable during crystallization. In chapter 7, all those methods have been reviewed and compared with confocal data sets. Mainly Crystallization kinetics is studied and interplay of density and bond order parameter is explained in detail. Finally, chapter 8 describes the dynamics of the hard-sphere system during nucleation event at the middle of coexistence region is given.

Chapter 2

Sample preparation and Characterization

This chapter starts with a brief introduction to colloidal model systems and solvents used in this thesis, followed by sample preparation. It covers the systematic comparison of PMMA particles in three different solvent combinations suitable for confocal studies. The PMMA particles were first comprehensively characterized in size, mass density, and refractive index (RI). Details on the procedures followed to obtain index and buoyancy matching are presented, and we also stress the different behavior of the colloidal system in various solvents. In the following, the description of the methods used to calculate the suspensions' volume fraction is given. Finally, a brief description of the sample cell preparation used throughout the experiment and the importance of coating the sidewalls and the base is explained.

2.1 Experimental system

The colloidal systems used in this work consist of poly-methyl-methacrylate (PMMA) spheres sterically stabilized by grafting a layer of short polymer chains onto their surface. The polymer chains stretch out and stabilize the colloids against aggregation in a suitable solvent; the colloidal particles effectively interact as hard spheres like particle. Depending on the solvent, the PMMA particles can also acquire charges which soften the interaction potential; the charges can be screened by adding salt to the suspension, which may re-establishing hard-sphere repulsion.

2.2 The particles and solvents

The particles used in this thesis have a diameter of 1.4µm with a size polydispersity of 5.6%, sterically stabilized by a chemically grafted layer of PHSA (figure 2.1). The thickness of these layers is about 5-20 nm, a tiny fraction of the radius. The repulsive potential due to polymer layers is relatively steep, giving rise to hard-sphere-like interaction. The particles used in this work have been prepared in Edinburgh (School of Physics) by Dr. Andrew B. Schofield. They are now almost a standard for modeling hard-sphere systems. The synthesis goes via dispersion polymerization [110],[26],[32],[52]. In addition, stabilizing the PHSA layer creates a positive barrier between the particles to avoid flocculation. Interaction between these layers of two adjacent particles results from a strong enough repulsion between the surfaces sufficient to dominant against the van der Waals attraction. Nevertheless, When two particles come closer, they tend to stick to each other. At this moment, by matching the refractive index of the particles to the solvent, van der Waal's forces become very small and hard sphere-like behavior is obtained.

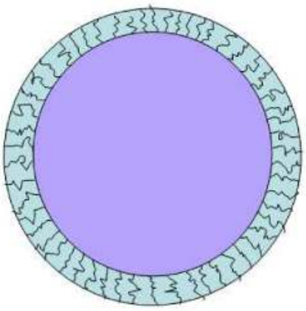

Figure 2.1: Schematic representation of sterically stabilized colloid with a presence of PHSA layer. The core diameter (violet) is 1.388 µm and the PHSA hair-like structure is about 20 nm [21].

In this work, we used different solvents: CDL(Cis-Decaline), a mixture of CDL and tetraline(TET), mixtures of CDL and TCE(TetraChloroEthylene), and CDL and CHB (Cyclohexylbromide)with and without TBAB (TetraButylAmmoniumBromide). A well-adjusted mixture of TCE and CDL simultaneously matches the particles' density and nearly refractive index. Another set of solvents used for the same particle is a mixture of CHB and CDL. It is speculated that the charge is originated by dissociation of functional groups on the surface of PMMA-PHSA particle. Thus, PMMA-PHSA particles dispersed in CHB have a measurable charge of up to several hundred elementary charges. Usually, one adds the salt TBAB to the solvent so that electrical charges are almost entirely screened and the particles appear as hard spheres [225]. The particles were stored in CDL until use. The particles are stained with fluorescent dye $DiIC_{18}$(1,1'-dioctadecyl-3,3,3',3'-tetramethylindocarbocyanine perchlorate). The spectra of this dye are shown in figure 2.2. Every dye has a specific set of spectra so that optimal excitation and detection can only be achieved within a small wavelength bandwidth. When excited, the dye absorbs photons leading to the shuttling of electrons to higher energy states. The electrons quickly return to the ground state and, in the process, lose energy and emit light. The emitted light is always of lower energy and longer wavelength than the excitation energy. The emission spectrum of the particles was measured with the confocal microscope SP8 and is measured by fixing the excitation wavelength and increasing it in steps of 10nm. Starting with λ =488 nm , the detected spectral ranges from 530 to 700 nm. The measured data agree well with the literature data. The literature reports that the dye fades slowly, generating no significant charge contributions [32].

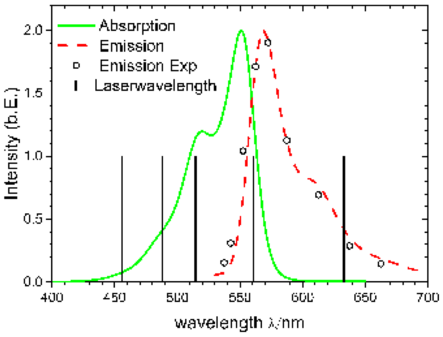

Figure 2.2: Absorption and emission spectrum of the fluorescent dye $DiIC_{18}$. The data points show the emission spectrum measured at known excitation wavelength in CDL / TCE starting from 488 nm. The vertical lines represent the laser wavelengths used in the experiment [114].

2.3 Solvents properties

There are a few criteria to characterize whether a given solvent mixture is good or not. The first is that the solvent must maintain the nearly HS behavior of the particles. It should not alter the interaction potential of the particles even under gravity match. Since the particles are sterically stabilized, the solvent must be suitable for PHSA layers. Secondly, the solvent must be chosen so that it matches nearly the refractive index of the particles. Usually, CDL is preferred, which has been more widely characterized. Also, the solvent should not penetrate the particles and have a slow evaporation rate. Preferably it should be harmless. While CDL is a nonpolar solvent with very low conductivity, CHB ($C_6H_{11}Br$) is more complex. CHB is brominated cyclohexane that has some tendency to dissociate by producing H^+ and Br^- ions. Charges are get absorbed on the surface , intern particles are charged. This means that any source enhancing dissociation should be excluded or set to a minimum. Dissociation can be induced by sonication, ultraviolet light, and heating; even more, extended storage will result in a higher ion density [167]. Therefore, samples were prepared with purified CHB (see below) not more than two months ago. The CDL was used as received from the manufacturer. For refractive index matches, TCE is used. For the system with CHB, different salt concentration varying from 1 µmol to 3.8 mmol of TBAB is used.

2.4 Storage and Purification of solvents

The particles are usually dispersed in Decaline (Sigma-Aldrich 99.9% pure) for storage and remain stable for years. Particles are first washed with CDL. For this purpose, the stock suspension is gently spun in a laboratory centrifuge at

Figure 2.3: First bottle containing CHB brought from sigma Aldrich without being subjected to filtering does not have a yellowish appearance; the second bottle contains CHB after the filter process. Even after storing it for a longer duration, it does not appear to have a brownish color.

300 rpm until the particles sediment. The supernatant is then removed using a pipette and replaced with filtered CDL(0.2 µm filter). Subsequently, the particles are re-dispersed in the sample vessel by keeping them on a rotating wheel. The procedure is repeated four times until the dispersion medium is completely replaced. At each step, the supernatant is withdrawn as long as a slight haze is still present. The aim is to remove small particles which are slowly sedimenting which are often present due to the synthesis.

As CHB (99.95 % purity, Sigma Aldrich) tends to dissociate, any source enhancing dissociation should be excluded or set to a minimum. It may have a very light yellowish appearance indicating the presence of bromide ions in excess. Then CHB must be purified as described below [225][167]. To remove Br_2 from the solvent, an equal amount of CHB and concentrated hydrochloric acid (37 % HCL) is taken in a separation funnel. After a good mixing, the low dense liquid will settle down, collected into a flask. In the following steps, the CHB is rewashed with deionized water, followed by sodium bicarbonate solution($NaHCO_3$) to neutralize any residual acid. This is again followed by deionized water. To remove moisture, 10ml of $CaCl_2$ is added to 250ml of CHB and mixed overnight. It is then separated by fritter glass filter and vacuum pump. The collected pure CHB is stored in an opaque glass bottle and stored in a dark place inside refrigerator.
In the picture 2.3 the first bottle refers to CHB brought from sigma Aldrich without being subjected to filtering. Even after storing it for a longer duration, it does not appear to have a brownish color, which suggest the purity of CHB. The second bottle contains CHB after the filter process which is used throughout the sample preparation. TBAB salt(Sigma Aldrich), which is hygroscopic in nature, is always kept in an air-tight desiccator filled with silica gel so that salt will not take up any moisture present in the surroundings. Humidity inside the desiccator is controlled using humidity meter. Water-free TBAB is then used to prepare solution of CHB until saturated, i.e., 3.8mM solution is obtained. It is continuously mixed for 7 days. All solvents were filtered before using a 200nm circular filter. In the picture 2.4 refers to mixture of CHB and TBAB. The picture was taken under visible light. The sample was maintained for more than 6 months to measure the changes appeared in the solution. After around a month of initial preparation, brown precipitation appears. As time goes by (6

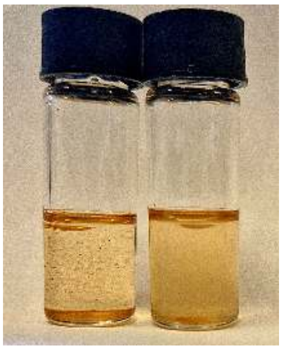

Figure 2.4: After around a month of initial preparation of the CHB+TBAB mixture, brown precipitation appears. As time goes by (6 months), the solution turns brown, suggesting the formation of Br_2 ions. Thus all measurements were performed within the 25 days before the dissociation of CHB starts. Every time new CHB with TBAB salt solution is prepared and stored in a cool and dark place to avoid dissociation and later used for sample dilution.

months), the solution turns brown, suggesting the formation of Br_2 ions. Every time new CHB with TBAB salt solution is prepared and stored in a cool and dark place to avoid dissociation and later used for sample dilution.

2.5 Particle charge

Since there are no functional groups at the surface of PMMA-PHSA particles that could dissociate, it is not clear yet why they exhibit an electric charge when dispersed in CHB. Leunissen [117] found no signs of electric charges in pure apolar solvents like CDL or CHB. They argue that the charges result from a dilute concentration of decomposed CHB leading to a small concentration of H^+ and Br^- ions. The protons would associate with the slightly polar carboxyl groups of the PHSA stabilizer and lead to an effective positive charge. Leunissen also mentions further that the protons could also associate with polar groups of the PMMA polymer network in the particle cores. A charge reversal can be observed upon adding a certain amount of the salt TBAC (tetrabutylammonium chloride) or TBAB. It can be explained by adsorbing Cl^- ions on the particle surfaces that first neutralize and then overrule the positive charges. Unlike Dinsmore et.al[49] and Leunissen [117] did not find the charge to be dependent on whether the particles were dyed or not. The schematic drawing of mechanism involved when PMMA particle acquiring positive charge is given the figure 2.5

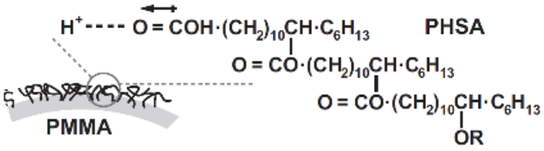

Figure 2.5: Schematic drawing of the mechanism by which the poly-12-hydroxystearic acid (PHSA) stabilized PMMA particles are thought to acquire their positive charge in cyclohexyl bromide. The HBr decomposition product of CHB partially dissociates, generating (solvated) protons. These protons can then associate with the somewhat polar carboxyl groups in the thin layer of steric stabilizer (ion-dipole association)[117].

2.6 Conductivity measurements

To estimate the ionic strength of a solvent mixture, we measured the conductivity of pure mixtures and its different concentration of TBAB in CHB. We used a conductivity meter, which is capable of measuring conductivities in the range of µS/cm to mS/cm(WTW LTA01, conductivity meter cond7110 with cell constant 0.1 1/cm). The final conductivity of 3.8mM TBAB-CHB solution was determined to be 0.7 µS/cm. Assuming a molar conductivity at finite dilution of 40nS/(cm µm) based on previous measurements[117] we obtain a degree of dissociation of about 0.005, which is in very good agreement with previous investigations[117]. Table 2.1 demonstrates the electrical conductivity of series of TBAB in CHB and mixture of CHB and CDL is presented at 23°C degree temperature.

solvents	conductivity in µS/cm	comments
CHB (not filtered)	0.05	–
CHB(filtered)	–	No results
1 µM TBAB in CHB	–	No results
10 µM TBAB in CHB	0.09	–
100 µM TBAB in CHB	0.12	–
CDL filtered	–	No results
CDL+ P.CHB	–	No results
U.CHB +3.8 mM TBAB	0.68	–
P.CHB+ 3.8 mM TBAB	0.69	–
U.CHB +3.8 mM TBAB + CDL	0.19	–
P.CHB + 3.8 mM TBAB + CDL	0.21	–

Table 2.1: Conductivity of different solvent and solvent mixture used throughout experiment. Here U.CHB refers to CHB taken directly from the bottle without subjecting to filtering process. P.CHB refers to filtered CHB as explained earlier.

2.7 Particle size

The particles were imaged using Scanning Electron Microscopy(SEM) and light scattering techniques to determine the core size. For this purpose, a submonolayer of particles was prepared on a cleaned silicon wafer. The SEM was

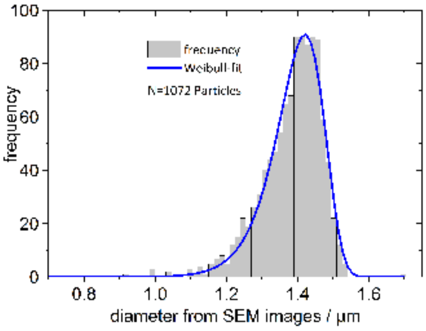

Figure 2.6: Particle size distribution by SEM (1072 particles). The blue line is a Weibull distribution fitted to the data. The mean diameter is 1.388±0.002µm and the size polydispersity 5.8± 0.1% [114].

operated at a low voltage of 0.2kV to avoid any charge effects on the non conductive particles. In SEM, particle size measurement was done for more than 1000 particles, which gives the distribution of particle size (figure 2.6). As seen from the figure, most particles are centered around 1.4 µm. The Weibull distribution describes the particle size distribution very well. The polydispersity from the Weibull distribution is 5.6 %, consistent with the polydispersity from the direct statistics.

The particle form factor and the diffusion constant are determined using static(SLS) and dynamic light scattering(DLS). The SLS radius and the hydrodynamic radius from DLS are given from the measured data. Both light scattering methods are based on a low concentration of suspension ($S(q) = 1$ in the entire q range). The SLS diameter is significantly larger in the CDL / TCE mixture than in pure CDL. The mean SEM diameter and the diameter measured in CDL by SLS are in good agreement. The particles' multiple scattering and optical inhomogeneities may explain the increased SLS polydispersity. Figure 2.7(a) shows the un-normalized particle form factor in the CDL / TCE mixture. For comparison, the particle form factor is shown for CHB and CHB+TBAB. The particle form factors in CDL / TCE after 1-5 days were measured and compared with Mie-form factors. Similarly $P(q)$ for CHB and CHB+TBAB is continuously maintained until swelling completed. Figure 2.7(b) shows the particle form factor in CHB and CHB+TBAB, shifted one over the other for better comparison. The fitted line corresponds to Mie form factors. As we can see the results shows that particle swell more in CHB and CHB+TBAB compared to TCE. The final resulting parameters are summarized in Table 2.2.

Methods	solvent	Diameter(2R/µm)	Polydispersity
SEM	dry	1.388± 0.02	5.6± 0.1
LSCM and wt% 1.19 g cm^{-3}	CDL+ TCE	1.389± 0.005	
SLS	CDL	1.393±0.02	6.2± 0.4
	CDL+ TCE	1.404± 0.02	6.3± 0.4
	CDL+ CHB	1.408± 0.04	6.3± 0.4
	CDL+ CHB+TBAB	1.4±0.003	6.4± 0.4
DLS	CDL	1.42±0.009	
	CDL+ TCE	1.429± 0.017	
	CDL+ CHB	1.457± 0.025	
	CDL+ CHB+TBAB	1.464± 0.02	

Table 2.2: Summary of particle diameters and polydispersities using different methods. SLS stands for Static light scattering and DLS stands for Dynamic light scattering.

2.8 Swelling behavior

Here we test the behavior of PMMA particles in three different solvents, an index-matching CDL-TCE mixture and an index-matching CHB-CDL mixture with and without the screening salt TBAB. In a time series, the swelling behavior of the particles in the mixture of CDL with TCE, CHB and CHB-TBAB was studied. For this purpose, a solvent mixture of TCE and CDL is used, to which a small amount of stock suspension is added. The particle form factor (P(q)) in a time series is measured. The first measurement was taken one hour after the preparation of the sample and the last one after five days. Similarly for solvent mixture of CHB and CDL with and without TBAB , small amount of stock was added and particle form factor is continuously measured until swelling is stopped.

The swelling behavior of the particles in the CDL / TCE mixture was determined by measurements of the particle form factor as a function of time. After an hour, an apparent deviation is recognized in the form factor. The position of the first minimums is shifted towards smaller scattering vectors. In contrast, the position of the second minima has not changed much. This course deviates from the scattering behavior of optically homogeneous spheres due to penetration attributable to the dispersant in the particles. On the other hand, a Mie form factor describes optically homogeneous spheres. According to 1, 2, and 5 days, the deviations between the form factors are not significant(figure 2.7(a)). The swelling process is therefore completed after one day in case of TCE. As a result, comparing form factors in pure cis-decalin and the CDL / TCE mixture gives a relative increase in particle radius. Similar behavior is found in the case of the CHB and CDL mixture. The CHB-CDL mixture took nearly seven days to have a stable particle size. For better clarity, measured P(q) for CHB after the completion of swelling is shown in the figure 2.7(b). The data is fitted by RGD form factor. The data suggests that CHB does not penetrate homogeneously because of core shell effect. As a result the RGD form factor shows deviation at the second minima. The core shell effect refers to the phenomenon where particles with a core-shell structure scatter light differently than particles without a core-shell structure. This is because the core and shell have different refractive indices, leading to an overall change in the scattering

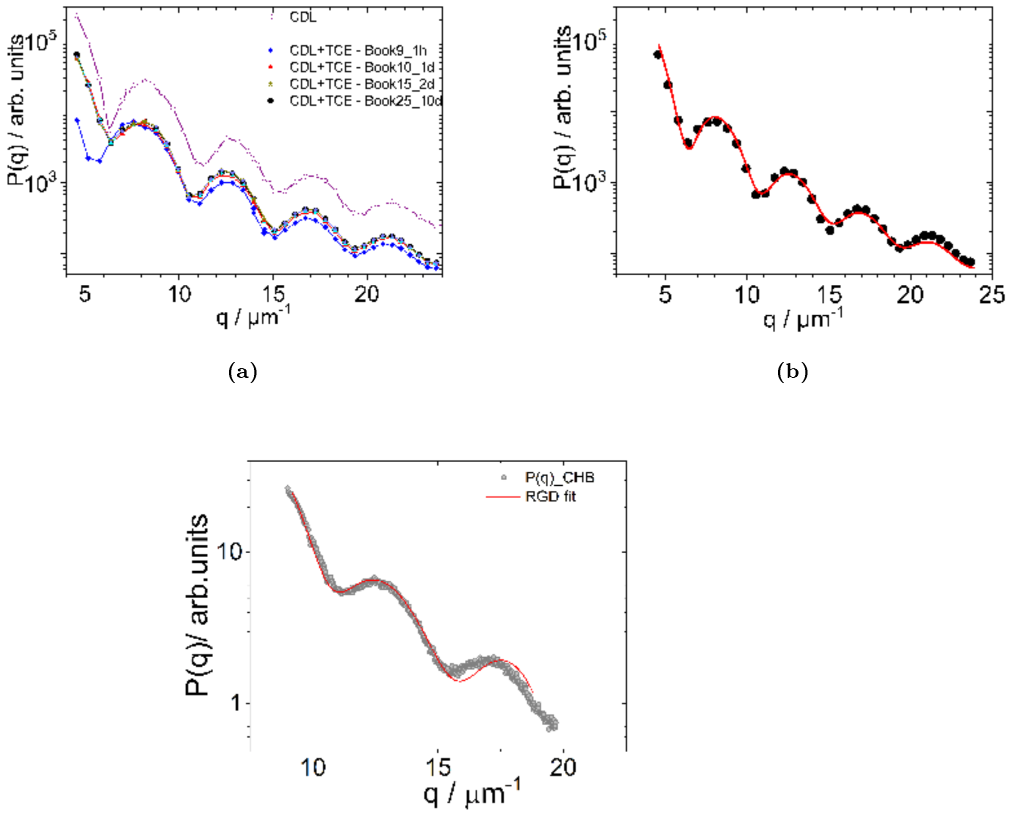

(a)

(b)

(c)

Figure 2.7: (a) Particle form factor in CDL+TCE mixture as a function of time [114].Swelling stops after 24 hr after mixing. (b) Particle form factor in CDL + TCE after swelling.The red line is a polydisperse Mie form factor fitted to the data [114]. (c)The measured form factor P(q) is for particles in CHB. RGD form factors are fitted to the data.

pattern. The deviation in the form factor with RGD form factor suggest this uneven absorption of CHB.

solvents	ρ in g cm^{-3}	η in mPas	n @ 23°C, 632nm
PMMA-particles ASM281B	1.189± 0.03		1.491
CDL	0.895± 0.001	3.13± 0.02	1.482
TCE	1.59± 0.1	0.93± 0.02	1.505± 0.001
CHB	1.32± 0.1	2.269± 0.02	1.493± 0.001
CDL+ TCE(48 vol% TCE)	1.189±0.003	1.37± 0.02	1.493±0.001
CDL+ CHB(76 vol% CHB)	1.189±0.004	2.29± 0.02	1.489±0.001
CDL+ CHB +TBAB(75 vol% CHB + TBAB)	1.189±0.004	2.3± 0.02	1.489±0.001

Table 2.3: The properties of the particles and solvents used are summarized. The refractive indices(n) were measured from the refractometer. Viscosity (η) is measured from Viscometer (RHEoSense m-VROC Viscometer). All the parameters are measured at 23°C. The volume fraction of solvent used for density match is given within brackets

2.9 Matching mass density and refractive index

Since gravitational force acting on a 'colloidal' particle is proportional to r^3 gravity quickly becomes essential while performing microscopic measurements at particle level. Therefore, the density mismatch between solvent and particles is crucial, and a new density match must be found. We also need to optimize the refractive index difference between solvent and particles to minimize attractive Van der Waals forces [213]. Values too small and large lead to poor contrast or too much turbidity for imaging. Therefore, choosing the solvents is more crucial.Controlling the temperature during centrifugation is very important since the density of solvent decreases faster with temperature than the density of the particles. During the density match procedure, the temperature was held constant at 23°C.

The sedimentation behavior of particles in solvent mixture under gravity is performed to determine the match point. A known amount of particles in CDL is taken, and a known volume of TCE/CHB is added. After a good mix, the mixture is centrifuged for an hour to accelerate the sedimentation. If the particles have risen to the top, indicating the solvent is too dense, additional CDL is added. If the particles sink to the bottom, the solvent is not dense enough, and additional TCE/ CHB/ CHB+TBAB is added. By measuring the height of the supernatant, one can determine the velocity with which particles and thus determine the density difference between the particle and solvent

The samples are spun in a centrifuge at 3000 rpm(100g) for about nine days. This accelerates the sedimentation and gets the correct amount of TCE/ CHB/ CHB+TBAB added for a good match. Correspondingly one can measure the distance traveled by particle or height of the supernatant and hence velocity which also gives the brief idea about the density of solvent mixture.(figure 2.8(a) and (b)). This procedure is continued until no sedimentation or creaming of particles occurs. Once the sample did not phase separately, a known amount (100-200 µL) of the suspension is taken from a calibrated pipette and weighed. The weighing is repeated at least 20 times, and the solvent mixture's mass density is found. In the last steps of the process, the addition of extra solvent was often enough to change the direction of particle movement. To get the correct ratio of the solvent mixture, the density of the different proportions of the solvent mixture is measured. The proportion of density match mixture is noted from the obtained density value. The density of the solvent ratio is then used to get the correct volume fraction to be used for the density match. The corresponding refractive index is also measured using a refractometer. The same volume mixture is used for preparing samples for confocal studies.

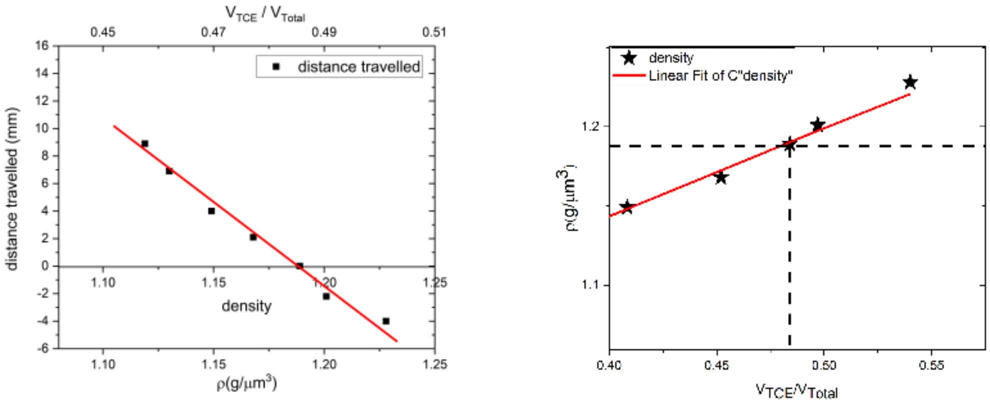

(a) (b)

Figure 2.8: (a) The plot of measured distance i.e distance traveled by particle for different density of solvent mixture. The density match point is where the guided line meets the x-axis. To obtain the a "perfect" match fine tuning is done and match point is determined as decribed in text. An extended point refers to the addition of more solvent showing particle motion in the opposite direction.(b) Plot of the density of suspension at various solvent compositions. The guided line refers to the point where density difference between particle and solvent are nearly equal.

The particles' refractive index(RI) was determined by turbidimetry [114]. Two diluted suspensions of identical volume fraction were prepared, one in CDL and another in CDL-TET. By varying the mixing ratio of CDL+TET, transmission through the suspension was determined using a turbid meter (λ=633nm) till the transmittance was maximized. At maximum transmission, the RI of the solvent is identical to the particles. The RI of the suspension was then determined using a refractometer (Abbe 60LR, Bellingham and Stanley) to be n=1.504. Table 2.3 gives an overview of solvent and solvent mixture properties at 23°C.

2.10 Determination of core volume fraction

The physical behavior of an HS system is determined solely by volume fraction ϕ and particle size distribution. In principle, it is possible to measure ϕ of the suspension by measuring its total mass, then removing all of the solvents, then measuring the total mass, which is assumed to be the mass of the particles.

A known suspension volume is allowed to dry until all the solvent has been removed. The weight fraction w_f is then given by

$$w_f = \frac{m_{dry}}{m_T} \tag{2.1}$$

Where m_T is the total mass of the suspension before drying and m_{dry} is its dry mass.

In order to minimize the experimental uncertainty, ten samples of 200 µL of suspension are placed on individual glass slides and dried in an oven for 24 hours at 120 degrees C. The corresponding mass was measured before and after drying using a high-precision scale (Kern ABT 220-8NM, Germany). The mass fraction of the stock was found to be w_f=0.341±0.00007. All samples in this study were prepared from this stock suspension. At first, the mass of the sample cell and its components (seal, lid) was determined with a high-precision scale. Subsequently, a known amount of the stock suspension was filled into this sample cell and weighed again. If the desired target concentration was higher than that of the stock suspension and/or the solvent composition had to be changed, the sample was centrifuged. The corresponding amount of CDL was removed, and the corresponding amount of the second solvent component (e.g., TCE) was added using high precision pipettes. The mass of the sample was determined after each preparation step. By this procedure, the mass fraction of the samples was tracked, and the concentration of the sample was known.

As the mass density of the particles and the solvent was known, the core volume fraction of the stock solution was calculated

$$\phi_{core} = \frac{V_p}{V_{susp}} = \frac{\frac{m_p}{\rho_p}}{\frac{m_p}{\rho_p} + \frac{m_{susp}}{\rho_{susp}}} \tag{2.2}$$

Here, V_p, V_{susp}, and $\rho_{p,susp}$ denote the volume, mass, and mass density of the particles in the solvent. In gravity-matched samples, the mass and core volume fractions are identical. The core volume fraction does not consider the stabilizing layer. Using LSCM, the number of particles N in the observed volume V_{sample} can be counted, which allows determining the particle number density ρ

$$\rho = \frac{N}{V_{sample}} = \phi_{core}/\frac{\pi}{6}(2R_c)^3 \tag{2.3}$$

which is linked with the core volume fraction and the (averaged) volume of a single particle in the dry state.

In colloidal suspensions with hard-sphere-like interaction, the hard sphere volume fraction can be determined by measuring physical observables as a function of particle concentration, whose behavior is precisely known from analytical theory and/or simulation-e.g., short-time diffusion, sedimentation velocity, equilibrium phase diagram, equilibrium fluid structure, equilibrium crystal structure, osmotic pressure. The known core volume fraction can then be scaled to the hard sphere volume fraction, whereby the correction factor α is the only fit parameter given by

$$\phi_{HS} = \alpha\phi_{core} \tag{2.4}$$

In the first approximation, the correction factor considers the particle's possible swelling and the stabilizing layer. It connects the core radius with the effective hard sphere radius $\alpha^{1/3} = \frac{R_{HS}}{R_c}$.

2.11 Sample cell

For colloidal studies, the sample cell required is nothing more than a chamber into which a suspension can be filled and sealed. It should also be optically suitable for microscopy. The confocal microscope works in a reflection mode, only the base of the sample cell needs to be optically suitable. The sample cell used here is appropriate for all samples, no matter how dense the suspension is.

2.11.1 Preparation of sample cell

For LSCM measurements, home-made sample cells with screw caps are used which allow a simple and very precise adjustment of the volume fraction. For sample cells, glass tubes with a thread of 12 mm diameter made of Duran are used. At the bottom, which was precisely cut and polished, a microscopy cover glass (thickness=0.17 mm) was glued on (Norland NAO 61). In order to mechanically stabilize this gluing point, a stainless steel ring of 3 mm thickness was glued to the cover glass and the glass tube, which was previously slipped over the tube. The pictorial representation is given below figure 2.9. Before filling with the suspension, the tightness of the container is checked. The sample can hold approximately 1ml of suspension. The sample containers were then cleaned with ultra pure water and Deconex (Borer Chemie AG) and dried in an oven. After that we tested the cells for leaks. They were filled with filtered CDL, and the total mass was monitored over several days. Only cells where the mass change was smaller than 0.01% within 7 days were used. Before the final sample preparation, the cells were rinsed with filtered CDL, dried and the dry mass of all components was determined again.

2.11.2 Suppression of Heterogeneous Crystallization

The cleaned glass slide is pre-coated with the aqueous suspension of PMMA particle size 2.33 µm to suppress the heterogeneous nucleation. Firstly, the cover slips are immersed in deconex solution(1% solution before working with Ultra pure water) for several hours and then rinsed with filtered ultra pure water(0.02 µm filter). Due to the intensive cleaning, adsorbents are removed from the coverslip, and the surface becomes hydrophilic, resulting in shallow and reproducible wetting angles. To this wetted area, 10 µl of the suspension (in this case, PMMA particle with size 2.33 µm) is added, and the sample is placed in a desiccator filled with NaCl solution with a constant high relative humidity of 83%. The slow drying process under stable conditions leads to extended low-defect crystalline layer covering the glass slide(picture 2.10). Finally, the substrates are sintered for 17 hours in an oven. The temperature (120°C) is slightly higher than the glass transition temperature of PMMA (105°C), so the contact points between the particles merge, and the contact surfaces enlarge the glass substrate. This connects the coating to the substrate and achieves higher durability. Shorter sintering times and lower sintering temperatures led to a lower coating strength. A regression of the structures was found for longer treatment times in the oven or higher sintering temperatures. The particles can melt at these temperatures and lose their original shape.

The holes and the cracks in the substrates are observed under the microscope before use. If present those were not used in preparation of sample cell, since it

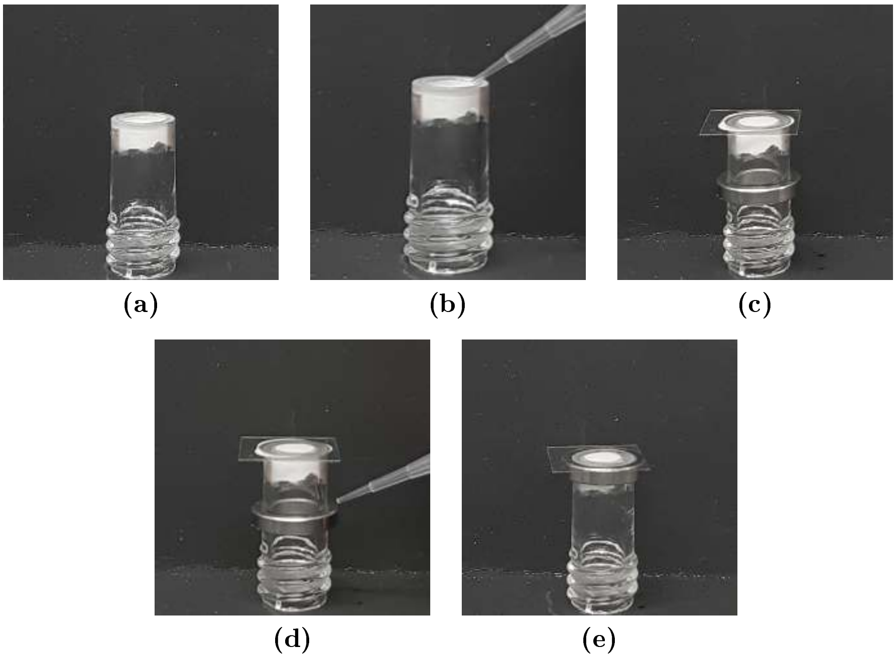

Figure 2.9: **(a)** side coated glass vial **(b)** Application of thin layer of UV glue **(c)** Placing the coated glass slide and placing it under UV for few minutes. **(d)** Application of glue to metal ring **(e)** The metal ring is slowly moved upwards and held for few seconds. Immediately kept under UV light for curing

leads to heterogeneous nucleation. The same type of substrates is produced on the container's walls to suppress the nucleation from the wall. The substrate on the sample cell wall is achieved by fixing the bottomless vial to a glass slide and then to the center of the mixing wheel. The wheel is set to rotate at a slow phase. At the same time, PMMA particles are added drop by drop so that the suspension starts to cover the wall of the container. The substrate begins to develop as the suspension slowly evaporates. The procedure takes time nearly 4 to 5 hours to dry and complete. Finally, the coated vial is sintered similarly, as explained before. Then wall is inspected by microscopy for coatings.

2.11.3 Final preparation

The first step is to prepare samples with a known volume fraction (picture 2.12(a)). Before use, the samples are each homogenized on a wheel mixer (picture 2.11). After thorough mixing, the sample is glued to the metal plate, which is designed to fit the microscopic stage of the confocal microscopy (2.12(b)). This is done in order to reduce the vibration of the confocal stage affecting the measurements. The glue used is regular paper glue which can be easily removed after measurements using acetone.

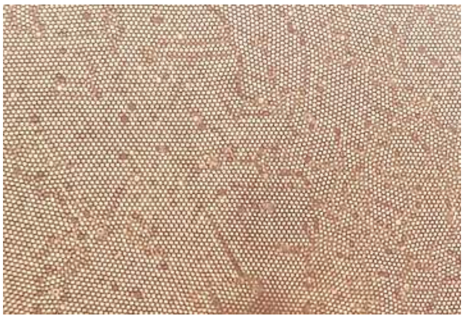

Figure 2.10: Layer of 2.33 µm particles are coated on the glass slide and after sintering process viewed under microscope

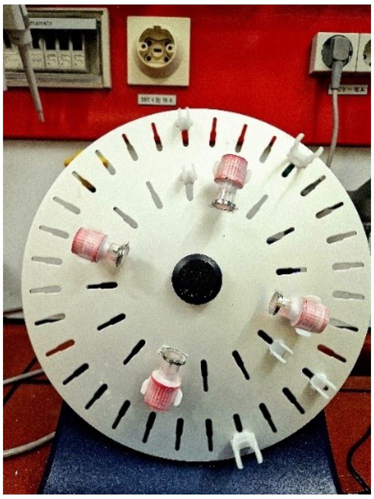

Figure 2.11: Samples are homogenized on a wheel mixer at two rotations per second

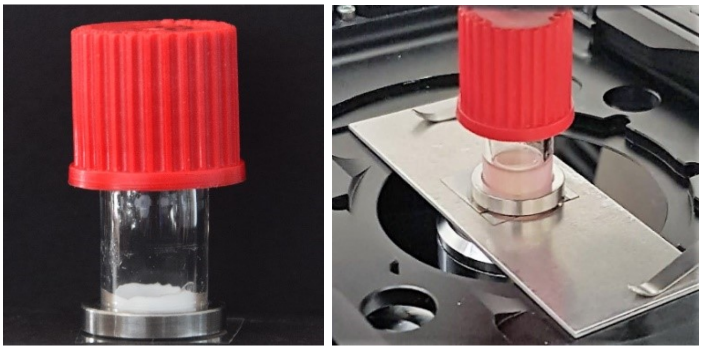

Figure 2.12: (a) Sample cell after cleaning (b) Sample cell glued to metal plate to reduce the vibration of the confocal stage affecting the measurement.

Chapter 3

Confocal microscopy of colloidal systems

Many optical techniques such as light scattering and optical microscopy are used to study colloidal systems. Combining these techniques provide complementary information from direct and reciprocal space. Confocal microscopy is a beneficial technique for studying colloidal suspension's structure and dynamics. The possibility to record three-dimensional images gives a lot of information in microscopic level. This section of the thesis is dedicated to confocal microscopy and its features. The chapter also describes the necessary criteria for scanning and resolution for good imaging using Confocal microscopy.

3.1 Introduction

Laser scanning confocal microscopy is an optical imaging technique. Compared to conventional optical microscopy, it offers increased contrast and the possibility to construct 3D images by using a spatial pinhole to eliminate out-of-focus light. Marvin Minsky developed confocal microscopy as early as 1957 [132], but it took another 16 years before intense laser light sources enabled the construction of a laser scanning confocal microscope. The technique became commercially available in the late eighties of the previous century and was initially used for biological applications. Extensive reviews can be found in, e.g. [186] [212] [220].

Confocal microscopy has been used in colloidal physics since the 90s to study the structural and dynamic properties of colloidal suspensions at the particle level. By using confocal microscopy, voluminous samples are investigated spatially. The system is composed of a regular fluorescence microscope and the confocal part, including scan head, laser optics, and computer. The confocal microscope uses fluorescence optics i.e. instead of illuminating the whole sample, laser light is focused onto a defined spot at a specific depth within the sample. This leads to the emission of fluorescent light from that point. A pinhole inside the optical pathway cuts off signals that are out of focus,and a optical filter thus allowing only the fluorescence signals from the illuminated point to enter the light detector, since the laser is used hence the name Laser Scanning Confocal microscopy(LSCM).

3.2 Principle

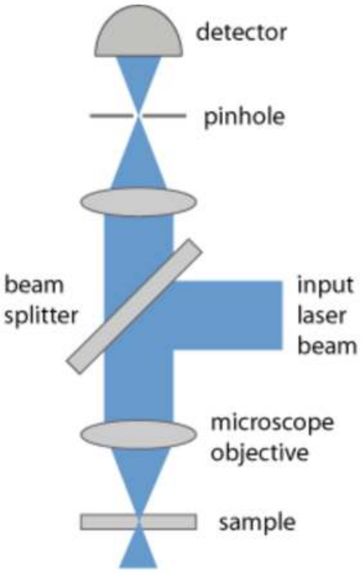

Figure 3.1: Setup of a confocal laser microscope.

The principle of confocal scanning microscope (figure 3.1) is as follows:

- A diffraction-limited collimated laser beam is tightly focused onto the sample, using a microscope objective (point illumination instead of illumination of the whole object).
- The light coming back from the focus point (e.g. through scattering in the sample, or fluorescence light) is imaged to a small pinhole and transmitted to a photodetector.
- The recorded intensity conveys information on just a single object point. A complete two-dimensional or three-dimensional image is obtained by systematically translating either the beam focus (with some kind of laser scanner, e.g. with oscillating mirrors) or alternatively the sample, scanning a certain area or volume in the sample.
- It is essential to ensure that the pinhole is adjusted such that one collects light exactly from the laser beam focus.
- The obtained optical power registered by the photo detector is usually small. Therefore, sensitive detectors such as photomultiplier tubes or avalanche photodiodes are normally used in order to limit the required exposure time.

In short, a LSCM illuminates the sample point-wise with a laser, rejects out of focus light with a pinhole, collects the signal with a detector, and post-renders the image with the help of computational power.

Figure 3.2 illustrates the basic components and its working.

- The diameter of the illumination point,is as determined by the numerical aperture of the objective. When a beam of light is focused on a specific area of a fluorochromatic specimen, the objective lens focuses the resulting illumination onto a plane above the objectives. On the focal plane above the objective is an aperture whose primary function is to block any stray light from reaching the specimen.
- The specimen typically rests on the plane of focus, which is the region between the camera lens and the perfect point of focus. Using the laser from the microscope, a plane on the specimen is scanned (beam scanning) or the stage is moved (stage scanning). The illumination is then measured by a detector, which produces an image of the optical section. Scannable optical portions are collected as data in a computer system to create a three-dimensional image. The image is measurable and quantifiable.
- Additionally, the aperture found above the objective, which blocks stray light, contributes to the favorable outcome. Using two high-speed oscillating mirrors, the microscope scanner scans the focused beam across a predetermined area to provide an image of the object. Their motion is made possible by galvanometer motors. Alternatively a Nipkow disc can also be used.
- The first mirror translates the beam along the lateral X-axis, while the second mirror translates it along the Y-axis. After an X-axis scan, the beam flies fast back to the origin to begin a new scan; this movement is known as fly-back. During the fly-back procedure, no data is gathered; hence, the laser scanner only illuminates the point of interest, which is the focal point.
- An image of the sample is then reconstructed pixel by pixel. It is also possible to move the focal point in the z-direction. Many 2D images can thus be grouped to form a z-stack, enabling a 3D reconstruction of the sample. This is illustrated in figure 3.3.

acquisition	No. of z-steps	steps in µm	duration(s)	Frequency(Hz)
xyt	1	–	0.068	12.87
xzt	-	0.25	0.217	4.61
xyzt	121	0.25	9.4	12.98

Table 3.1: Duration of recording images. It is calculated for a resonant Laser scanner with a sampling rate of 8 kHz, bidirectional, 1024x1024 voxels, slice thickness = 250nm for a particle diameter of 1.4 µm. The image size is 82x82µm. By increasing the z-steps, the frame rate also increases but to have an optimal resolution, it is always good to have z-step less than optical sectioning.

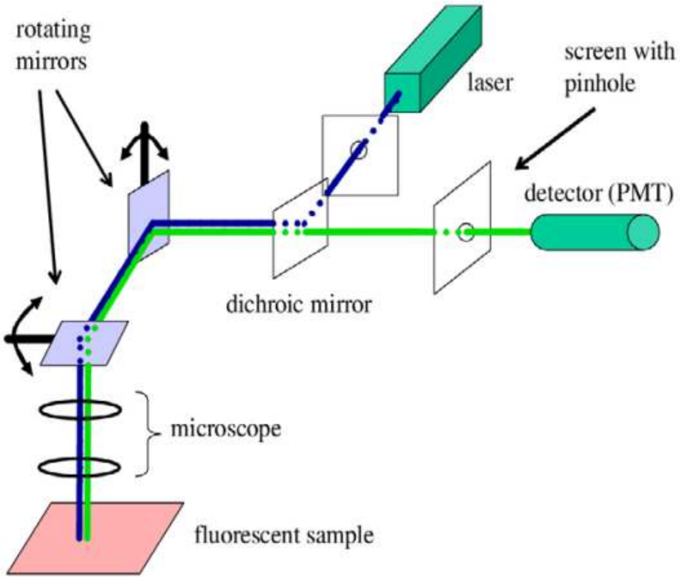

Figure 3.2: Diagram of a laser scanning confocal microscope highlighting the main components. The illuminating (blue) and emitted (green) beams are displayed. A filter after the laser can change the profile or intensity of the beam. Scanning is done using two rotating mirrors. Fluorescent light is collected with the objective and guided to the detector. The dichroic mirror reflects laser light (blue) and lets fluorescent light (green) pass through. Only light originating from the focal point inside the sample can pass the pinhole[157].

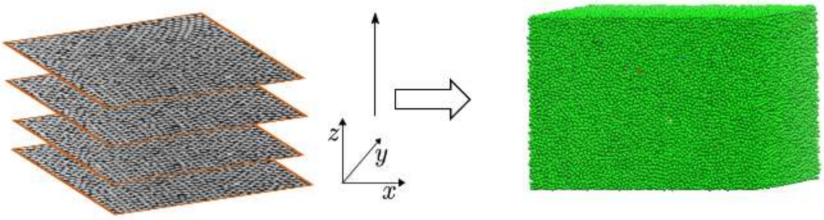

Figure 3.3: Many images from different z-heights are combined into a three-dimensional volume.

3.3 Scanning

The term scanning implies sequential illumination of a selected section of an objective. The portion of the sample to be imaged by the LSCM has to be scanned by the available laser source. The selected laser light is usually focused by the objective lens to a diffracted limited spot on the sample. As the light hits the sample, photons are emitted, and some enter the objective lens. Some of these photons eventually pass through the confocal AOTF(Acoustic-Optical Tunable filters) and reach the detector. The laser spot can be moved across the specimen using mirrors. Moving the galvo-mirror in one direction would result in a line of points on the sample being illuminated, and photons emanating from those points are being detected. By scanning the specimen in a raster pattern, images of one single optical plane are created. 3D objects can be visualized by scanning several optical planes and stacking them using a suitable microscopy deconvolution software (z-stack). For better understanding, the frequency corresponding to z-stack value is given in the table 3.1.

3.3.1 Acousto-optic deflectors(AODs)

In confocal microscopy, the light beam is usually raster scanned in the xy plane, often using a pair of mirrors (one for each axis, x and y), each mounted on a galvanometer scanning coil. The fastest way to implement this approach is called resonant scanning, by which the galvanometers are driven to resonate (oscillate) back and forth at high speed. However, this has certain limitations, including non linearity of the motion, which is sinusoidal to a first approximation. Ideally, the beam should be scanned at a constant velocity for uniform pixel intensity. Recently, confocal and multiphoton microscope builders and users have attempted to avoid these speed and non linearity limitations by scanning the laser using acousto-optic deflectors (AODs) instead of galvanometers.In an acousto-optic configuration, an acoustic wave is applied to some type of optically transmissive glass or crystal through which the laser light passes. For visible light applications, the acoustic wave is in the radio-frequency regime. This causes photo elastic deformations of the material, resulting in a periodic modulation of the optical properties, including the refractive index. An AOD is configured to use this effect as a transmissive diffraction grating.

3.3.2 Acoustic-Optical Tunable filters (AOTFs)

The acousto-optic effect has been also shown to be beneficial through the creation of a quite different type of photonic component called an acousto-optic tunable filter (AOTF). This device acts as a dynamic (user-tunable) bandpass filter. An AOTF uses birefringent material, which is a crystalline material in which the refractive index depends on the polarization of the incoming laser beam. A radio-frequency actuator bonded to the side of the crystal causes acoustic waves that modulate the refractive index of the crystal material as in an AOD. Again, this AOD is configured to diffract most (>90%) of the incident light into a first-order deflected beam, which leaves the device through an aperture. But by using a birefringent material and a different internal geometry, the AOTF selectively deflects only one wavelength because of a phenomenon called phase matching. The end result is a tunable device for which changing the radio frequency changes the wavelength at which the phase-matching condition is met. And if the crystal is cut and aligned correctly, changing the radio frequency does not change the angle at which the diffracted (and now wavelength-filtered) light leaves the device. The AOTF is thus a transmissive optic that acts as a wavelength-tunable narrow bandpass filter (Figure 3.4). The performance of acousto-optic devices, including AODs and AOTFs, is very dependent on the quality of the optical crystal element as well as on the quality the radio-frequency power source. These factors affect the maximum transmission of all acousto-optic devices and the transmitted wavefront quality, as well as factors such as the out-of-band extinction of an AOTF. These parameters, in turn, affect the microscope performance in terms of speed and image signal-to-noise ratio, particularly when two or more devices are used in the same microscope.

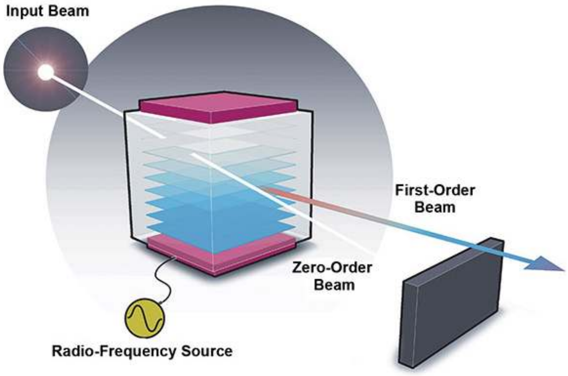

Figure 3.4: An acousto-optic tunable filter acts as a tunable bandpass filter in which the peak transmission wavelength depends on the frequency of the applied radio-frequency power. Courtesy of G&H.

3.4 Leica TCS SP8

As part of this research, an inverse laser scanning confocal microscope Leica TCS SP8 with resonant scanner unit is used. A schematic is shown in figure 3.5. The most important components are described below. A unique feature of this microscope is the resonant piezo mirror, with the image lines, frequency of 8 kHz that can be recorded. Bidirectional can thus two lines per pass through, which captures a maximum of 16,000 lines per second. This corresponds to a frame rate of 16 fps at 1024 x 1024 pixels. Because in the resonant mode, the exposure time is given by the digital resolution and the line frequency. It is with samples with low signal contrast necessary to rasterize the lines several times to a sufficient to achieve contrast.

3.5 The Leica spectrophotometer(SP) detection system

The SP-Detector employs a prism with unique geometry, a “Pellin-Broca-Prism” [149]. This geometry ensures minimal losses, simplifies adjustments, and enhances the mechanical stability of the whole setup. In a classical slit-spectrometer, the desired fraction of the color spectrum is selected by a pair of blackened barriers that are individually movable and, therefore, allow any desired band to be selected from the whole spectrum.The second step in the SP-detector applies the slit concept with modifications. Instead of blackened metal, the barriers are coated with a highly reflective layer on the incident side. They are also arranged at an angle. The reflected light can then enter a further arrangement of mirror sliders and sensors. Cascading such arrangements allows the entire spectrum to be split into a series of spectral bands(figure 3.6). The center frequency and bandwidth of each band are continuously tunable. The arrangement of prism and mirror-slit cascaded sensors is virtually polarization-independent and highly transparent. Therefore, it features a very high photon efficiency needed to collect as much as possible of the precious fluorescence photons by applying illumination with as low intensity as possible. Detected intensity values are displayed as gray levels. The display range of a typical 8-bit monitor covers 256 gray levels. The full range of the LUT (Look Up Table) is utilized if an image shows all shades of gray between black (=0) and white (=255). The gray levels might be presented in pseudo-colors. The number of sensors may be chosen according to the application's needs. They can be classical photomultiplier tubes (PMT) or Hybrid Detectors (HyD) with a highly efficient GaAsP-photocathode. As the gain of each sensor is controlled independently, the dynamic range in each channel can be adapted appropriately to enhance the S/N (signal to noise) ratio. That capability is advanced compared to array-detectors operating with only one gain setting. Numerical adjustments offered with array detectors to adjust a number of channels to various intensity ranges do not improve the signal quality.

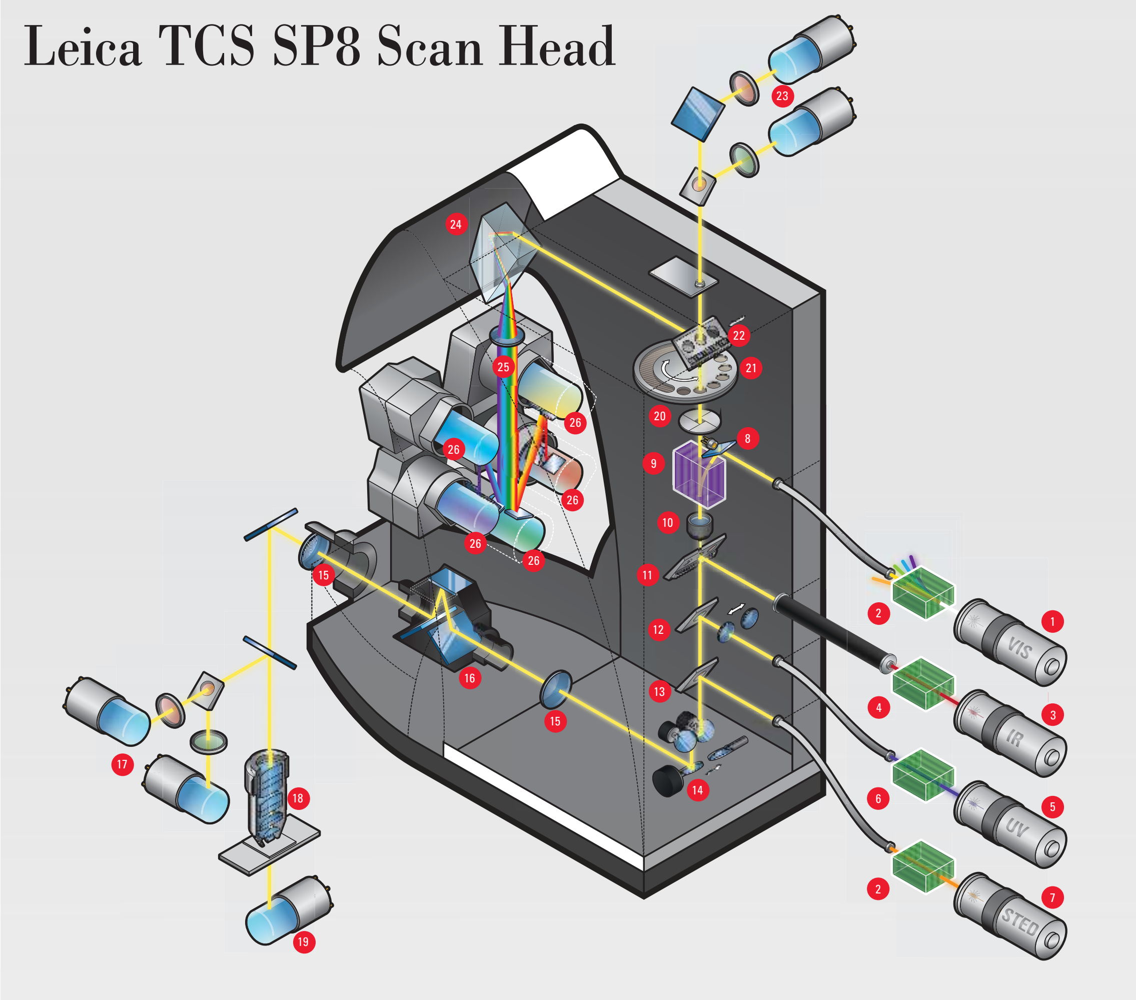

1 Visible line lasers or white light laser
2 Acousto-optical tunable filter (AOTF)
3 Infrared (IR) lasers *
4 Electro-optical modulation (EOM)
5 Ultraviolet (UV) lasers *
6 AOTF or direct modulation (DMOD)
7 STED laser *
8 Monitoring diode for Setlight
9 Acousto-optical beam splitter (AOBS), other options available
10 FRAP Booster *
11 IR laser incoupling
12 UV laser incoupling with CS2 UV optics
13 STED laser incoupling
14 FOV Scanner with Tandem Scanner option
15 Scan optics with alternative UVIS, HIVIS or VISIR coating
16 Scan field rotation (Abbe-König rotator) *
17 Reflected light detection (RLD) in non-descanned position *
18 Objective lens (different options available)
19 Transmitted light detection (TLD) in non-descanned position *
20 Square confocal pinhole
21 Fluorifier disc *
22 Outcoupling with X1 port *
23 External detection *
24 Prism-based dispersion
25 SP Detector with spectrophotometer arrangement
26 Up to five photo-multipliers (PMT) or up to four hybrid photo-detectors (HyD)*
*optional

Figure 3.5: Leica SP8 scan head explained with the parts. The picture is taken from Leica Manual [1].

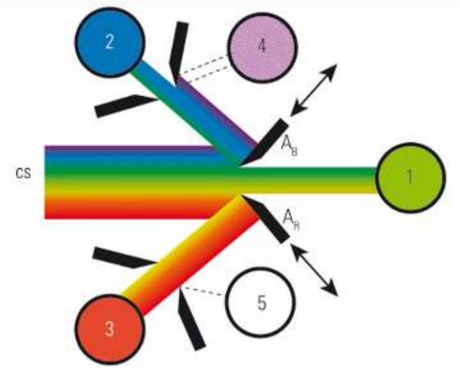

Figure 3.6: Principle of tunable multiband detection system Leica SP-Detector. The color spectrum(CS) generated from a prism is separated into up to 5 individual fractions using motorized mirrors. The bandwidth and center frequency of each band is tunable independently. A_B and A_R are motorized slit [1].

3.6 Resolution

The resolution of an optical system is the ability to determine two different points, or objects, as singular, distinguished entities. In a confocal microscope, the image of a point-like source is a three-dimensional pattern known as the point spread function(PSF)[157][144] due to the diffraction through the circular aperture. The transverse cross-section of the PSF on the image plane is an Airy disc, whose size depends on the numerical aperture of the objective lens and the wavelength of the light source. Generally, two closely spaced luminous points in the sample plane result in overlapping discs leading to an intensity distribution with two peaks, as shown in figure 3.7.

Now minimum separation is required between the discs to create a reasonable 'dip' in between for the peaks to be resolved -this sets the maximum resolution of the microscope. Following Rayleigh criteria, this separation is the full width half maximum, FWHM of the airy disc (when the first minimum of an airy disc aligns with the central maximum of the second one), leading to a dip of roughly about 26%. For the optical setup of most commercially available confocal microscopes, this separation is about 200nm. The position of an isolated fluorescent point-like source corresponds to the center of mass of its spatially extended airy disc image. Suppose the disc is about N pixel wide and each pixel is M micrometers across. In that case, the center of the disc can be estimated to ≈M/N accuracy, which is higher than the optical resolution.

Resolution controlling factors in confocal microscopy are

- XY (image resolution) depends on emission wavelength, the numerical aperture of the objective, immersion medium, stability of the system, brightness/contrast settings, pixel size.
- z (optical section thickness) depends on pinhole size, cover glass
- the thickness of the cover glass (0.17mm), immersion medium
- t (time resolution) depends on hardware parameters like scanning speed

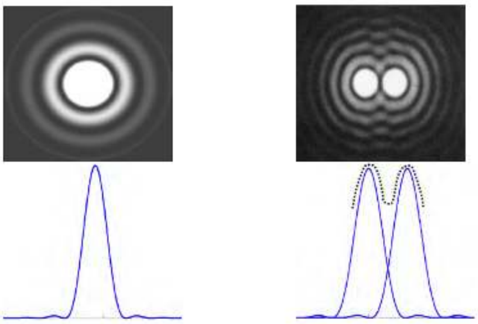

Figure 3.7: Circular diffraction pattern (airy disc) and corresponding intensity distribution resulted from imaging a point-like source in the field of view. Right: Diffraction field and intensity distribution for two closely space luminous points in the field of view.

- λ (spectral resolution) depends on the spectrophotometric device (SP) and beam splitters and filters
- i (dynamic range) depends on bit-resolution

Numerical aperture(NA) is most important in resolution, not magnification. Here we have used 63x1.4 oil immersion objective for all the experiments.

3.7 Immersion Liquids

x Several factors need to be considered to examine specimens at high magnifications using the microscope. These include resolution, numerical aperture (NA), the working distance of objectives, and the refractive index of the medium through which the image is collected by the front lens of an objective. Here, it is explained briefly how using an immersion medium between the cover-slip and the objective front lens helps increase the NA and resolution. In addition, we will consider the refractive index of air and the glass with which slides and cover-slips are composed and how an immersion medium is used to partially reduce the mismatch when light travels from one medium to another. One of the main problems in light microscopy is to overcome some of the limits of optical resolution and to increase the NA of the system. Having an immersion liquid in place of the air gap between the front lens of an objective and the cover glass of a specimen increases the resolution of an objective. When light passes from one medium to another (for example, through the glass to air), it refracts - in other words, it bends and scatters. Any light rays which are refracted into the air, reflected by the cover glass, or blocked by the metal housing of the objective front lens do not contribute to the image formation. The purpose of the immersion liquid is to decrease the amount of refraction and reflection of light from the specimen and increase the ability of the objective to capture this otherwise deviated light (figure 3.8). Leica Immersion Oil (standard and type F) is used throughout the measurement, having an RI of 1.51.

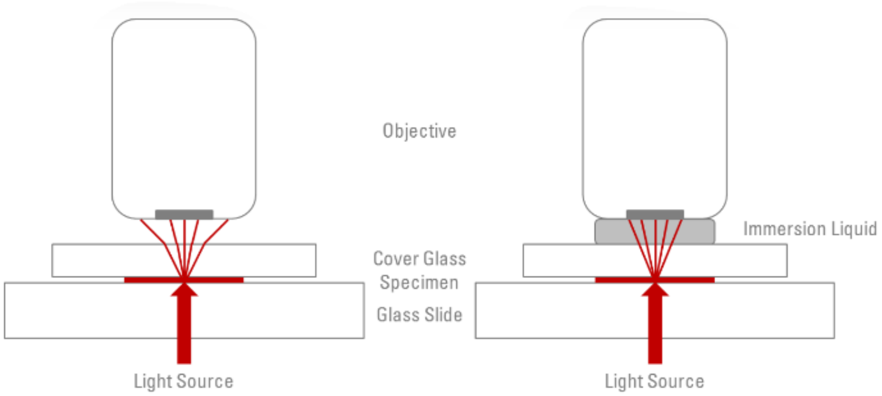

Figure 3.8: Left: When light passes two media with different refractive indexes (RI) (for example, through the glass to air), it refracts. Any light rays which are refracted into the air, reflected by the cover glass, or actually blocked by the metal housing of the objective front lens do not contribute to the image formation. Right: An immersion liquid with a refractive index matched to the refractive index of the cover glass and the medium the specimen is mounted decreases the amount of refraction and reflection of light from the sample[1].

3.8 Nyquist Sampling for Z stacks

If information is to be preserved in all three dimensions, the images must be collected with appropriate x, y, and z dimensions. These dimensions are determined by the Nyquist sampling theorem. Nyquist Sampling dictates that the analog signal must be sampled at least 2.3 times to represent an analog signal in digital space optimally. In microscopy terms, this means that the pixel size of an image needs to be at least 2.3 times smaller than the object that is being resolved. Suppose one attempt to capture the highest resolution image possible with a given microscope configuration (objective, camera/scanner, excitation and emission wavelength, etc.). In that case, one must ensure that the pixel size is at least 7 times smaller than the calculated resolution of the objective. On a confocal microscope, the pixel size can be adjusted. This is achieved by scanning at a higher image resolution (e.g., 1024x1024 instead of 512x512). If there are more pixels, each represents a smaller area. Adjusting the zoom will result in the pixel being smaller at the cost of a smaller sample area imaged. It is also essential to apply Nyquist sampling rates to Z-stacks and time lapse imaging. For z-stacks, one must set the z-step size to 2.3 times smaller than the Z-resolution of the objective. The Leica confocal microscopes have inbuilt calculators that use the Optimal settings when placing XY resolution and Z stacks.

3.9 Recording images

For all measurements, 63x1.4 oil objective is used. The time to acquire the image depends on the type and quality required. For recording 3D images, one has to keep in mind that the movement of the objective also takes time. In

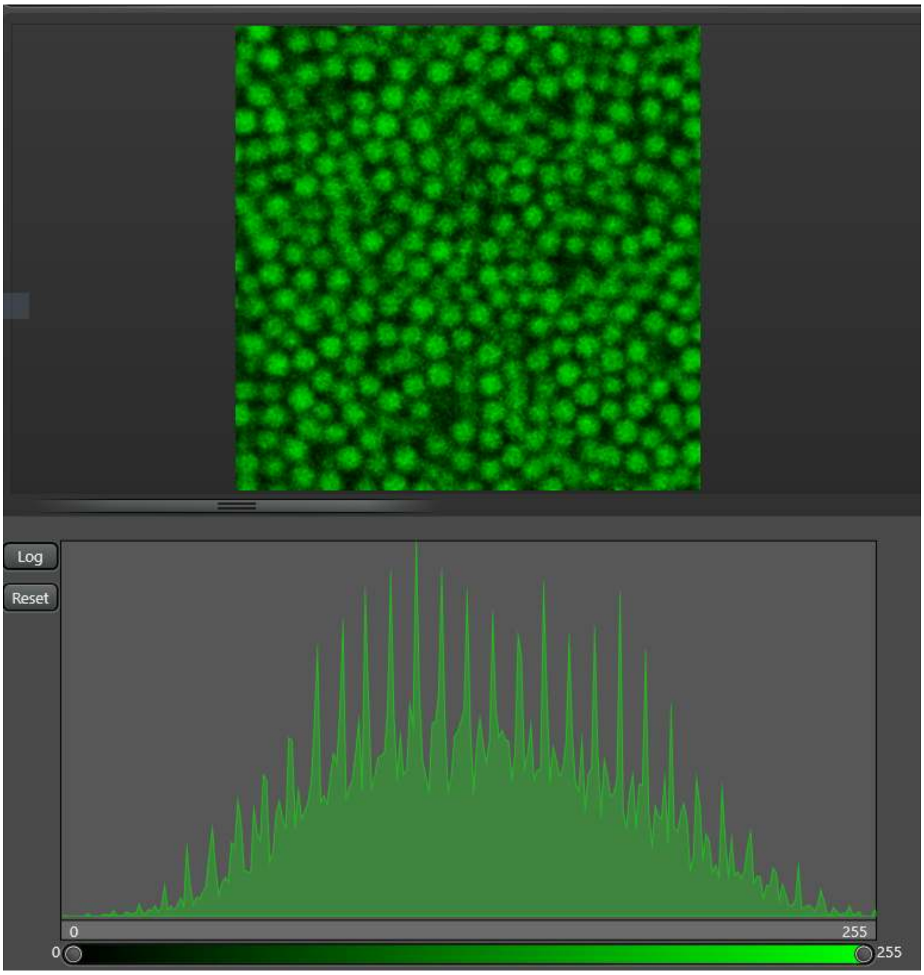

Figure 3.9: View of particles in CDL/TCE from confocal microscopy and its intensity distribution. The size of the image is 45x45µm^2 having the line average of 8. The intensity distribution covers the entire range of LUT corresponding to the 8-bit depth.

most 3D measurements, stacks of 30-120 images were recorded with a distance z = 0.25µm between the slices. In practice, for most of the physical quantities, are determined from coordinates of the particles. The detection of particles is explained in detail in chapter 4. In resonance mode with 8 lines averaging, it takes about 60 s to scan such a volume.Faster data acquisition (smaller volumes) in less concentrated samples compensates for the influence of particle diffusion on the accuracy of the particle position. Each g(r) was calculated from at least 30 independent 3D measurements. In offset on the photon detector is raised or lower to make the image brighter or darker. However, the images are somewhat washed out, with

- being overall too bright and
- being overall too dark.
- The PMT gain has been increased, resulting in an image with better contrast, more dynamic range, and a much clearer image overall.

It can also be seen in fig 3.9 the intensity distribution of scanned images which covers the entire range of the LUT (Look Up Table) is utilized.

3.10 Movie processing

The microscope is controlled via the software LAS-AF (Leica GmbH). The picture series are stored together with a meta file in which the set of measurement parameters are stored in .lif container files. Leica Microsystems GmbH, a limited version (LASAF Lite) software, is available free of charge to read the image files[2]. The next step in the multiple particle tracking techniques is to extract a list of particle trajectories from the movie of particle motions acquired with the confocal microscope.

Chapter 4

Data Analysis

This chapter comprehensively discusses obtaining particle coordinates from the confocal microscope. This begins by describing how best to capture images so that they contain all of the available information from the samples. It also gives detailed information about image analysis for accurate particle positions and how the local structures can be assigned at the single-particle level using Bond-order parameters. Furthermore, using time-resolved measurements and Bond order analysis, the temporal evolution of the crystal structure can be studied.

4.1 Introduction

In confocal microscopy, one can capture slices through a sample at different depths z. One can either take 2D images at a fixed depth or capture whole stacks of slices at equidistant z positions to obtain a 3D image that is a snapshot of the observed sample volume. In 1996, Crocker and Grier [39] introduced an algorithm that has been commonly used in many experiments. With the use of particle detection and particle tracking algorithms, one can determine the entire trajectories of the particles in a colloidal suspension. This means that the complete phase space information is available in the recorded volume of the sample, and it enables the possibility of calculating a large number of desired physical quantity. Since many physically relevant quantities obtained from confocal laser scanning experiments depend directly or indirectly on the particle coordinates, accurate tracking is essential. A systematic error in determining the particle coordinates leads to an error in the physical quantities such as mean square displacement from confocal microscopy [157] which cannot be directly compared with the one from Dynamic light scattering [206].

4.2 Data acquisition

Confocal microscopy allows the investigation of colloidal suspensions in direct space at the single particle level in three dimensions (3D). The starting point for the data analysis is the exact knowledge of the positions of all particles in the observed volume. The microscopic measurements were carried out using a Leica TCS SP8 white-light-laser scanning confocal microscope with a 63x1.4

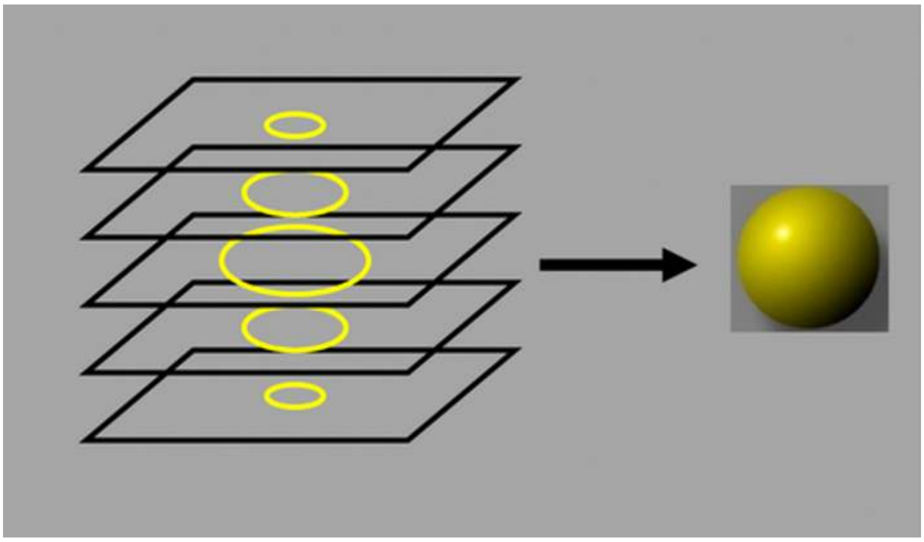

Figure 4.1: Pictorial representation of 1.4 µm particle from z-slice of the 2D image.

oil immersion objective. The microscope was operated in fluorescence mode using a wavelength range of 480-550 nm for illumination to optimally excite the fluorophore ($DiIC_{18}$) and to have only a very small overlap with its emission spectrum. The emitted light was detected in a range of 560-700 nm.

Samples cells with number density $\rho=$ 0.1-0.34 are prepared. Before use, the samples are each homogenized on a wheel mixer (picture 2.11). For g(r) measurements, particle positions were determined in a volume 30-50 µm above the bottom of the cell. At this distance, layer formation induced by the flat glass wall no longer occurs. Depending on the particle concentration, we scanned different large volumes. At high volume fractions close to the fluid crystal phase boundary, we scanned volumes of 82x82x40µm^3 (1024x1024x120 voxels).

Scanning in 3D is a prerequisite for observing crystal nucleation, as detecting a rare event requires scanning a sample volume containing as many particles as possible. The field of view is chosen as large as possible to image many particles with a resolution allowing for accurate single particle detection. The 3D scanning yields image stacks with resolutions of 1024x1024x100 voxels. Each particle should typically appear on 9x9x5 pixels to obtain sufficient information to determine particle positions with sub-pixel accuracy.

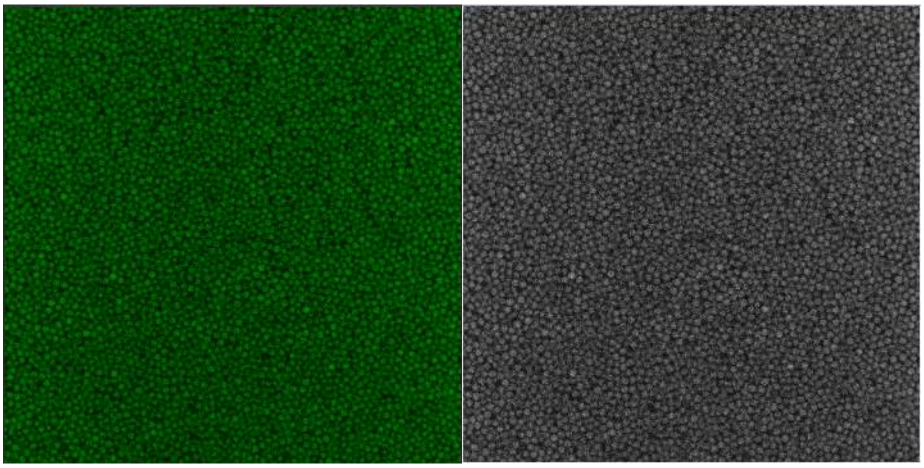
(a) (b)

Figure 4.2: Confocal image of PMMA particle 1.4 µm taken at 20 µm away from the cell bottom. The left picture is the image seen on the screen during measurement. The picture on the right is obtained using Leica software in grey scale.

4.3 Image analysis

The next step in the experiment is to take visual data contained in the 3-dimensional image stack and turn it into particle positions. To do this, IDL (Interactive Data Language), a popular data analysis language, is used. From the positions of all colloidal particles in the chosen region of interest, we can obtain information about the volume fraction, sedimentation velocity, diffusion coefficient, crystal growth, etc. The LSCM software outputs the image format as Tagged Image File Format or Tiff (*.tif) corresponding to the 8-bit. The file is a stack of grey scale images with a black background, and the fluorescing spheres show up white. The term bit depth refers to the binary range of possible gray scale values used by the analog to digital converter, to translate analog image information into discrete digital values capable of being read and analyzed by a computer. The most popular 8-bit digitizing converters have a binary range of 256 (2^8) possible values.

4.3.1 Particle coordinates

To extract a set of coordinates from the 3D images that represent the particle positions in the scanned volume with high accuracy, the volumetric 3D images were first filtered with a 3D band-pass filter. For this procedure, we used the algorithm implemented by Eric Weeks in IDL [213]. To determine the particle positions from the filtered 3D images, a self-written IDL routine was used, which basically contains the concepts of the algorithm developed by Jenkins [94]. First of all, particles are identified by searching for brightness maxima within local environments. The particle position can then be determined by fitting a brightness distribution to the region around the brightness maxima of the 3D-images.

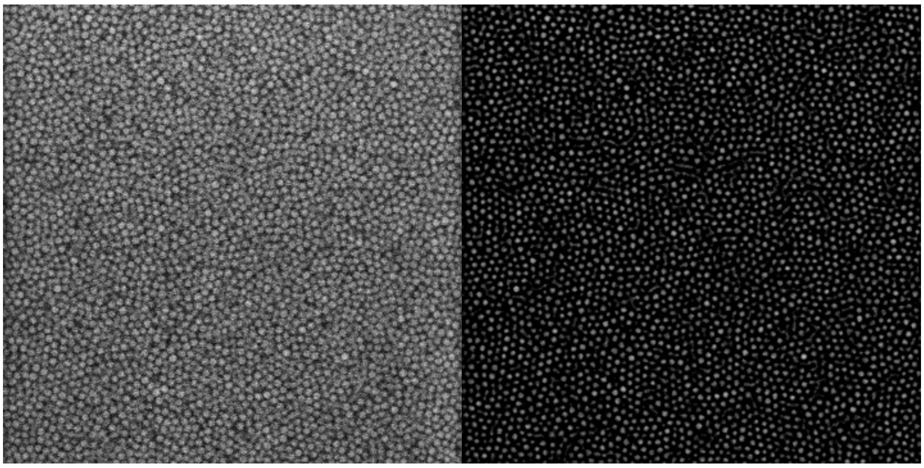

Figure 4.3: Comparison before and after using the bandpass filter technique.

4.4 Tracking particles

Every particle's position will be tracked over time from the particle positions of a time series. Individual trajectory as well as ensemble-averaged mean square displacement can be calculated. Eric Weeks has provided an algorithm that makes it possible to track moving particles between several time steps for observing particle dynamics. This IDL algorithm is freely available and will remain the same in this research. The individual trajectory of the particle in x, y, and z direction is shown in the figure 4.5 and all particles identified in the frame and its trajectories are seen in the figure 4.4

4.4.0.1 Positional Errors

Quantitative position errors are measured by determining the mean square displacement from an immovable sample. For this method, a dense particle sediment is prepared using a centrifuge in which the particles are immobile. A time series of 3D images taken and coordinates sets are generated from this static particle arrangement. From the data sets, the mean square displacement is determined(Figure 4.6). From extrapolation to smaller time, the position error can be estimated. From a time series of 3D images, the position uncertainty was determined to be $\delta r/2R_{HS} = 4.8\%$ in the xy-plane and 6.3% in the z-direction. This results in a mean error in the distance determination between two particles $\Delta r_{ij} = |r_i - r_j|$ of $\delta r_{ij}/2R_{HS} = 7.7\%$ [114].

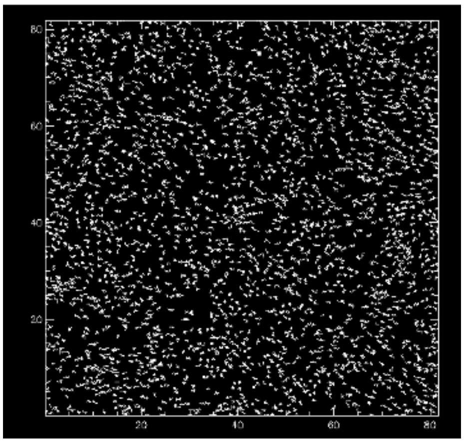

Figure 4.4: Trajectories of tracked particles

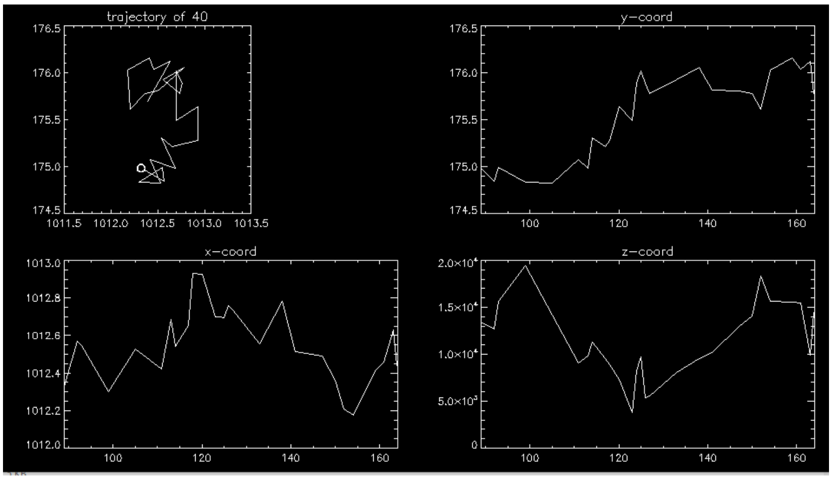

Figure 4.5: Trajectories of tracked single particle with id=40 and its displacement in x and y and z direction

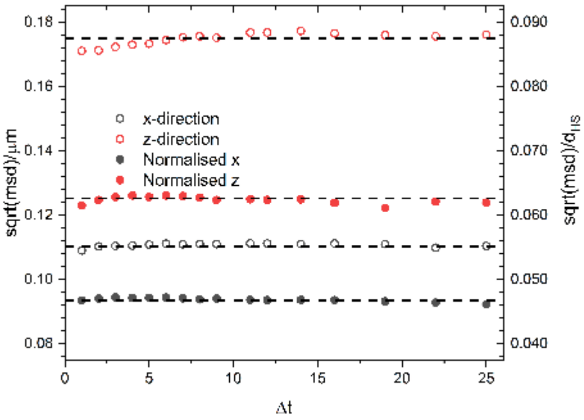

Figure 4.6: (a) Mean square displacement measured for static sample, and normalized MSD on the left scale of the axis

4.5 Radial distribution function g(r)

In order to be able to compare theoretical g(r)'s directly with the experimental ones from LSCM, the PSD and the experimental position errors must be considered. First, the g(r) was calculated based on the measured PSD. The polydisperse g(r) was then folded with a Gaussian distribution with a normalized standard deviation of 7.7% to account for the error in the distance determination Δr_{ij}. Further detail explanation is given in the chapter 5.

4.6 Bond order analysis

Among the particle positions obtained from a supercooled sample, crystal nuclei must be identified in a "sea" of particles with a liquid-like surrounding. Due to the small size of these nuclei, the detection has to be accomplished with a local method that does not rely on the bulk crystal's long-range translational and orientational order. This can be accomplished with local bond-order parameters(LBOP), initially developed to obtain a quantitative measure of the local order in random structures [219] [193].

To determine which particles belong to a crystalline cluster, one must determine whether a particular particle is in a locally crystalline or liquid environment. This is done based on Steinhardt order parameter [197] as explained in the following. For each particle i a complex vector $q_{lm}(i)$ is defined as

$$q_{lm}(i) = \frac{1}{N_b}\sum_{j=1}^{N_b} Y_{lm}(\theta(r_{ij}), \phi(r_{ij})) \tag{4.1}$$

where $Y_{lm}(\theta, \phi)$ are spherical harmonics, $\theta(r_{ij})$ and $\phi(r_{ij})$ spherical coordinates of a bond r_{ij} in a fixed reference frame, and N_b is the number of neighbors.

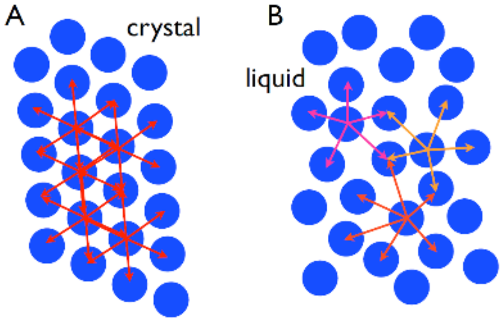

Figure 4.7: A 2D sketch of the bond orientational order in (a) a crystal and (b) a liquid [68].

The indices l and m indicate degree and order of the function. To calculate the Steinhardt order parameters, each particle is first assigned a set of nearest neighbors. The connecting vectors r_{ij} between the central particle i and the neighboring particles are developed according to spherical surface functions. The orientation of the unit vector r_{ij} is determined by the polar and azimuthal angles θ_{ij} and ϕ_{ij} . The rotationally invariant local bond order parameters are then defined as follows:

$$q_l(i) = (\frac{4\pi}{2l+1}\sum_{m=-l}^{l}|q_{lm}(i)|)^{\frac{1}{2}} \tag{4.2}$$

$$w_l(j) = \frac{\sum_{m_1+m_2+m_3=0}\begin{bmatrix} l & l & l \\ m_1 & m_2 & m_3 \end{bmatrix} q_{lm_1}(j)q_{lm_2}(j)q_{lm_3}(j)}{(\sum_{m=-l}^{l}|q_{lm}(i)|^2)^{3/2}} \tag{4.3}$$

The integers m_i are limited to the number range from -l to l, but only combinations that satisfy $m_1 + m_2 + m3 = 0$ are allowed. The term in brackets represents the Wigner-3j symbol, whose explicit expression can be found in the literature [109]. An IDL code has been implemented to calculate the local orientation order parameters according to equations 4.1, 4.2, 4.3 [114].

The rotational invariance of q_l and w_l is given only for even l. The q_l and w_l are sensitive to different crystal symmetries. A method for assigning crystal-like structures is introduced in the next section. The values of the Steinhardt order parameters depend on the system's configuration and on the number of nearest neighbors taken into account for calculating the order parameter. When comparing the order parameters of different experiments, it must also be considered with which method the next neighbors are assigned along with the positional uncertainties. Several methods for assigning the nearest neighbors have been reported by Mickel et.al. [131] summarized and compared. For a completely random particle configuration, the order parameters scale with $q_l = \frac{1}{N_b}(1 \pm \frac{1}{\sqrt{4l+2}})$ [164] was used. The back term gives the typical range of variation of the order parameter in a completely random configuration. The fewer particles are available for calculating the order parameters, the larger the random fluctuations and the greater the average of the order parameters.

4.6.1 Cluster assignment via the dot product

Using the LBOP, particles can be assigned to an ordered phase at the single-particle level. Adjacent particles of a phase can be grouped into spatially extended clusters. One way to identify locally-oriented clusters is to compare neighboring orientations of adjacent particles [12] [163]. Starting from the Steinhardt ordering parameters at $l = 6$, a rotationally invariant scalar product is introduced. The normalized scalar product of the complex vectors q_{6m} of two particles i and j is defined as

$$S_{ij} = \frac{\sum_{m=-6}^{6} q_{6m}(i) \cdot q_{6m}^*(j)}{\sqrt{\sum_{m=-6}^{6} |q_{6m}(i)|^2} \sqrt{\sum_{m=-6}^{6} |q_{6m}(j)|^2}} \tag{4.4}$$

The scalar product measures the correlation between the orientations of the nearest neighbors of central particles i and central particles j. The scalar product is normalized such that $S_{ij} = 1$ if the correlation is complete, i.e., the particles are considered connected. and $S_{ij} = 0$ if the correlation is incomplete. A large dot product value indicates that the neighboring environments of the compared particles have the same spatial orientation. The scalar product thus represents a measure of the spatial correlation of the local environment which often names as q_{66}.

Correlated orientation particles may be associated when the scalar product exceeds a threshold ST. These particles are called connected. A particle is assigned to a cluster when a minimum number of neighboring particles are attached to the particle. All adjacent particles that meet this cluster criterion are given to the same cluster. This method defines locally ordered regions as clusters. Since minimum correlation of the orientation of neighboring coordination shells is expected in the fluid phase, a distinction can be made between the criterion and the local "fixed" phase. The exact structure of each cluster will not be included in this method. Information from the next and the next but one neighboring particle flows into the evaluation.

4.6.2 Structural analysis according to Lechner-Dellago

The crystal structure determination described above can be improved by using the following averaged form of the local bond order parameters:

$$\bar{q}_l(i) = \sqrt{\frac{4\pi}{2l+1} \sum_{m=-l}^{l} |\bar{q}_{lm}(i)|^2}, \tag{4.5}$$

where

$$\bar{q}_{lm}(i) = \frac{1}{\tilde{N}_b(i)} \sum_{k=0}^{\tilde{N}_b(i)} |q_{lm}(k)|, \tag{4.6}$$

Here, the sum from $k = 0$ to $N_b(i)$ runs over all neighbors of particle i plus the particle i itself. Thus, to calculate $\bar{q}_l(i)$ of particle i, one uses the local orientational order vectors $q_{lm}(i)$ averaged over particle i and its surroundings. While $q_{l(i)}$ holds the information of the structure of the first shell around particle i, its averaged version $\bar{q}_l(i)$ also takes into account the second shell. One might

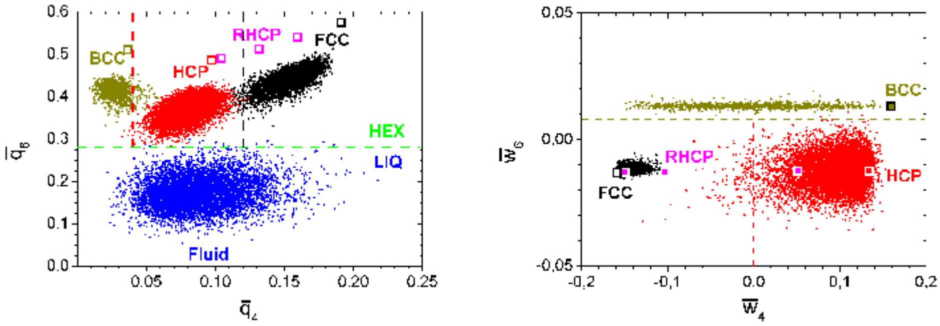

(a) (b)

Figure 4.8: (a) Structural mapping in the averaged $\bar{q}_4 - \bar{q}_6$ map. Plotted are the positions determined by test data sets for perfect structures (large squares) and thermally fluctuating structures (points) of the FCC (black), HCP (red), and BCC structures (yellow) and for three RHCP stacking sequences (magenta) as well as for an HK fluid (blue). In addition, dividing lines between HEX and LIQ areas (green) and the lower limit of the q_4 parameters for the HCP (red) and FCC structures (black) are drawn. (b) Structure-mapping in the averaged $\bar{w}_4 - \bar{w}_6$. For reasons of clarity, the fluid particles are not drawn. In this plot, HCP and FCC structures can be separated by the drawn vertical line (black) and BCC structures separated by the horizontal line (yellow) [114].

say that using the parameter $\bar{q}_l$ instead of q_l increases the accuracy of the distinction of different structures at the price of a coarsening of the spatial resolution. In this sense, the averaged local bond order parameter is similar to the scalar product of eq.4.4 used to decide whether a particle is in a solid-like or liquid-like environment. Also, the second particle shell is effectively taken into account in that case. The averaged orientational order parameter $\bar{q}_{lm}$ can also be used to define an averaged version $\bar{w}_l$ of the order parameter w_l,

$$\bar{w}_l(j) = \frac{\sum_{m_1+m_2+m_3=0} \begin{bmatrix} l & l & l \\ m_1 & m_2 & m_3 \end{bmatrix} \bar{q}_{lm_1}(j)\bar{q}_{lm_2}(j)\bar{q}_{lm_3}(j)}{(\sum_{m=-l}^{l} |\bar{q}_{lm}(i)|^2)^{3/2}} \tag{4.7}$$

4.6.3 The cutoff distance

Test data sets were generated for FCC, BCC, HCP, and fluid structures [114]. For the crystal-like structures, ideal lattices were created by the periodic continuation of the lattice vectors. Small fluctuations in the ideal lattice sites were also allowed to account for the influence of thermal fluctuations and were smeared on the basis of the LindemannâĂŹs criterion and additional position errors were added, which could be estimated from the experiment. Both effects are simulated by adding normally distributed random numbers to coordinates. Thus generated records are used to test the values associated with the structure. Thus, distinction can be made between different structures based on the order parameters. The averaged LBOP, according to Lechner and Dellago, contains information about the next and the next but one neighbor of a particle.

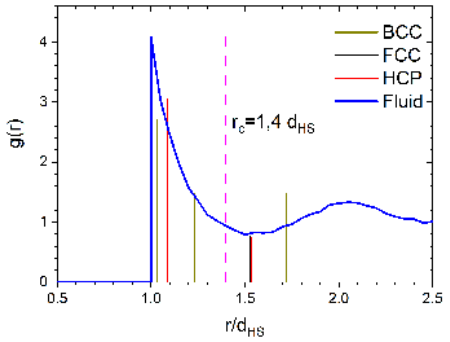

Figure 4.9: Positions of the first coordination shells for FCC, HCP, and BCC ordered structures in the melt volume fraction ($\phi_{eff}^{PD} = 0.545$). At a Cutoff value of $1.4d_{HS}$, particles of the first of the second coordination shell (FCC, HCP) or particles of the second of the third coordination shell (BCC) can be discriminated. The pair distribution function of a monodisperse HS fluid ($\phi_c = 0.415$) is plotted for comparison [114].

Therefore, up to five layers must be considered to create a local crystal-like structure.

For each particle in the observation volume, a set of nearest neighbors is defined by a cutoff distance. The distance is set to $r_c = 1.4d_{HS}$, corresponding to a length of $r_c = 2.0\,\mu\text{m}$. Figure 4.9 shows the equilibrium pair distribution function of a hard-sphere system ($\phi = 0.415$) along with the first major peaks of the FCC, HCP, and BCC crystal structures (all at $\phi = 0.545$). The first major peaks for FCC and HCP structures coincide. The Cutoff distance is chosen for all crystal structures, the minimum value between two coordination shells. As a result, only the first coordination shell in FCC and HCP structures and the first two coordination shells in BCC structures are nearest neighbors. The central particle is assigned 12 nearest neighbors (FCC, HCP) and 14 nearest neighbors (BCC) in the ideal crystal. The Cutoff distance is on the left side of the minimum of the pair distribution function of the equilibrium fluid.

4.6.4 Threshold

Equation 4.4 is used to calculate the normalized scalar product for neighboring particles, and the thresholds ST and NT are used to define particle clusters. The limits ST(Scalar product threshold) and NT(Nearest neighbor threshold) are chosen so that the particles are assigned to the wrong phase. Cluster identification is performed on the test data sets to determine the threshold values. For calculation, test data were smeared on the basis of the LindemannâĂŹs criterion and additional position errors were added, which could be estimated from the experiment.

To determine the threshold the frequency distribution of the scalar product values per particle for the different phases is considered. In each case, the smeared data records were taken. The value of the scalar product of the fluid has its peak at zero, but is very widely distributed. For the crystalline structures, the peak values are in the range 0.7-1 and are narrower. In the crystalline phases, at a threshold of $q_6 q_6 \geq \mathrm{ST} = 0.5$, almost all neighbors are connected. At this threshold, however, also occur a significant number of compounds in the fluid. For a clear distinction between the fluid and the crystalline phase, a second criterion is needed, the minimum number of connected nearest neighbors NT. To do this, varying the two threshold values ST and NT for the crystalline phases the fraction of particles erroneously identified as fluid and, for the liquid phase, the proportion of particles erroneously identified as being crystalline. For the threshold values ST=0.5 and NT=8, the fluid structure and the FCC phase mismatches are less than 0.5%. These thresholds will be used in the following analyzes unless noted otherwise. Comparable results are achieved with the settings ST=0.7 and NT=5 [114]. These thresholds require less connected neighbors. This leads to a more reliable analysis near the wall. The thresholds used are consistent with those of Sandomirski et al. used values [171].

Thus cut-off distance and threshold values are very important and must be determined for each system used individually. Otherwise results cannot be compared. This will leads to wrong assignment of crystalline and fluid particles. Since these parameters depends on interaction potential, polydispersity and position uncertainty, one must always determine these parameters individually for each system.

4.6.5 Cluster assignment via LBOP

Figure 4.8 shows the average order parameters $\bar{q}_4$ and $\bar{q}_6$ for different structures on the left. The associated averaged order parameters w_4 and w_6 are shown on the right side. Test data sets which is explained in the next section for different crystal structures were generated to assign the local structure types to obtain averaged LBOP.

Structure	colour	$\bar{q}_4$	$\bar{q}_6$	$\bar{w}_4$	$\bar{w}_6$
HCP	red	0.04 - 0.12	$\geq$0.28	$\geq$0	-0.05 - 0.008
FCC	black	0.12 - 0.25	$\geq$0.28	<0	-0.05 - 0.008
BCC	yelow	0.00 - 0.07	$\geq$0.30		0.008 - 0.05
HEX^1	green		$\geq$0.28		
LIQ	blue		<0.28		

Table 4.1: The limits for defining different types of clusters. HEX denotes hexagonal unregistered structures. LIQ denotes the fluid-like structures. 1: denotes no HCP, FCC or BCC [114].The threshold ST=0.5 and NT=8 is used for analysis.

Table 4.1 summarizes the limits of discrimination between different structures. In addition to the crystal-like structures HCP, FCC, and BCC, two further structural types are defined, HEX and LIQ. The crystal-like structure HEX denotes hexagonal unregistered layers. A high q_6 value characterizes these, but an assignment in one of the crystal-like structures fails based on the other order parameters. The structures cannot be assigned to the RHCP stacking sequences. This circumstance suggests that they are hexagonal structures but not in locked positions.Furthermore, fluid-like ordered cluster particles are defined (LIQ). These are characterized by the absence of a high q_6 order parameter. The local structure of these particles averaged over the nearest neighbor environment does not differ significantly from the structure in the fluid.

Chapter 5

Fluid-structure: Study of charged, screened charged, and hard spheres fluids by confocal microscopy and reviewed by theory and simulation

After all the preliminary work on sample preparation and particle detection, tracking, and the production of samples, this chapter is dedicated to the results from the study of charged, screened charged, and hard spheres fluid from the confocal microscopy experiments. The measurements are done on PMMA particles in CDL+TCE and CDL+CHB with and without TBAB. The final results are explained in detail.

5.1 Abstract

The structure of the colloidal system in its thermodynamic equilibrium has been studied using confocal microscopy. Particle coordinates were obtained by confocal microscopy and used to study the system's structures with volume fractions ranging from 0.1 to 0.5. From the particle positions, g(r) and structure factor S(q) of the hard spheres colloidal model system have been obtained from various measurements. Hard sphere(HS) properties of the colloidal model system are first reviewed with Percus-Yevick's (PY) theory. Samples at volume fractions up to a freezing point are analyzed. Hard sphere-like behavior is observed in the TCE system by observing structure. The interaction is tuned using different solvents and adding organic salt to screen the electrostatic charge. The results show a discrepancy from HS-like behavior for other systems. The experimental 3D radial distribution functions are modeled by analytical theory and computer simulations taking polydispersity and the experimental position uncertainty into

account. The quantitative comparison between experiment and simulation/ theory establishes hard-sphere-like behavior for particles in CDL+TCE for a wide range of particle packing fractions. Furthermore, charged sphere behavior is confirmed both for the CDL+CHB and the CDL+CHB+TBAB solvents, and it is demonstrated that a finite particle concentration reduces screening in the CDL+CHB+TBAB system compared to the bulk solvent. Thus, by combining experiment and simulation, this chapter gives an extensive analysis and description of the structure of colloidal suspensions.

5.2 Data Acquisition

The Data are collected at 30-50 µm from the vessel bottom. Volumes of size 82x82x30 μm^3 are examined. The digital resolution is 1024x1024x120 voxels. The size of a voxel is lateral 80.2 nm and axially 251.8 nm. The measurements are carried out for short periods to study fluids long before the onset of crystal nucleation. In resonance mode with 8 lines averaging, it takes about 60 s to scan such a volume. Faster data acquisition (smaller volumes) in less concentrated samples compensates for the influence of particle diffusion on the accuracy of the particle position. Each g(r) was calculated from at least 30 independent 3D measurements. In the observation volume, typically, 10^4 particles are found.

Using LSCM, the number of particles N in the observed volume V_{sample} can be counted, allowing to determine the particle number density $\rho^{\#}$ given by eq 2.3. By inserting R_c value from SEM, we get

$$\phi_{core} = \rho_N . V_P = \frac{\pi}{6} \rho_N \langle d^3 \rangle_{PSD} = (\rho_N \mu\mathrm{m}^3).1.399 \tag{5.1}$$

The particle number densities obtained from image analysis are plotted against the prepared core volume fraction is shown in figure 5.1. The linear relationship (eq 2.3) allows an independent measure of the core diameter to be $2R_c = (1.388 \pm 0.005)$ µm, which is in excellent agreement with the SEM measurements. Consequently, the core volume fraction can also be determined from the LSCM measurements. Furthermore, it reflects the accuracy of our sample preparation.

In colloidal suspensions with a hard sphere-like interaction, the hard sphere volume fraction can be determined by measuring physical observables as a function of particle concentration, whose behavior is precisely known from analytical theory and/or simulation-e.g., short time diffusion [17], sedimentation velocity [108] [143], equilibrium phase diagram, [25] [59] equilibrium fluid structure[150], equilibrium crystal structure [202], osmotic pressure [34] [152]. The known core volume fraction can then be scaled to the hard sphere volume fraction, whereby the scaling factor α is the only fit parameter(eq 2.4).

To determine the scaling factor in this study, we analyzed the equilibrium fluid structure measured by LSCM. Figure 5.2 shows an experimentally determined radial distribution function for particles dispersed in CDL+TCE in comparison with (a) monodisperse, (b) polydisperse, and (c) polydisperse and error-spread g_{PY}(r). Figure 5.2 at the top right shows the first peak in more detail. The polydisperse and error-spread PY pair correlation function accurately describes the height and the shape of the peak. The comparison illustrates that considering polydispersity and position error propagation is necessary to

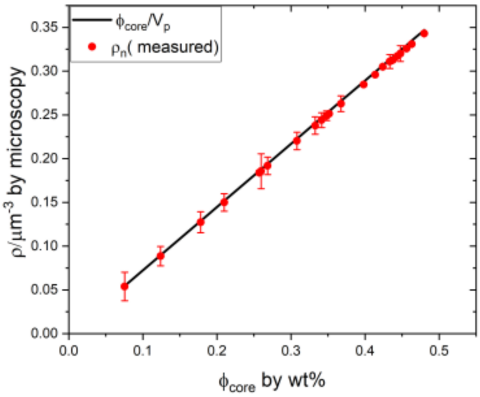

Figure 5.1: Plot of number density measured from confocal microscopy versus prepared core volume fraction from weight fraction for TCE. The line represents the expected relationship between core volume fraction and particle number density.

describe the experimental data. One must note that the polydispersity and the position error are accessible via independent measurements. These, therefore, do not represent additional fit parameters. The only fit parameter is the hard sphere radius. In the shown example, the minimum in Chi^2 is obtained at $2R_{HS} = 1.443\,\mu\text{m}$. In order to be able to compare theoretical g(r)'s directly with the experimental ones from LSCM, the (PSD)Particle size Distribution, and the experimental position errors must be considered. First, the g(r) was calculated based on the measured PSD. The polydisperse g(r) was then folded with a Gaussian distribution with a normalized standard deviation of 7.7% to account for the distance determination Δr_{ij} error.

To study the structure and perform the analysis, we measured the 3D radial distribution functions (g(r)) of the particles suspended in the solvents for different number density. The obtained g(r) is then compared with corresponding theory and simulation data to understand the interaction potential better.

5.2.1 Fluid-structure for particles in different solvent mixture from Confocal measurements

Samples are prepared with varying number density $\rho^{\#} = 0.05\text{-}0.3$. Before use, the samples are homogenized on a wheel mixer. Recalling the discussion of g(r) reported in Chapter 1, we remind the reader that, in the case of pure hard-spheres interactions, the position of the first peak of g(r) is volume fraction independent. It accounts for inter-particle separation at contact and can be used to measure particle size. A change in the position of the first peak of the radial distribution function shows the presence of soft, long-range repulsion, which modifies the effective particle size. For a good particle characterization, it is essential to know as much as possible about the particle interaction. The best way to get the knowledge is via the pair correlation function and structure factor of the particles in colloidal suspensions since it comprises of an ensemble averaged interaction. For the same reason, PMMA particles in CDL with

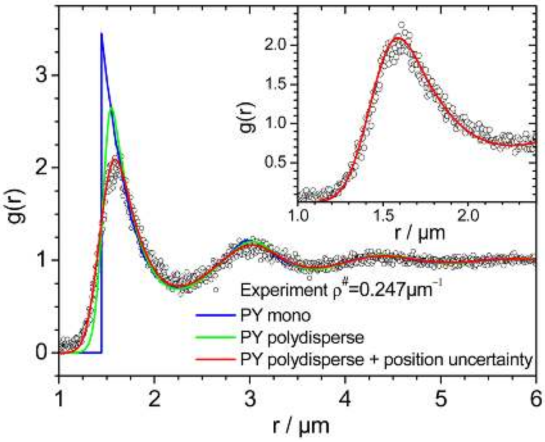

Figure 5.2: Experimental radial distribution function of PMMA particles dispersed in CDL + TCE in comparison with g(r) calculated using the Percus-Yevick relation: monodisperse (blue line), polydisperse (green line) and polydisperse and position error-spread solutions (red line) are shown. The inset gives a detailed view of the first peak.

different solvents are studied. S(q) and g(r) are computed from the position of several thousands of particles. as one can directly see in the figure 5.3, the position of the first peak in case of CDL+TCE remains same whereas in case of CDL+CHB and CDL+CHB+TBAB the position shifts towards left as the number density increases. Lets review the experimental data with theory and simulations.

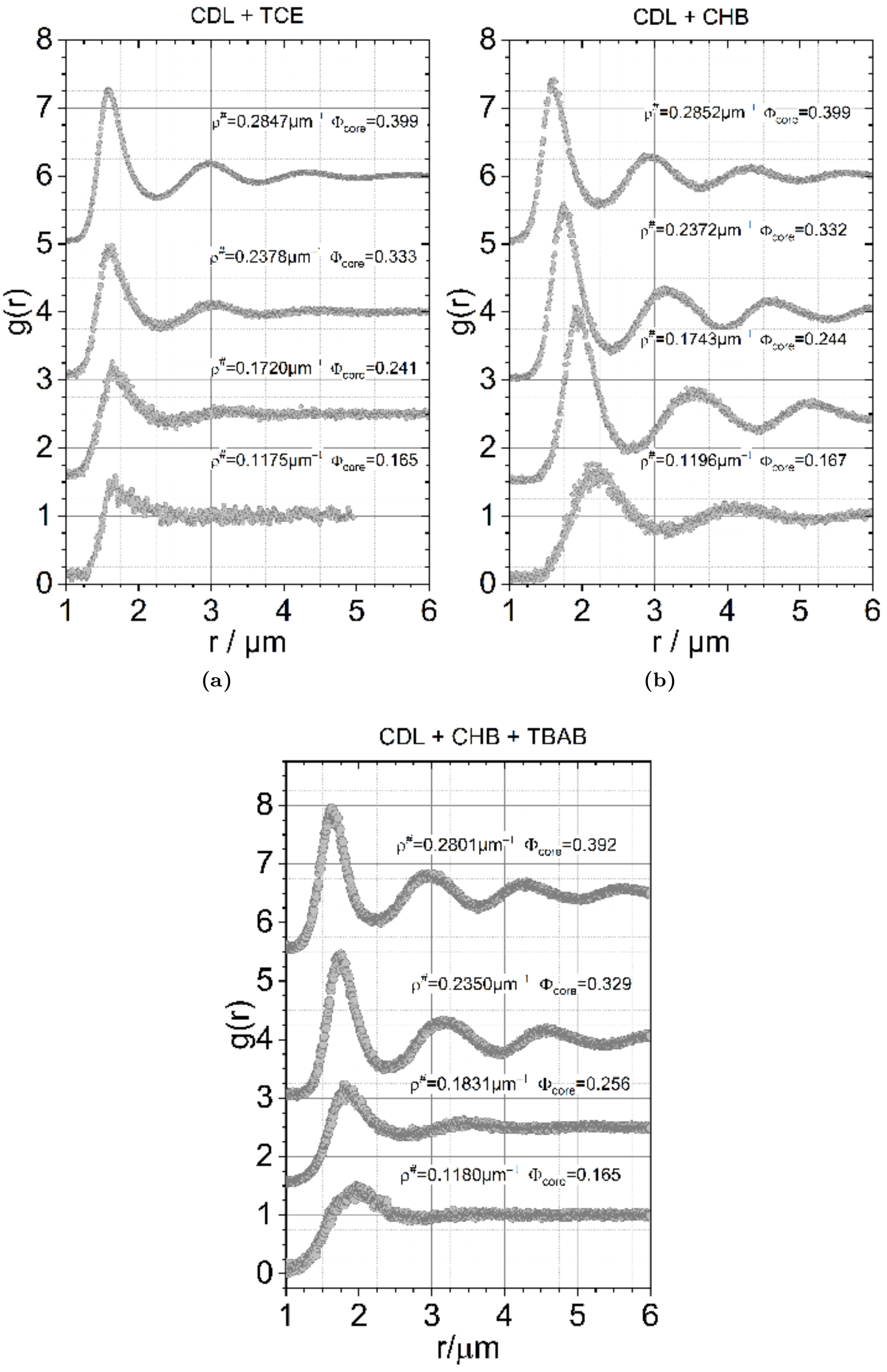

(a) (b)

(c)

Figure 5.3: (a) Measured g(r) from confocal microscopy for sample in CDL+TCE (b) in CDL+CHB (c) in CDL+CHB+TBAB and corresponding number density measured is labeled inside the graph for clarity.

5.3 Theoretical Study

In liquid state theory, g(r) of a fluid can be calculated from the Ornstein-Zernike integral equation using a suitable closure. Computer simulations offer an alternative approach. For hard spheres, the Percus-Yevick-closure (PY) allows the Ornstein-Zernike integral equation to be solved and the PY radial distribution function g_{PY}(r) or the static structure factor S_{PY}(q) can be calculated analytically citeequationofstate [215] [10]. Different algorithms have been presented to calculate g_{PY}(r) and S_{PY}(q) in polydisperse HS-fluids [147] [67]. To calculate the polydisperse g_{PY}(r) a self written Mathematica program based on the methods presented in the thesis was used.

In charged stabilized colloidal fluid, where particles interact via screened coulomb repulsion

$$U(r) = \frac{Z^2 e^2}{4\pi\epsilon\epsilon_0} \frac{exp(\kappa(\ 2R - r)}{(\ 1 + \kappa R)^2\ r} \tag{5.2}$$

(effective charge Z, screening parameter k, particle distance r), the so called Penetrating Background corrected Rescaled Mean Spherical Approximation (PB-RMSA) [191] [82] is the best choice to calculate g(r) analytically. For this purpose, we used the Algorithm developed by M. Heinen [81]. Unfortunately, there is no way to take the particle size polydispersity and the charge polydispersity into account.

5.3.1 PY-theory

The measured pair distribution function is compared with PY theory for the prepared number density in order to describe whether the particle behaves as hard sphere or not. As one can see in the figure 5.4(a), the measured g(r) in case of CDL+TCE is well defined by the PY-theory. The corresponding PY diameter is determined. The PY diameter agrees with the DLS diameter in CDL+TCE within the error limits. In confocal microscopic investigations, no indications of a long-range electrostatic repulsion or an attractive interaction exist. The structure of the colloidal model system is consistent with the structure of the HS fluid in case of CDL+TCE. Over the entire volume fraction range, the PY-g(r) agrees very well with the measured data. Both the position and height of the first peak and the periodicity of the courses are in harmony with each other. The curves show that a PY approximation can describe the fluid structure of the colloidal sample system in the case of CDL+TCE. With the advantage of the constant scaling factor, the measurement data are adequately described in the entire area. By fitting the PY-g(r) to the experimental data, the scaling factor and the effective HS-radius are obtained: $\alpha^{1/3} = 1.03818$ ±0.0023 and $2R_{HS} = 1.441 \pm 0.004$µm .

In the case of CDL+CHB and CDL+CHB+TBAB, the PY-g(r) does not agree with experimental g(r)(Figure 5.4(b) and (c)). The peak height and peak position also vary with the number density. The periodicity over the entire range shows that PY-theory is not correct to fit the measured g(r), so one has to choose another theory or simulation to explain the system's behavior.

5.3.2 PB-RMSA

For charged stabilized systems where particles interact via screened coulomb potential, the so-called Penetrating Background Corrected Rescaled Mean spherical approximation(PB-RMSA) is the best choice to calculate g(r) analytically. For this purpose, we used the software developed by M.Heinen[81]. Unfortunately, there is no way to take the particle size polydispersity and the charge polydispersity into account. To check the influence of TBAB salt does indeed screen the particles interaction effectively, we investigated the colloid-colloid interactions via pair distribution function g(r).

In the figure 5.5, a comparison between experiment and fitted convoluted PB-RMSA data is shown. For charged systems, the position of the first peak of g(r) increases with decreasing volume fraction. Columbic repulsion inhibits colloids from coming close to each other at low-volume fractions, resulting in a larger effective particle size. Dispersed in CDL-CHB dyed PMMA-PHSA particles are charged. For CDL + CHB alone, the fluid structure is well described by monodisperse PB-RMSA theory - beyond the first peak in g(r), there is a very good agreement between experiment and theory, while the first peak is not characterized correctly. As expected, the experimental g(r)s reflect the typical behavior of a colloidal charged sphere fluid. With increasing particle concentration, the principal peak shifts to smaller r-values; the nearest neighbor distances decrease. The experimental data are in good agreement with the monodisperse PB-RMSA g(r).

Charge-stabilized colloids present a multi-component system comprised of colloidal macro-ions and microscopic counter and co-ions, all immersed in a solvent. Adding salt to such a dispersion allows columbic repulsions between the colloids to be screened, so the particles behave almost like a one-component hard sphere system. As primary expectation is that TBAB in CHB leads to additional free ions and therefore screening. It is already known that density-matched and refractive index-matched mixtures of CDL-CHB interact through electrostatic repulsions over distances larger than the particle size[225]. Since alkyl halides are self-prone to dissociation, i.e., in CHB, the dissociation would lead to the formation of HBr. Only a small amount of HBr is dissolved in CHB, which could explain charge conductivity in many previous study cases. However, after the addition of TBAB, maybe it is Br- ion preferentially ends up in the PMMA spheres. The process of this adsorption is still in debate. Contrary to what was reported by other authors, we see that charges have not been fully screened(Figure 5.4 and 5.5). In the case of added TBAB, we observe that the surface charge cannot be effectively screened even upon using nominal large salt concentrations. Thus as one can observe the peak position also shifts similarly as in case of CHB.

5.3.3 Simulations

(Simulation was done by Prof. Martin Oettel)

We performed Monte Carlo (MC) simulations in the canonical ensemble for a multidisperse mixture with N particles. The radii $R_i (i = 1...N)$ were distributed according to the experimentally determined distribution of Fig. 1 and multiplied with a factor of 1.043 to account for the swelling of the particles. As a result, the mean diameter is $2<R>\approx 1.4\,\mu m$. Particles interact via the pair interaction energy

$$U_{ij}(r) = \begin{cases} \infty, & (\ r{<}R_i + R_j) \\ \frac{Z_i Z_j e^2}{4\pi\epsilon\epsilon_0} \frac{exp(\kappa(\ R_i+R_j-r)}{(\ 1+\kappa R_i)\ (\ 1+\kappa R_j)\ r}, & (\ r \in \left[R_i + R_j, r_c\right]) \\ 0, & (\ r{>}r_c) \end{cases} \tag{5.3}$$

which is of hard sphere-Yukawa (HSY) form, its electrostatic part is the multi-component generalization of the potential in eq.5.3. Particles were assumed to have a constant surface charge density such that an individual effective charge Z_i is determined from a mean charge $< Z >$ via $Z_i = Z\ R_i^2 < R_2 >$. The screening length is determined from

which is of hard sphere-Yukawa (HSY) form, its electrostatic part is the multi-component generalization of the potential in eq.5.3. Particles were assumed to have a constant surface charge density such that an individual effective charge Z_i is determined from a mean charge $< Z >$ via $Z_i = Z\ R_i^2 < R_2 >$. The screening length is determined from

$$\kappa^{-1} = \Big(\frac{\epsilon_0 \epsilon k_B T(\ 1 - \Phi)}{e^2(\ Z\rho^{\#} + 2000 c_s N_A)}\Big)^{\frac{1}{2}} \tag{5.4}$$

where the solvent relative dielectric constant is ϵ=5.8, the temperature is T = 300 K, Φ=(4/3)$< R^3 >\rho^{\#}$ is the volume fraction of the particles, c_s is the concentration of free salt ions (in mol), and N_A is Avogradro's constant. Thus, it corresponds to the standard definition of the Debye-Huckel screening with the modification that free charges are salt ions and counter ions released from the particles, and their concentration is a concentration in the free volume (simulation volume minus the volume of the hard core of particles), giving rise to the correction factor $1 - \Phi$. The cutoff r_c in eq.5.3 was chosen as r_c = max(4$< R >$, 2$< R >$ + 10κ^{-1}).

For a given particle number density $\rho^{\#}$ of an experimental sample, we fitted the pair correlations by varying the mean charge $< Z >$ (in the case of CDL+CHB where there are no free salt ions, $c_s = 0$) and by varying $< Z >$ and c_s (in the case of CDL+CHB+TBAB).For some parameter choices, we assessed polydispersity's influence by comparing to simulations with monodisperse particles, whose mean radius and mean charge are equal to the polydisperse system. We used N = 864 particles, displacements in single particle moves were chosen such that the acceptance ratio was between 0.3 and 0.6. For low Z, thermalized configurations could be obtained by performing 10^4 thermalization sweeps, starting from a crystal configuration. For high $< Z >$, we used a low $< Z >$ equilibrated configuration and thermalized it further. For g(r) measurements, we used between 5x10^5, and 10^6 sweeps, performing measurements every 100 sweeps.

For comparison, the simulation results showed with the same mean charge, but taking charge and size polydispersity in to account(Figure 5.6). There is a noticeable effect on the first two peaks; the peaks are broader and slightly asymmetric. If the mean charge is adjusted freely, excellent agreement with the experimental data can be achieved. The simulations describe the first two peaks much better. It is worth noting that the sample at $\rho^{\#}$=0.2372µm^{-3} displays an asymmetry in the second peak, indicating that this sample might be out of equilibrium. In the performed simulations, the system crystallized. The sample was not monitored long enough to detect crystallization in the experiment.

In the figure 5.6 experimental data from CDL+CHB and CDL+CHB+TBAB are compared with simulations at four different densities. As explained before for two higher densities there is no clear evidence of substantial salt screening are evident: the first peak is unchanged in height and position. For 0.28 the subsequent oscillations are bit more pronounced and for 0.237 the first minimum is less pronounced. For smaller densities 0.174 and 0.119 , the effect of TBAB addition seems to be both height reduction of the first peak and a damping of the subsequent oscillations.

Denisity µm^{-3}	Z	c_s in µ M	κ^{-1}nm	κR
0.118	100±20	0.15±0.05	193±33	≈4
0.1831	83±10	0.075±0.025	247±39	≈3
0.2350	575±175	0.75±0.25	73±12	≈10
0.2801	270±30	0.75±0.25	70±11	≈10

Table 5.1: Charge, salt concentration, screening length and normalized screening parameter based on the simulated g(r) fitting the experimental CDL + CHB + TBAB data

The experimental data can be very well described using simulated g(r) with similar charges as in the CDL + CHB system and effective salt concentrations in the mM range. Due to stronger screening, polydispersity must be taken into account-a description using monodisperse PB-RMSA does fail(5.5). In contrast to the CDL + CHB system, good simulation results can be obtained using a larger variation in the effective charge and salt concentration- there is a significant uncertainty in these fit parameters. An extreme example is g(r) at $\rho^{\#} = 0.2350$µm^{-3}. Here, the experimental data can be described very well using a combination of $< Z > = 750$ and c_s=1mM as well as using $< Z >=$ 400 and $c_s = 0.5$ mM. The corresponding Chi^2 values are almost identical. The performed curve fitting allows determining the effective interaction between the colloidal particles and thus the screening length. Table 5.1 summarizes results obtained from the fits shown in Figure 5.6.

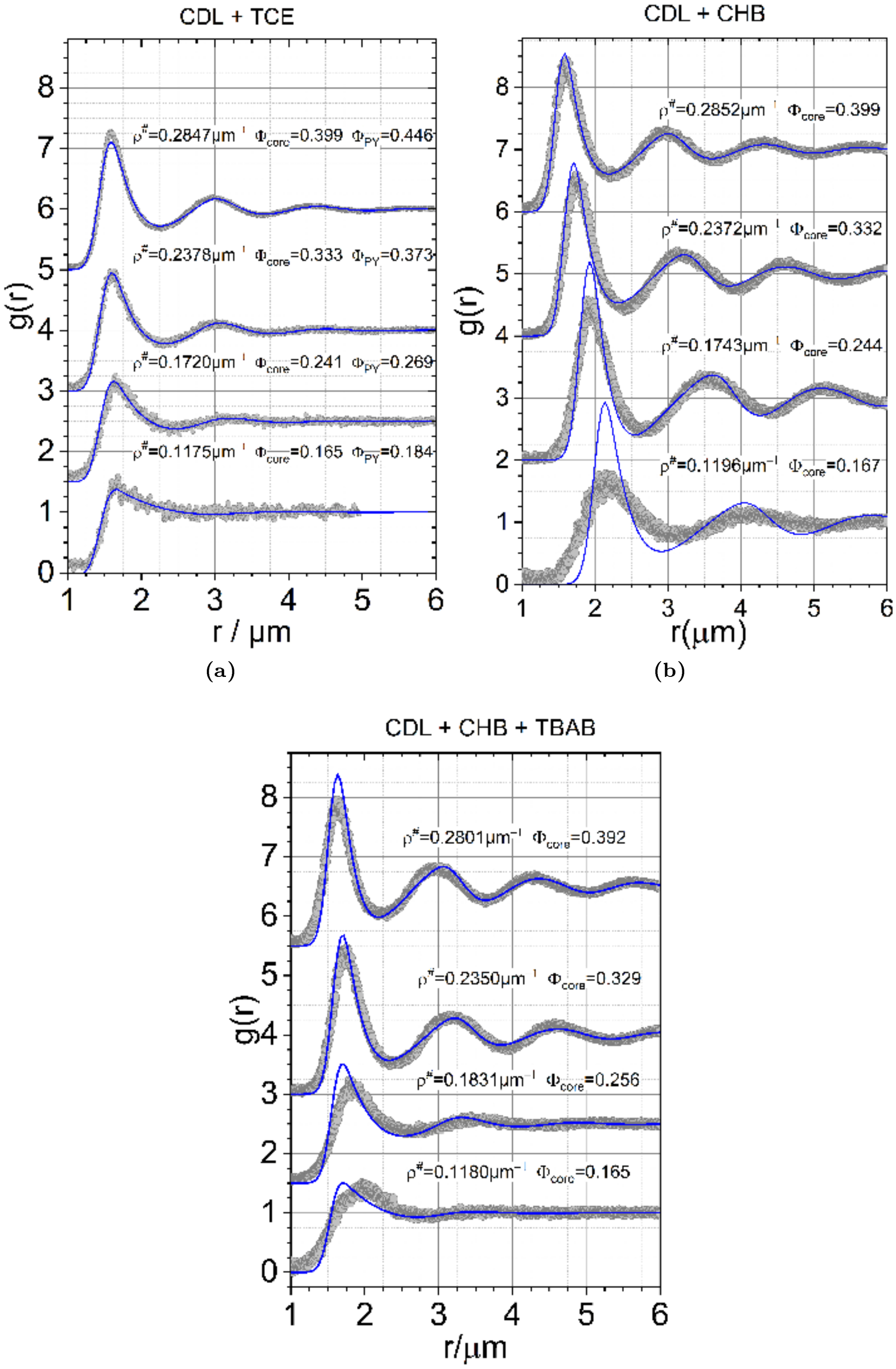

(a) (b)

(c)

Figure 5.4: (a) Measured g(r) from confocal microscopy and the blue lines are polydisperse, position error-spreaded PY-g(r) for hard sphere volume fractions as indicated for sample in CDL+TCE (b) in CDL+CHB (c) in CDL+CHB+TBAB .

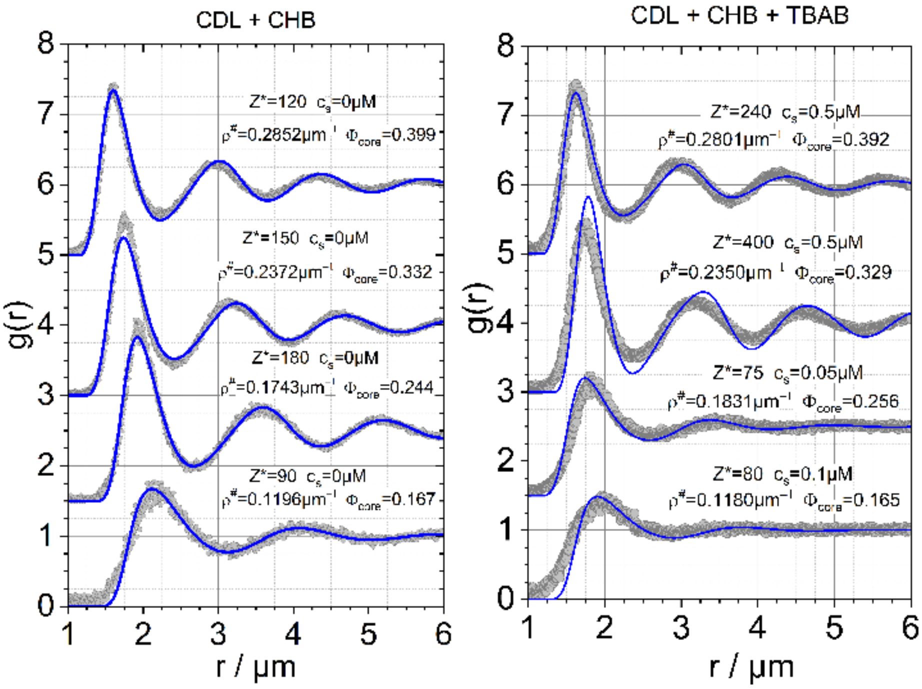

(a) (b)

Figure 5.5: (a) Measured g(r) from confocal microscopy for sample in CDL+CHB (b) in CDL+CHB+TBAB. The blue lines in the plot are monodisperse, position error-spreaded PBRMSA- g(r) and corresponding number density measured is labeled inside the graph for clarity.

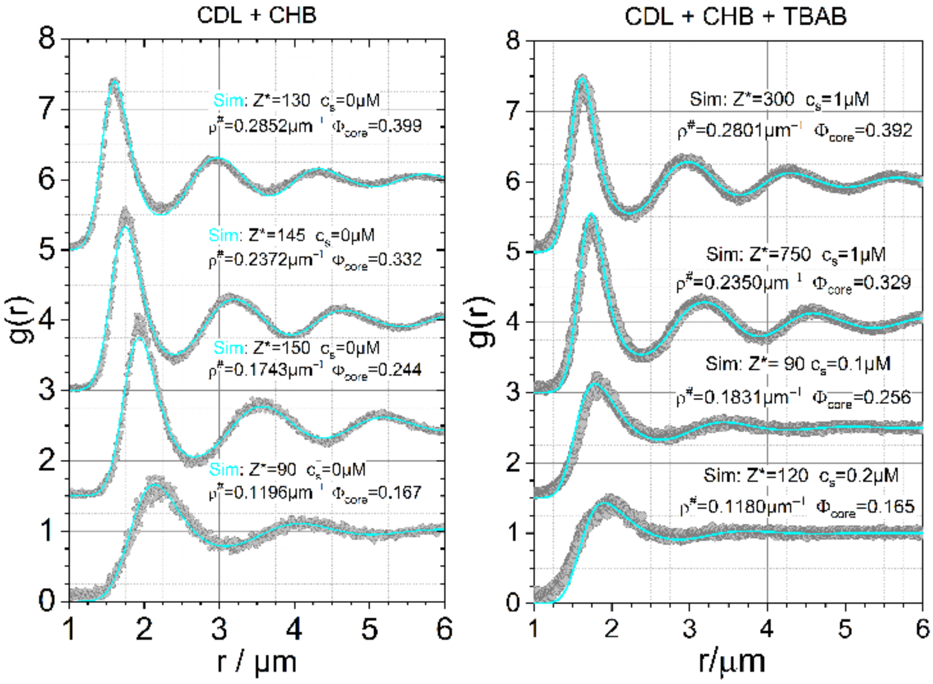

(a) (b)

Figure 5.6: (a) Measured g(r) from confocal microscopy for sample in CDL+CHB (b) in CDL+CHB+TBAB. The light blue lines are polydisperse, position error-spreaded g(r) from simulation with effective charges as indicated. and corresponding number density measured is labeled inside the graph for clarity

5.4 Reproducibility

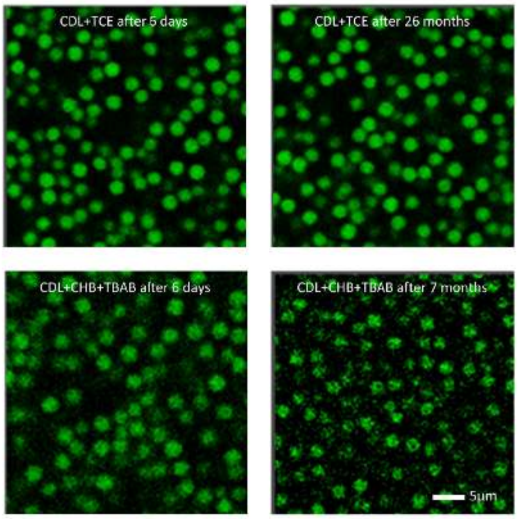

Figure 5.7: Confocal microscopy images (38x38mm^2) of samples in the equilibrium fluid state at different times after sample preparation. Top:CDL + TCE sample ($\rho^\# = 0.136$ µm^{-3}) 6 days (left) and 26 months (right). Bottom: CDL + CHB + TBAB sample ($\rho^\# = 0.1470$ µm^{-3}) 6 days (left) and 7 months (right) after sample preparation.

In our lab, we typically reproduce experimental data using at least one other set of samples in repeated measurements to get an idea of the systematic error before we analyze and interpret the measurements. The CDL+TCE and CDL+CHB data could be easily reproduced with high precision. Unfortunately, this was not the case for the CDL+CHB+TBAB data. In Figure 5.8, we show the experimental g(r) of four different samples prepared using the identical protocol for the CDL+TCE and CDL+CHB+TBAB samples. While the CDL+TCE samples give almost identical results, this is not true for CDL+CHB+TBAB. Here we observed significant discrepancies between the data sets. The origin of this strange behavior is unknown. We speculate that it may be correlated with adhesive fixing the coverside to the glass tube[140].

Furthermore, we noticed some significant changes in the distribution of the dye in the particles when particles were dispersed in a solvent containing CHB, making it impossible to obtain meaningful data in samples older than 2 months. Figure 5.7 shows confocal microscopy images of particles in CDL + TCE and CDL + CHB + TBAB a few days and months after sample preparation. While the particles in CDL + TCE display no significant change, the image of the particles in CDL + CHB + TBAB becomes very noisy after a few weeks. It is obvious that the distribution of the dye within the solvent influences PMMA particles, so an exact determination of the particle's position becomes impossible.

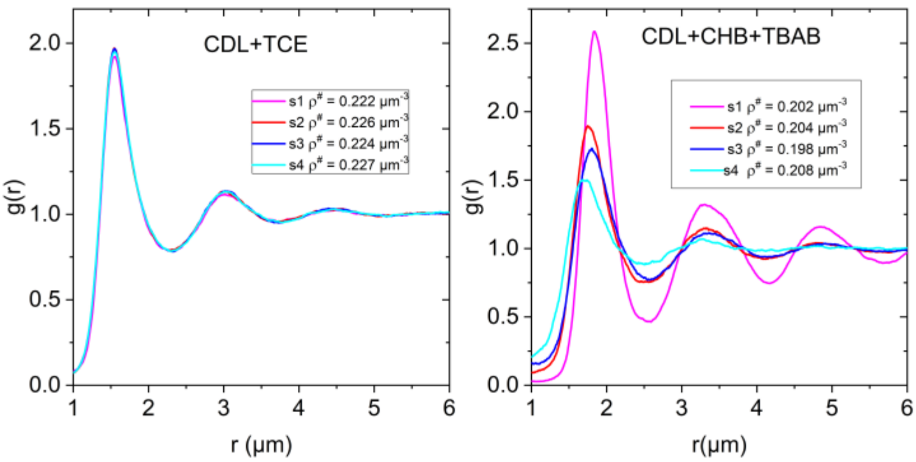

(a) (b)

Figure 5.8: Experimental radial distribution functions of particles in CDL + TCE and CDL + CHB + TBAB for particle number densities as indicated. Data are smoothed by 25 point floating average for clarity. All sample were prepared in the same manner in different sample cells.

5.5 Different concentration of TBAB in CHB

This study uses different TBAB concentrations, such as 3.8 m M(saturated solution), 1 m M, and 1 µ M TBAB in CHB. For more clarity only two number density such as 0.2 and 0.24µm^{-1} having different concentration of TBAB is shown in the figure 5.9(a) and (b).

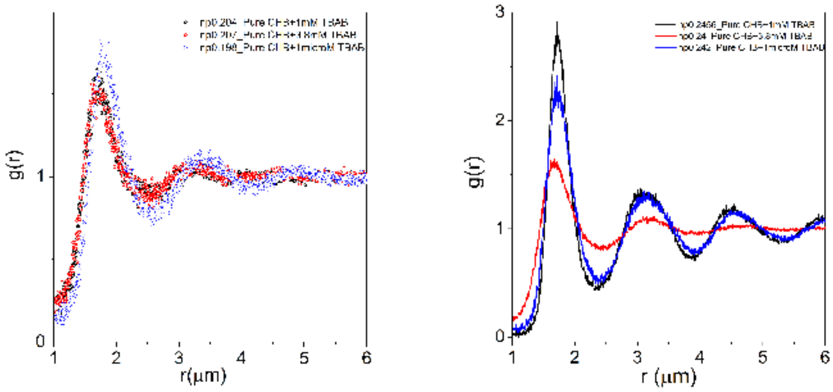

(a) (b)

Figure 5.9: Experimental radial distribution functions of particles in CDL + CHB + TBAB for particle number densities and corresponding salt concentration is indicated.

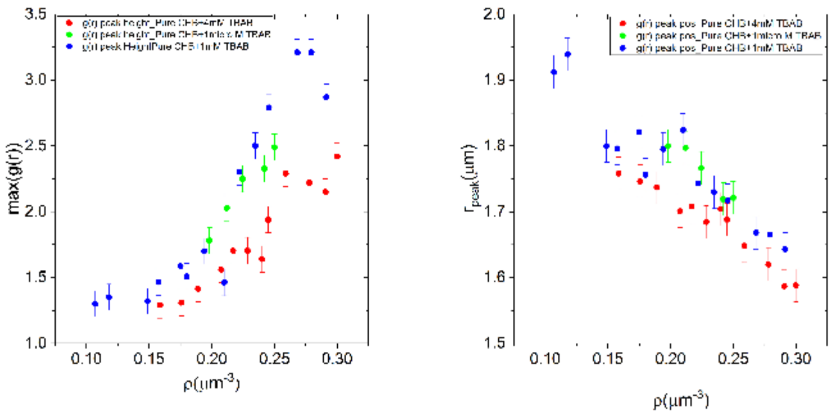

(a) **(b)**

Figure 5.10: (a)Position of the first peak in g(r) measured in CDL + CHB+TBAB having different concentration of TBAB in CHB as indicated. (b) height of the first peak in g(r).

Starting with the saturated solution of TBAB(3.8 m M) in CHB, samples were prepared having number density varying from 0.09 to 0.35. Similarly concentration of salt is been reduced further to 1 m M and to 1 μ M and samples were prepared in order to see the influence on the structure of colloidal fluids. As one can see in the figure 5.9(a) more damped oscillations can be seen in case of higher concentration in 3.8 m M. Similarly the oscillations are also seen in figure 5.9(b) but not efficiently. In order to see the differences one can also see the variation of the peak height in terms of charge obtained by fitting the first peak of g(r) to PBRMSA data obtained from Marco Heinen software. As mentioned before, adding polydispersity was impossible. From the figure 5.10 as one can see the position of the first peak increases and the peak height decreases with increase in number density. Thus it is worth to note that even with different salt concentration, the system does not behave hard sphere like. Unfortunately, we were not able to measure electrostatic measurements because the CHB dissociates even in presence of stray light which leads to incorrect values of particle charge.

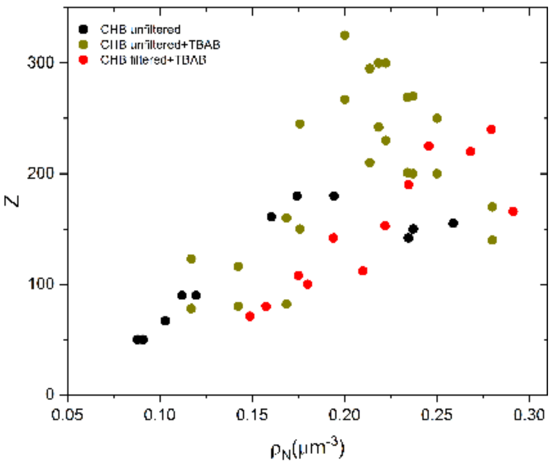

Figure 5.11: Obtained charge Z for corresponding measured data for CHB unfiltered, CHB unfiltered +TBAB and CHB filtered + TBAB. The Z values were obtained by fitting the first peak of experimental g(r) with PBRMSA data from Marco Heinen software.

5.6 Results

In order to specify systematically the deviations in the experimentally determined structure of the equilibrium fluid from the PY theory, we have determined the position and height of the first peak in the radial distribution function and the static structure factor. The static structure factor was calculated from the experimental g(r). The results are shown in figure 5.12. Please note that the PY data of a polydisperse system were smeared with the experimental position error as described before. While the position in g(r) indicates, the nearest neighbor distance d_{NN} (particle diameter in HS), the position of the structure factor maximum reflects the average particle distance $< d >$ (periodicity of g(r)). The height of the peak of g(r) reflects the relative probability of finding particles at the nearest neighbor distance. In contrast, the height in S(q) measures the degree of long-range periodicity. In the following, we will discuss the behavior of the different systems in turn.

CDL + CHB: The nearest neighbor distance d_{NN} and the average particle distance $< d > \approx 1/q_{peak}$ decrease strongly with increasing particle concentration. In particular, the average particle distance displays the expected behavior $q_{peak} = 2\pi/< d > \approx \rho^{1/3}$ of charged sphere fluids. Analyzing the peak height in g(r) and S(q), we observe first a strong increase with increasing concentration ($0.09\,\mu\mathrm{m}^{-3}$ $0.17\,\mu\mathrm{m}^{-3}$), followed by a saturation ($0.17\,\mu\mathrm{m}^{-3} < 0.25\,\mu\mathrm{m}^{-3}$) and a decrease after that. Increasing particle concentration (decreasing d_{NN}) increases the electrostatic interaction between the particles, according to eq.5.2). The high peak values in S(q) in comparison with the Hansen-Verlet-criterion [77] and the split in the second peak in g(r) in the plateau region suggest that these samples are out of equilibrium. Similar observations were reported previously [167].

CDL + CHB + TBAB: Since we could not obtain reproducible results adding TBAB to CHB, we plot three different data sets. One which behaves similarly to the CDL + CHB samples (series s1), one where we got somehow reproducible results (mean of s2 and s3), and one where we observed the largest screening (s4). The nearest neighbor and averaged particle distance of data s1 show no significant difference compared to the discussed charged sphere data. Looking at the peak heights, we see that the increase at lower particle concentrations is weaker and that the cross-over to non-equilibrium appears at slightly higher concentrations.

Remarkably, the maximum peak heights are larger than in the CDL + CHB samples. The samples s2 and s3 display significant surface charge screening, but the interaction is still not hard sphere-like. Although the peak heights in g(r) and S(q) up $\rho \approx 20\,\mu\mathrm{m}^{-3}$ are not inconsistent with the prediction for HS, the nearest neighbor and averaged particle distance, display strong deviations. Beyond a particle concentration of $\rho \approx 0.20\,\mu\mathrm{m}^{-3}$ the measured peak heights increase rapidly, and the fluid crystal phase boundary is crossed at $\rho \approx 0.23\,\mu\mathrm{m}^{-3}$. The same applies to sample s4. Here, at low concentrations, a behavior similar to that of a hard sphere suspension is observed, changing at $\rho \approx 0.22\,\mu\mathrm{m}^{-3}$ into the typical behavior of weakly screened charged particles.

CDL + TCE: The experimental peak positions and heights in g(r) and S(q) of the CDL + TCE data show excellent agreement with the predicted values for HS. In S(q), VW-correction(68) is necessary to describe the experimental peak height approaching the freezing transition.

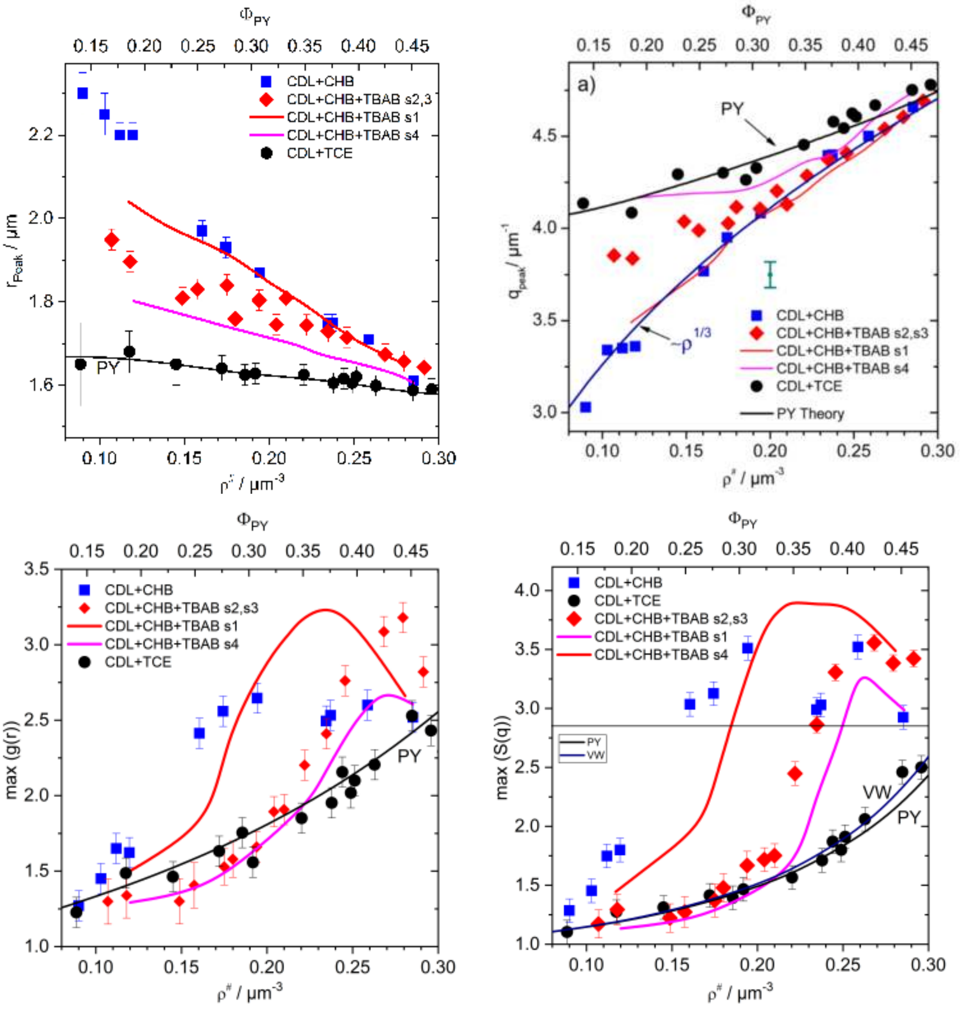

Figure 5.12: Characteristic measures of the fluid structure in direct space. (a) position of the first peak in g(r) measured in CDL + CHB (blue squares), CDL + CHB + TBAB (red diamonds, red line and magenta line) and CDL + TCE (black dots) The black line is the prediction for a polydisperse and position error-spreaded PY-g(r) with 2R = 1.441µm. (b) height of the first peak in g(r)-symbols and lines as in (a).

5.7 Conclusion

In short, we have answered two long-standing questions posed by Weeks, Royall and Poon. We demonstrated that PMMA-PHSA particles dispersed in CDL + TCE display a hard sphere behavior while in CHB containing solvents, this is not the case. It is possible to determine the hard sphere volume fraction in colloidal suspensions with high accuracy. We have determined the fluid structure of fluorescent PMMA-PHSA particles in three different solvents (CDL + CHB, CDL + CHB + TBAB, CDL + TCE) by LSCM and compared it with analytical theory and simulations. To this end, the suspensions, the experimental set up and the data evaluation must first be characterized with high accuracy. The precise knowledge of the particle size distribution and the uncertainty in the particle position determination is mandatory in order to be able to successfully compare theory and experiment.

The relevance of these results lies in the context of defining suitable colloidal model systems for simple particle interactions. First, the CDL-TCE system is clearly a good model system for hard spheres. This has been speculated about before [137] but has now been confirmed via the agreement between experimental and theoretical pair correlations over a wide range of densities. Secondly, we confirm that the CDL + CHB system is a good model system for charged hard spheres. Thirdly, we demonstrate that the CDL + CHB + TBAB system must be used with caution as a model system for (strongly screened) charged spheres. Through the quantitative agreement between experimental and theoretical pair correlations, we conclude that it is not sufficient to characterize the screening length in the system using the pure bulk solvent, rather we see that screening depends on the presence of the colloidal particles and it is weaker than estimated from bulk conductivity measurements.

This finding provides a clear indication that the CDL+TCE model system can be utilized to measure rate densities and potentially resolve the long-standing discrepancy between simulations and experiments. As a result, in the next chapter, we aim to determine the rate densities using this hard sphere-like system.

Chapter 6

Crystallization study of HS using confocal microscopy

6.1 Abstract

Crystal Nucleation is a much-studied phenomenon, yet the rate at which it occurs remains challenging to predict. Small crystal nuclei form spontaneously in supersaturated solutions, but unless their size exceeds a critical value, the so-called critical nucleus, they will re-dissolve rather than grow. It is this rate-limiting step that has proved challenging to probe experimentally. We explore crystal nucleation in a colloidal hard-sphere system using Laser Scanning confocal microscopy by resolving each colloidal particle individually. It allows one to characterize the detailed nucleation path and formation of crystals with greater precision than any other experiments. Direct imaging in three dimensions offers the unique possibility of observing crystal nucleation and growth on the particle level, giving detailed information about the fluid-to-crystal phase transformation. Particles with crystal-like surroundings are identified using the average bond order parameter by quantifying the orientation of the nearest neighbors of the particle. We are investigating the temporal evolution of ensemble-averaged and local structures to identify the nucleation mechanism. We determine the Rate densities directly and within the framework of CNT. Thus, results show that the rate densities from the experiment and CNT diverge by several orders of magnitude, we conclude the cause of this discrepancy is due to shortcomings of the CNT.

The Hard sphere Nucleation data from experimental and theoretical studies diverge by several orders of magnitude, and the curves are qualitatively different. One of the primary goals of our research is to identify the underlying reason for this discrepancy. We studied the crystallization by changing the density mismatch between particle and solvent and introducing different solvent inducing charge and so on and compare it with other experimental and simulation data.

6.2 Introduction

The crystallization of a metastable melt is one of physics' most important non-equilibrium phenomena. An in-depth understanding of the crystallization process is not just from the view of fundamental research but also plays a crucial role in the targeted development of new materials with tailored properties. Crystal nucleation is particularly important in crystallization since it is the "birth" of the resulting stable phase or new material. It is therefore not surprising that this research focus is intensively worked on in experiment and theory, and different systems (metals, colloids, proteins, polymers, bio-minerals, etc.) have to content. The key advantages of using colloids for crystallization (phase transition) study are accessibility to individual "atoms" by optical methods in space and at convenient timescale in dynamics, adjustability of the morphology of colloids (size, shape, and their distributions), interparticle interactions (by chemical grating, electric, and magnetic fields), and concentration (by gravity, temperature, and temperature gradient). This research field of colloidal crystallization is making progress along several frontiers: (i) Capture the morphology of the nuclei, demanding refinement in nucleation theory; (ii) quantitatively understand the sensitivity of nucleation rate to the detail of inter-particle interactions, especially the softness of nearly hard spheres; (iii) incorporate novel techniques to measure the crystallization kinetics, such as droplet microfluidics for emulsion crystallization investigation and microgravity environment for long-term observation; (iv) bridge to close fields, such as melting, crystal-crystal transformation, phonons, kinetics of defects in crystals and amorphous solids; (v) develop applications of colloidal crystals, such as the fabrication of photonic crystals and chemical sensors.

The crystallization process in atomic systems is difficult to evaluate experimentally due to the underlying time and length scales. Further problems arise due to high crystallization rates, high heat of crystallization in combination with limited heat transfer, and strong influence of heterogeneous nucleation. Colloidal model systems provide an alternative approach: specially synthesized colloidal suspensions of spherical particles with well-defined inter-particle interaction. These systems have been around for several decades and have been used successfully for fundamental and application-related aspects to study the phase transition kinetics. Colloidal suspensions present an experimental model by which we might gain insight into crystallization kinetics. These suspensions render time and length scales amenable to empirical measurement. Colloidal crystals' mechanical fragility and slow regrowth after shear melting overcome some major experimental hurdles in molecular systems.

6.3 Literature review

Data can be sorted into three groups(Figure 6.1). One is those obtained by Schatzel and Ackerson (PMMA, a = 500 nm s = 0.05, in tetraline/decalin, squares) [177], He et al (PMMA, a = 495 nm, s = 0.05, in tetraline/decalin, dots) [80] and Sinn et al (PMMA, a = 445 nm, s = 0.025, in tetraline/decalin, diamonds) [79]. The second experimental data group comprises data of Harland et al. (PMMA, a = 495 nm, s = 0.05, in tetraline/ decalin, down triangles) [177], He et al. (PMMA, a = 215 nm, s = 0.07, in tetraline/decalin, up triangles) [80],

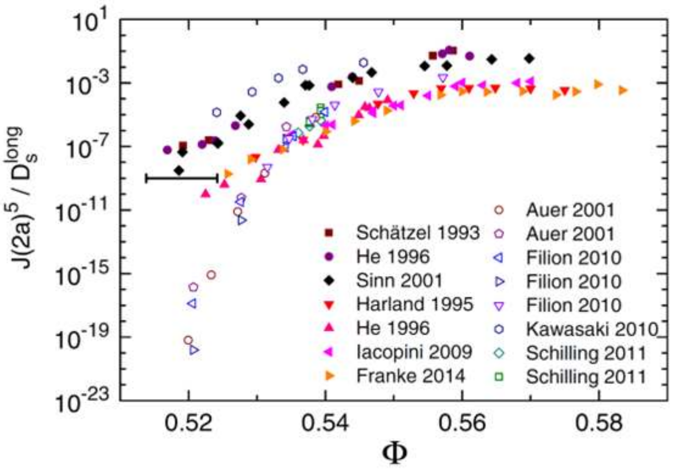

Figure 6.1: Scaled nucleation rate densities from experiment (closed symbols) and simulation (open symbols) in dependence on effective HS packing fraction [146].Details of the plot are given in the text with citations.

Iacopini et al. (polystyrene micro-gels, cross-link density 1:10, a = 423 nm, s= 0.065, in 1-EN, left triangles) [93] and Franke (polystyrene micro-gels, cross-link density 1:30, a = 410 nm, s = 0.055, in 1-EN, right triangles) [65]. The horizontal error bar gives an estimate for an uncertainty in packing fraction of ±0.0051 in Φ. The simulation data for HS systems form another group. Here we show data of Auer and Frenkel for monodisperse HS (circles) [63] and HS with s = 0.05 (pentagons) [16], of Filion et al. [62] [63] for monodisperse HS obtained from a Bennett-Chandler type theory where the nucleation barrier is determined using umbrella sampling simulations (left triangle), by forward flux sampling (right triangle) and by molecular dynamics (down triangle) as well as those Schilling et al [178] obtained for monodisperse HS by molecular dynamics simulations (diamonds) and Monte Carlo simulations (squares). These simulations of HS show a much stronger packing fraction dependence of the scaled nucleation rate density at low Φ than experimental data. At large Φ, the agreement between simulation data and experimental data of the second group is quite remarkable. For comparison, we also show the simulation data of Kawasaki et al. (hexagons) [99] for a monodisperse system of spheres with WCA interactions used to approximate HS interactions [214].

An interesting observation can be made in Figure 6.1 within the experimental data. Caution is needed here because of the significant systematic uncertainties remaining in the packing fraction determination. Therefore, an exemplary optimistic error bar is included in Figure 6.1. Considering the apparent grouping, one may ask for possible correlations with other sample properties. PS micro-gel particles are only observed in the lower data group; PMMA particles are observed in both groups. In the case of the PMMA spheres investigated by He [80], the authors note that both systems were synthesized, coated, conditioned, and characterized the same way. Thus, the systematic error can be neglected, and another reason for the discrepancy must be sought. Some possibilities have already been indicated by He et al. First, the smaller particles could have a slightly softer potential because their coating is more extended than the particle radius. However, a notably increased J^* is expected for a softer potential, as seen from Kawasaki et al. [99] simulations, which used particles with a Weeks Chandler Andersen potential [214]. Also, Gasser et al. found for slightly charged HS (P= 0.38) [111] that their rates from confocal microscopy were larger than for HS particles and showed only little dependence. However, the smaller experimental HS of [93] shows a lower J. A second possibility to slow nucleation is poly-dispersity, as, for example, seen by comparing the two data sets of Auer and Frenkel [63] [178]. In the experiments, the smaller PMMA species have the larger polydispersity. However, the size similar large PMMA species of Sinn [65] are found within the same group as the large PMMA spheres of He, despite a factor of two difference in polydispersity.

Another difference between the two PMMA species, already pointed out by the authors, could be gravity's influence, as Russo et al. noted [162]. The two data groups are sorted by significantly different Peclet numbers, Pe, which characterize the ratio of diffusion to sedimentation time scales. The upper group shows P $\approx$ 0.3, and the lower group is P$\approx$ -10. Also, the sedimentation-free simulations agree considerably better with the lower group. Data extracted from simulations with sedimentation, performed by Russo et al [221](plot not shown here) on particles with WCA interaction at P = 0.3, agree reasonably well with the upper group data. At low, the simulation data are significantly above the upper experimental group, which might also be an effect of the slightly soft potential used. Using a two-state model, the authors could further improve the agreement between their simulation and the upper experimental group data [162]. More interestingly, these data are ten orders of magnitude above the other sedimentation-free simulation data. Thus, if one considers the difference between the two experimental data groups significant, sedimentation seems to be a viable candidate for its origin. However, the actual mechanism is not yet understood. This conjecture could be checked in further experiments of differently sized PMMA-spheres and computer simulations, including an external gravitational field and possibly also addressing density fluctuations during sedimentation [93], for example, driven by the different nuclei densities.

The only control parameter for HS fluid is Φ volume fraction occupied by spheres. Experimentally, the HS system is reasonably well realized with suspensions of monodisperse colloidal particles that interact through the steep repulsive potential [158]. Nevertheless, quantifying colloidal suspensions as Hard spheres requires a deep understanding of the potential and characteristics properties of particles and solvents involved. According to simulations, the absolute crystal nucleation rate of the colloidal system depends dramatically on Φ with polydispersity and slight softness in the inter-particle potential. This 15-order of magnitude increase in rate was found in simulations for Φ=0.52 to Φ=0.54 [16]. This behavior is attributed to different computational techniques [63]. However, this behavior is not observed in experiments where weak Φ dependence is found [177] [78]. Over the decades, despite numerous attempts to address the possible causes, the discrepancy persists [146] [12] [63]. In short, neither experiment nor numerical predictions exhibit a profound flaw.

Previous experimental studies which considered the size polydispersity [16] [227], electrostatic charge [14], hydrodynamic coupling between solvents and particles [162] and sedimentation have not resolved the disagreement. Meanwhile, the simulation results from various groups have been reproduced with different rare event sampling techniques. We believe that discrepancy arises from uncertainties in the knowledge of the pair interactions, and these details have not been incorporated into the study of nucleation kinetics. Another important reason lies in the disparities between experimental quantities and models' predicted quantities. Consequently, a fundamental understanding of the governing principle of the crystallization process is still lacking.

Kinetic data on CS nucleation have made notable strides in this area since 1999, studying several single-component systems and mixtures. Thorough deionization and time-resolved static light scattering have been used to examine these systems thoroughly. One species, PnBAPS68, has undergone extensive study, with researchers using various techniques to track nucleation behavior over several orders of magnitude in J. Data for pure species and mixtures which indicate a qualitatively similar dependence on particle concentration. The early and substantial increase of J with Φ, like that of HS, is particularly noteworthy (figure 6.2). The observed slowing of the increase in J at higher concentrations is attributed solely to an increased interfacial free energy, γ These findings offer researchers valuable insights and will undoubtedly inform future studies..

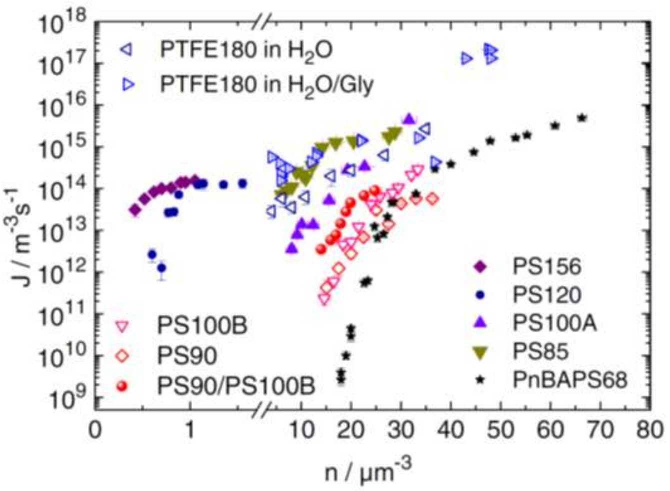

Figure 6.2: Absolute nucleation rate densities were obtained as a function of number density for several species of thoroughly deionized highly charged colloidal spheres and one mixture redrawn from [182] [217] [218]. In the quoted lab codes, PTFE denotes polytetrafluoroethylene particles, PS denotes polystyrene particles, and PnBAPS denotes polystyrene-poly-n-butylacrylamide copolymer particles. The numbers give the particle diameters in nm. Data on PnBAPS68 (stars) were obtained from different techniques, including microscopy; all other data are from time-resolved static light scattering [217]. PS100B (open down triangle) and PS90 (open diamond) were investigated, both as pure species and in an equimolar mixture (balls) [218]. PTFE180 was investigated in pure water (left triangle) or a buoyancy-matching H2O/glycerol mixture (right triangle) [182].

6.4 Possible explainations for discrepancy

6.4.1 Systems

In crystallization studies, researchers have made significant progress in adjusting mutual interactions between colloidal particles through various synthesis and sample preparation methods. In order to meet theoretical demands and the unique needs of optical experiments, interactions are primarily adjusted for spherical particles. However, other geometries, such as rods, ellipsoids, cubes, and related polygons, have also been explored. Colloidal model systems for crystallization studies usually involve spherical particles, but other shapes such as rods [105], ellipsoids [50], cubes, and polygons [166] [138] have also been studied. The most commonly studied systems include repulsive hard spheres(HSs) [18], [205], charged spheres [194], and spheres with attractive depletion interaction(AS) [9] [122], [20]. Polydispersity can be a concern, so synthesis and sample preparation often reduce particle size distribution. A good model system for studying crystallization kinetics should have a well-characterized interaction, corresponding phase behavior, and a good match of solvent and particle properties for optical experiments. Additionally, the system should be able to be studied for long durations without sedimentation effects. However, studies on crystallization kinetics for so-called colloidal molecules are still lacking.

6.4.2 Volume fraction

It is important to note that while many studies have focused on potential errors in the y-axis of Figure 6.1, errors in the x-axis may also contribute to discrepancies between experimental and simulation results. Measuring accurate volume fractions can be challenging, and differences in nucleation rate densities between experiments and simulations could be a matter of just a few percent in the volume fraction. These discrepancies are often related to errors in sample preparation, and accurately extracting volume fractions from the post-processing of images can also be challenging. While matching the radial distribution function can help confirm prepared volume fractions within a few percent, even a small variation in volume fraction can make a significant difference in agreement with simulations. This was evident in the Gasser (2001) study, which only vaguely reported volume fractions, referring to the critical low Φ regime as "$0.45 < \Phi < 0.53$". Additionally, it is worth noting that the Gasser study quotes nucleation rates below $\Phi = 0.45$, suggesting that their volume fractions are not calibrated to coincide with the phase diagram of hard spheres. To address this, we have developed a new technique for performing real-space confocal microscopy measurements that allows us to include as many particles as possible and obtain accurate freezing and melting volume fractions within acceptable error limits. It is also worth mentioning that it can be challenging to observe an entire nucleation event at the low-volume fractions where discrepancies exist, as this process can take months, even for relatively small particle systems.

It is worth noting that when plotted in terms of effective packing fractions, the significant difference between experimental and simulated nucleation rates highlights one potential issue in comparing the two: accurately determining effective packing fractions. Even a slight difference of 1-2% in the freezing density can significantly impact the position of the nucleation rate drop-off. While evaluating effective volume fractions in simulations is relatively straightforward, deducing the same information from experiments is more subtle. However, it is essential to note that this is not the whole story, as the large discrepancy between experimental and numerical nucleation rates at lower densities cannot be fully accounted for simply by rescaling the density axis.

6.4.3 Charge and screened charge

It is important to note three significant challenges in the experimental realization of the colloidal hard sphere system: polydispersity, charge, and sedimentation of the particles [168]. The polydispersity of the particles can affect the crystallization of hard spheres [159] [16], and a polydispersity of 7% or higher can prevent crystallization. However, in significant polydisperse (12-14%) hard-sphere systems, both simulations [119] and experiments [29] have observed that particle polydispersity has little effect. For nearly hard-sphere colloids, such as sterically stabilized poly(methyl methacrylate) (PMMA) spheres, polydispersity below 5% can be achieved, and these particles are commonly used for studying nearly hard spheres with confocal microscopy. These particles can be density and refractive index matched using halogenated solvents [225], which makes them ideal for studying confocal microscopy and prone to swelling and significant charging [168]. Introducing salt, such as tetrabutylammonium bromide (TBAB), can minimize the effects of charges by screening. However, due to the limited solubility of these salts, it is challenging to reduce the typical minimal Debye length K^{-1} (around 100 nm) [168] [117] [210]. The effect of charges on the nucleation of spheres has been studied in simulations and experiments [14] [13]. The presence of charges on the colloidal particles shifts the phase behavior to lower values of the volume fraction, which can be corrected by estimating the effective particle diameter [168]. Additionally, the presence of charge on the particles lowers the interfacial free energy of the solid-fluid interface, resulting in higher nucleation rates [14] [13].

One study carefully compared experimental nearly hard sphere measurements with Brownian dynamics simulations using a Yukawa potential and found reasonable agreement between the nucleation rates of the two at moderate supersaturation (Φ-$\Phi_m > 0.01$) [199]. The dynamics were matched by fitting the structural relaxation times from the experiments' and simulations' intermediate scattering functions. However, no agreement was found between the simulations and experiments for lower supersaturations and, therefore, lower crystallization rates. It was hypothesized that this was due to the limited size of the particle systems in the simulations compared to the experiments.

The role of residual charges in the nucleation rate of hard spheres has been extensively studied. Auer and Frenkel [16] showed that introducing a small charge increases the nucleation rate via two mechanisms. Firstly, the supersaturation increases at constant density due to the shift in fluid-solid phase boundaries to lower packing fractions. Secondly, the fluid-solid interfacial free energy is considerably reduced at constant supersaturation due to the charge effect. However, a recent numerical study [42] has shown that for highly screened electrostatic interactions, the phase behavior depends almost entirely on the screening length, with a nucleation barrier that increases with increasing screening length at fixed supersaturation. This trend suggests that charge effects would speed up nucleation rates rather than slow them down, which may explain the observed discrepancy between experiments and simulations of hard spheres. Moreover, the smaller particles in the experiments that reached the discrepancy regime had extensive Debye lengths. Therefore, while electrostatic interactions may shift the density dependence of the nucleation rate, it is unlikely that they can fully explain the observed discrepancy between simulations and experiments.

6.4.4 Sedimentation

Sedimentation has a pronounced influence on the crystallization of hard spheres, affecting not only the structure of the crystal [231] but also the nucleation rates [102] [222] [169]. In experiments, a local enhancement of the particle dynamics due to a density difference between the particles and the solvent mixture has been reported [102]. Additionally, a study combining experiments and simulations showed a decrease in local five-fold symmetry in the supersaturated fluid for larger density mismatches [222], resulting in higher nucleation rates. However, the increase in nucleation rates due to sedimentation cannot fully account for the large difference between nucleation rates observed in experiments and simulations [222]. For the nearly hard sphere system composed of PMMA particles in a halogenated solvent mixture [225], the particles can be density-matched, resulting in sedimentation lengths of the particles much larger than the height of the experimental container [157]. Gravity is often ignored in the nucleation process in simulations despite its importance. High nucleation rates are reported in colloidal suspensions with non-density matched solvents, while density-matched colloidal suspensions have reported nucleation rates slightly closer to the simulation data. Future studies of the nucleation process should consider gravity's effects and other aspects of the sedimentation process.

6.4.5 Polydispersity

The particle size polydispersity is an inherent property of all colloidal suspensions and has been shown to influence crystallization kinetics. Bolhuis and Kofke [25] used Monte Carlo techniques to determine the crystal-fluid phase boundaries of polydisperse systems. Their work demonstrated that fractionation of particles during crystallization is possible, and in later work, they showed that such fractionation increases with volume fraction. This highlights the importance of considering particle size polydispersity when studying crystallization kinetics in colloidal suspensions [104]. The duration of the induction stage, which is the time taken for detectable crystals to first appear after supersaturating a suspension, has been shown to increase with particle size polydispersity. This delay in the onset of primary nucleation arises because the local fractionation required to facilitate the conversion from unregistered layers to rhcp crystallites becomes increasingly difficult as either polydispersity or volume fraction is increased. This process becomes entirely frustrated at high volume fractions close to the glass transition, and the sample is locked into a compressed crystal precursor structure. These findings highlight the significant impact of particle size polydispersity on the crystallization kinetics of colloidal suspensions [181].

Studies have shown that particle size polydispersity can increase the barrier of crystal nucleation through a twofold mechanism. Firstly, it has been suggested that the direct random disorder effect may play a role by destroying crystal-like bond orientation order in a supercooled liquid, a critical first step in crystal nucleation [170]. Secondly, the enhancement of icosahedral ordering with increased polydispersity has been observed. It is known that the size disparity between the particles and their surrounding neighbors stabilizes the icosahedral order [187]. However, the symmetry of the icosahedral order is inconsistent with that of the equilibrium crystal polymorphs, leading to strong, frustrating effects on crystallization. These findings highlight the complex interplay between particle size polydispersity and crystallization kinetics and the need for further research.

6.4.6 Heterogeneous nucleation

Colloidal suspensions have also been used to study heterogeneous crystallization, where the crystal nucleates from a surface [172]. The presence of a straight hard wall has been found to speed up the crystallization of hard spheres in comparison to bulk crystallization [304], as observed in simulations [48] [171] and experiments [66] [171] [216] . Hard sphere crystals are known to wet a flat wall, leading to heterogeneous crystallization occurring before bulk (homogeneous) nucleation start [48] Crystallization rates of heterogeneous crystallization from seed can induce frustations in the crystal [44]. As the curvature of the wall increases towards the curvature of the particles themselves, the wall is seen as an impurity that hinders the nucleation concerning crystallization in bulk [31] [43]. Recently, it has been found that introducing a spherical impurity with a radius 15 times the radius of the particles can catalyze the crystallization process by initially nucleating the crystal near the impurity, after which the crystallite is detached and grows further in the bulk fluid [6]. Using small crystallites as seeds in the supercooled fluid has also enabled the measurement of nucleation rates at low supercooling, where nucleation events are too rare for traditional simulation methods [56]. Furthermore, the influence of the structure of small crystallites on the shape, orientation, and domain size of the resulting crystal has been studied in both simulations and experiments [31] [86]. These findings highlight the significant impact of surface effects on the crystallization kinetics of colloidal suspensions and the need for further research.

6.4.7 Instrumentation

Light scattering is a powerful optical method used to study colloidal Crystallization. It involves directing a laser at a sample and detecting the light scattered from the sample at a given angle. One way to use this technique is through static light or Bragg scattering, which monitors the intensity of laser light scattered off one or more sets of lattice planes. Time resolution can be provided by monitoring several scattering angles simultaneously. These techniques provide a powerful way to study the complex process of colloidal Crystallization over a wide range of lengths and time scales. Researchers studying colloidal systems may encounter increased turbidity and multiple scattering challenges at high concentrations, even when the refractive index matches the solvent. Small-angle X-ray or neutron scattering (SAXS or SANS) can effectively study polymer particles. In contrast, ultra-small angle X-ray scattering (USAXS) may be more suitable for inorganic particles like silica. Regardless of the approach, scattering methods offer valuable insights into colloidal system structures and dynamics at different length scales, contributing to a deeper understanding of these complex materials. To overcome the problem in this method, fluorescence microscopy is introduced, which offers a solution by using the contrast between dyed and undyed portions of the sample to produce an image. These microscopes are designed to capture images of thin sections of a sample while rejecting light that comes from outside the focal plane. This allows for a more precise and focused image, making them much better suited for studying dense colloidal systems.

6.4.8 Simulations

The study of colloidal and nanoparticle systems and the nucleation process often involves the use of hard-sphere systems, considered one of the most straightforward systems for theoretical analysis. These systems are ideal for investigating various computational methods for studying nucleation and comparing the results with experimental data. Some of the commonly used methods include molecular dynamics (MD) simulations, umbrella sampling (US), forward flux sampling (FFS), and transition path sampling (TPS). Despite the usefulness of these methods, there are still significant discrepancies between the predicted nucleation rates in hard-sphere systems and experimental results. For instance, Auer and Frenkel [14] used umbrella sampling simulations to study crystal nucleation of hard spheres and found a significant difference between their predicted rates and the experimental rates of Refs. [78] [189] [177]. However, the origin of this difference remained unclear. To address this issue, researchers have compared the nucleation rates for hard-sphere systems from MD, US, and FFS simulations with the experimental results of Refs. [78] [189] [177]. By doing so, they hope to shed light on the factors contributing to the observed discrepancies and to improve our understanding of the nucleation process.

6.5 Sample preparation and Data acquisition

The methods are described in detail in Chapter 2 and briefly summarized here. To follow the process of crystal nucleation, we used polymethylmethacrylate (PMMA) spheres sterically stabilized by chemically-grafting poly(12(hydroxy stearic acid (PHSA)) about 20nm onto their surface. The particles are stained with fluorescent dye $DiIC_{18}$, having a diameter of 1.4µm with a polydispersity of 5.6%. Having absolute volume fraction values is convenient for comparing simulations, theories, and future experiments. To review the interaction properties, comparing the equilibrium phase diagram of a colloidal system with the theoretically expected phase diagram is essential and valid as a model system for the HS system. For a colloidal model system, the proportion of the crystalline phase, which depends on the volume fraction, must be determined over the entire coexistence region. The freezing and melting volume fractions are determined by measuring the equilibrium phase diagram [114]. A standard method for determining this is given by Paulin and Ackerson [148]. This method involves sedimentation, which may shift the freezing and melting volume fractions. Thus, the density-matched sample was prepared to ensure the correctness of the measured freezing and melting volume fraction, and wall crystallization was monitored for various volume fractions. Our results shows values i.e $\phi_{core,F}$ = 0.4153 and $\phi_{core,M}$= 0.4491 [114]. By scaling the core volume fraction at the freezing point, the freezing volume fraction$\phi_{core,F} = 0.5075$ of the theoretical phase diagram, the effective volume fraction can be calculated [114]. Since we have measured the phase diagram of the system, one can define the rate densities calculated for various volume fractions in terms of coexistence region α=(ϕ-ϕ_F)/(ϕ_M - ϕ_F).

In order to suppress the heterogeneous nucleation, the bottom and side walls of the sample cell are precoated before preparation. A detailed description of sample cell preparation and coating is given in Chapter 2. To confirm the hard sphere nature of the particles, we determined the experimental pair correlation function g(r) and structure factor S(q). We compared it with the PY approximation [96]. We obtain excellent agreement with measured and calculated PY-g(r) in the fluid regime. The details on the fluid structure are given in Chapter 5. The data for the nucleation process are taken 20-80 µm above the wall. The microscope Leica TCS SP8 used has a reproducibly adjustable microscope table. This allows precise large-volume scanning by successive inclusion of several sub-volumes. The measurements are based on 25 adjacent sectors arranged in a square pattern. Every sector comprises a volume of 82x82x60 µm^3. The size of a voxel is lateral 80.2nm and axial 130nm. Successively, the areas are scanned continuously throughout the experiment without a break until Crystallization.

6.6 Data Analysis

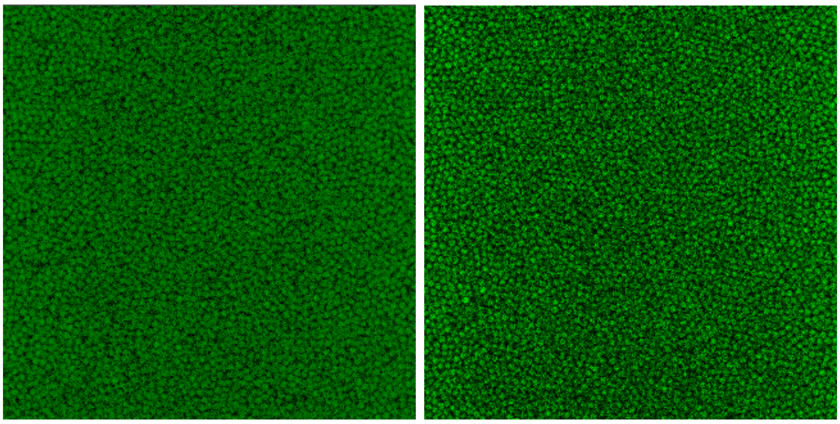

(a) (b)

Figure 6.3: (a) The confocal image(2D) at the beginning(a) of the measurement and (b) at a time when Crystallization sets in. The particle of size 1.4µm stained with a fluorescent dye is seen in green with a dark background. At the beginning of the measurement, the particles are arranged randomly, while during the Crystallization, the particles are arranged in an orderly fashion.

The method used to identify crystals is explained in Chapter 3. It is explained here briefly. This study identifies the particle as crystalline if it has at least 8 nearest neighbors in a distance smaller than 1.4 times d_{HS}, and the q_6q_6 scalar product must be larger than 0.5. Thus, four or more connected crystalline particles are identified as a crystalline cluster. Confocal microscopy allows one to follow the formation of individual crystals, and thus, one can determine nucleation rate density most directly. The investigation of the solidification kinetics shows a multi-step nucleation scenario, forming near-ordered clusters in the beginning. Later, local crystalline structures are formed. The development of individual clusters was traced, and a microscopic impression of the nucleation process was obtained. For example, two pictures of a 2D slice of the sample imaged through confocal microscopy are shown in Figure 6.3. The first picture is taken at the beginning of the measurement, and the second is taken during the crystallization set-in. At the beginning of the measurement, the particles are arranged randomly, while during crystallization, the particles are arranged in an orderly fashion. If the sample is not coated from the sides and at the bottom, heterogeneous nucleation occurs, and particles stack one over the other before the crystallization sets(Figure 6.4). On the other case, the bottom of the cell is coated with appropriate particle size, here in our case 2.33 µm. The confocal investigation of these layers are shown in the picture 6.5(a) and (b). The first picture is taken above 4 µm from the bottom of the cell, where particles coated are seen in black. As moved further, above 8 µm, coated particles are start to diminish. The height of monolayer depends on the coating thickness. Just above monolayer, about 10 µm, the particles of 1.4µm can be seen clearly. The comparison clearly signifies the importance of coating.

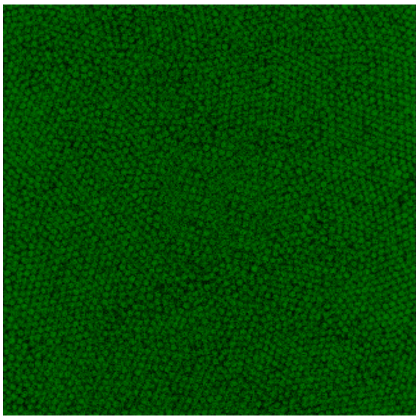

Figure 6.4: The confocal image(2D) at the bottom of a sample cell without coating. The particle of size 1.4µm stained with a fluorescent dye is seen in green with a dark background. Within a few minutes of the measurement, the particles are stacked one over the other before the crystallization sets in, pointing to heterogeneous nucleation.

6.6.1 Coarse graining

The crystallization behavior is analyzed based on ensemble-averaged quantities. The number of particles N in the observed volume can be identified and counted. Depending upon the threshold described before, the crystalline particles are identified in each sub-volume as a function of time. Thus, ensemble-averaged $< X_{cg} >$ is defined as the number of crystalline particles in total observed volume over time. Similarly, the ensemble-averaged cluster size $< CS_{cg} >$ is

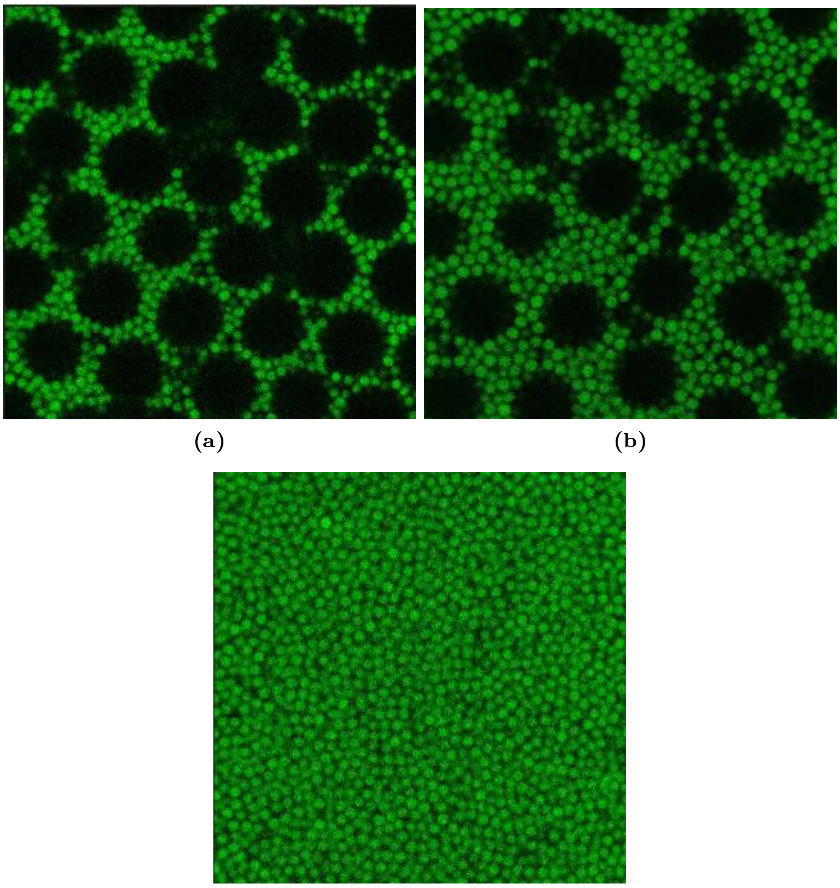

(a) (b) (c)

Figure 6.5: The confocal image(2D) at the bottom of a sample cell with coating. The particle of size 1.4µm stained with a fluorescent dye is seen in green. PMMA particle size 2.33 µm is coated at the bottom can be seen as black. (a)The image is taken just above 4 µm from the glass slide in-order to see the arrangement and coating of cover slip. (b)The image is taken just above 8 µm from the glass slide. (c)The image is taken just above 10 µm from the glass slide after disappearance of monolayer

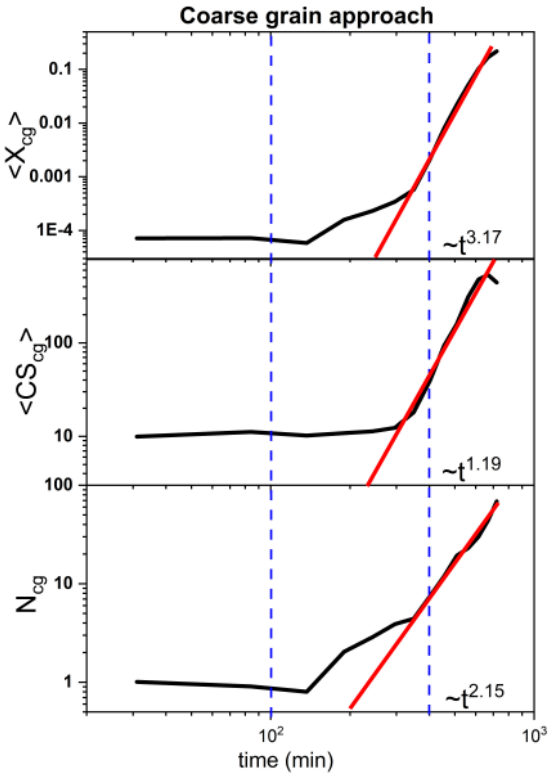

Figure 6.6: From the coarse graining, the measured ensemble averaged Crystallinity $< X_{cg} >$ (Top)and cluster size $< CS_{cg} >$(middle) for all crystalline particles in the total measured volume over the time is given. The Crystallinity to cluster size ratio will result in the number of clusters $< N_{cg} >$, obtained at that time(bottom). The red line shows the linear fit, indicating when Crystallization sets in. The corresponding growth component(t^{μ}) is also mentioned. This quantity is measured for effective volume fraction 0.5389, corresponding to $\alpha=$ 0.7566 in terms of coexistence value.

given by the number of particles in the cluster at that time. The ratio of $< X_{cg} >$ and $< CS_{cg} >$ gives the number of clusters $< N_{cg} >$ identified in that time.

As shown in the Figure 6.6 crystalline particles and the corresponding cluster size is given. The crystallinity and corresponding cluster size remain low at the beginning of the measurement up to time t≈100 min. At 100 $>$ t $>$ 200 min, the crystallinity starts to increase, but the cluster size remains the same. At 200$<$ t$<$ 400 min, the crystallinity increases further, whereas the cluster size increases only after 300 min. After t =400 min, the crystallinity and cluster size increases drastically with the growth rate of $t^{3.17}$. The number of clusters also shows a characteristic similar to crystallinity. It remains constant at the beginning, and at around 200 minutes, the number of cluster starts to increase.

Another example for coarse graining method is given in the figure 6.7. The quantity such as crystallinity and crystal volume fraction as a function of time is given. As shown in the figure 6.7(top), crystallinity starts to increase after around 150 min and later increases isotropically until it reaches 90 percent of

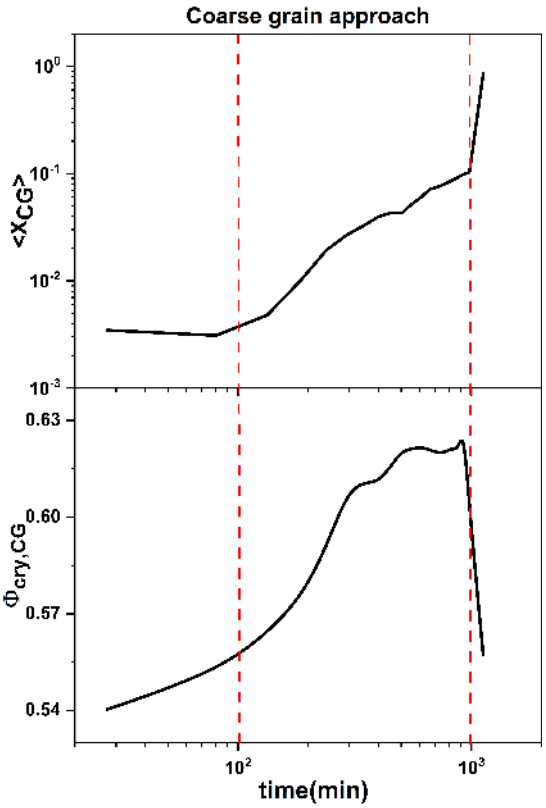

Figure 6.7: From the coarse graining, the measured ensemble averaged Crystallinity $< X_{cg} >$ (top)and measured crystal volume fraction for all clusters is given.This quantity is measured for effective volume fraction 0.54, corresponding to $\alpha=$ 0.78313 in terms of coexistence value.

crystallinity. the crystal volum fraction as function of time is measured using voronoi tessellation. Voronoi tessellation is an extremely useful technique capable of quantifying the free space around each individual particle and thus determining the local packing fraction based on the ratio between the particle volume and its local free space. Voronoi tessellation constructs cells that enclose the space around each particle which is closer to it than any other neighbouring particle [183] [58]. When Voronoi cells are constructed, the local packing fraction can be calculated for each particle by dividing the particle volume by its enclosing Voronoi cell volume, giving the most accurate possible measure of local packing fraction resolved down to the individual particle level. Thus, from the voronoi volume crstal volume farction is computed(Figure 6.7(b)).

In the Figure 6.8 the average order parameters $\bar{q}_4$ and $\bar{q}_6$ are plotted at four different times for the cluster particles for the fluid particles. Shortly after the beginning of the experiment, the system is almost fluid. The few cluster particles are characterized by increased values compared to the fluid particles. At time t=165 min, the number of particles in the cluster has increased. There is a significant increase in the bond order parameter values. At time t=483 min, the particles in the clusters increased significantly, thus forming local structures.

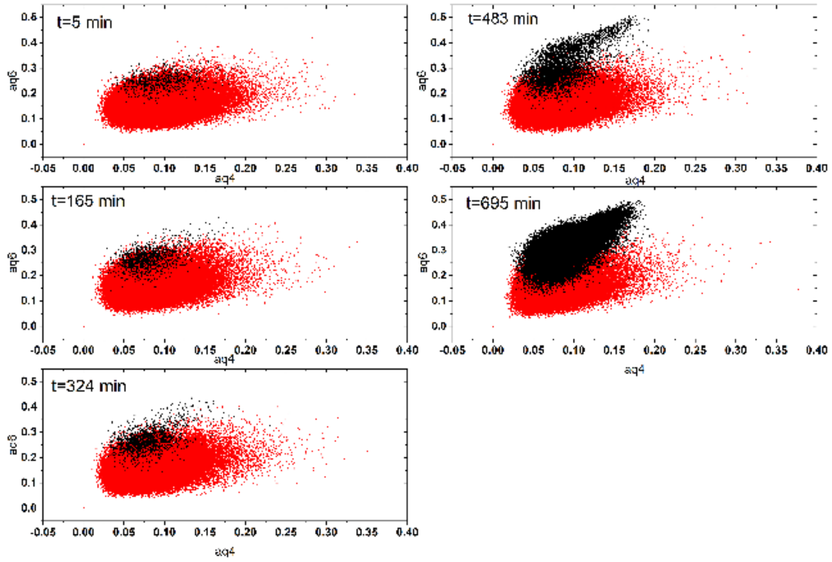

Figure 6.8: Average q_4q_6 map for the particles in the fluid phase and crystalline particles at different times as indicated. The cluster particles are defined via q_6q_6 scalar product larger than 0.5. The red cloud indicates the fluid particles, whereas the black cloud represents the cluster particles. Over time, the black cloud increases as the crystallization sets in and increases until the end of measurement. The quantities are measured for effective volume fraction 0.5389, corresponding to α=0.7566 in terms of coexistence value.

After time t=695 min, there is clear evidence of a linear correlation between $\bar{q}_4$ and $\bar{q}_6$ order parameters. The cluster particles show crystalline symmetry. No significant change is observed over the entire time range for the particles in the fluid phase. In summary, it can be said that the number of particles in the cluster phase increases at early times, but no unique crystalline structure can be found. At a later stage, the particles in the cluster phase transformed into the pronounced ordered structure due to an increase in q_4 and q_6 values. The plot is also a time trace of how crystal structure develops. After the crystallization sets in, the black cloud grows and shifts higher q_6 values.

6.6.2 Growing cluster only

One can identify all the clusters over time from the coarse graining method. From these clusters, only clusters which grow in time will be identified. Thus, keeping these identified clusters from coarse grain approach at the last time step as the reference, one can obtain the individual clusters' trajectory. For this purpose, the number of clusters $< N_{cg} >$ is determined as a function of time. All crystalline particles' average growth rate is determined at first. Then, in the last step of the measurements, all clusters larger than a threshold are selected. The threshold is calculated by multiplying the time interval between the last two measurements with the lower one-sigma limit of the average crystal growth rate. These clusters are then traced backward in time until they disappear, Thus following individual crystallization trajectories, and the number of growing crystals N_g are determined. The total clusters obtained from this method are then used to calculate the Nucleation rate.

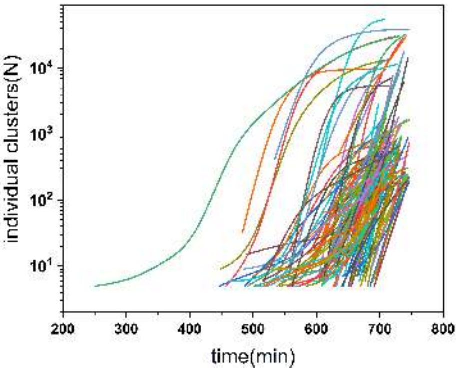

Figure 6.9: Individual identified clusters traced from backward until they disappear. From this, one can also identify the clusters' critical size and individual induction time. These are measured for effective volume fraction 0.5389, corresponding to α=0.7566 in terms of coexistence value.

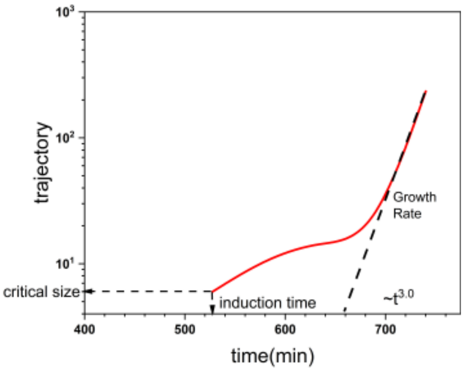

Figure 6.10: Considering one cluster(taken from the previously identified trajectory) and its trajectory as shown in the Figure (red). The black line is the linear fit, which gives the growth rate of that cluster. From this, one can also identify the induction time as 525 min and the critical size of five particles.

The individual clusters trajectory obtained from this method are shown in Figure 6.9. The different colors represent different clusters. Different clusters have different induction times. Similarly, as shown in Figure 6.10, the slope obtained by a linear fit to these individual trajectories gives the growth rate. One can also identify the individual critical size and induction time for each cluster from these trajectories. The obtained critical size and induction time are given in Figures 6.12. It provides crucial information about the Nucleation. This indicates that the small size will lead to the cluster's growth over time. Induction time will help in the determination of the nucleation rate.

The individual critical size and induction times display a widespread(Figure 6.12), the critical size distribution is highly skewed. Most of the crystals start their life with an unexpectedly small size (< 10), but there are also critical nuclei

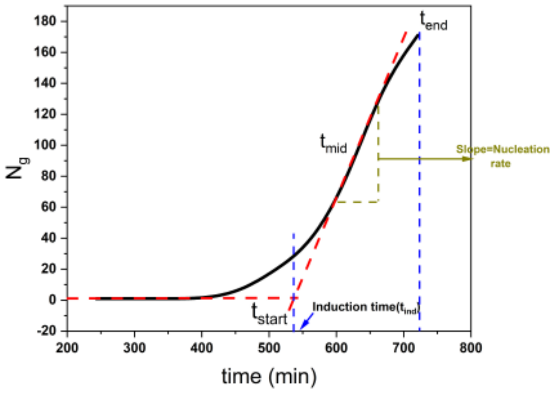

Figure 6.11: Total cluster N_g identified from coarse graining over time is shown. The red line shows the linear fit, the slope of which will determine the Nucleation rate. The blue line indicates the time when the clusters start to grow.

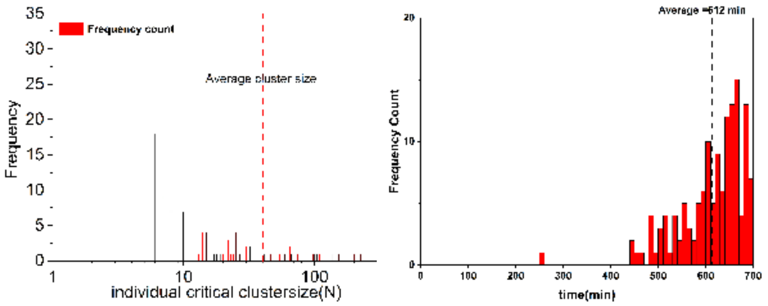

(a)

(b)

Figure 6.12: (a) Frequency distribution of individual critical cluster size and (b) Induction time for all identified growing clusters. The red dotted line in (a) represents the average value of 35 particles, and the thick black line in Fig (b) gives the average induction time of 612 min.

containing more than a hundred particles. The mean value of 35, represented in the Figure 6.12, agrees with other non-CNT-based methods. Thus, clusters identified at each step over time are given in the Figure 6.11. From this data, one can also identify when clusters start to grow(t_{start}) and when it ends(t_{end}). From this, the growth rate can be determined from the linear fit. As explained in the case of the coarse grain method, here, one can also describe the temporal evolution of bond order parameters for growing clusters. For more clarity, the evolution of the one cluster from its induction time is shown in Figure 6.13. In the beginning, the critical size has a value of 5 particles. Over time, the particle starts to form more orderly, increasing the orientation order of the corresponding particles. Finally, a more ordered crystal structure formed.

The scalar product $q_6 q_6$ values are computed for particles in the growing cluster and summed up (figure 6.14). Most of the particles in the cluster have $q_6 q_6$ values greater than 0.6 and has it peak value around 0.7. The time range close to the induction time is considered and there after time is also considered to

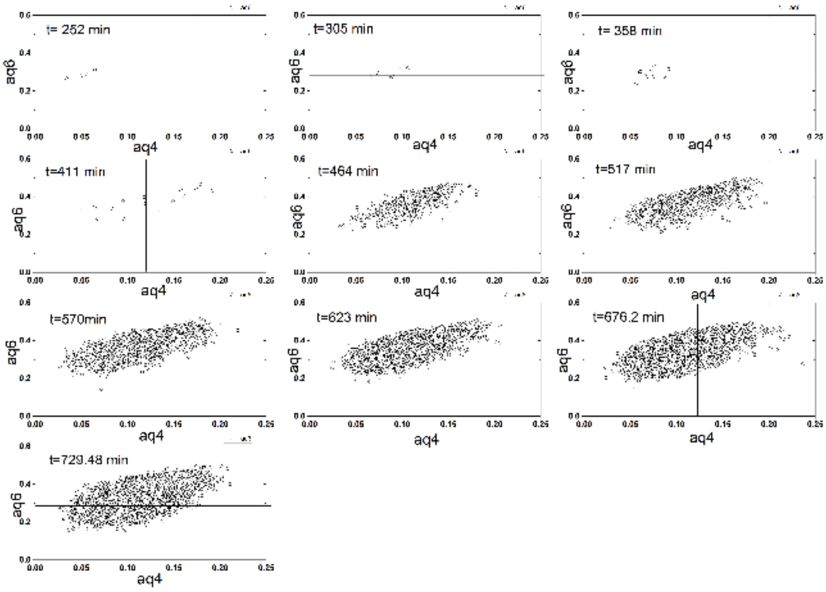

Figure 6.13: Averaged q_4q_6 map for the particles in a cluster at different times as indicated. Over the time, cluster size increases, and corresponding q_6 values shift to higher values. For better clarity one "biggest" cluster data is shown here. The quantities are measured for effective volume fraction 0.5389, corresponding to α=0.7566 in terms of coexistence value.

see the growth. During the induction period (indicated as t_{ind}) and afterward, however, there is a significant increase in the range $q_6q_6 > 0.5$. As time proceeds, the q_6q_6 values reach a maximum of around 0.7. At t> t_{ind}, the clusters start to grow, and significant changes appear in the plot as time progresses. At the end of t= t_5, the q_6q_6 reaches maximum.

6.6.3 Nucleation rate densities(NRD)

- As explained earlier, the number of clusters in each time step can be determined using coarse graining and by considering growing clusters. To explain this, the figure 6.11 is used here which is obtained by considering only growing cluster. The linear fit from the point where clusters start grow will results in Nucleation rate.

  Thus, the Nucleation rate density(J) is then calculated using the equation

  $$J = \frac{Slope}{V_{freeVol}((t_{start} + t_{end})/2)} \tag{6.1}$$

  in µm$^3 min^{-1}$ where $V_{freeVol}$ is the system's available free volume. The factor describes the change in the cluster number between two time steps.

- The nucleation rate density(J) can be determined as a function of time. From the obtained Nucleation rate over time, one can fit the steady-state nucleation rate given by Kaschieve [98]. One can also obtain the averaged

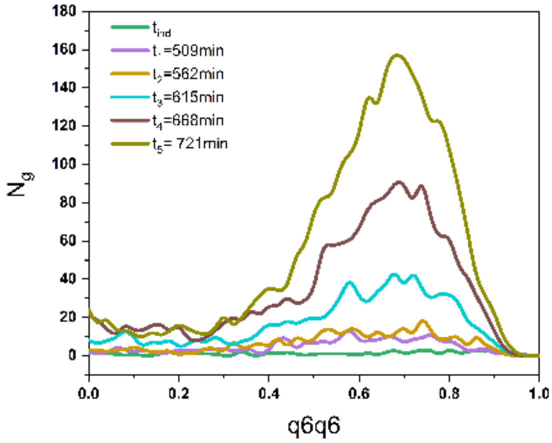

Figure 6.14: q_6q_6 dot product value for growing cluster. The data points were for different time steps. It shows the total frequency distributions for all growing clusters identified. The values were summed for all growing clusters. The quantities are measured for effective volume fraction 0.536, corresponding to α=0.6875 in terms of coexistence value.

value of NRD after the induction time, J_{avg}, which is the corresponding maximum value of NRD-J_{max}.

These NRD is calculated for Coarse grain data by considering all particles and growing clusters data. Thus, one can get various NRD values. The figure 6.16 shows the values obtained from all possible ways. From these plots, one can also infer that there is not much difference in obtained values.

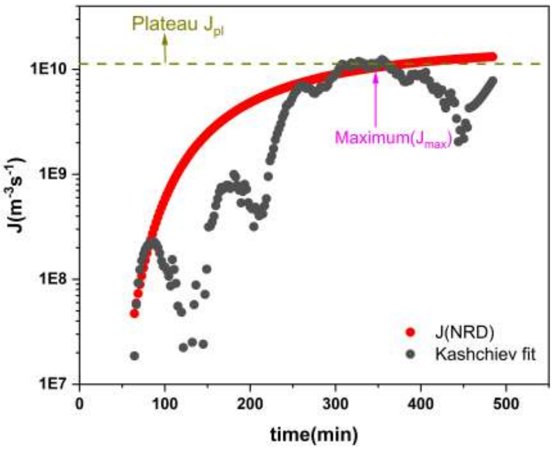

Figure 6.15: The Nucleation rate density at each time step is given(black). The red line is the Kaschieve fit to get the steady state Nucleation rate density. The maximum value of NRD is also indicated, and the average value can also be calculated. These values are determined for effective volume fraction 0.547, corresponding to $\alpha=$ 0.95181 in terms of coexistence value.

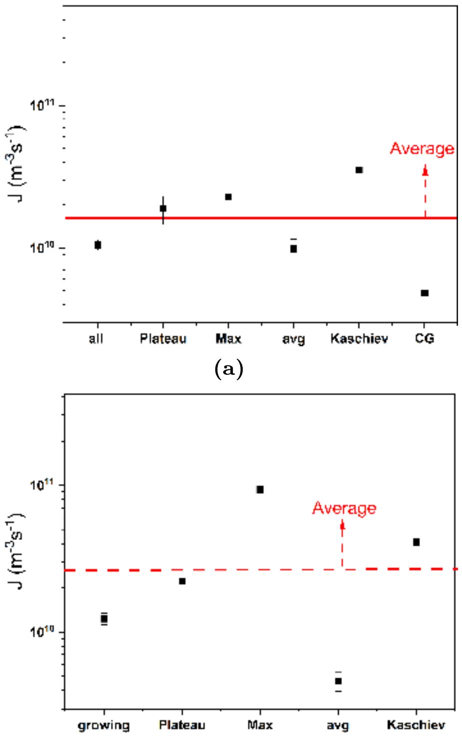

(a)

(b)

Figure 6.16: The various NRD obtained from the data are given in Figures (a) and (b). The name in the x-axis suggests the method used to calculate NRD. The red line shows the average value of the obtained NRD. Here, "CG" refers to coarse graining approach. From this approach one can determine NRD value at "plateau" region, average "avg" value after induction time, "Kaschiev" refers to NRD obtained from Kaschiev fit and "max" refers to maximum NRD obtained. In figure (b), the similar values are obtained by considering only growing clusters("growing").

6.7 Testing the existing hypothesis for the discrepancy

6.7.1 Sedimentation

We defined the system to exhibit hard sphere-like interactions in the case of TCE and explained how rate densities calculated from measurements fall short of fully explaining the discrepancy between simulations and experiments. To address this, we decided to vary the density between the solvent and particle, using it as a starting point for our investigation.

The sedimentation of colloids is characterized by their Peclet(Pe) number, which is the ratio of the time a particle takes to diffuse its radius to the time it takes to sediment its radius. The time to diffuse a radius a can be calculated using the Stokes-Einstein form of the diffusion coefficient, D_0.

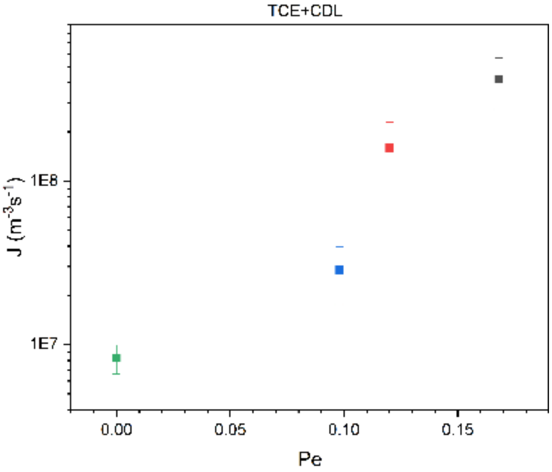

Figure 6.17: Nucleation rate determined in case of TCE+CDL by varying Pe number is given. The data seems to have 2 orders of magnitude difference. The quantities are measured for effective volume fraction 0.529, corresponding to α=0.5 in terms of coexistence value.

$$t_d = \frac{a^2}{D_0} = \frac{6\pi\mu_f a^3}{K_B T} \tag{6.2}$$

Where 'a' is the particle radius, μ_f is the dynamic viscosity of the liquid, and $K_B T$ is the thermal energy. The time to sediment a radius is given by the time taken for a particle to move a radius while traveling at the Stokes velocity given in equation

$$V_s = \frac{2a^2\Delta\rho g}{9\mu_f} \tag{6.3}$$

Where $\Delta\rho$ is the difference in density between the colloid and the solvent, the Peclet number then reads as in Equation

$$Pe = \frac{t_d}{t_s} = \frac{12\pi g\Delta\rho a^4}{9K_B T} \tag{6.4}$$

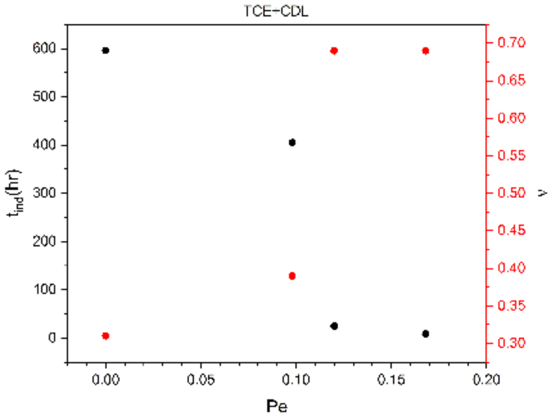

Figure 6.18: Induction time (black) and growth component(t^{μ})(red) for the corresponding Pe number are given.The quantities are measured for effective volume fraction 0.53, corresponding to α=0.5 in terms of coexistence value.

The experiment involved preparing a sample with an effective volume fraction of 0.53 with a coexistence value α=0.5. The sample is prepared with a known Pe Number by varying the density mismatch between TCE and CDL. The NRD is calculated as explained earlier(Figure 6.17). Figure6.18 shows the determined induction time t_{ind} for varying Pe numbers. For Pe= 0.168, the nucleation is too fast, around 500 minutes. For Pe= 0, the time for crystallization to set in takes more than 550 hours. However, when it comes to nucleation rate, there is not much difference. The nucleation rate increases with increasing Pe number, but the difference is around two orders of magnitude with error. Overall, these findings highlight the importance of density match and flow rate control in studying nucleation events and provide valuable insights into the factors that influence the kinetics of phase transitions.

6.7.2 Charge

Since we have not measured the phase diagram of a system with CHB and TBAB, one can express the Nucleation rate in terms of number density ρ. Hence, the samples are prepared with the same number density for better comparison.

The samples was prepared at number density ρ = 0.3095µm^3 in this experiment. The sample cells are bottom and sides coated; the suspension was density matched. Before the nucleation measurement, the charge of the particular sample is determined using Marco Heinen software. In the case of CHB, it has Z= 110±10; in TBAB, it has Z = 145±10. Further details on the charge for various systems are given in Chapter 5. The concentration of TBAB used for crystalization measurement is 3.8mM. To prepare density-matched samples, we followed the procedure outlined in Chapter 2.

Figure 6.19 shows the crystallinity determined from the coarse-graining. Since the crystallization sets in the case of CHB faster, and in case of TCE, it takes days, the plot is shown accordingly. The inset figure is for CHB and TBAB. In the case of the CHB sample, the Crystallinity starts to grow around 55min whereas in the case of TBAB, the Crystallinity starts to increase after

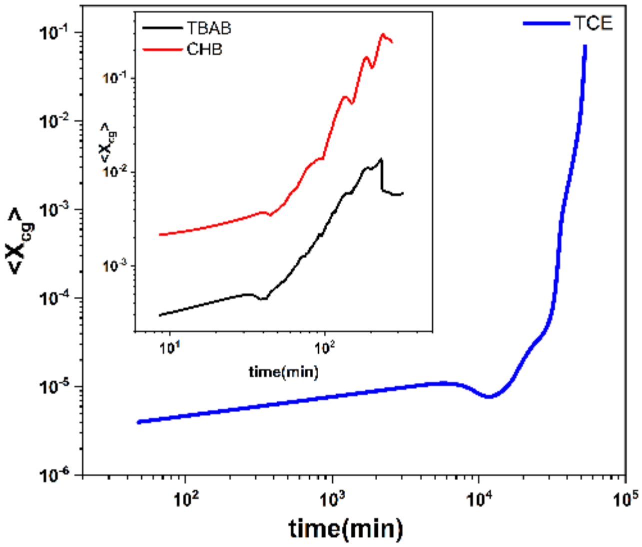

Figure 6.19: Measured crystallinity in the case of TCE(blue) over time is given. The inset shows the measured Crystallinity in CHB(Red) and TBAB(Black). All data shown here has the number density ρ= 0.3095µm^3.

93min after the experiment started. In the case of TCE, the Crystallinity shows a substantial increase only after 596 hours(figure 6.21). The Nucleation Rate was calculated similarly to the coarse grain method in all cases. Since CHB is a charged colloidal system, the NRD was relatively higher than the TCE system, nearly four orders of magnitude. The obtained Nucleation rate is given in Figure 6.20. As mentioned before and also known from the previous study [14] [13],showed that introducing a small charge increases the nucleation rate via two mechanisms. Firstly, the supersaturation increases at constant density due to the shift in fluid-solid phase boundaries to lower packing fractions. Secondly, the fluid-solid interfacial free energy is considerably reduced at constant supersaturation due to the charge effect. However, a recent numerical study [42] has shown that for highly screened electrostatic interactions, the phase behavior depends almost entirely on the screening length, with a nucleation barrier that increases with increasing screening length at fixed supersaturation. Thus these suggests that charge effects would speed up nucleation rates rather than slow them down.

6.7.3 Heterogeneous Nucleation

As explained earlier, one of the reasons for the discrepancy may be heterogeneous nucleation. In order to overcome this, the sides and walls of the sample cell are precoated. The procedure to prepare such samples is given in chapter 2. The measurement is done for a density-matched TCE system with the same effective volume fraction 0.547, corresponding to α = 0.952. To see the effectiveness of side coating, we performed two measurements with two samples, one with sides coated and another without any side coating.

The measured crystallinity using a coarse-grain approach is given in Figure

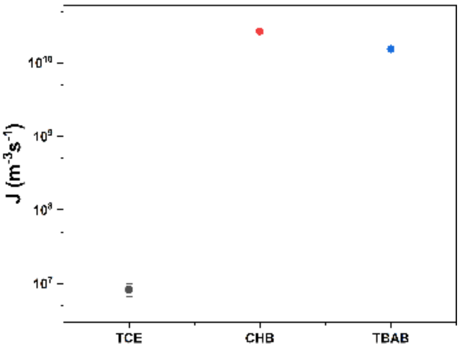

Figure 6.20: Determined nucleation rate in case of TCE, CHB and TBAB is given. All data shown here has the number densityρ= 0.3095µm^3

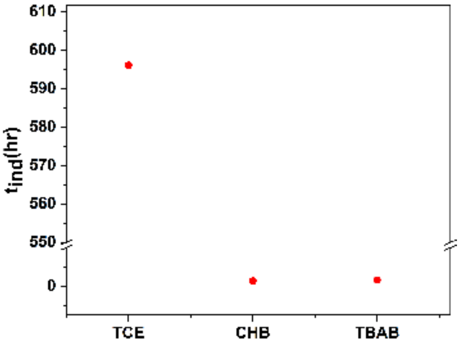

Figure 6.21: (a)Determined induction time(hours) in case of TCE, CHB and TBAB is given. All data shown here has the number densityρ= 0.3095µm^3.

6.22. In the beginning, the Crystallinity is low in both cases, but later, it shows significant in the case of the "sides coated" sample. The cluster started to appear in the bulk region. In the case of the "no sides coated" sample, even though Crystallinity is slightly increased, clusters form more at the wall than in the bulk region. Thus, when a sample is prepared only with the bottom coated, the smooth surface of the wall favors heterogeneous nucleation.

Similarly, the measured cluster size using a coarse grain approach is given in Figure 6.23. The cluster size increases as time proceeds in the case of sides coated. In contrast, for the system with no coated sides walls, cluster size remains nearly the same for that period except for the last time step, where there was a slight increase, possibly due to the growth of clusters forming at the walls extending up to the subvolumes of the measured area. Therefore, to study homogeneous nucleation in bulk, it is essential to prepare the sample cell in all possible ways to avoid heterogeneous nucleation. As the name suggest the nucleation should not be influenced by the any seed. But in the presence of flat wall, the particles starts to form layering favoring heterogeneous nucleation. Hence the side and bottom coating is necessary.

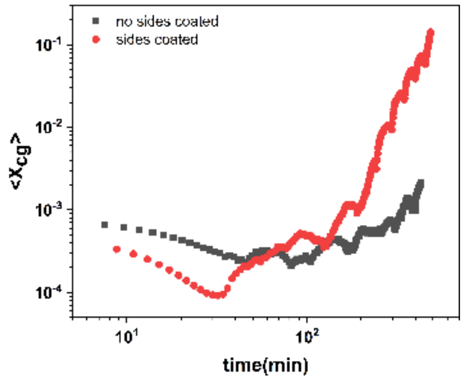

Figure 6.22: From the coarse graining, the measured ensemble averaged crystallinity $< X_{cg} >$ for both sides coated(red) and no sides coated(black) in the total measured volume over time. This quantity is measured for effective volume fraction 0.547, which corresponds to $\alpha = 0.952$ value.

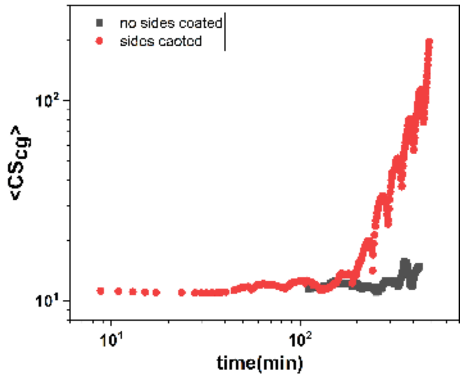

Figure 6.23: From the coarse graining, ensembled averaged cluster size $< CS_{cg} >$ for all crystalline particles for both sides coated(red) and no sides coated(black) in the total measured volume over the time is given. This quantity is measured for effective volume fraction 0.547, which corresponds to $\alpha = 0.952$ value.

6.7.4 Data acquisition

In order to determine the nucleation rate, it is necessary to have a larger sample volume to be measured in a shorter time. For this purpose, confocal microscopy is used to accumulate large volumes in a short time to follow the Nucleation kinetics and statistically meaningful data. This is done by including several particles of around 10^6 to 10^7 and scanning sequentially. Since crystallization kinetics with low supersaturation is slow, scanning many volumes is fast enough to follow crystallization kinetics. Involving these many particles also helps to compare results from other research groups, especially from simulations. Here, we have explained the coarse graining, which can include all particles in the measurement volume to calculate the nucleation rate. If one is only interested in the growing clusters, following individual trajectories and getting the nucleation rate is also possible. Here, we showed both methods and inferred that not much difference is observed.

6.7.5 Polydispersity

Our system has a polydispersity of 5.6%. Since this affects the duration of the induction stage, it is essential to quantify this property correctly. It has also been shown that induction time increases with polydispersity. The most important point to emerge from various studies is that all samples behave similarly in the early stages of solidification, regardless of volume fraction or polydispersity. Thus, polydispersity also does not have much effect on the nucleation rate. However, it will probe some factors in the middle of the coexistence region.

All these analysis suggest that the nucleation rate is not affected by various factors, as explained above.

6.8 NRD in the TCE system from direct method

We have measured the nucleation rate for different volume fractions varying from 0.555 to 0.5289, corresponding to $\alpha = 1.3$ to 0.5 value. The nucleation rate obtained, as explained before (growing clusters method), is given in the Figure 6.24. For further comparison, the Nucleation rate is normalized by factor of $2a^5/D_s^L$where D_s^L corresponds to long-time diffusion coefficient. It can be seen from the figure that rate density decreases as the volume fraction decreases. But it still did not explain the discrepancy.

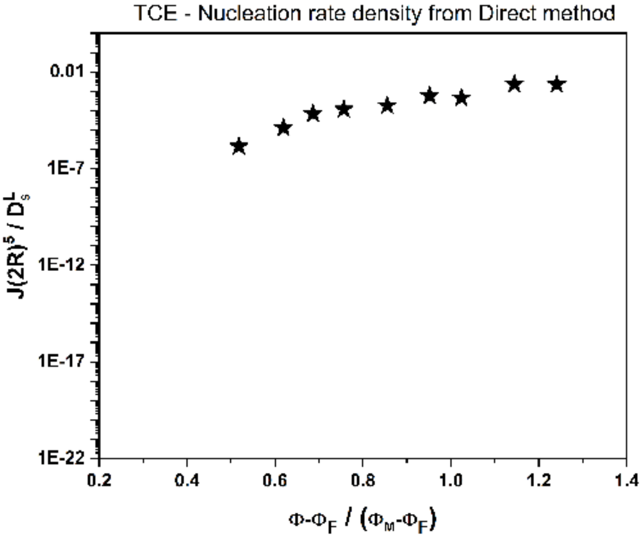

Figure 6.24: The nucleation rate obtained directly in the case of the TCE system is given in terms of α. For more further comparison with other available data, the Nucleation rate is normalized with corresponding long-time diffusion D_s^L.

6.9 Nucleation rate density from CNT method

The classical Nucleation theory(CNT) restricts the kinetic pathways by which nucleation occurs, assuming clusters grow or shrink only by single particle adsorption/emission. In reality, the merging and fragmentation of entire clusters cannot be excluded as necessary kinetic pathways in some systems. Particularly in dense systems or near the critical point, where clusters acquire an extended and ramified structure-such kinetic pathways are expected to contribute significantly [103]. The behavior near this critical point also suggests the inadequacy, at least in some cases, of treating clusters as purely spherical [174]. Various attempts have been made to remedy these limitations and others by explicitly accounting for the microscopic properties of clusters. However, the validity of such extended models is debated. One difficulty is the exquisite sensitivity of the nucleation rate to the free energy ΔG^*; even small discrepancies in the microscopic parameters can lead to enormous changes in the predicted nucleation rate. This fact makes first-principles predictions nearly impossible. Instead, models must be fit directly into experimental data, which limits the ability to test their fundamental validity [15].

In order to get valuable insights into the nucleation process, it is useful to understand CNT. It is explained briefly here. CNT assumes that the crystal phase forms via the formation and subsequent growth of a crystal nucleus of spherical shape. The total Gibbs free energy cost to form a nucleus is

$$\Delta G(R) = 4\pi\gamma\ R^2 - \frac{4}{3}|\Delta\mu|\rho_s R^3 \tag{6.5}$$

where $\Delta\mu$ is the difference in the chemical potential between the metastable liquid and the thermodynamically stable crystal phase, γ is the surface free energy of the interface between solid and liquid, R is the radius of the spherical nucleus with N particles, and ρ_s is the number density of the solid. The probability that the crystal nuclei form in the metastable liquid is described by a Boltzmann distribution given by

$$P(N) \propto exp(\frac{-\Delta G(N)}{K_B T}) \tag{6.6}$$

Only crystals larger than the critical size R_{crit} i.e. $R_{crit} = 2\frac{\gamma}{|\Delta\mu|\rho_s}$ overcome the nucleation barrier

$$\Delta G(R)_{crit} = 16\pi\gamma^3/3\rho_s^2|\Delta\mu|^2 \tag{6.7}$$

and grow continuously, gaining energy. Thus, NRD is given by the product of the probability that a critical nucleus is formed and the kinetic prefactor J_0

$$J = J_0 exp(\frac{-\Delta G_{crit}}{K_B T}) \tag{6.8}$$

where J_0 is expressed by the particle attachment rate K^+, the Zeldovich Z, and the number density of the fluid.

$$J_0 \propto K^+\rho_{liq}Z = A * \sqrt{\gamma} * D_L^s * R^{-5} * \phi_s^{-(1/3)} * \phi_{fl}^{-(5/3)} \tag{6.9}$$

where A is the scaling constant with particle radius R and volume fraction of solid ϕ_s and fluid ϕ_{fl}.

As already described in detail by Auer and Frenkel, the nucleation barrier and, thus, the critical radius is the parameter that strongly influences the Nucleation rate density. In the following section, we will determine the critical radius using different methods and compare it with the simulation data. In the following, we first use the same approach to determine ΔG(N) as in the corresponding simulations [16] [15] [62] [63].

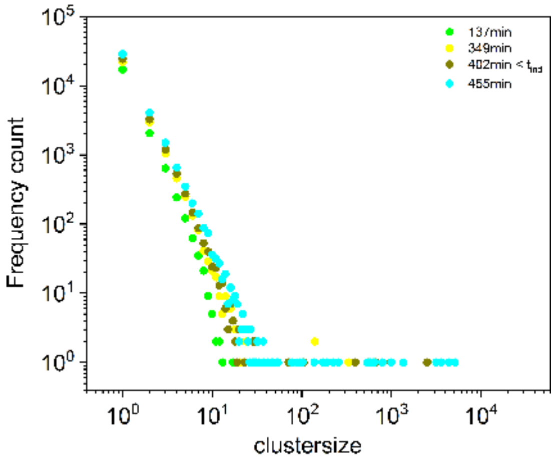

Figure 6.25: Crystalline cluster size distribution at $\alpha = 0.7566$ for different times as indicated. The induction stage is given by the color green, followed by others in the main crystallization stage.

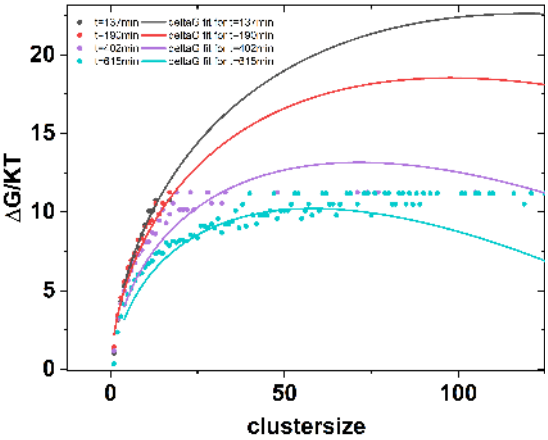

Figure 6.26: Gibbs free energy for α =0.7566 shortly before and after crystallization sets in is shown here. From the fit(thick line), the surface tension is obtained.

Within the framework of CNT, the statistics of the crystalline clusters f(N) give access to the nucleation barrier ΔG_{crit}, the surface tension γ, and the critical size R_{crit}; experimentally, Gibbs free energy can be determined by fitting

$$-ln(f(N)) = A + \Delta G_{crit}(N) \tag{6.10}$$

to the measured data with A and the surface tension γ as free fit parameters where f(N) is the absolute frequency of the crystals of size N. $\Delta\mu$ is calculated from the equation of state [4] and ρ_s is measured via Voronoi construction analyzing the crystalline clusters.

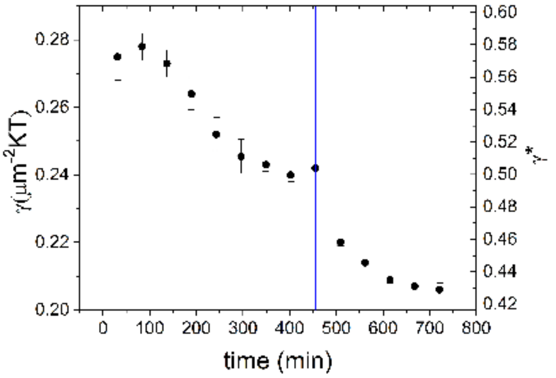

Figure 6.27: The surface tension γ was calculated by fitting eq.6.10 to Gibbs' free energy. The blue line indicates the time of the first growing crystals. The reduced interfacial tension γ^* is plotted against time on the other side for α =0.7566.

Figure 6.25 shows the frequency distribution of crystalline clusters at different times, as indicated. The Gibbs free energy of the crystals at t=402 min, which is close to the induction time followed by the continued time steps. ΔG from the above equation is given in the figure 6.26. From the fit function, surface tension is obtained for each time step as shown in Figure 6.27.

The interfacial tension between the crystal and fluid phases is a critical parameter that controls the nucleation process. However, γ is difficult to calculate [145] [101] and to measure experimentally. However, with our data, we can measure γ by examining the statistics of the nuclei obtained at each time, as shown in the figure above. Initially, the interfacial tension is higher and starts to reduce as time increases and, at the later stages, starts to flatten. The reduced crystal surface tension$\approx$ 0.5 before the crystal growth sets in agrees with the analytical theory in equilibrium(γ^*= 0.546 to 0.574) [40]. Since the crystal size distribution stays approximately constant before crystallization sets in(295min to 455 min) and changes significantly during the crystallization, the assumption of quasi-state as assumed by CNT is justified only in the time interval mentioned above. As seen in the figure 6.27, the reduced interfacial tension is plotted against time. γ^* starts to decrease as the time increases. At the induction time, the plateau reaches and then reduces again.

The critical size obtained by different methods is given in Figure 6.28. The critical radii from the analysis of f(N) in the CNT framework show a decreasing size with increasing supercooling from N = 280 from the middle to N= 40 at the end of the coexistence region. The CNT-based critical radii are incompatible with the real ones within the fluid crystal coexistence region, significantly above $>$ 0.9. This is also true in the case of NRD, which shows the most significant discrepancy. Using the barrier height from the cluster size distribution(by eq P(N)), NRD was obtained within the framework of CNT (J and J_0). A is chosen such that data meet the experimental NRD at the highest supercooling

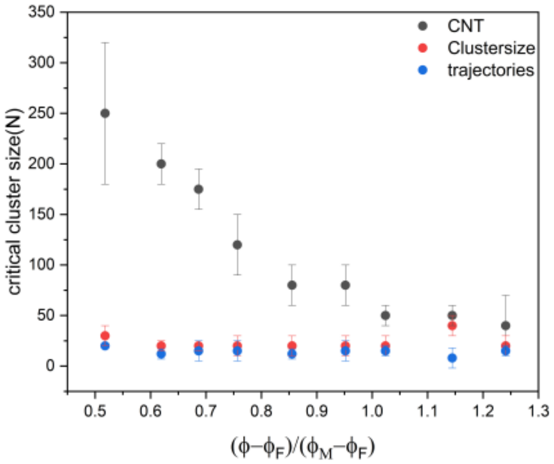

Figure 6.28: Critical nucleus size as a function of metastability/ undercooling by analyzing the crystal size distribution f(n) using CNT(black), direct measurements(red), and individual trajectories(blue).

$\alpha = 1.241$.

As seen in Figure 6.29, the data set from CNT reproduces the simulation data [16] [62] [63] [178] [99] [214] etc. fairly well. In summary, the nucleation barriers and critical radii determined from the experimental cluster size distributions within the framework of CNT and the NRD calculated on the basis of these data using CNT agree well with those in simulations but do not reflect the critical radii and Nucleation rate density determined from the direct method.

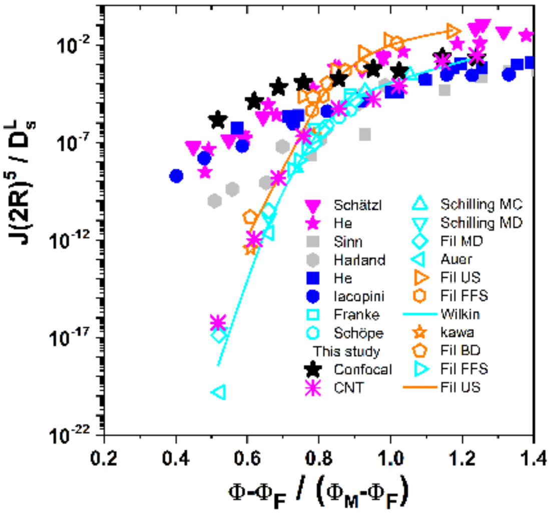

Figure 6.29: Normalised crystal nucleation rate densities as a function of metastability. Data from the previous experiments [177] [80] [79] [177] [80] [93], and simulations [16] [62] [63] [178] [99] [214] as indicated. The lines are the guides to the eye to highlight the numerical data. NRD was determined from this study by counting growing clusters(black star) and within the CNT framework using the experimental barrier height(pink cross

6.10 Summary

The early phase of the crystallization scenario for the colloidal model system is observed by confocal microscopy. The nucleation scenario is studied, and parameters such as critical size, Nucleation barrier height, interfacial tension, and NRD are calculated. The critical size from the experimental data and one calculated from CNT are shown in Figure 6.28. The direct observations of the structure and evolution of crystalline nuclei allowed us to characterize the critical processes of the nucleation and growth of colloidal crystals and quantitatively determine the essential parameters that control this process. As soon as the sample is kept under observation, the small clusters are found in the metastable fluid. The initial phase shows an increase in the number of metastable areas without the cluster growth. In this range, averaged bond order parameters remain constant. After the induction time, the crystallization phase begins. In this phase, t $>t_{ind}$ shows the isotropic growth with continuous nucleation. In this range, cluster size and averaged bond order parameters show clear structure formation.

In summary, the nucleation barriers, the critical radii, and the NRDs determined from the experimental data within the framework of CNT agree with those from simulations but do not reflect the critical radii and NRDs determined directly from the experiment without assuming any model. CNT and the performed simulations are obviously not able to describe crystal nucleation in the correct way. In the following, we will identify possible reasons for these shortcomings.

The simulations in the middle of the fluid crystal coexistence region have been performed with Umbrella Sampling (US) or Forward Flux Sampling (FFS).

Using US in the first step the nucleation barrier is determined by analysing the cluster size probability distribution P(N) in a Monte Carlo simulation. From this, ΔG_{crit} is calculated. In the second step, J is computed. The size fluctuation of a critical cluster is monitored around its equilibrium size in a kinetic Monte Carlo (KMC) simulation. From this K^{+} is determined. Using the obtained parameters ΔG_{crit} and K^{+}, the NRD is calculated. Thus this method implicitly represents an implementation of CNT. Using FFS in KMC the number of particles in the largest crystalline cluster in the system is chosen as reaction coordinate. FFS allows to determine the transition probability of a starting configuration in the fluid to the final state (largest crystalline cluster) and thus the NRD. For this purpose, the configuration phase space between fluid and crystal is divided into a sequence of "interfaces" (intermediate configurations) and the simulation paths that successfully propagate from interface to interface to the target are selected. As mentioned, there is evidence for significant discrepancies between the experiments and simulation near the middle of the coexistence region, i.e., the reason is the CNT description, which is also unclear. Our analysis suggests that the CNT framework cannot explain the nucleation scenario clearly.

Chapter 7

Nucleation Kinetics in Hard Sphere System

7.1 Abstract

Transitioning from a liquid to a solid state is a complex phenomenon involving multiple intermediate structures before reaching the final state. The exact pathways of this process are not well understood, as direct observations are difficult to make. However, recent advancements in experimental techniques have enabled the study of the evolution of symmetry and density in various colloidal systems during the liquid-to-solid phase transition with single-particle resolution. In this study, we report single-particle level measurements on the kinetics of three-dimensional colloidal crystallization for symmetry and density transformations. Our extensive studies across different volume fractions have enabled us to identify universal kinetics during the transition process. Our results show the formation of ordered precursor structures with varying symmetries, which convert into metastable solids. Our findings provide valuable insight into the crystallization process, shedding light on the intermediate structures and pathways involved in the liquid-to-solid phase transition.

7.2 Introduction

Crystallization plays a vital role in materials science and condensed matter physics. A liquid transforms into a solid during this process, and significant changes occur in symmetry and density. However, the exact kinetic pathways involved in the liquid-to-solid transition are not yet fully understood, and a consensus has not been reached. The classical nucleation theory (CNT) provides a framework for understanding crystallization but only describes some aspects of the nucleation process. CNT assumes that the emerging nucleus and the surrounding fluid have the properties of their respective bulk phases, which may not be entirely accurate in real liquids and colloidal suspensions. The exact correlation between density and symmetry depends on the kinetic transformations among intermediate structures, which are best studied using single-particle-level experiments.

To better understand the crystallization process from a microscopic perspective, it is necessary to track the nucleation process from the initial event to the growth of the crystalline nucleus beyond its critical nucleus size. In order to do so, researchers utilize local order parameters to describe the degree of translational and orientational orders around individual particles. These parameters enable the construction of a statistical map of the microscopic pathway to crystallization in a multiple-order-parameter space. While molecular simulations on model systems have contributed significantly to our understanding of this process [99] [100] [169] [170] [179] [170], recent confocal microscope experiments have also started to shed light on the process in colloidal systems [200].

7.3 Literature review

Understanding the microscopic mechanisms involved in the liquid-to-solid transition is still a topic of debate despite the fact that it is characterized by the spontaneous breaking of both positional and orientational symmetry. While classical nucleation theory (CNT) and density functional theories (DFT) [142] assume that the crystallization process is primarily controlled by positional ordering in a uniformly distributed liquid background, recent experiments [180] [175] [93] and simulations [139] [99] [179] [112] have revealed deviations from this classical picture. These findings suggest that the crystallization process could be more complex.

Scholars Lutsko and Nicolis [126] [124] [125] have extensively researched the mass conservation and finite transport speeds in the fluid, particularly in the vapor-liquid nucleation of Lennard-Jones particles. Their findings suggest that early density changes will likely occur on a larger scale than the initial nucleus. While densification in fluid-solid transitions is generally not as crucial as in vapor-liquid transitions due to the smaller difference in densities of the two phases, computer simulations of hard sphere crystallization by Schilling et al. [179] as well as experiments [180] [230] have reported the phenomenon of early densification. In a computational study by Russo and Tanaka [170] the relationship between structure and density changes during nucleation trajectories was examined. The study focused on a number density of $\Phi\sigma^3 \approx 1.02$, where σ is the diameter of a particle. The authors found that there was a coupling of order and density, but they noted that the restructuring of the nucleus foreshadowed the density increase, suggesting an "order-first" position. Based on optical microscopy, Tan et al. presented two distinct nucleation pathways for their colloidal system. Both pathways began with hexagonally ordered precursors, which then developed into either bcc or fcc metastable structures. The authors described a three-step process, with the final phase being either bulk bcc or RHCP, depending on the radius of the particles. Although the presence of bulk bcc and the dependence on radius indicated that forces other than excluded volume were important in these experiments, the authors stated that the nucleation sites were not correlated with increased local density. This finding contradicts the claim that nucleation rarely starts from the densest regions [200]. The study remains an interesting reference, and its results were further discussed and analyzed by Granasy and Toth [70].

In addition to the earlier studies, there have been other investigations into the relationship between density and nucleation events. Lu et al. [123] also used microscopy and found that nucleation events rarely start from the denser regions of colloidal samples. Similarly, Kawasaki and Tanaka [100] found medium-range ordered precursors of sizes more significant than the critical nucleus in simulations of hard spheres. The ordering was not icosahedral but rather hcp with multiple defects. Schilling et al. [179], [178] also reported a similar observation where low symmetry clusters of considerable size spontaneously transformed into highly ordered crystals. The presence of ordered precursor structures on crystallization should reduce the surface tension, which is consistent with the experiments of Gasser et al [69]. They found strongly aspherical shapes for the critical or near-critical nuclei.

In a two-step scenario, one expects the crystalline nucleus to appear inside a region where the relevant order parameter is higher than the rest of the melt. The size of this region should also increase with supercooling. It is well known that the length-scale of density fluctuations barely changes with supercooling, other articles showed that the correlation length of bond orientational order increases with supercooling. Direct observation of nucleation events shows that the nuclei appear to form inside regions of high bond-orientational order. The literatures on hard sphere nucleation presents an overview of whether it is a two-step process and whether densification and ordering can be separated. The emergence of contradictory statements raises questions about the physical benefits of this idea and the order in which these processes occur. Therefore, there is a need to examine the onset of crystallization in detail.

7.4 Data analysis

Let's start analyzing data by introducing the order parameters used in this study. We will describe here their basic properties while for the exact mathematical definition defined in Chapter 4. We will always adopt a microscopic approach by studying local order parameters (defined at a particle level). Since the liquid-to-solid transition is characterized by density fluctuations and orientational symmetry breaking, we wish to monitor both properties during crystallization. A suitable order parameter which expresses the relative spacing between particles in the system, is the density ρ_{pre}. This is easily computed using Voronoi diagrams, which assign a local volume V to each particle. We define bond orientational order parameter as described in chapter 4, a rotationally invariant scalar defined for each particle. These are important because they are suitable to detect precursor regions, as we will show later. Finally, it addresses the question of whether crystal nuclei emerge from dense precursors or not.

7.5 Precursor

The onset of crystallization was analyzed by Russo and Tanaka in their 2012 study, using bond order in the Gaussian core model, a prototype for soft spheres. They noted that crystallization occurs in precursor regions of high bond orientation order and that the crystal that first nucleates is the one that has the closest symmetry to the ordered regions in the supercooled state. A later investigation by J.T. Berrymann and T. Schilling in 2016 of the bond order in a compressed hard sphere fluid found that the hexagonal ordering appeared simultaneously with the density fluctuation at the onset of crystallization. Recent research suggests that liquid heterogeneity plays a crucial role in crystallization mechanisms and determining the glass formation ability of various materials. While classic nucleation theory assumes that random fluctuations in the homogeneous liquid drive crystallization events, the formation of precursor regions in the liquid highlights the crucial role of thermal fluctuations and heterogeneity in driving crystallization events. Various studies have reported the presence of precursor-mediated nucleation mechanisms during crystallization, where preordered regions in the liquid form before the appearance of crystallites within the centers of the precursors. These "two-step" mechanisms have been observed in several materials, including colloids, hard spheres, ice, metal alloys, and proteins [195] [170] [47] [229] [129] [179] [113] [200]. Overall, these findings challenge the traditional understanding of nucleation and highlight the need for further research to understand the onset of crystallization in materials fully.

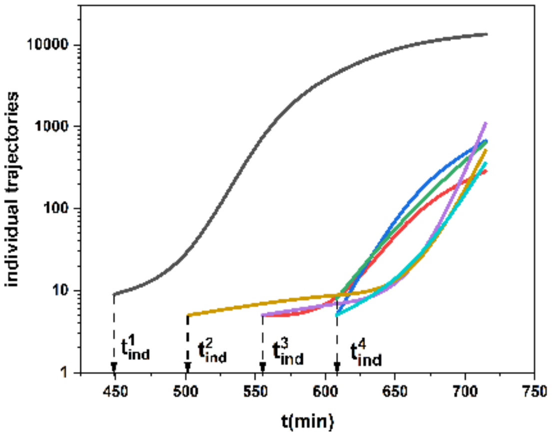

Figure 7.1: Individual identified clusters traced from backward until they disappear. From this, one can also identify the clusters' critical size and individual induction time as indicated. For clarity, only few clusters are shown which has different induction times. These are measured for effective volume fraction 0.5389, corresponding to α=0.7566 in terms of coexistence value.

We begin by considering clusters that grow in time. During cluster formation, the appearance of a nucleus grows over the critical size. For each time step, clusters growing in time are identified. As explained in the last chapter, the clusters are traced back in time to get the critical nuclei from where it emerge as shown in the figure 7.1. The point where the critical nucleus is identified, the mean value of averaged bond order parameter mean $\bar{q}_4$, $\bar{q}_6$, $\bar{w}_4$ and $\bar{w}_6$ is determined and also average crystal volume farction $\Phi_{pre}$is calculated. Thus these parameters corresponds to precursor data for the corresponding measured volume fraction Φ.

Here, we find the packing fraction Φ_{cry} of precursors, significantly influencing the transformation pathway during crystallization. Figure 7.2 shows the frequency of occurrence of averaged Φ_{cry} in identified precursors for effective volume fraction Φ = 0.5389, Φ =0.536 and Φ =0.5332. The red line shows the averaged value for the precursors, which is 0.596 in the case of 0.5389 (Figure

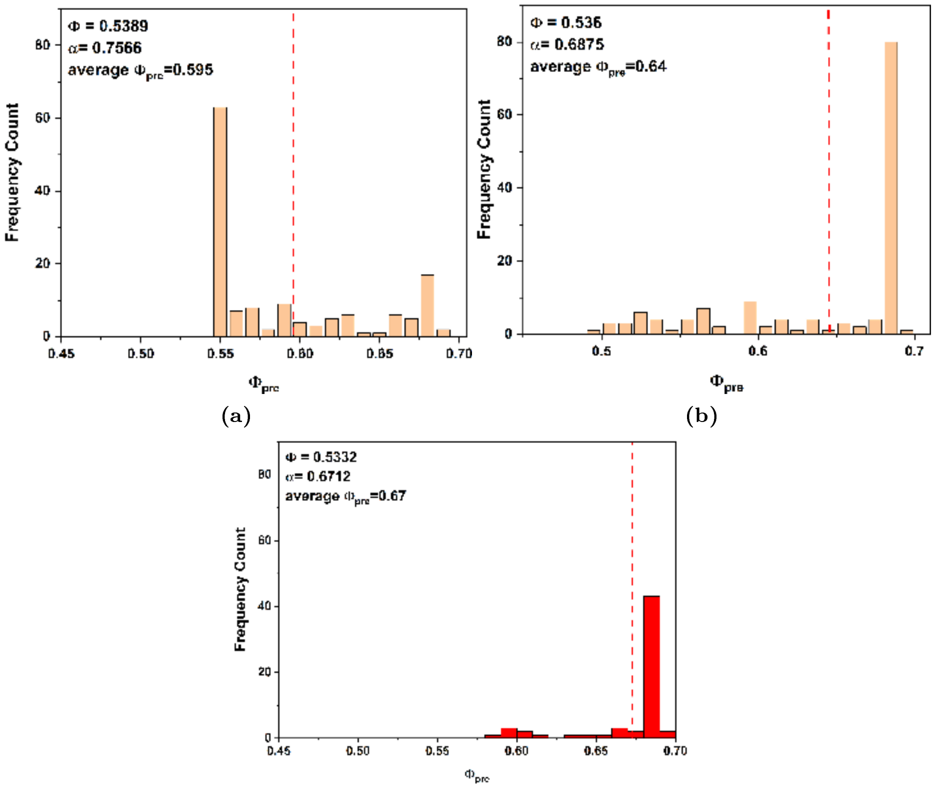

(a) (b)

(c)

Figure 7.2: Packing fraction of precursors determined using Voronoi volume computed for each particle and averaged over each cluster. (a)Histogram of Φ_{cry} for a effective volume fraction of 0.5389 and (b) for 0536 corresponds to α=0.7566, 0.6875, and 0.619.The red dotted line corresponds to an average value of 0.596±0.07 for 0.5389 and 0.6404±0.06 for 0.536 and 0.6712±0.027 for 0.5332. All histogram has same bin size of 0.01.

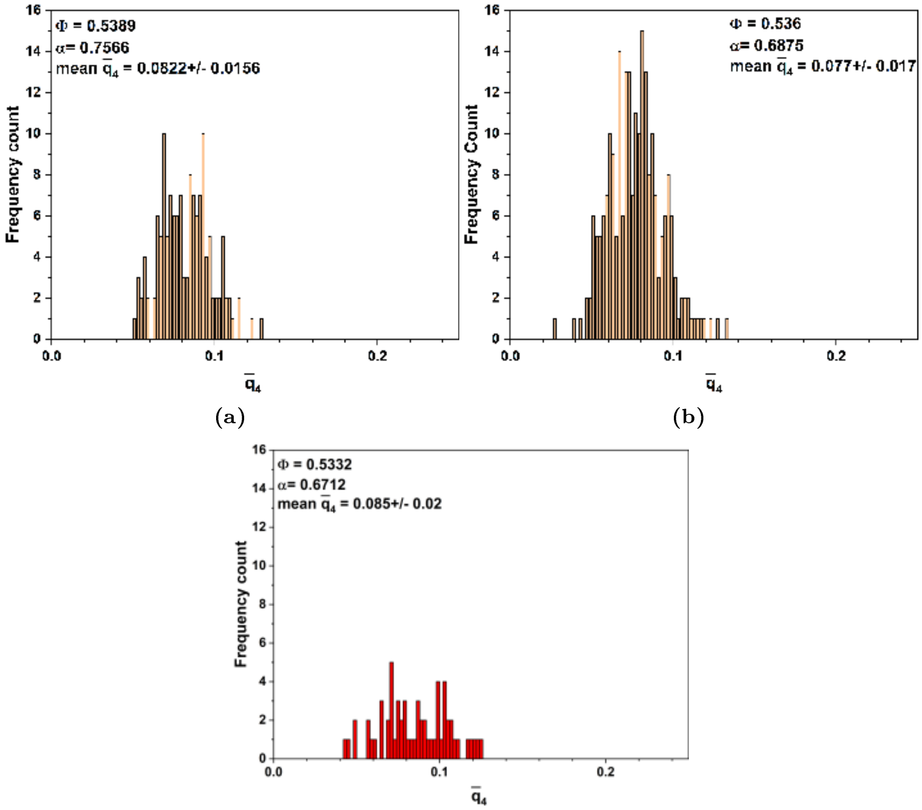

(a) (b)

(c)

Figure 7.3: (a) Histogram of the mean of $\bar{q_4}$ for the volume fraction of 0.5389 and (b) for 0536 and (c) 0.5332 corresponds to α =0.7566, 0.6875, and 0.619. The values are computed for particles in the precursors only. All histogram has same bin size of 0.02. The threshold for HCP like cluster has $\bar{q_4}$ value ranging from 0.04 to 0.12, whereas for FCC the values varies from 0.12 to 0.25. For BCC like cluster $\bar{q_4}$ has values from 0 to 0.07.

7.2(a)) and 0.64 in the case of 0.536 (Figure 7.2(b) and 0.67 for 0.5332 (Figure 7.2(c)). The density at which the crystals start forming has a high value above 0.55. The occurrence of these values is high in all cases. As seen from the histogram, there are other possible values where the cluster nuclei have high density, which grows into clusters. The overall trends shows that the packing fraction of precursor increases with decreasing volume fraction.

The mean of $\bar{q_4}$, $\bar{q_6}$, $\bar{w_4}$ and $\bar{w_6}$ for the critical nucleus is obtained by determining the average value of the bond order parameter and finding its mean over all the particles present in that cluster. By having a histogram of these values, one can have a clear picture of the distribution of these observables. Peaks in the histogram indicate regions where the orientation order is more high occurrences. Gaps or low frequencies suggest regions where the system has less occurrences. Figure 7.3 shows the histogram of the mean of $\bar{q_4}$ and $\bar{q_6}$ for each particle in precursors for different volume fraction as indicated. Similarly, Figure 7.4 shows the histogram of averaged wigner parameters $\bar{w_4}$ and $\bar{w_6}$.

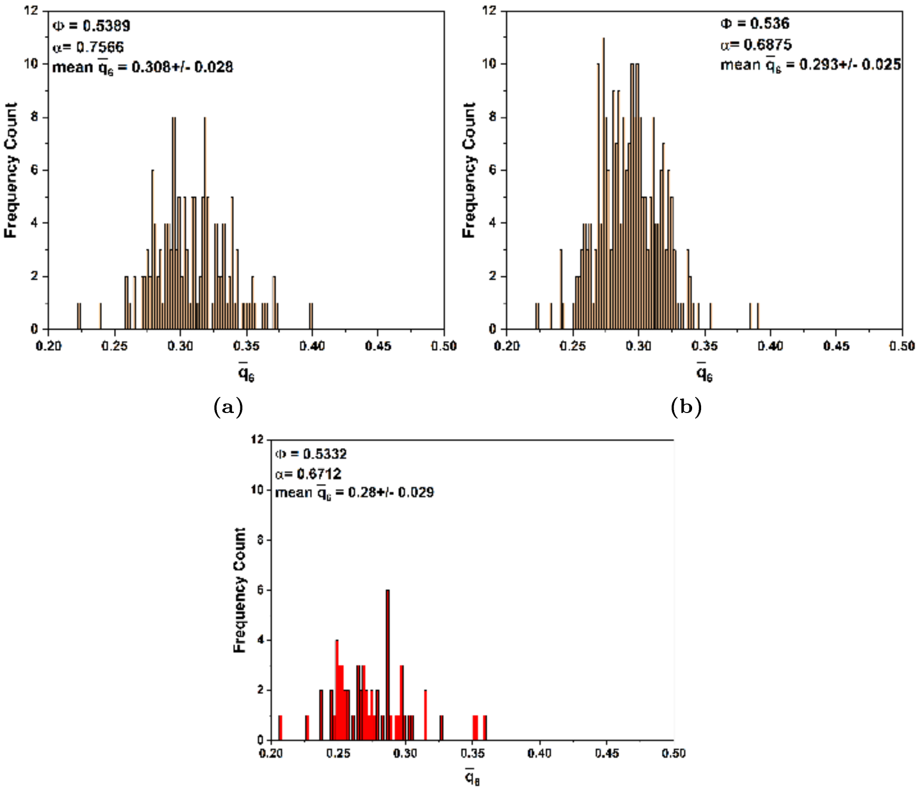

(a)

(b)

(c)

Figure 7.4: (a) Histogram of the mean of $\bar{q}_6$ for the volume fraction of 0.5389 and (b) for 0.536 and (c) 0.5332 corresponds to $\alpha=$ 0.7566, 0.6875, and 0.619. The values are computed for particles in the precursors only. All histogram has same bin size of 0.02. The threshold for HCP and FCC like cluster has $\bar{q}_6$ value ≥ 0.28. For BCC like cluster $\bar{q}_6$ has values ≥ 0.3 whereas for fluid like particle, the $\bar{q}_6$ has values ≤ 0.28.

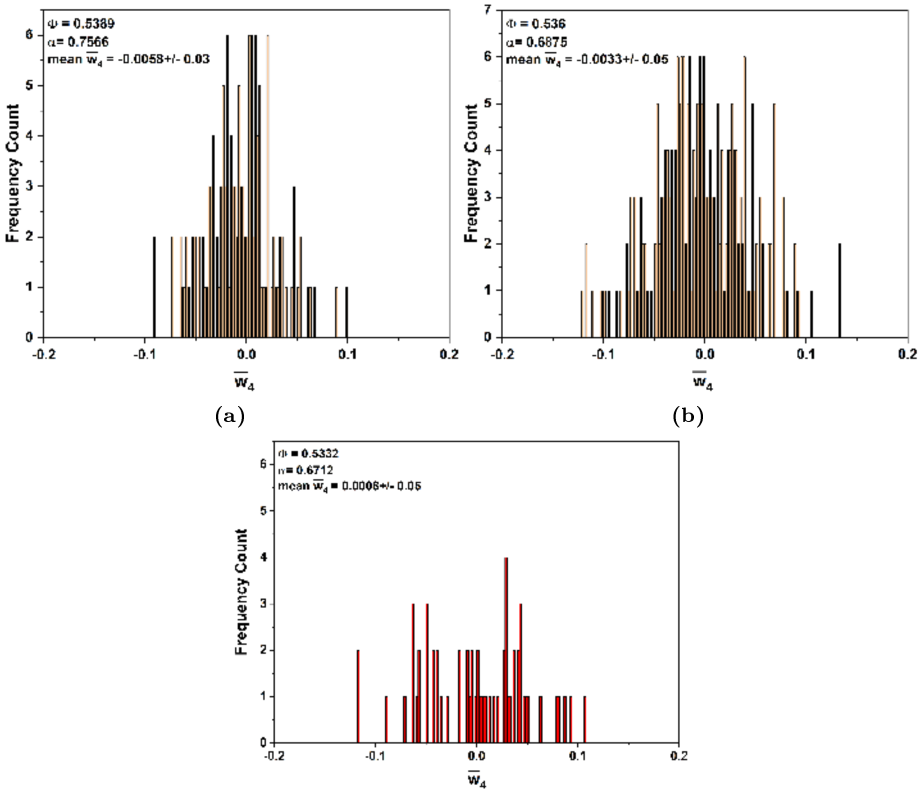

(a) (b) (c)

Figure 7.5: (a) Histogram of the mean of $\bar{w}_4$ for the volume fraction of 0.5389 and (b) for 0.536 and (c) 0.5332 corresponds to α= 0.7566, 0.6875, and 0.619. The values are computed for particles in the precursors only. All histogram has same bin size of 0.02. The threshold for HCP like cluster has $\bar{w}_4$ value ≥ 0, whereas for FCC $\bar{w}_4$ value ≤ 0.

A bin size of 0.002 allows for a fine-grained analysis of the data. Each bin represents a small range of orientation order values, helping to identify subtle variations in ordering. Peaks in the histogram indicate ranges of orientation order values where colloidal particles are highly aligned. This suggests the presence of well-ordered structures or crystalline regions. Similarly, there are low-frequency regions, suggesting lower alignment or particle ordering, possibly indicating defects, disordered structures, or amorphous regions. In Figure 7.4, the particle in the precursor has a high mean value of $\bar{q}_6$ in the range of 0.28 to 0.33. The frequency count in this range is high, implying that precursors have a high orientational order. In the case of ϕ=0.5389 and ϕ=0.5332 , the values for q4 range from 0.06 and above, suggesting less occurrence of BCC but more occurrence of HEX/HCP/FCC. In the case of ϕ=0.536, these q4 values start above 0.02, suggesting the possibility of the occurrence of BCC along with HEX/HCP/FCC.

Similarly, Figure 7.5 and 7.6 shows a histogram of the mean $\bar{w}_4$ and $\bar{w}_6$ for precursors for different volume fraction as indicated. A decrease in the $\bar{w}_6$

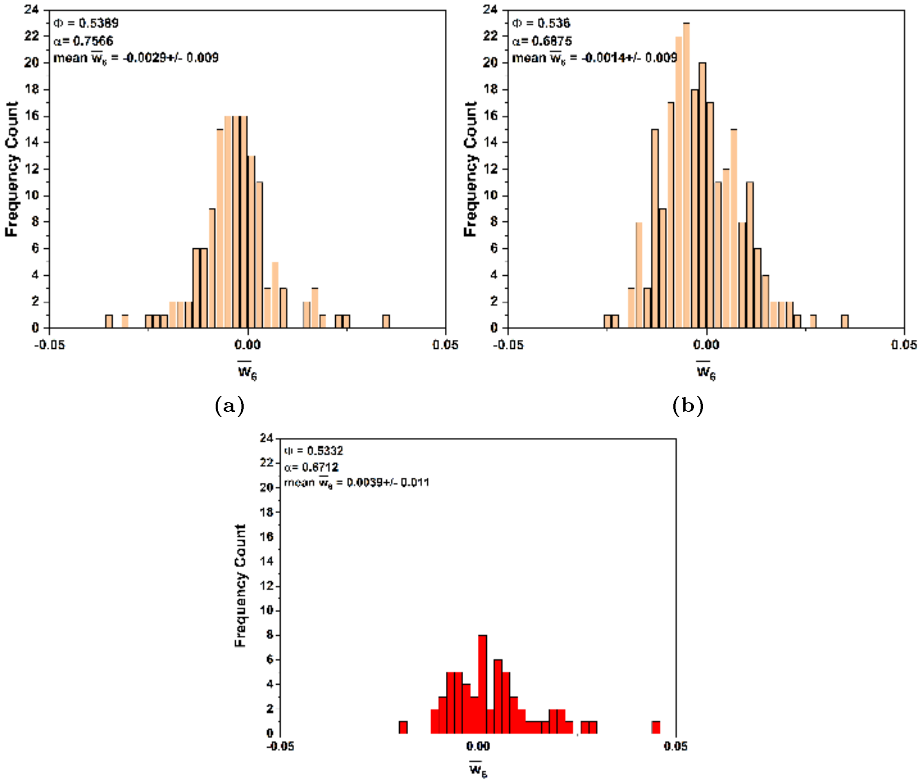

(a)

(b)

(c)

Figure 7.6: (a) Histogram of the mean of $\bar{w}_6$ for the volume fraction of 0.5389 and (b) for 0.536 and (c) 0.5332 corresponds to $\alpha=$ 0.7566, 0.6875, and 0.619.The values are computed for particles in the precursors only. All histogram has same bin size of 0.02. The threshold for HCP and FCC like cluster has $\bar{w}_6$ values ranges from -0.05 to 0.008. For BCC like cluster $\bar{w}_6$ has values ranging from 0.008 to 0.05

value and an increase in the $\bar{q}_6$ value are associated with hexagonal ordering. However, a larger decrease in the $\bar{w}_6$ ($\bar{w}_6 <$ -0.023) [116] and a slight decrease in $\bar{q}_6$ signify icosahedra. We have no notable count in this range in the case of $\bar{w}_6$. Thus, it can be inferred that there is no signal of icosahedral order as an aspect of the nucleation process in these cases. The different crystal-like structural orderings (bcc-like, fcc-like, hcp-like) are characterized by these order parameters. A particle belongs to FCC-like crystal is indicated by $\bar{w}_4 \leq 0$, while for HCP-like crystalline atoms ($\bar{w}_4 \geq 0$).

Direct observation of precursor shows that nuclei appear to form inside region of relatively high bond order parameter with relatively high packing fraction. Thus in two step scenario, the expectation of crystalline nucleus to appear inside a region where the order parameter is higher hold valid. The precursor stage is characterized by the spatially orders and temporal fluctuations among them. Then, in the later stage, the lifetime and the spatial coherency of HCP/HEX-type order gradually increase with time, promoting the nucleation of the most stable solid.

To explain the nucleation pattern unveiled in the previous section, we will address the question of how density(ρ_{cry}) and order parameters are coupled by taking few examples such as by considering all growing clusters, by considering few slow growing cluster and few biggest cluster from different volume fractions.

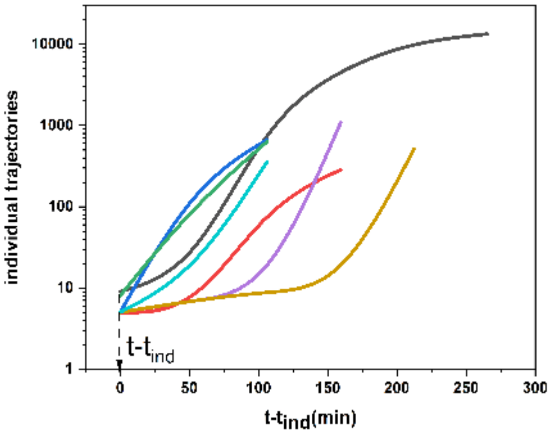

Figure 7.7: Individual identified clusters shown to start from the same time t. These are measured for effective volume fraction 0.5389, corresponding to α=0.7566 in terms of coexistence value.

Some clusters grow within a few minutes, but others take much longer, as shown in the figure 7.1, indicating the time from where the clusters starts to grow. Because nucleation events are randomly distributed in time, it is necessary to define a time t for each trajectory so that the time series collected over different nucleation events can be averaged together. Thus, all the quantities are represented here after this time t i.e t-t_{ind}, where all clusters are meant to start simultaneously. For clarity the trajectories from the previous figure 7.1 is shown again in the figure 7.7 such that all trajectories starts from the same time t=0. From here onwards all data represented in the figure are shown for time t-t_{ind}.

7.6 The interplay between density and bond order parameter for all growing clusters

The interplay between bond order parameter and density is crucial for understanding the system's behavior in a hard sphere colloidal system. The changes in bond order may be related to structural transitions or dynamic rearrangements of colloidal particles, while density variations reflect the packing density of hard spheres. Hence, we traced all growing clusters and determined mean values of bond order parameters and packing fractions(Φ_{cry}) of clusters using Voronoi volume V_{cry}. Here, we present four cases, represented by their effective volume fraction as 0.544, 0.5389 and 0.536, 05332, corresponding to α= 0.78313, 0.7566, 0.6875, and 0.619 shown in the figure 7.8.

- 0.544 (Figure 7.8(a))

As time progresses, in the case of 0.544, the values of $\bar{q_4}$ and $\bar{q_6}$ increase, indicating that particles are more likely to align, suggesting higher order in their orientation. Meanwhile, the values of w_4 and $\bar{w_6}$ mainly represent the cluster type, with initially high values. However, as time passes, the values of w4 switch from positive to negative and then back to positive, indicating the formation of the HCP structure. The density increases isotropically from the start, indicating a denser and more ordered structure. Initially, the density and the order parameters $\bar{q_4}$ and $\bar{q_6}$ increase. However, the values of w4 and w6 switch back and forth. The trend suggests that the density and $\bar{q_4}$ and $\bar{q_6}$ parameters go hand in hand, but this is not true for $\bar{w_4}$ and $\bar{w_6}$.

- 0.5389 (Figure 7.8(b))

  Initially, as the concentration of particles increases, the density values rise, and the bond order parameter of the particles aligns more coherently. However, as the system evolves, changes in the order parameter, including w_4 and $\bar{w_6}$, indicate intricate behavior, possibly involving phase transitions or structural reorganization. It's important to note that while density may remain high, the stabilization of density suggests that the system has dense packing. Despite the stable density, the order parameter remains reduced, indicating that the colloidal system has transformed, and the particle alignments are not as ordered as in the initial phase. The positive value of w_4 at the end suggests that the structure evolved mainly as HCP. In summary, these findings suggest that density and order parameters may initially show a positive correlation. Still, changes in the order parameter might indicate more complex behavior as the system evolves. Therefore, it's crucial to consider these dynamic relationships when analyzing the behavior of colloidal particles, possibly associated with the hard sphere colloidal system undergoing structural modifications or phase transitions.

- 0.536 (Figure 7.8(c))

  The q_6 values increase from 0.2703 to 0.32 as time progresses, and q_4 varies similarly. In case w_4 starts from a positive value, it is suggested to have a stable initial structure. Additionally, w_6 values show little difference. This indicates that the colloidal particles tend to align more over time, suggesting a higher order in their orientations. The density values show fluctuations but generally exhibit a slight increase. This increase in density implies that more colloidal particles are in the system, forming an ordered structure. In this hard-sphere colloidal system, the rise in orientation order suggests a tendency for particles to align, indicating some form of ordering or structural changes. The increase in density may be associated with the packing of particles or changes in the colloidal suspension, which can contribute to the observed changes in orientation. This system correlates with density and orientation order. As the density increases, a trend toward higher orientation order indicates that these two parameters go hand in hand.

- 0.5332 (Figure 7.8(d))

  As time progresses, the values of q_4 show a positive increase while the values of q6 start to decrease. The values of w4 start from positive and

> later switch to negative, while the same trend is observed for w_6. There is a general trend of variation in bond order parameters over time. Despite this variation, the density values remain consistently high. In a hard sphere colloidal system, this suggests that the overall packing of particles remains the same. However, the trend in orientational order indicates a growing alignment or order in the orientation of the colloidal particles. Interestingly, the orientational order evolves independently of density. While the density remains constant, the orientational order changes and evolves. This indicates that these two parameters do not necessarily go hand in hand, and one can change while the other remains constant.

More clear picture can also obtained using mean $\bar{q}_4$ vs. mean $\bar{q}_6$ and mean $\bar{w}_4$ vs. mean $\bar{w}_6$ plot for respective volume fraction. The dotted line shows the cutoff values for different cluster types. For reference, the names of cluster types are also indicated. The threshold used in this analysis is given in the chapter 4.

Figures 7.9 show the mean $\bar{q}_4$ vs. mean $\bar{q}_6$ map and $\bar{w}_4$ vs. mean $\bar{w}_6$ map for an effective volume fraction of 0.544 corresponding to $\alpha = 0.78313$. The mean values in the $\bar{q}_4$ vs. mean $\bar{q}_6$ map suggest the HEX, HCP cluster type, whereas the corresponding $\bar{w}_4$ vs. mean $\bar{w}_6$ clearly indicates HCP formation.

Figure 7.10 shows the map of mean $\bar{q}_4$ vs. mean $\bar{q}_6$ and $\bar{w}_4$ vs. mean $\bar{w}_6$ for an effective volume fraction of 0.5389 corresponding to α =0.7566. Here, in the $\bar{q}_4$ vs. mean $\bar{q}_6$ map, the mean values suggest the HEX, HCP cluster type, whereas the corresponding $\bar{w}_4$ vs. mean $\bar{w}_6$ map indicates Hex to HCP transformation at the later stage.

Figure 7.11 shows the map of mean $\bar{q}_4$ vs. mean $\bar{q}_6$ and $\bar{w}_4$ vs. mean $\bar{w}_6$ for an effective volume fraction of 0.536 corresponding to $\alpha = 0.6875$. Here, in the $\bar{q}_4$ vs. mean $\bar{q}_6$ map, the mean values suggest the HEX, HCP cluster type, whereas the corresponding $\bar{w}_4$ vs. mean $\bar{w}_6$ map indicates HEX formation and may be transforming to HCP at a later stage.

Figures 7.12 show the mean $\bar{q}_4$ vs. mean $\bar{q}_6$ map and $\bar{w}_4$ vs. mean $\bar{w}_6$ map for an effective volume fraction of 0.5332 corresponding to $\alpha = 0.619$. The mean values in the $\bar{q}_4$ vs. mean $\bar{q}_6$ map suggest the HEX, HCP cluster type, whereas the corresponding mean $\bar{w}_4$ vs. mean $\bar{w}_6$ clearly indicates HEX formation.

Regarding density, $\bar{q}_4$ and $\bar{q}_6$ tend to go together in the case of 0.544. However, this is different for $\bar{w}_4$ and $\bar{w}_6$. On the other hand, for 0.5389, there may be a positive correlation between density and orientational order. But for 0.536, as density increases, there is a trend toward higher orientation order, indicating that these two parameters may be related. In the scenario of 0.5332, the order parameter changes independently of density. Therefore, analyzing these results does not provide a specific path, but it shows that both order parameter and density fluctuations can occur together or one after the other. In general, there are multiple ways in which crystallization kinetics can be influenced.

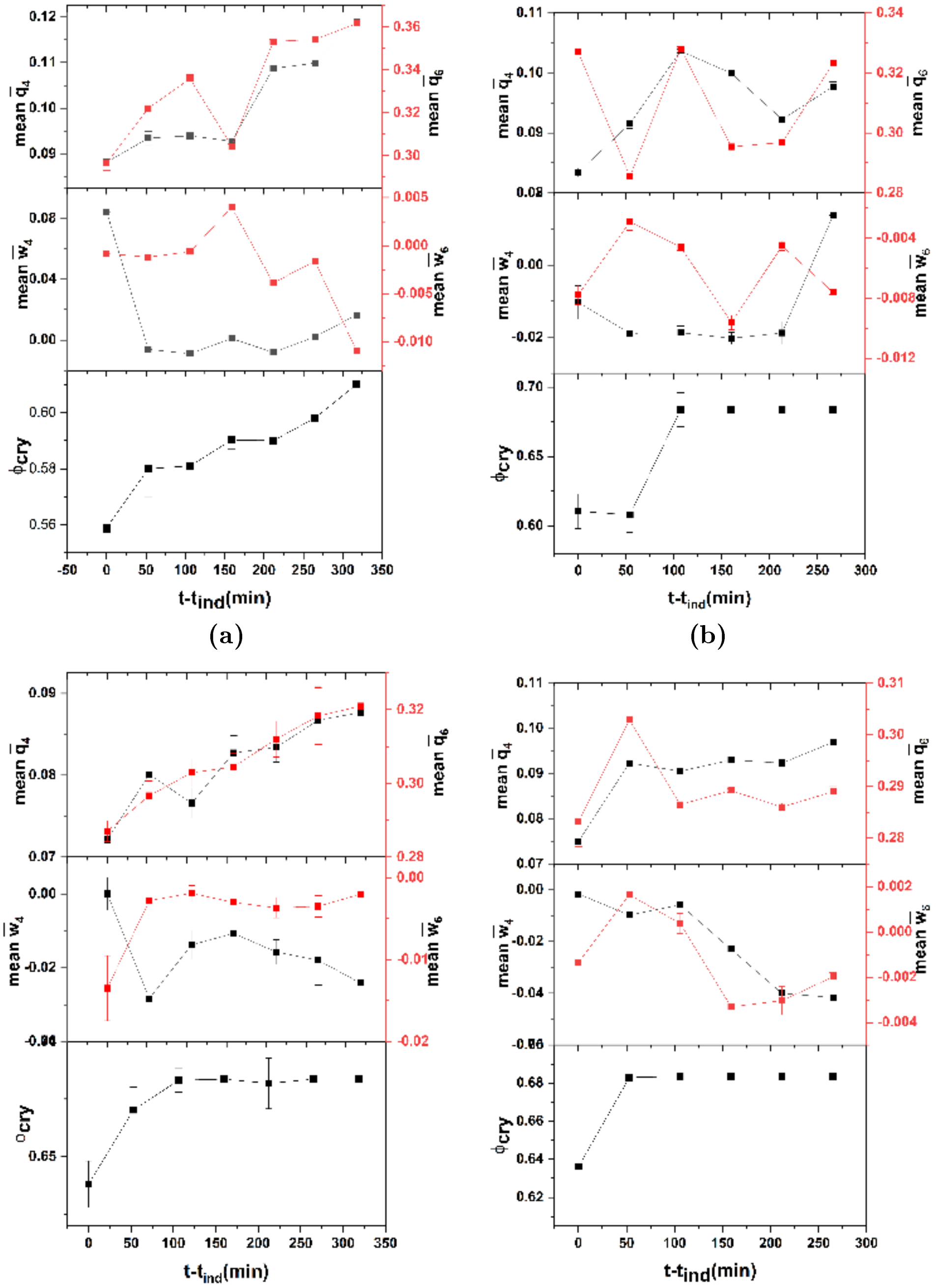

(a) (b)

(c) (d)

Figure 7.8: Comparison of mean bond order parameter, mean $\bar{q}_4$, $\bar{q}_6$, $\bar{w}_4$, $\bar{w}_6$ and Φ_{cry} for (a) 0.544 and (b)0.5389 (c)0536 and (d)0.5332 corresponds to α= 0.78313, 0.7566, 0.6875, and 0.619 is shown. The parameters mean $\bar{q}_4$, $\bar{q}_6$ are given at the top. In the middle $\bar{w}_4$, $\bar{w}_6$ and at the bottom, Φ_{cry} is given. All parameters are shown here concerning changes that appear in time(t-t_{ind})

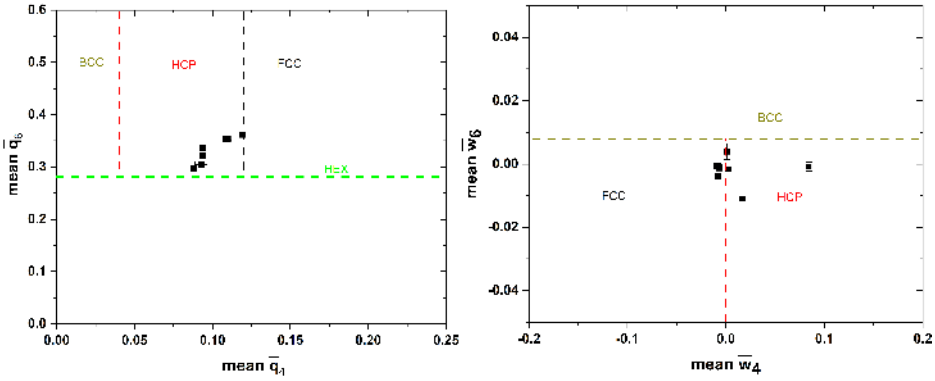

(a) (b)

Figure 7.9: mean $\bar{q}_4$ vs. mean $\bar{q}_6$ and $\bar{w}_4$ vs. mean $\bar{w}_6$ for 0.544 corresponding to $\alpha = 0.78313$. The dotted line shows the cutoff values for different cluster types. For reference, the names of cluster types are also indicated.

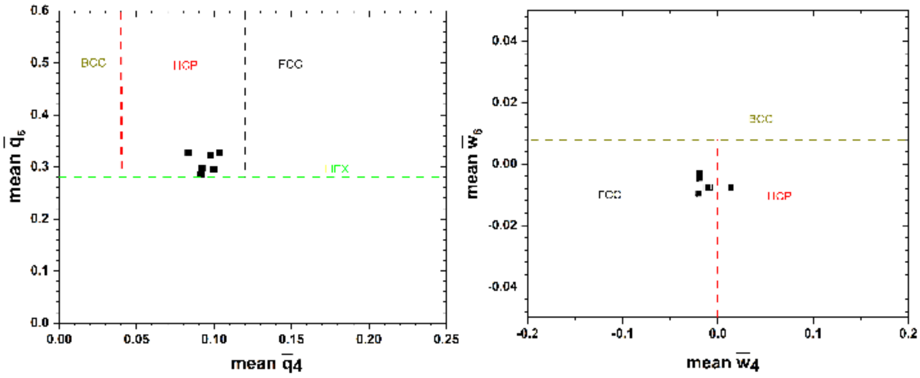

(a) (b)

Figure 7.10: mean $\bar{q}_4$ vs. mean $\bar{q}_6$ and $\bar{w}_4$ vs. mean $\bar{w}_6$ for 0.5389 corresponding to α =0.7566. The dotted line shows the cutoff values for different cluster types. For reference, the names of cluster types are also indicated.

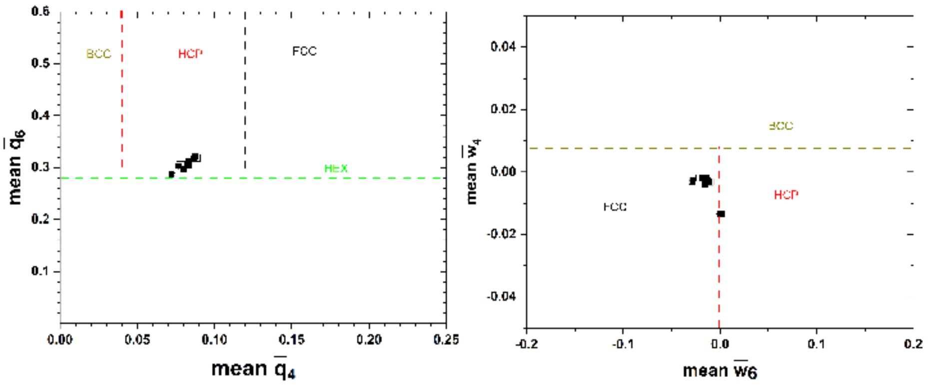

(a) (b)

Figure 7.11: mean $\bar{q}_4$ vs. mean $\bar{q}_6$ and $\bar{w}_4$ vs. mean $\bar{w}_6$ for 0.536 corresponding to $\alpha = 0.6875$. The dotted line shows the cutoff values for different cluster types. For reference, the names of cluster types are also indicated.

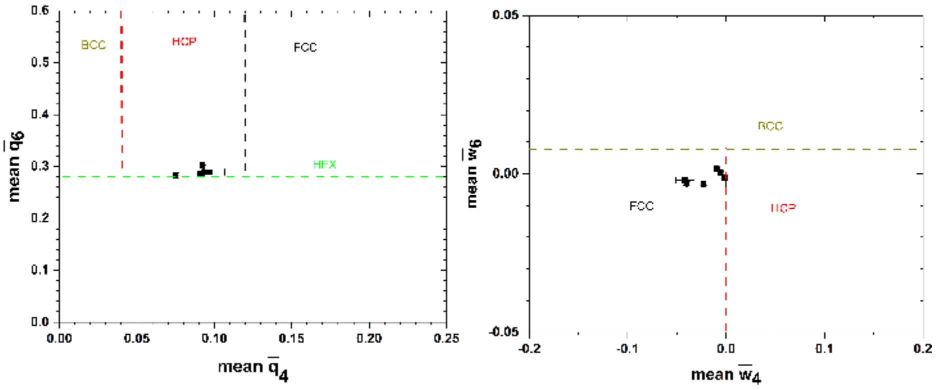

(a) (b)

Figure 7.12: mean $\bar{q}_4$ vs. mean $\bar{q}_6$ and $\bar{w}_4$ vs. mean $\bar{w}_6$ for 0.5332 corresponding to $\alpha = 0.619$. The dotted line shows the cutoff values for different cluster types. For reference, the names of cluster types are also indicated.

7.7 The interplay between density and bond order parameter for "Slowest" clusters

Since the above analysis involves all growing clusters, the following analysis considers three different clusters from the each above-mentioned volume fraction for a detailed view. The cluster used in this analysis has a 'long tail' or, in other words, the growth of this cluster is slow and has more time steps. Hence the name "Slowest cluster". This type of cluster may helps in analyzing the variation of order parameters and density more clearly.

7.7.1 0.544

The three slowest clusters for the volume fraction of 0.544 corresponds to $\alpha=$ 0.78313 is shown in the figure 7.13.

In the first cluster shown in the figure 7.13(a), the average values of $\bar{q}_4$ and $\bar{q}_6$ change simultaneously over time. However, these values eventually decrease. On the other hand, $\bar{w}_4$ always remains positive, indicating a structural change from the beginning. Density, on the other hand, consistently increases from the start. Initially, a low-density HCP cluster was formed, which later continued to grow with a high packing fraction at the end. In this case, density and order parameter initially change together, but later diverge from each other.

In the second cluster shown in the figure 7.13(b), the mean values of $\bar{q}_4$ and $\bar{q}_6$ change simultaneously over time, while w4 remains consistently positive and $\bar{w}_6$ remains relatively stable, indicating a structural modification from the beginning. Density consistently increases from the outset and eventually reaches a saturation point. Initially, a low-density HCP cluster is formed ($\bar{w}_4 > 0$), which later grows into a high packing fraction cluster. In the end, it is possible that a combination of FCC/HCP clusters is formed. In this scenario, density and q_6 order parameter initially have a positive correlation, but later density stabilizes while $\bar{q}_6$ continues to change. Meanwhile, $\bar{w}_4$ and $\bar{w}_6$ start to decrease, but ultimately the cluster with high density is formed.

Within the third cluster shown in the figure 7.13(c), an intriguing structural modification is apparent. The $\bar{q}_4$ and $\bar{q}_6$ values change in tandem over time, while $\bar{w}_4$ and $\bar{w}_6$ remain consistently positive. This transformation is indicative of a significant shift from the beginning. The density within the cluster consistently grows, reaching a maximum soon after. Beginning as a less dense cluster, the HCP cluster eventually grows, displaying a high packing fraction cluster with $\bar{w}_4 > 0$. In this context, the density stabilizes faster, and the $\bar{q}_6$ order parameter oscillates. However, $\bar{w}_4$ and $\bar{w}_6$ remain positive throughout. Thus, the density precedes the order parameters in this case, highlighting the significance of this transformation.

7.7.2 0.5389

The three slowest clusters for the volume fraction of 0.5389 corresponds to $\alpha=$ 0.7566 is shown in the figure 7.14.

The first cluster shown in the figure 7.14(a). The order parameter is a measure of how well-organized colloidal particles are. In this case, the $\bar{q}_4$ and $\bar{q}_6$

values initially fluctuate, indicating some disorder. However, there is a significant increase in the q6 value, which suggests a more orderly arrangement. The density values remain relatively constant, indicating a stable packing or arrangement of hard-sphere colloidal particles. This consistent density also implies that the particles maintain a regular spatial distribution. Moreover, the $\bar{w}_4$ and $\bar{w}_6$ values change significantly over time. The $\bar{w}_4$ value changes from negative to positive, whereas the $\bar{w}_6$ value changes from positive to negative. This indicates a structural change from BCC to HCP. The initial density fluctuations may be due to the system reaching stability, followed by an increase in the order parameter. In summary, in this particular example, density varies before any significant changes in order parameter are observed over time.

The second cluster is shown in the figure 7.14(b), where the mean values of $\bar{q}_4$ fluctuate while $\bar{q}_6$ increases over time and eventually stabilizes. Initially, $\bar{w}_4$ values are positive, but in the middle, they switch to negative, whereas $\bar{w}_6$ changes from negative to positive, indicating a structural modification from the beginning, At first, a low-density cluster is formed, which gradually grows into a high packing fraction cluster. This is an indication of the cluster starting from HCP, converting into HEX, and finally switching back to HCP. In this scenario, the density and $\bar{q}_6$ order parameter initially have a positive correlation, but later both stabilize, while $\bar{q}_4$ continues to change. Meanwhile, $\bar{w}_4$ and $\bar{w}_6$ fluctuate, but ultimately, the cluster with high density is formed.

The third cluster is shown in the figure 7.14(c), where the values of $\bar{q}_4$ and $\bar{q}_6$ change together over time. On the other hand, $\bar{w}_4$ and $\bar{w}_6$ remain consistently negative. The density within the cluster grows steadily and reaches a maximum. Initially, the HEX cluster is less dense, but it eventually grows into a high packing fraction cluster. In this context, the density stabilizes first, and the $\bar{q}_6$ order parameter oscillates. However, $\bar{w}_4$ and $\bar{w}_6$ remain negative throughout. Therefore, the density leads the order parameters in this case, emphasizing the importance of this transformation.

7.7.3 0.536

The three slowest clusters for the volume fraction of 0.536 corresponds to $\alpha=$ 0.6875 is shown in the figure 7.15.

The first cluster shown in the figure 7.15(a). At the beginning, the values of $\bar{q}_4$ and $\bar{q}_6$ fluctuate, but as time goes on, they increase. This indicates that there is a highly ordered structure towards the end. Meanwhile, the values of $\bar{w}_4$ and $\bar{w}_6$ switch back and forth between positive and negative multiple times. Both values start as positive, then move to negative, and eventually switch back to positive values. This switching over is an indication of the structure changing from HCP to HEX, and then back to HCP. However, at the end, it switches to a negative indication, which suggests further development in the structure, probably combination of HEX and HCP. In terms of the packing fraction, the values initially start at a low value but drastically increase during the HEX to HCP conversion. Later, the packing fraction remains constant. Therefore, density precedes the order parameter fluctuations.

The second cluster is shown in the figure 7.15(b). Initially, the values of $\bar{q_4}$ and $\bar{q_6}$ increase in a manner similar to the packing fraction. After approximately 150 minutes, there is a significant rise in both q4, q6, and the density of the cluster. This indicates the formation of a more ordered and densely packed cluster. Towards the end, the packing fraction remains constant while the values of $\bar{q_4}$ and $\bar{q_6}$ decrease. For $\bar{w_4}$, there is a switch from a negative to a positive value, indicating a structural transformation from HEX to HCP as time progresses. Regarding $\bar{w_6}$, the values change from positive to negative and stay negative later on. However, towards the end, $\bar{w_6}$ switches back to negative, as more and more particles accumulate and the system changes from HCP to HEX. Initially, density and $\bar{q_4}$ and q6 go hand in hand, but $\bar{w_4}$ and $\bar{w_6}$ fluctuate.

The third cluster is shown in the figure 7.15(c). In the beginning, both the values of $\bar{q_4}$ and $\bar{q_6}$, and $\bar{w_4}$ begin to increase in a way that is similar to the packing fraction. This gradual increase suggests that an ordered structure is forming as time passes. On the other hand, the value of $\bar{w_6}$ decreases as time progresses. However, towards the end, the positive value of $\bar{w_4}$ changes to negative, indicating that the stable hcp cluster has converted to a HEX structure due to an increase in the number of particles. This example clearly demonstrates a positive correlation between the density and order parameters, $\bar{q_4}$, $\bar{q_6}$, and $\bar{w_4}$.

7.7.4 0.5332

The three slowest clusters for the volume fraction of 0.5332 corresponds to $\alpha=$ 0.6712 is shown in the figure 7.16.

The first slowest cluster is represented in the figure7.16(a). Initially, $\bar{q_4}$ and $\bar{q_6}$ values fluctuate. After 200 minutes, the $\bar{q_4}$ and $\bar{q_6}$ values increase, indicating a highly ordered structure. However, the $\bar{q_4}$ and $\bar{q_6}$ values decrease towards the end, suggesting less ordering. In the meantime, $\bar{w_4}$ and $\bar{w_6}$ values begin increasing from the start. Both values start at negative, move to positive, and stabilize in the same state. As time passes, $\bar{w_4}$ maintains a positive value, whereas $\bar{w_6}$ switches back to negative. These changes are primarily responsible for the stable cluster transformation from HEX to HCP. Regarding the packing fraction, the values remain stable initially but drastically increase during HEX to HCP conversion. This is an example where density stabilizes first while the order parameter fluctuates.

The second slowest cluster is represented in the figure7.16(b). In this case, both $\bar{q_4}$ and q6 values fluctuate from the beginning. Meanwhile, $\bar{w_4}$ and $\bar{w_6}$ values switch multiple times from positive to negative. At a later stage, they continue to stay negative. Initially, the density of the cluster is low, but it slowly increases until it reaches maximum after around 300 minutes. The multiple switch-overs of $\bar{w_4}$ value indicate an orderly arrangement of particles, but later, the increase in particle density leads to a less order structure. This is an example of density preceding the order parameter.

The third slowest cluster is represented in the figure7.16(c). In this case, both the $\bar{q_4}$ and $\bar{q_6}$ values fluctuate from the beginning but later start to decrease.

Meanwhile, the $\bar{w}_4$ and $\bar{w}_6$ values switch multiple times from positive to negative. At a later stage, they continue to stay negative. Initially, the density of the cluster is low, but it slowly increases until it reaches its maximum after around 250 minutes. The multiple switch-overs of the $\bar{w}_4$ value indicate an orderly arrangement of particles, but later, the increase in particle density leads to a less ordered structure. This is also an example of density preceding the order parameter, meaning that an increase in density can lead to a decrease in order.

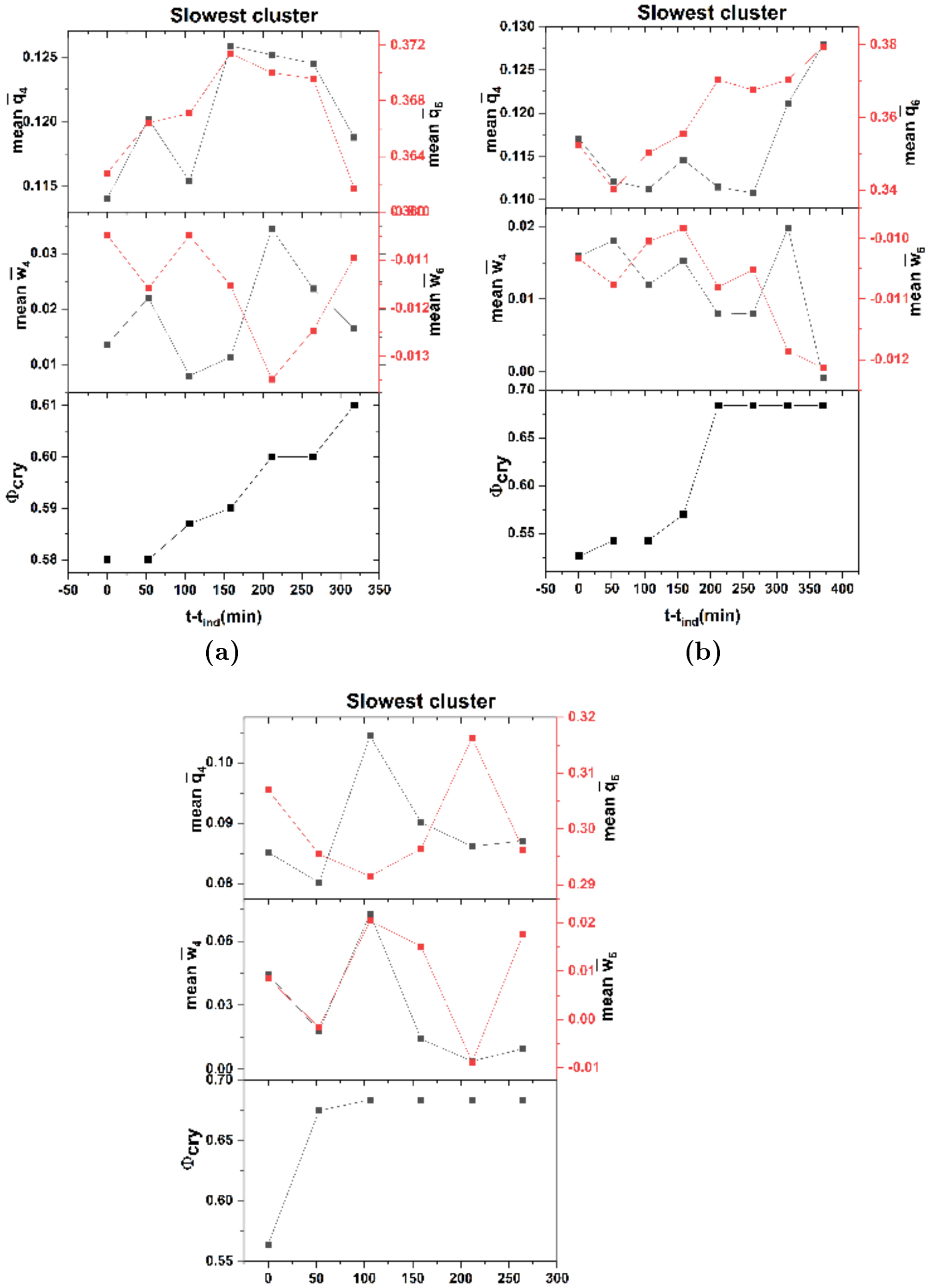

(a) (b) (c)

Figure 7.13: Comparison of mean bond order parameter, mean $\bar{q}_4$, $\bar{q}_6$, $\bar{w}_4$, $\bar{w}_6$ and Φ_{cry} for one cluster in the effective volume fraction 0.544 corresponds to α= 0.78313 is shown. The parameters mean $\bar{q}_4$, $\bar{q}_6$ are given at the top. In the middle $\bar{w}_4$, $\bar{w}_6$ and at the bottom, Φ_{cry} is given. All parameters are shown here concerning changes that appear in time(t-t_{ind})

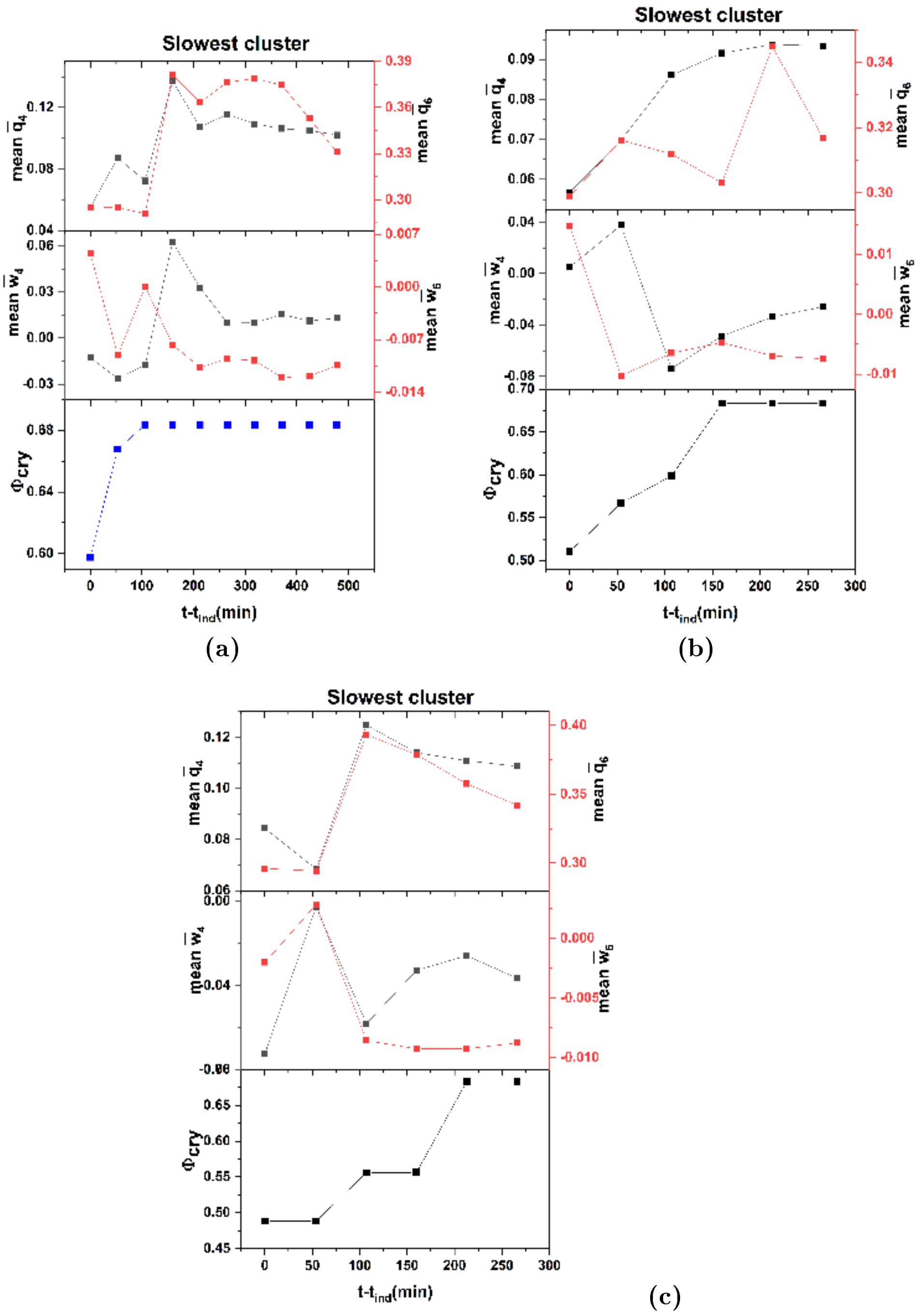

(a)

(b)

(c)

Figure 7.14: Comparison of mean bond order parameter, mean $\bar{q}_4$, $\bar{q}_6$, $\bar{w}_4$, $\bar{w}_6$ and Φ_{cry} for three different cluster for the effective volume fraction 0.5389 corresponds to α= 0.7566 is shown. The parameters mean $\bar{q}_4$, $\bar{q}_6$ are given at the top. In the middle $\bar{w}_4$, $\bar{w}_6$ and at the bottom, Φ_{cry} is given. All parameters are shown here concerning changes that appear in time(t-t_{ind})

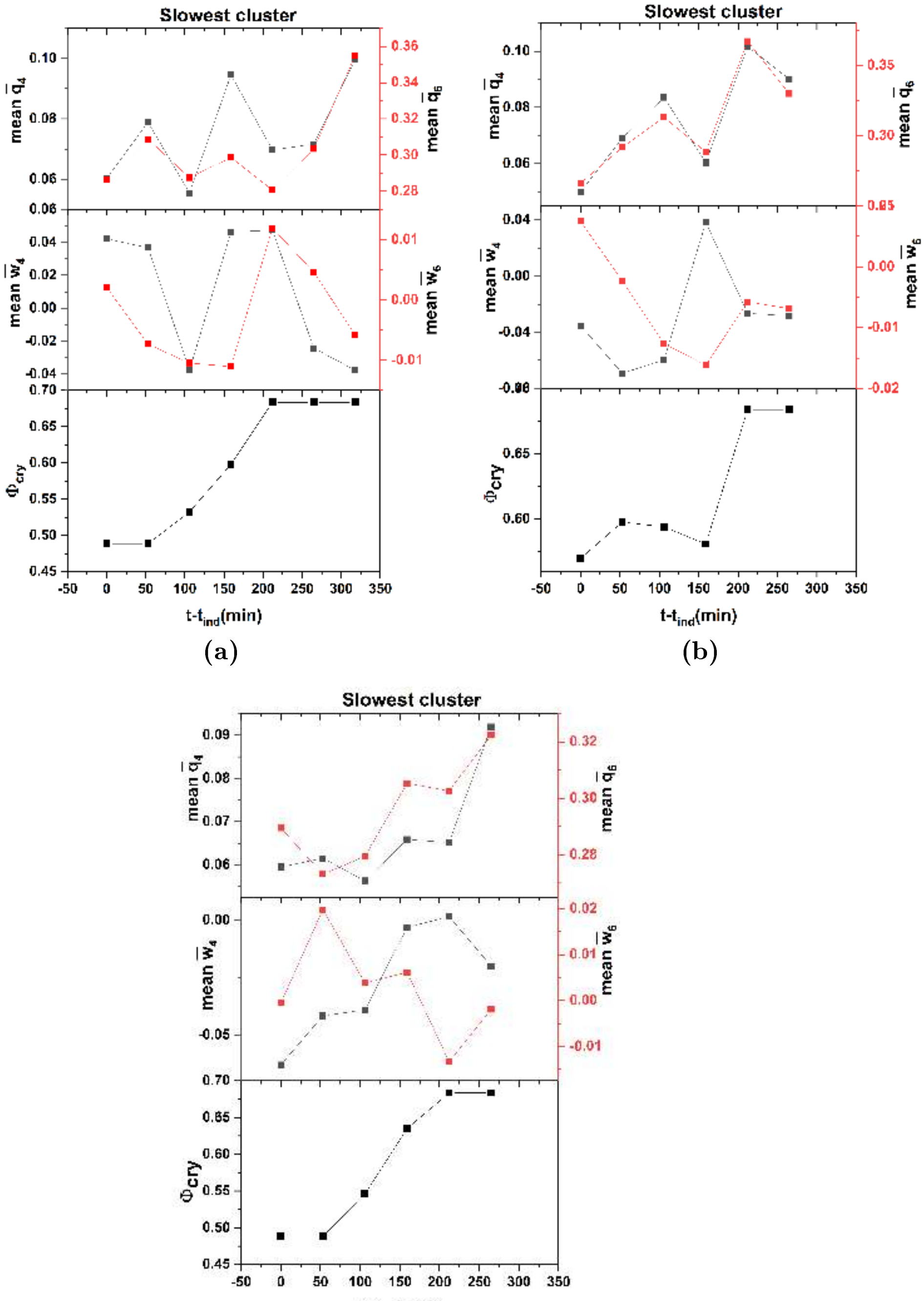

(a)

(b)

(c)

Figure 7.15: Comparison of mean bond order parameter, mean $\bar{q}_4$, $\bar{q}_6$, $\bar{w}_4$, $\bar{w}_6$ and Φ_{cry} for three different cluster for the effective volume fraction 0.536 corresponds to α= 0.6875 is shown. The parameters mean $\bar{q}_4$, $\bar{q}_6$ are given at the top. In the middle $\bar{w}_4$, $\bar{w}_6$ and at the bottom, Φ_{cry} is given. All parameters are shown here concerning changes that appear in time(t-t_{ind})

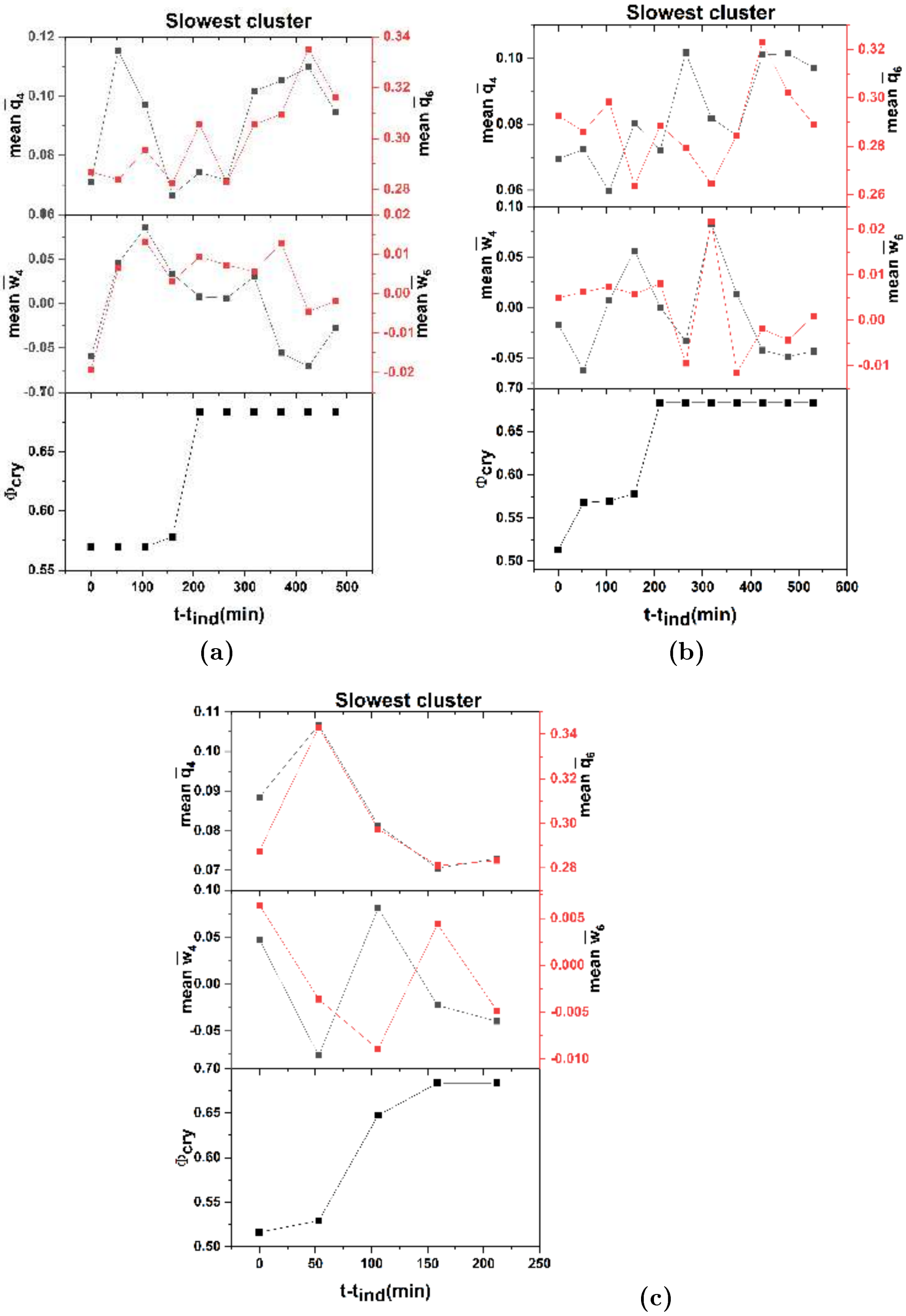

(a) (b)

(c)

Figure 7.16: Comparison of mean bond order parameter, mean $\bar{q}_4$, $\bar{q}_6$, $\bar{w}_4$, $\bar{w}_6$ and Φ_{cry} three different cluster for the effective volume fraction 0.5332 corresponds to α= 0.6712 is shown. The parameters mean $\bar{q}_4$, $\bar{q}_6$ are given at the top. In the middle $\bar{w}_4$, $\bar{w}_6$ and at the bottom, Φ_{cry} is given. All parameters are shown here concerning changes that appear in time(t-t_{ind})

7.8 The interplay between density and bond order parameter for "Biggest" clusters

The cluster used in this analysis has a 'highest' number of particles at the end. Hence the name "Biggest" cluster. This type of cluster may helps in analyzing the variation of parameters more clearly. One can analyze the trends in volume fraction and orientation order to determine the sequence of events. If the increase in volume fraction precedes the increase in orientation order, it suggests that more particles are initially entering the system, followed by their alignment. If the trends co-occur, it implies a more synchronized relationship between changes in volume fraction and orientation order. If orientation order increases first, followed by an increase in volume fraction, it could indicate that particles align before an overall increase in volume fraction.

7.8.1 0.544

The three biggest clusters for the volume fraction of 0.544 corresponds to $\alpha=$ 0.78313 is shown in the figure 7.17.

The first biggest cluster shown in the figure 7.17(a). Initially, in this case, both the $\bar{q_4}$ and $\bar{q_6}$ values, and the packing fraction increase. After around 100 minutes, the density reaches its maximum value, but $\bar{q_4}$ and $\bar{q_6}$ decrease. $\bar{w_4}$ values stay positive initially, but later switch to negative and remain negative thereafter. These values do not clearly indicate the formation of a cluster type. As $\bar{q_6}$ values decrease, the particles start to accumulate more but with less order state. This is an example where the density precedes the order parameter during crystallization.

The second biggest cluster shown in the figure 7.17(b). In this case, the cluster starts with a high density and stays the same throughout the process. Initially, $\bar{q_4}$ has a high value but later starts to decrease, while $\bar{q_6}$ shows a dip in the middle but later increases. The increase in $\bar{q_6}$ value indicates a more orderly arrangement. $\bar{w_4}$ values increase from negative to positive and remain positive, whereas $\bar{w_6}$ remains positive throughout. The $\bar{w_4}$ value indicates the transformation of HEX to HCP. This is an example where density remains constant while the order parameter fluctuates. There is no correlation between density and order parameter.

The third biggest cluster shown in the figure 7.17(c).In this scenario, the packing fraction remains constant throughout the process. However, the values of $\bar{q_4}$ and $\bar{q_6}$ increase from the beginning and reach their maximum at the end. Regarding $\bar{w_4}$, the value stays positive throughout, indicating that the initial structure remains the same throughout the process. On the other hand, the value of w6 stays negative all the time. This is an example where the initial HCP structure continues to grow with a high packing fraction and a more orderly arrangement. In this particular case, the density has no relation to the order parameter.

7.8.2 0.5389

The three biggest clusters for the volume fraction of 0.5389 corresponds to $\alpha=$ 0.7566 is shown in the figure 7.18.

The first biggest cluster shown in the figure 7.18(a). In this scenario, the values of $\bar{q_4}$, $\bar{q_6}$ and packing fraction are interdependent. Initially, $\bar{w_4}$ and $\bar{w_6}$ have high positive values, but later they change to negative and remain negative throughout. The cluster starts with a high value of $\bar{q_6}$ and $\bar{w_4}$, indicating a stable phase. As time progresses, particles accumulate in an orderly arrangement. However, no perfect cluster type is observed. In this case, density plays a more crucial role than the order parameter.

The second biggest cluster shown in the figure 7.18(b). In this scenario, the values of $\bar{q_4}$, $\bar{q_6}$, and packing fraction are interdependent. $\bar{q_4}$ and $\bar{q_6}$ values slowly increases and stabilizes later. Initially, $\bar{w_4}$ and $\bar{w_6}$ have positive values, but later, these change to negative. Later on, $\bar{w_4}$ switches back to a positive value and remains the same thereafter. The values of $\bar{w_6}$ change from negative to positive and remain constant later on. The density of the cluster slowly increases and later stabilizes. In this example, both the density and order parameter $\bar{q_4}$ and $\bar{q_6}$ go hand in hand.

The third biggest cluster shown in the figure 7.18(c). Initially, the values of $\bar{q_4}$, $\bar{q_6}$, and packing fraction are closely related. As time progresses, $\bar{q_4}$ and $\bar{q_6}$ increase and reach their maximum at around 100 minutes before decreasing again. The values of $\bar{w_4}$ change from negative to positive and remain constant throughout, while the values of $\bar{w_6}$ change from negative to positive. These changes indicate the stable formation of a cluster. At first, there is a positive correlation between the packing fraction and the $\bar{q_4}$ and $\bar{q_6}$ values. Later, the density stabilizes while the order parameter fluctuates.

7.8.3 0.536

The three biggest clusters for the volume fraction of 0.536 corresponds to $\alpha=$ 0.6875 is shown in the figure 7.19.

The first biggest cluster shown in the figure 7.19(a). In this scenario, the values of $\bar{q_4}$ and $\bar{q_6}$ both increase with time, while the values of $\bar{w_4}$ and $\bar{w_6}$ start with a positive value and then change to a negative value. The packing fraction initially starts with a low value and later drastically increases, stabilizing further. In this case, packing fraction of cluster precedes the order parameter.

The second biggest cluster shown in the figure 7.19(b). In this case, both $\bar{q_4}$ and $\bar{q_6}$ increase over time and eventually stabilize. Meanwhile, $\bar{w_4}$ and $\bar{w_6}$ start off with a positive value but transition to a negative value afterwards. The packing fraction begins high and remains constant throughout. Density stabilizes first, followed by fluctuations in the order parameter that later stabilizes.

The third biggest cluster shown in the figure 7.19(c). Similar to the previous case, both q4 and q6 increase over time and eventually stabilize. Meanwhile, w4 and w6 start with a positive value but transition to a negative value afterward. However, in this case, the packing fraction starts with a low value and increases thereafter, reaching a constant value throughout. In this scenario, Density stabilizes first, followed by fluctuations in the order parameter that later stabilizes.

7.8.4 0.5332

The three biggest clusters for the volume fraction of 0.5332 corresponds to $\alpha=$ 0.6712 is shown in the figure 7.20.

The first biggest cluster shown in the figure 7.20(a). In this scenario, the values of $\bar{q}_4$ and $\bar{q}_6$ increase from the beginning and then stabilize around 100 minutes. In the case of $\bar{w}_4$, it switches from positive to negative initially and later remains in the same state, whereas w6 stays positive and then shifts to negative at the end. These changes in the values of $\bar{w}_4$ and $\bar{w}_6$ suggest a switch over of different cluster types. The packing fraction starts initially low and then drastically increases and stabilizes later on. Here, we can see that the density dominates first, while $\bar{q}_4$, $\bar{q}_6$, and $\bar{w}_4$, $\bar{w}_6$ fluctuate initially and then stabilize later.

The second biggest cluster shown in the figure 7.20(b). In this scenario, the values of $\bar{q}_4$ and $\bar{q}_6$ increase steadily from the beginning until the end. However, the value of $\bar{w}_4$ remains negative throughout, while the value of $\bar{w}_6$ switches from positive to negative and then back to positive later on. The packing fraction also starts with a high value, increases quickly, and then stabilizes over time. In this scenario, the packing fraction has a dominant effect, while the order parameter still varies.

The third biggest cluster shown in the figure 7.20(c). In this scenario, the $\bar{q}_4$ values initially decrease and then slightly increase, while the $\bar{q}_6$ values remain almost constant. For $\bar{w}_4$, the value changes from negative to positive, indicating structural changes, and then switches back to negative. On the other hand, $\bar{w}_6$ shows a change from negative to positive and then remains the same. As time progresses, the density increases and stabilizes.

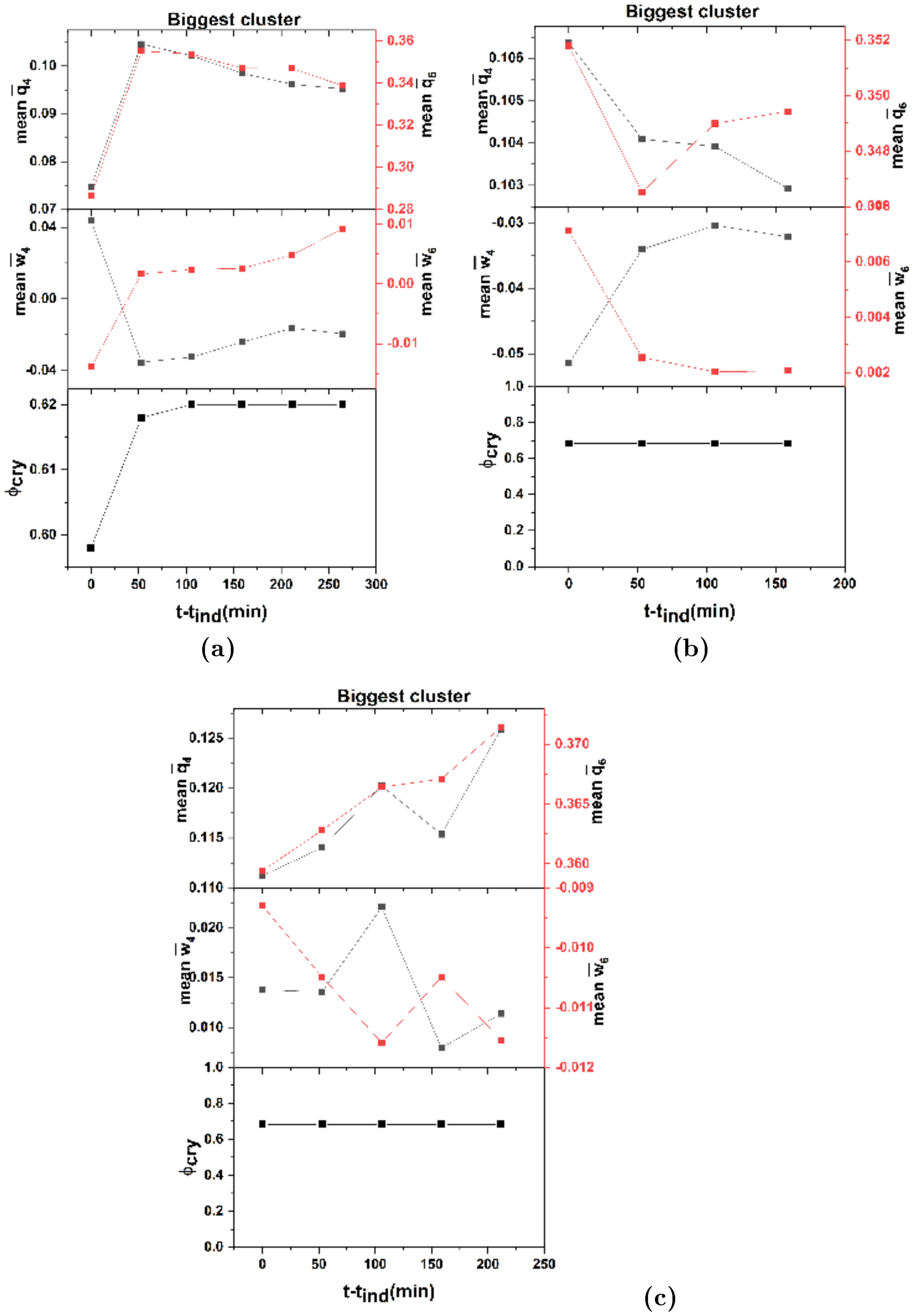

Figure 7.17: Comparison of mean bond order parameter, mean $\bar{q}_4$, $\bar{q}_6$, $\bar{w}_4$, $\bar{w}_6$ and Φ_{cry} for three different cluster for the effective volume fraction 0.544 corresponds to α= 0.78313 is shown. The parameters mean $\bar{q}_4$, $\bar{q}_6$ are given at the top. In the middle $\bar{w}_4$, $\bar{w}_6$ and at the bottom, Φ_{cry} is given. All parameters are shown here concerning changes that appear in time(t-t_{ind})

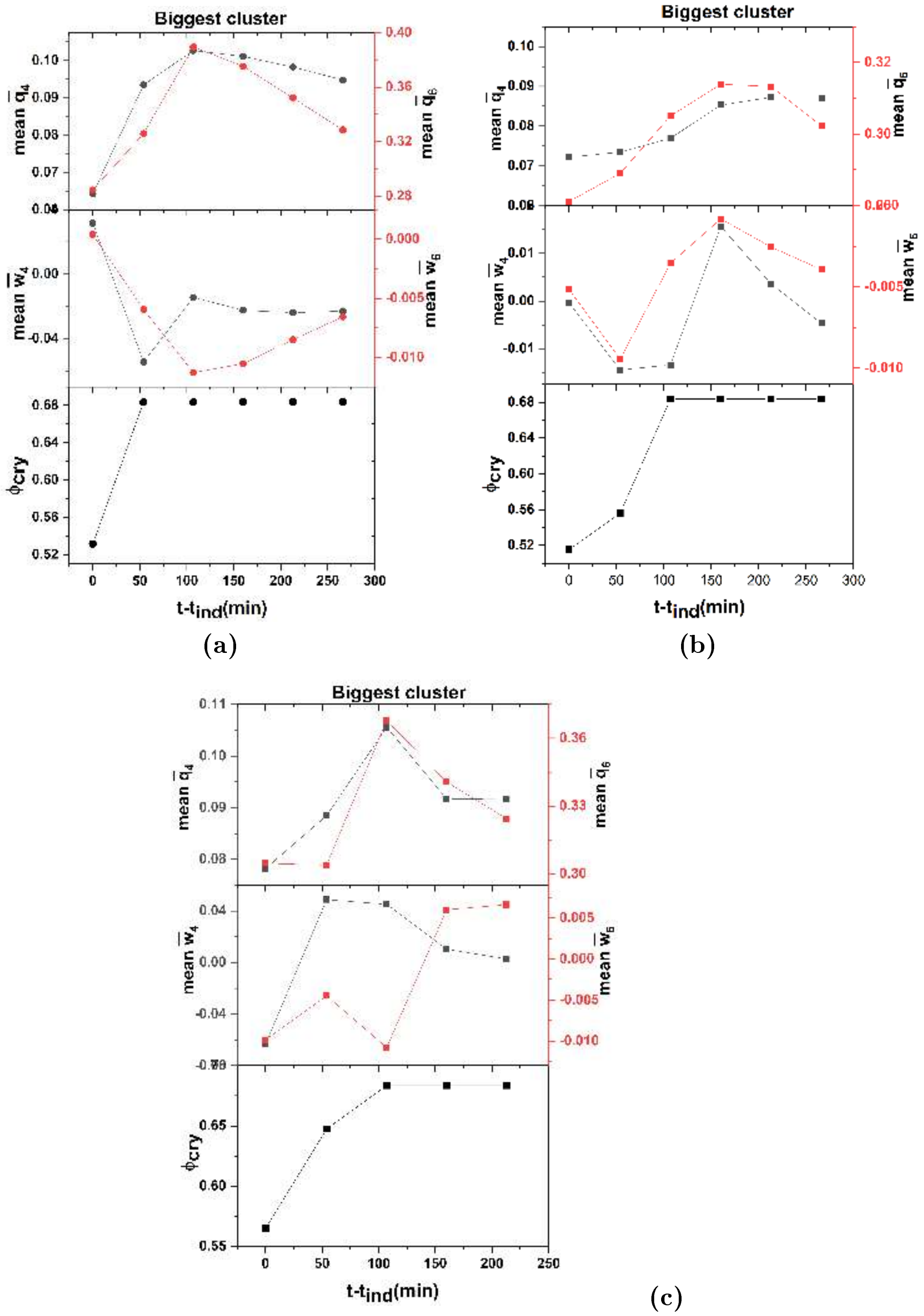

(a)

(b)

(c)

Figure 7.18: Comparison of mean bond order parameter, mean $\bar{q}_4$, $\bar{q}_6$, $\bar{w}_4$, $\bar{w}_6$ and Φ_{cry} for three different cluster for the effective volume fraction 0.5389 corresponds to α= 0.7566 is shown. The parameters mean $\bar{q}_4$, $\bar{q}_6$ are given at the top. In the middle $\bar{w}_4$, $\bar{w}_6$ and at the bottom, Φ_{cry} is given. All parameters are shown here concerning changes that appear in time(t-t_{ind})

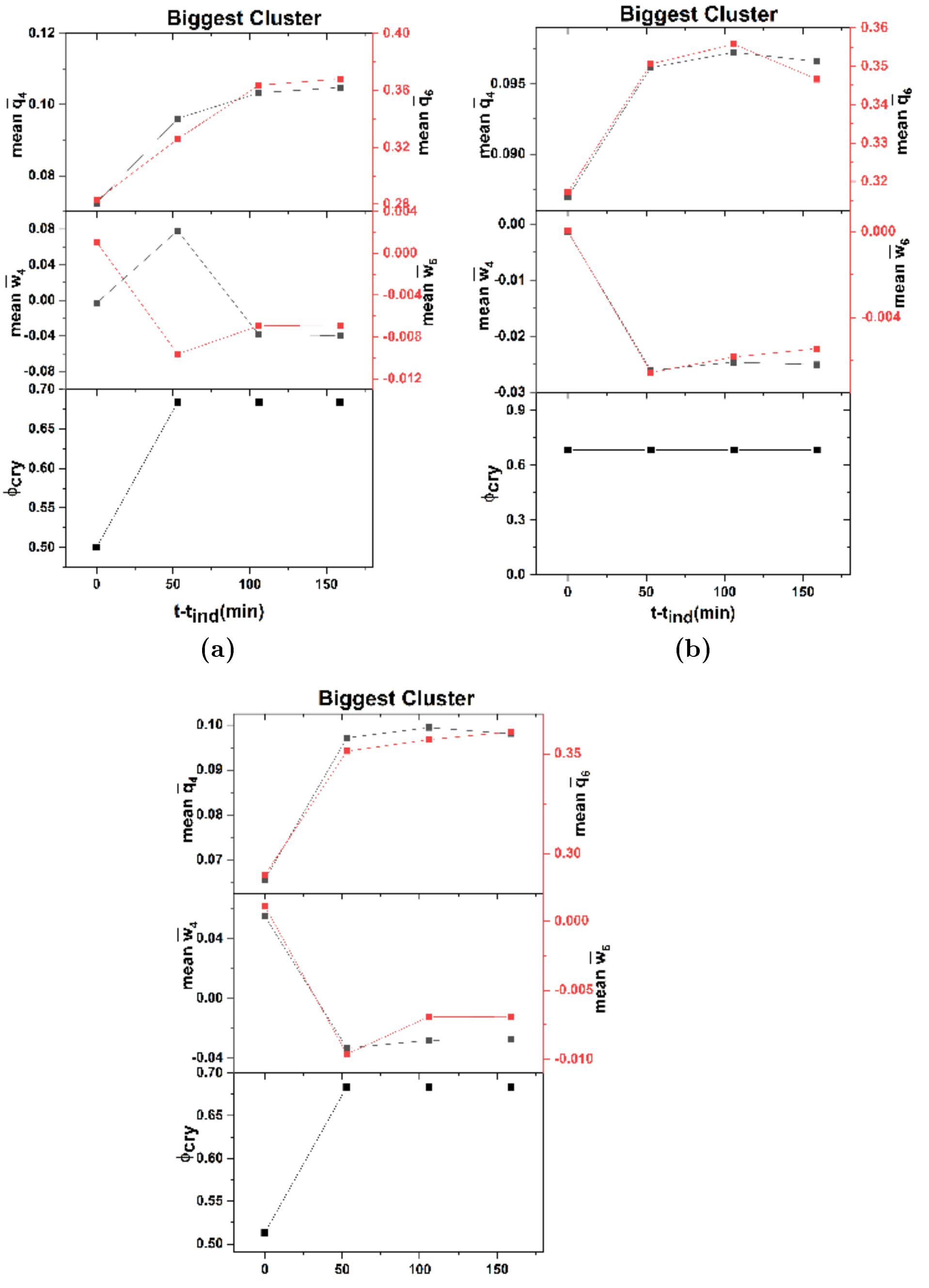

(a) (b)

(c)

Figure 7.19: Comparison of mean bond order parameter, mean $\bar{q}_4$, $\bar{q}_6$, $\bar{w}_4$, $\bar{w}_6$ and Φ_{cry} for three different cluster for the effective volume fraction 0.536 corresponds to $\alpha = 0.6875$ is shown. The parameters mean $\bar{q}_4$, $\bar{q}_6$ are given at the top. In the middle $\bar{w}_4$, $\bar{w}_6$ and at the bottom, Φ_{cry} is given. All parameters are shown here concerning changes that appear in time(t-t_{ind})

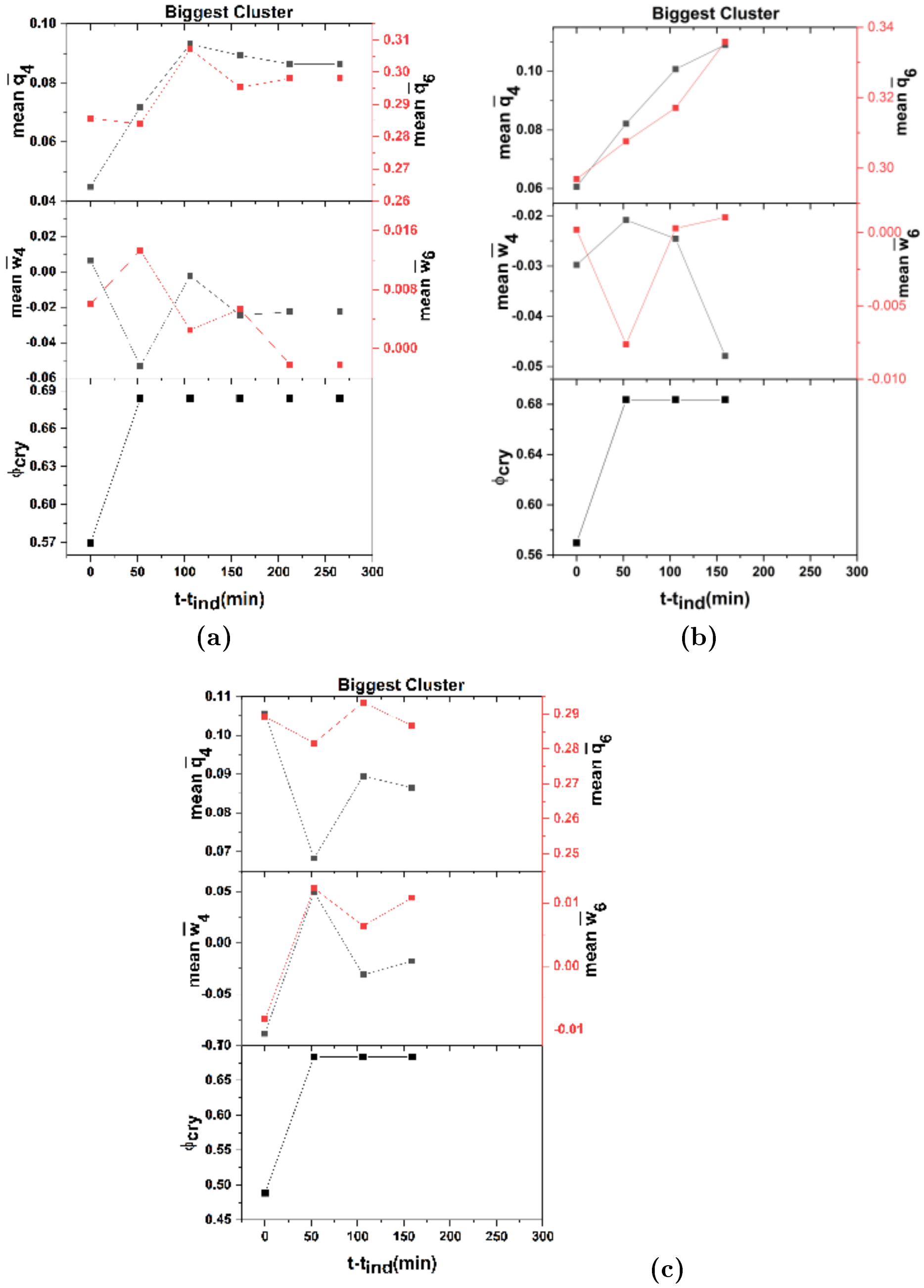

(a) (b)

(c)

Figure 7.20: Comparison of mean bond order parameter, mean $\bar{q}_4$, $\bar{q}_6$, $\bar{w}_4$, $\bar{w}_6$ and Φ_{cry} for three different cluster for the effective volume fraction 0.5332 corresponds to α= 0.6712 is shown. The parameters mean $\bar{q}_4$, $\bar{q}_6$ are given at the top. In the middle $\bar{w}_4$, $\bar{w}_6$ and at the bottom, Φ_{cry} is given. All parameters are shown here concerning changes that appear in time(t-t_{ind})

7.9 Conclusions

This chapter examines the crystallization kinetics by considering the density and bond order parameters and also analyzes the early stage of crystal nucleation by studying precursors. The research shows that densification and orientational ordering co-occur in the case of precursors. The birth of crystal nuclei from a liquid begins with crystalline precursors, regions of near crystalline bond order spontaneously formed in a supercooled liquid. The most stable precursor gradually becomes dominant while increasing its spatial coherence and lifetime. The conversion of precursor to solid is studied first by considering all growing clusters. In this case, densification occurs earlier than the improvement of crystalline structure. However, individual trajectories can also be considered to provide more insight into the evolution of crystalline structure. Therefore, slow-growing and biggest clusters are analyzed to shed light on the interplay between density and bond order parameters. Both cases show a large variety of pathways to the final crystalline structure. In some cases, it starts with highly compressed regions with low bond order; in others, it starts with high bond order but low volume fraction. In general, all possible ways can occur during the formation of crystalline structures. This study experimentally establishes a particle-level picture of the elementary kinetic pathway of colloidal crystallization. It provides new insights into the crystallization kinetics from a microscopic perspective. The basic physical scenario in this study may apply to crystallization in a wide range of systems

Chapter 8

Understanding the dynamics of the colloidal model system during Crystallization

8.1 Abstract

Measuring mean square displacement (MSD) during nucleation has emerged as a powerful technique for understanding the kinetics and dynamics of the nucleation process. MSD analysis provides information about the crystal nuclei's mobility, the nucleation's onset, and the crystal growth rate. This chapter summarizes results in MSD analysis during nucleation, with a focus on the rate of crystal growth. Overall, measuring mean square displacement during nucleation provides a valuable tool and has the potential to impact a wide range of fields, from materials science to biophysics. In our study, we have utilized confocal microscopy to gain insight into the dynamics of colloidal suspensions. By preparing a high-density colloidal suspension, we were able to track the movement of thousands of colloidal particles during Crystallization. Interestingly, we found that the motion of these particles slowed considerably. By processing movies acquired from confocal microscopy, we could extract the trajectories of the colloidal spheres undergoing Brownian motion. We then calculated a statistical quantity called the Mean Square Displacement (MSD) and related it to the material's mechanical properties. This chapter presents the initial findings of our measurements and discusses potential avenues for future analysis.

8.2 Introduction

Studying colloidal particles is a great way to explore various phenomena, from gravitational collapse [23] to two-dimensional Crystallization [83] [228] [46] and glass transition [188]. They are a well-suited model system [156] for understanding principles on all length scales. Understanding their dynamics is also essential for developing microscopic lab-on-a-chip devices [196] and devices for controlled drug release [224].

Mean square displacement (MSD) is a crucial parameter in studying colloidal systems, particularly those of hard spheres. Colloidal hard spheres are particles with negligible interactions except for excluded volume effects, making them a model system for understanding fundamental aspects of condensed matter physics. The MSD quantifies the average squared displacement of particles over time and is often used to probe diffusive behavior. It is a direct measure of particle mobility. Tracking individual particles over time can reveal changes in their diffusion behavior as the system undergoes Crystallization. This information is crucial for understanding how particle dynamics evolve during different stages of Crystallization. Changes in particle mobility and clustering can indicate the formation of nuclei, providing insights into the nucleation kinetics and mechanisms.

MSD measurements enable tracking individual particles as they contribute to crystal growth. Observing how the displacement of particles evolves provides information about the growth rate and the spatial distribution of crystals within the system. Different crystalline phases may exhibit distinct MSD profiles. By analyzing the MSD of particles during Crystallization, one may gain information about the types of crystals that form and their relative stability. According to a study published by Vekilov et al. (2004), analyzing the MSD data during the initial stages of nucleation can provide information about the critical size of the crystal nuclei, which is the minimum size required for a nucleus to grow into a stable crystal. The study found that the MSD data can be used to estimate the nuclei's critical size and predict the nucleation's onset. Moreover, the crystal growth rate during nucleation can also be determined by analyzing the slope of the MSD curve. According to a study published by Sear and Meldrum (2008), the MSD curve's slope reflects the particle movement rate within the crystal structure, which can be used to estimate the crystal growth rate. The study found that the MSD analysis can provide insight into the kinetics of nucleation and crystal growth. In addition, analyzing the MSD data during nucleation can provide information about the shape of the crystal nuclei. According to a study published by ten Wolde et al. (1997), the shape of the nuclei can influence the diffusion of the particles, which can be reflected in the MSD data. The study found that the MSD analysis can provide insight into the nuclei's shape and the particles' diffusion.

Numerous studies have investigated the dynamics of colloidal hard spheres, with experimental techniques such as dynamic light scattering and particle tracking providing valuable insights. Notable work by Pusey and van Megen (1986) and subsequent contributions by others have explored the dynamics of colloidal suspensions, including the behavior of MSD as a function of particle concentration, size, and temperature. The dynamics of colloidal hard spheres exhibit distinct regimes, transitioning from short-time ballistic motion to long-time diffusive behavior. The Einstein-Stokes relation, linking diffusion coefficient to particle size, is often validated through MSD analysis in these systems. As reviewed by Royall and Williams (2015), recent advancements have extended our understanding of colloidal dynamics, shedding light on phenomena such as caging effects and non-Gaussian behavior in MSD curves. In conclusion, the mean square displacement on colloidal hard spheres serves as a critical metric for unraveling the dynamic behavior of these model systems. Its analysis, informed by experimental and theoretical studies, contributes to our broader understanding of colloidal science and condensed matter physics.

Nucleation studies using techniques like microscopy, X-ray diffraction, or spectroscopy provide data that can be analyzed through MSD to reveal information about the nucleation rate, critical nucleus size, and growth kinetics. Research by Kelton and Greer (2010) emphasizes the importance of understanding nucleation in materials science. The application of MSD in nucleation studies allows researchers to identify different stages of nucleation, from the initial formation of clusters to the subsequent growth or dissolution of these clusters. Furthermore, recent work by Auer and Frenkel (2001) demonstrates the use of computer simulations to investigate nucleation events. It emphasizes the role of MSD in characterizing the dynamics of particles during phase transitions. Analyzing the MSD during nucleation provides quantitative measures of particle mobility, revealing information about the nucleation pathways and the influence of external factors such as temperature, pressure, or concentration. In summary, measuring MSD during nucleation experiments offers a powerful tool for unraveling the kinetics and mechanisms involved in phase transitions. This information is essential for understanding nucleation processes in diverse scientific disciplines.

The simplest quantity that characterizes the motion of a single Brownian particle is its mean square displacement defined as $< \Delta r^2(t) >$

$$< \Delta r^2(t) >=< |r(t) - r(t=0)|^2> \qquad (8.1)$$

where r(t) is the position coordinate of the Brownian particle at time t»τ_B. The mean square displacement varies linearly with time. For times much smaller than the âĂIJBrownianâĂİ relaxation time τ_B, friction with the solvent is inefficient, so the velocity of a colloidal sphere is essentially constant.

Further details on Diffusion is given in Chapter 1 including short time and long time regime.

Inspection of different supposedly diffusive processes, such as the Brownian motion in an inhomogeneous medium [54], reveals that the previous framework is not always fulfilled. Instead, the mean square displacement deviates from the linear temporal evolution. One of the most common anomalous behaviors is given by

$$\lim_{t\to\infty} \langle r^2 \rangle \sim t^{\beta} \qquad (8.2)$$

where $\beta \neq 1$ is a real positive number [130] [135] [54] [134]

The origin of this discrepancy is the tacit assumption that the Brownian particle moves in an infinite structureless medium acting as a heat bath. This assumption is generally incorrect when the Brownian motion occurs in a complex medium. We illustrate in Figure 8.1, the mean square displacement $\langle x^2(t) \rangle$ as a function of t for three distinct Brownian motions in one dimension. From the upper curve downwards, we have $\beta = 1.5$ (superdiffusion), $\beta = 1$ (normal diffusion), and $\beta = 0.5$ (subdiffusion).

In the case of hard spheres, which are non-interacting spheres that collide elastically, free diffusion implies that the particles move independently without any significant influence from each other or their surroundings. Free diffusion of hard spheres assumes that collisions are purely elastic, with no attractive or repulsive forces between the particles. As a result, each particle's motion is solely determined by its kinetic energy and the collisions with other particles. This

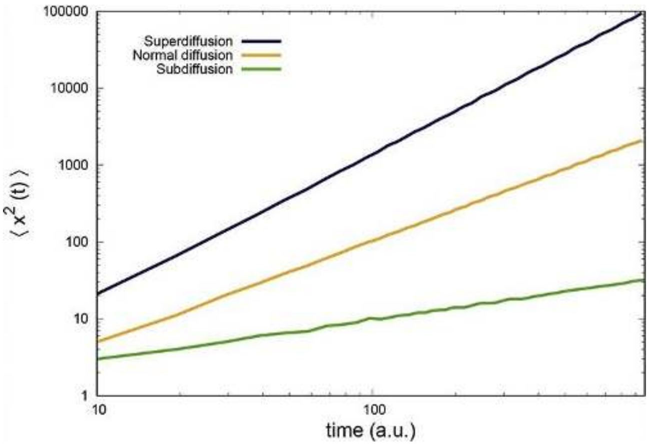

Figure 8.1: Time evolution of the mean square displacement (in arbitrary units) for normal and anomalous diffusion. For the upper curve, β=1.5 (super-diffusion); for the middle curve, $\beta = 1$ (normal diffusion); and for the lower curve, $\beta = 0.5$ (subdiffusion) [141].

leads to a random and unbiased distribution of particles over time, promoting equalization of concentration throughout the system.

Sub-diffusion refers to a slower-than-expected rate of particle movement compared to classical diffusion. This deviation from normal diffusion behavior can arise from constraints or hindrances imposed on particle motion within the system. In a hard sphere system, where particles are non-interacting, and collisions are elastic, sub-diffusion can be attributed to various factors. One significant factor is the presence of obstacles or crowding within the system, leading to a more tortuous and constrained path for particle movement. Unlike free diffusion, where particles move independently, sub-diffusion involves particles experiencing hindered motion due to restricted pathways and interactions with neighboring particles. This behavior may be modeled using mathematical equations that reflect the sub-diffusive nature of the particle trajectories. Common sub-diffusion models include fractional diffusion equations or anomalous diffusion models, which introduce parameters for deviation from standard diffusion behavior.

Caging behavior refers to a particle's temporary immobilization or confinement due to its interactions with neighboring particles. In a system of hard spheres, the particles do not experience attractive forces but repel each other when they come into contact. The repulsion arises from the exclusion principle, preventing particles from overlapping or occupying the same space. When a hard sphere collides with its neighboring spheres, it experiences a repulsive force that can result in a temporary trapping effect. The surrounding spheres create a cage-like structure, restricting the movement of the central particle within a confined space for a specific duration. This caging effect is dynamic, with particles continuously interacting, leading to a series of temporary traps and releases. Caging behavior significantly influences the diffusion and dynamics of hard spheres in a colloidal system. The temporary confinement slows the overall particle movement, contributing to sub-diffusive behavior. The mean square displacement of particles exhibits non-linear relationships with time due to these dynamic trapping and releasing events.

8.3 Experimental system

For our study, we utilized poly(methyl methacrylate) (PMMA) spheres that were sterically stabilized by chemically grafting poly(12-hydroxy stearic acid (PHSA)) about 20nm onto their surface. These particles were stained with fluorescent dye DilC18 and had a diameter of 1.4µm with a polydispersity of 5.6%. We immersed these particles in a mixture of cis-decalin and TCE. This solvent was chosen as it simultaneously matched the particle index of refraction and density, which helped mitigate the effects of scattering and sedimentation.

8.4 Data acquisition

The data was collected 40 µm above the wall, and the image size was 82x82x3µm^3. During the crystallization measurements, we captured 3D images with a time resolution of 6 seconds over 3 minutes just after each time step. The position of each particle within the optical plane was obtained using standard particle techniques as described in [39]. In order to analyze the dynamics of a data set, we break it down into smaller temporal portions and calculate the mean square displacement (MSD) $< r^2 >$ for each portion. The angle brackets signify that the average is taken over all particles and all initial times within each temporal portion. This approach allows us to obtain a more detailed understanding of the movement of the particles and their interactions with the solvent molecules.

8.5 Results

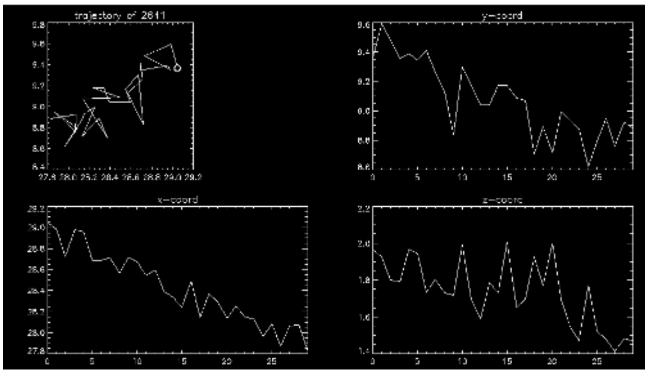

Figure 8.2: A typical trajectory for 30 sec for a single particle. The particle was tracked in 3D; the 2D projection is shown. You can see in this case that as the particle makes a jump in the X coordinate, it is also moving in Z (bottom right graph), and after the jump in X is finished, the particle continues to move slowly in Z for a longer time.

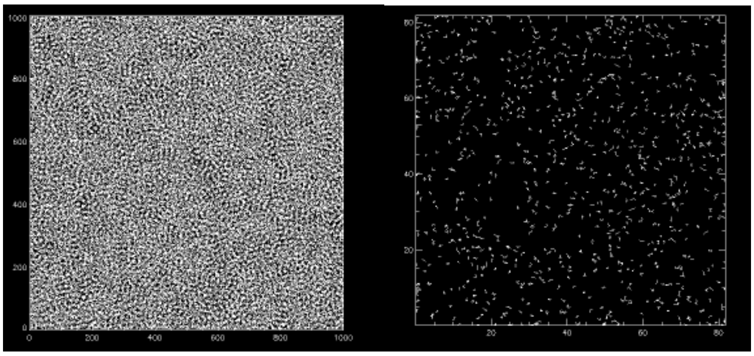

(a) (b)

Figure 8.3: (a)The trajectories of all particles were tracked for 3 minutes. (b) A typical trajectory for 30 seconds for a portion of particles from the previous picture. The particle was tracked in 3D; the 2D projection is shown. The figure is the projection of the particles found onto the XY plane. Some particles that look close together are probably far apart in Z. As one can see, particles are not moving much.

Particle Tracking is a powerful technique that enables the simultaneous tracking of multiple micron-sized particles using video microscopy. To extract the individual trajectories of the particles undergoing Brownian motion, one can record video microscopy movies and utilize the image processing software available on the website "Particle tracking using IDL". Also, please keep in mind that some particles may move out of focus, which will end their tracking, and they may come back into focus, which will initiate a new trajectory, even if it is potentially the same particle. The multiple particle tracking technique's output is trajectories 8.2, commonly 2D for 2D measured files and 3D for 3D dimensional measurements. The method used to identify and track those identified particles is explained in Chapter 3.

It is important to consider several key points to use the procedure described on the website effectively [38]. During pre-tracking, which involves detecting and locating particles in each frame, the software performs noise discrimination by selecting valid detections based on the morphology of the identified features. This is done using the provided procedures: polycut.pro or eclip.pro. It is worth noting that the radius and integrated mass of the brightness profile exhibit specific variations with the altitude of the particles in the volume of observation of the microscope, so paying attention to these variations is crucial for accurate pre-tracking. Clipping the radius and integrated mass parameters during pre-tracking requires careful consideration of the depth of tracking in the experimental setup. For more detailed information on this aspect, refer to the article by Savin and Doyle (2008). Once particle positions are detected, the track.pro procedure is used to form trajectories. It is important to note that the msd.pro procedure can be slow if there are many short trajectories. To address this, the "Goodenough" parameter in track.pro can be used to set the minimum trajectory duration in the tracked array. However, selecting this value too high can result in the loss of essential trajectories. Moreover, the track.pro procedure provides the number of particles in the tracking volume as a function of time, with a vector containing as many elements as the time steps of the tracked array. However, note that particles detected in the first frame and disappearing within Goodenough frames will not appear in the tracked array. Finally, the MSD is calculated in each direction using the msd.pro procedure on the tracked data.

8.6 MSD during nucleation

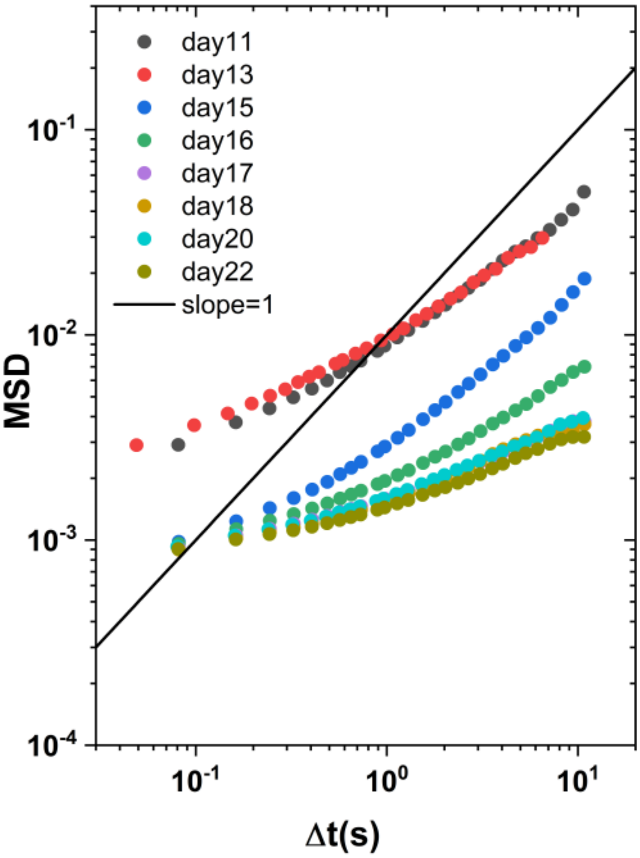

Figure 8.4: MSD for effective volume fraction of 0.529, corresponding to alpha = 0.5 during the crystallization measurements. Different color represnts data from different days. Slope of 1 is given by a thick line.

MSD data is shown figure 8.4 for phi = 0.53, corresponding to α= 0.5. The MSD measurement was done daily until crystallization was finished. As one can see, the MSD also decreases as the day proceeds. For reference, a slope of 1 is also shown in the figure. The slope from logarithmic MSD(β) is calculated, and corresponding crystallinity is also determined using the coarse grain method. Figure 8.5 shows the variation of slope and corresponding crystallinity over different days. The crystal volume fraction is calculated from Voronoi volume, as explained in the earlier Chapter.

8.6.1 Free diffusion (Before crystallization)

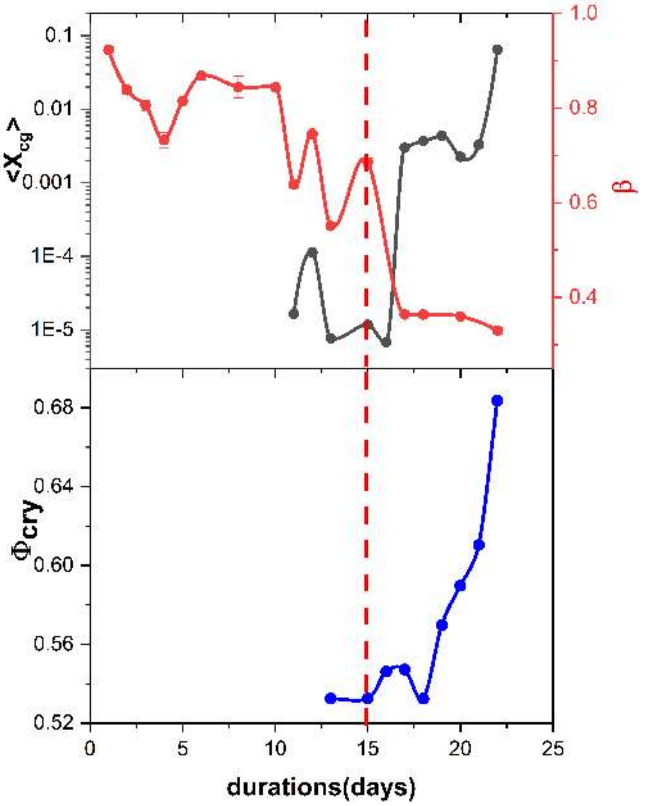

Figure 8.5: The slope from MSD for various measurement days is given and represented in terms of hours. Corresponding crystallinity is given. The thick dotted line corresponds to the induction time, where Crystallization sets in. For clarity, data is joined by splines.

The mean square displacement (MSD) slope measures the rate at which particles diffuse over time. Before crystallization (t<15), the gradual decrease in slope indicates a reduction in particle mobility, possibly due to increasing interactions among hard spheres. At t=15, the abrupt change in slope suggests a significant shift in the system's behavior, coinciding with the onset of crystallization. The decreasing slope suggests typical behavior seen in free diffusion, where particles move relatively freely and exhibit a decrease in mean square displacement over time. The gradual decline in slope indicates a gradual reduction in particle mobility as the system evolves.

8.6.2 Sub-diffusion (After crystallization at t=15)

The abrupt change in slope at t=15 signifies a shift in particle dynamics. After crystallization, the slope reduction may indicate sub-diffusion behavior, often occurring in constrained environments or when particles are hindered in movement. Crystallization introduces an ordered structure, impacting particle dynamics. After t=15, the continued decrease in slope suggests reduced particle mobility, possibly indicating sub-diffusion behavior. In sub-diffusion, particles may experience constraints or obstacles in their movement, leading to a slower decrease in mean square displacement than free diffusion. The ordered arrangement of particles in the crystal restricts their freedom of movement, resulting in a more gradual reduction in displacement.

The data indicates a transition from free diffusion to potentially sub-diffusion behavior after crystallization sets in. Before crystallization, the decreasing slope signifies a diminishing trend in particle mobility. After crystallization, the sustained slope reduction suggests an ordered structure's influence, possibly leading to sub-diffusion as particles navigate the constraints imposed by the crystal lattice. In summary, the dynamics analysis captures the nuanced changes in particle dynamics over time, reflecting the influence of hard sphere interactions, free diffusion, and the impact of crystallization on the system's behavior. The change in slope serves as an indicator of the evolving particle dynamics in the system.

8.7 Conclusions

Understanding nucleation processes is crucial in various scientific fields, and measuring Mean Square Displacement (MSD) plays a significant role in probing the dynamics of nucleation events. Nucleation involves forming new phases or structures, and studying MSD provides valuable insights into the kinetics and mechanisms involved. The MSD during nucleation experiments is often analyzed to characterize the mobility of particles undergoing phase transitions. The MSD measurement is done for various volume fractions, and analysis of these data provides more information on nucleation dynamics. In colloidal systems undergoing crystallization, sub-diffusion behavior, and caging play distinctive roles in capturing the dynamics of particles as they transition into an ordered, crystalline structure. The temporary traps arising from the evolving crystalline structure lead to sub-diffusive behavior as particles encounter hindrances in their movement. Caging involves the temporary confinement or immobilization of particles within local regions due to interactions with neighboring particles. As the colloidal system progresses towards crystallization, the surrounding ones can temporarily cage the approaching particles. Caging events can hinder the migration of particles, promoting the assembly of ordered structures and contributing to the nucleation and growth of crystals. In summary, during crystallization in a colloidal system, sub-diffusion behavior arises due to the constrained movement of particles within the evolving crystalline lattice. Caging events, where neighboring ones temporarily confine particles, play a pivotal role in promoting the assembly of ordered structures during this phase transition. The dynamic interplay between sub-diffusion and caging provides insights into the intricate processes in colloidal systems undergoing crystallization.

Our studies shed light on the crystallinity and dynamics involved during Crystallization. These data can infer that the particles are transitioning from a disordered state to an ordered state. This increase in slope reflects the increase in particle movement and diffusion as the particles rearrange themselves into more ordered configurations. This process is known as the pre-nucleation stage and is characterized by fluctuations in the density and structure of the particles.

Chapter 9

Summary

This research involves the experimental evolution of the crystallization process in colloidal hard spheres using confocal microscopy. A fluorescently labeled colloidal PMMA-PHSA system was used. The PMMA particles were first comprehensively characterized in size, mass density, and refractive index (RI). Detailed procedures are explained to obtain index and buoyancy matching. The sample cell preparation used throughout the experiment and the importance of coating the sidewalls and the base of the sample cell signifies the importance of suppressing heterogeneous nucleation. Since Confocal microscopy is used for studying colloidal suspension structure and dynamics, The possibility of recording three-dimensional images is explained in detail. It also describes the necessary criteria for scanning and resolution for good imaging. This research also describes how best to capture images so that they contain all available information from the samples. It also gives detailed information about image analysis for accurate particle positions and how the local structures can be assigned at the single-particle level using Bond-order parameters.

The direct observation of interaction properties using the pair distribution function is determined over a wide volume fraction range. The system is also characterized in terms of interaction potential and extensively studied. Hard sphere(HS) properties of the colloidal model system are first reviewed with Percus-Yevick's (PY) theory. Samples at volume fractions up to a freezing point are analyzed. Hard sphere-like behavior is observed in the TCE system by observing structure. The interaction is tuned using different solvents and adding organic salt to screen the electrostatic charge. The results show a discrepancy from HS-like behavior for other systems. The experimental 3D radial distribution functions are modeled by analytical theory and computer simulations, considering polydispersity and the experimental position uncertainty. The quantitative comparison between experiment and simulation/ theory establishes hard-sphere-like behavior for particles in CDL+TCE for a wide range of particle packing fractions. Furthermore, charged sphere behavior is confirmed both for the CDL+CHB and the CDL+CHB+TBAB solvents, and it is demonstrated that a finite particle concentration reduces screening in the CDL+CHB+TBAB system compared to the bulk solvent. Thus, by combining experiment and simulation, the research gives an extensive analysis and description of the structure of colloidal suspensions. The results are published [96].

The crystallization of a metastable melt is one of physics's most important non-equilibrium phenomena. An in-depth understanding of the crystallization process is not just for viewing fundamental research but also plays a vital role in the target development of new materials with tailored properties. Within crystallization comes crystal nucleation, which is particularly important since it is the birth of the resulting stable phase or new material. It is therefore not surprising that this research focus is intensively worked on experiments with different systems.

In the last three decades, numerous experiments have been carried out by different working groups to study the crystallization process in colloidal model systems. However, a direct comparison of experimental nucleation rate densities as a function of chemical potential difference with the nucleation rate densities from the simulations shows a highly unsatisfactory result. The experimental and theoretical data diverge by several magnitudes, and the curves of the experiment and simulation are qualitatively different. The reasons for the observed discrepancy between experimental and theoretical data remain unexplained. One of our research goals is to find the underlying reason for this discrepancy - if there is any. Direct imaging in three dimensions offers the unique possibility of observing crystal nucleation and growth on the particle level, giving detailed information about the fluid-to-crystal phase transformation.

We present a systematic study investigating crystal formation in colloidal hard spheres in direct space using laser scanning confocal microscopy, in which, for the first time, we vary the volume fraction over a wide range from the center of the fluid-crystal coexistence region to beyond the melting volume fraction. Furthermore, we managed to monitor the trajectories of about 3 million colloidal particles. In our study, we follow the formation of individual crystallites and, thanks to the large observation volume, determine ensemble-averaged quantities with high accuracy. Among other things, we determine nucleation rate densities and critical radii in two different ways - a) directly from the data without recourse to any model by counting the numbers of growing crystals and b) within the framework of classical nucleation theory by extracting the nucleation barrier analyzing the crystal size distribution. The direct data analysis reproduces the experimental data sets from Bragg and small angle scattering, while the CNT-based analysis reproduces the simulation data. The latter is a significant and total surprise. However, as mentioned above, the two data sets are incompatible.

Moreover, some of the simulation methods are implicit implementations of CNT. Accordingly, we conclude that the cause of this discrepancy is due to shortcomings of the CNT. We argue that the temporal evolution of phonons - a phenomenon not considered in the CNT framework is essential for the crystal nucleation process. Our work, therefore, has far-reaching consequences as it points to the necessity of a paradigm shift in the physics of crystallization. This work is submitted to the Nature Journal.

The possible causes for the discrepancy, such as sedimentation, the effect of charge, and adding salt to screen the charge are also studied in the middle of the coexistence region. It shows that the charge in the system relatively increases the rate densities. Meanwhile, implementing density mismatch at the coexistence region affects nucleation rate density, resulting in only three orders of magnitude. Thus, the possible reasons, such as sedimentation, charge, screened charge, and heterogeneous nucleation, do not explain the discrepancy.

Another goal of our research is to study the kinetics involved in the Crystallization of colloidal hard spheres using CDL and TCE. As very few experimental investigations are available, this research is crucial in helping to understand the phenomenon of fluid-to-crystal transformation using bond order parameters. This study reports single-particle level measurements on the kinetics of three-dimensional colloidal crystallization for symmetry and density transformations in this study. Our extensive studies across different volume fractions have enabled us to identify the kinetics during the transition process. It is well-established that structural and dynamical heterogeneities can be present in supercooled liquids. However, only in recent years have we witnessed increasing evidence suggesting that liquid heterogeneity plays a crucial role in crystallization mechanisms and determining the glass formation ability of various materials. One of the main assumptions in CNT is that random fluctuations in the homogeneous liquid drive crystallization events. Nevertheless, forming precursor regions in the liquid highlights the crucial role of thermal fluctuations and heterogeneity in driving crystallization. These precursors are characterized by the initial formation of pre-ordered regions in the liquid that precede the formation of crystallites.

The study of coupling between density fluctuations and translational ordering during crystallization plays a crucial role in Nucleation. In the process of crystallization, the establishment of crystalline order is naturally accompanied by density change. The exact correlation between density and symmetry depends on the kinetic transformations among intermediate structures, which are best studied using single-particle-level experiments. This research proves the existence of precursors, and its local structure is also studied extensively. We illustrate the correlation between these by directly measuring local density ρ_{cry}, which is determined by the Voronoi diagram, and local order is quantified by the orientational bond order. Good statistics are obtained from the measurements for more than 10^6 particles in the early crystallization stage. We have analyzed the early stages of crystal nucleation in hard spheres. Our analysis finds that high-order compact precursors form the base for crystallization.
Moreover, the precursors exhibit symmetries that resemble the crystal structure that grows during crystallization, highlighting the important role of precursors. These consisted of forming a cluster of hexagonal close-order particles and, finally, order HCP structures. This investigation shows the solidification process via the precursor phase in the colloidal hard sphere system. After precursor formation, the density and bond orientation order parameter changes to form the final crystal structure. The analysis in the chapter considers all the growing, slow-growing, and most prominent forming clusters and their growth in terms of crystal volume fraction and bond order analysis. Our finding concludes that all possible ways can happen during crystallization. Thus, these analyses shed light on the controversy between density or structural changes during nucleation. The results will be submitted to the journal in the coming months.

In the final chapter of the thesis, the study sheds light on the dynamics involved during crystallization. These data can infer that the particles are transitioning from a disordered state to an ordered state. This logarithmic slope of MSD increase reflects particle movement and diffusion as the particles rearrange themselves into more ordered configurations. This process is known as the pre-nucleation stage and is characterized by fluctuations in the density and structure of the particles. Later, just before the crystallization set in, the logarithmic slope of MSD decreases considerably, further implicating the sub-diffusion behavior of colloids during crystallization.

List of Figures

List of Tables

Bibliography

[1] Leica official website.

[2] Leica software.

[3] Development of model colloidal liquid crystals and the kinetics of the isotropic-smectic transition. *Philosophical Transactions: Mathematical, Physical and Engineering Sciences*, 359(1782):997–1015, 2001.

[4] Bruce J. Ackerson and Klaus Schätzel. Classical growth of hard-sphere colloidal crystals. *Phys. Rev. E*, 52:6448–6460, Dec 1995.

[5] B. J. Alder and T. E. Wainwright. Phase transition for a hard sphere system. *The Journal of Chemical Physics*, 27(5):1208–1209, 1957.

[6] Elshad Allahyarov, Kirill Sandomirski, Stefan U. Egelhaaf, and Hartmut Lowen. Crystallization seeds favour crystallization only during initial growth. *Nature Communications*, 6, 2015.

[7] Rosalind J. Allen, Patrick B. Warren, and Pieter Rein ten Wolde. Sampling rare switching events in biochemical networks. *Phys. Rev. Lett.*, 94:018104, Jan 2005.

[8] John L. Anderson. Colloidal dispersions. by w. b. russel, d. a. saville and w. r. schowalter. *Journal of Fluid Mechanics*, 222:692–694, 1991.

[9] Valerie J. Anderson and H N W Lekkerkerker. Insights into phase transition kinetics from colloid science. *Nature*, 416:811–815, 2002.

[10] N. W. Ashcroft and J. Lekner. Structure and resistivity of liquid metals. *Phys. Rev.*, 145:83–90, May 1966.

[11] S. Auer and D. Frenkel. Line tension controls wall-induced crystal nucleation in hard-sphere colloids. *Phys. Rev. Lett.*, 91:015703, Jul 2003.

[12] S. Auer and D. Frenkel. Numerical prediction of absolute crystallization rates in hard-sphere colloids. *The Journal of Chemical Physics*, 120(6):3015–3029, 2004.

[13] S. Auer, W. C. K. Poon, and D. Frenkel. Phase behavior and crystallization kinetics of poly-12-hydroxystearic-coated polymethylmethacrylate colloids. *Phys. Rev. E*, 67:020401, Feb 2003.

[14] Stefan Auer and Daan Frenkel. Crystallization of weakly charged colloidal spheres: a numerical study. *Journal of Physics: Condensed Matter*, 14(33):7667, aug 2002.

[15] Stefan Auer and Daan Frenkel. Quantitative prediction of crystal-nucleation rates for spherical colloids: A computational approach. *Annual Review of Physical Chemistry*, 55(1):333–361, 2004. PMID: 15117256.

[16] Frenkel.D Auer.S. Suppression of crystal nucleation in polydisperse colloids due to increase of the surface free energy. *Nature*, 413,711-713, 2001.

[17] Adolfo J. Banchio and Gerhard Nagele. Short-time transport properties in dense suspensions: From neutral to charge-stabilized colloidal spheres. *The Journal of Chemical Physics*, 128(10):104903, 03 2008.

[18] P. Bartlett and W. van Megen. *Physics of hard-sphere colloidal suspensions*, pages 195–257. Springer, 1st edition, 1994.

[19] Paul Bartlett and Patrick B. Warren. Reentrant melting in polydispersed hard spheres. *Phys. Rev. Lett.*, 82:1979–1982, Mar 1999.

[20] E. Bartsch, T. Eckert, C. Pies, and H. Sillescu. The effect of free polymer on the glass transition dynamics of microgel colloids. *Journal of Non-Crystalline Solids*, 307-310:802–811, 2002.

[21] Volfango Bertola. *Introduction to Transport Phenomena in Complex Fluids*, pages 1–26. Springer International Publishing, Cham, 2020.

[22] Martin H Blees. Foundations of colloid science: R.j. hunter, second ed., clarendon press, oxford, 2001. 806 pp., isbn 0-19-850502-7; Âč 60.00. *Colloids and Surfaces A: Physicochemical and Engineering Aspects*, 210(1):125, 2002.

[23] J. Bleibel, S. Dietrich, A. Domínguez, and M. Oettel. Shock waves in capillary collapse of colloids: A model system for two-dimensional screened newtonian gravity. *Phys. Rev. Lett.*, 107:128302, Sep 2011.

[24] Ludmila Boinovich. Dlvo forces in thin liquid films beyond the conventional dlvo theory. *Current Opinion in Colloid and Interface Science*, 15(5):297–302, 2010.

[25] Peter G Bolhuis and David A Kofke. Numerical study of freezing in polydisperse colloidal suspensions. *Journal of Physics: Condensed Matter*, 8(47):9627, nov 1996.

[26] Gilles Bosma, Chellapah Pathmamanoharan, Els H.A. de Hoog, Willem K. Kegel, Alfons van Blaaderen, and Henk N.W. Lekkerkerker. Preparation of monodisperse, fluorescent pmma-latex colloids by dispersion polymerization. *Journal of Colloid and Interface Science*, 245(2):292–300, 2002.

[27] R.J. Buehler, Jr. Wentorf, R.H., Hirschfelder J.O., and C.F. Curtiss. The Free Volume for Rigid Sphere Molecules. *jcp*, 19(1):61–71, January 1951.

[28] Michael W. Burke, Riccardo Leardi, Russell A. Judge, and Marc L. Pusey. Quantifying main trends in lysozyme nucleation-the effect of precipitant concentration, supersaturation, and impurities. *Crystal Growth and Design*, 1(4):333–337, 2001.

[29] Bernard Cabane, Joaquim Li, Franck Artzner, Robert Botet, Christophe Labbez, Guillaume Bareigts, Michael Sztucki, and Lucas Goehring. Hiding in plain view: Colloidal self-assembly from polydisperse populations. *Phys. Rev. Lett.*, 116:208001, May 2016.

[30] A. Cacciuto and D. Frenkel. Simulation of colloidal crystallization on finite structured templates. *Phys. Rev. E*, 72:041604, Oct 2005.

[31] A. Cacciuto and D. Frenkel. Stresses inside critical nuclei. *The Journal of Physical Chemistry B*, 109(14):6587–6594, 2005. PMID: 16851739.

[32] Andrew I. Campbell and Paul Bartlett. Fluorescent hard-sphere polymer colloids for confocal microscopy. *Journal of Colloid and Interface Science*, 256(2):325–330, 2002.

[33] Norman F. Carnahan and Kenneth E. Starling. Equation of State for Nonattracting Rigid Spheres. *The Journal of Chemical Physics*, 51(2):635–636, 09 2003.

[34] Norman F. Carnahan and Kenneth E. Starling. Equation of State for Nonattracting Rigid Spheres. *The Journal of Chemical Physics*, 51(2):635–636, 09 2003.

[35] P.M Chaikin, P Pincus, S Alexander, and D Hone. Bcc-fcc, melting and reentrant transitions in colloidal crystals. *Journal of Colloid and Interface Science*, 89(2):555–562, 1982.

[36] Naomi E. Chayen, Emmanuel Saridakis, and Richard P. Sear. Experiment and theory for heterogeneous nucleation of protein crystals in a porous medium. *Proceedings of the National Academy of Sciences*, 103(3):597–601, 2006.

[37] N.E. Chayen, E. Saridakis, R. El-Bahar, and Y. Nemirovsky. Porous silicon: an effective nucleation-inducing material for protein crystallization11edited by r. huber. *Journal of Molecular Biology*, 312(4):591–595, 2001.

[38] John Crocker and Eric Weeks. Particle tracking using idl.

[39] John C. Crocker and David G. Grier. Methods of digital video microscopy for colloidal studies. *Journal of Colloid and Interface Science*, 179(1):298–310, 1996.

[40] Ruslan L. Davidchack. Hard spheres revisited: Accurate calculation of the solid-liquid interfacial free energy. *The Journal of Chemical Physics*, 133(23):234701, 12 2010.

[41] P.G. de Gennes. Polymers at an interface; a simplified view. *Advances in Colloid and Interface Science*, 27(3):189–209, 1987.

[42] Marjolein de Jager and Laura Filion. Crystal nucleation of highly screened charged colloids. *The Journal of Chemical Physics*, 157(15):154905, 10 2022.

[43] V W A de Villeneuve, D Verboekend, R P A Dullens, D G A L Aarts, W K Kegel, and H N W Lekkerkerker. Hard sphere crystal nucleation and growth near large spherical impurities. *Journal of Physics: Condensed Matter*, 17(45):S3371, oct 2005.

[44] Volkert W. A. de Villeneuve, Roel P. A. Dullens, Dirk G. A. L. Aarts, Esther Groeneveld, Johannes H. Scherff, Willem K. Kegel, and Henk N. W. Lekkerkerker. Colloidal hard-sphere crystal growth frustrated by large spherical impurities. *Science*, 309(5738):1231–1233, 2005.

[45] Christoph Dellago, Peter G. Bolhuis, Felix S. Csajka, and David Chandler. Transition path sampling and the calculation of rate constants. *The Journal of Chemical Physics*, 108(5):1964–1977, 02 1998.

[46] Sven Deutschländer, Antonio M Puertas, Georg Maret, and Peter Keim. Specific heat in two-dimensional melting. *Physical review letters*, 113(12):127801, 2014.

[47] Grisell Díaz Leines, Ralf Drautz, and Jutta Rogal. Atomistic insight into the non-classical nucleation mechanism during solidification in ni. *The Journal of chemical physics*, 146(15), 2017.

[48] Marjolein Dijkstra. Capillary freezing or complete wetting of hard spheres in a planar hard slit. *Phys. Rev. Lett.*, 93:108303, Sep 2004.

[49] A. D. Dinsmore, Eric R. Weeks, Vikram Prasad, Andrew C. Levitt, and D. A. Weitz. Three-dimensional confocal microscopy of colloids. *Appl. Opt.*, 40(24):4152–4159, Aug 2001.

[50] Aleksandar Donev, Frank H. Stillinger, P. M. Chaikin, and Salvatore Torquato. Unusually dense crystal packings of ellipsoids. *Phys. Rev. Lett.*, 92:255506, Jun 2004.

[51] Sven Dorosz and Tanja Schilling. On the influence of a patterned substrate on crystallization in suspensions of hard spheres. *The Journal of Chemical Physics*, 136(4):044702, 01 2012.

[52] Roel P. A. Dullens, Claesson, Didi Derks, Alfons van Blaaderen, and Willem K. Kegel. Monodisperse coreshell poly(methyl methacrylate) latex colloids. *Langmuir*, 19(15):5963–5966, 2003.

[53] Roel P. A. Dullens and Willem K. Kegel. Topological lifetimes of polydisperse colloidal hard spheres at a wall. *Phys. Rev. E*, 71:011405, Jan 2005.

[54] Xavier Durang, Chulan Kwon, and Hyunggyu Park. Overdamped limit and inverse-friction expansion for brownian motion in an inhomogeneous medium. *Phys. Rev. E*, 91:062118, Jun 2015.

[55] João Medeiros e Silva and B. J. Mokross. Solidlike phase transitions in a screened wigner lattice. statics. *Phys. Rev. B*, 21:2972–2976, Apr 1980.

[56] Jorge R. Espinosa, Carlos Vega, Chantal Valeriani, and Eduardo Sanz. Seeding approach to crystal nucleation. *The Journal of Chemical Physics*, 144(3):034501, 01 2016.

[57] A. Esztermann and H. Löwen. Wetting of topographically structured surfaces by crystalline phases. *Journal of Physics Condensed Matter*, 17(9):S429–S441, March 2005.

[58] Sebastian C. Kapfer et.al. Fabian M. Schaller. Set voronoi diagrams of 3d assemblies of aspherical particles. *Philosophical Magazine*, 93(31-33):3993–4017, 2013.

[59] Moreno Fasolo and Peter Sollich. Equilibrium phase behavior of polydisperse hard spheres. *Phys. Rev. Lett.*, 91:068301, Aug 2003.

[60] Moreno Fasolo and Peter Sollich. Fractionation effects in phase equilibria of polydisperse hard-sphere colloids. *Physical Review E*, 70(4), oct 2004.

[61] Paul L. Fehder. Anomalies in the Radial Distribution Functions for Simple Liquids. *The Journal of Chemical Physics*, 52(2):791–796, 09 2003.

[62] L. Filion, M. Hermes, R. Ni, and M. Dijkstra. Crystal nucleation of hard spheres using molecular dynamics, umbrella sampling, and forward flux sampling: A comparison of simulation techniques. *The Journal of Chemical Physics*, 133(24):244115, 12 2010.

[63] L. Filion, R. Ni, D. Frenkel, and M. Dijkstra. Simulation of nucleation in almost hard-sphere colloids: The discrepancy between experiment and simulation persists. *The Journal of Chemical Physics*, 134(13):134901, 04 2011.

[64] Paul J. Flory. Thermodynamics of High Polymer Solutions. *jcp*, 10(1):51–61, January 1942.

[65] Markus Franke. *Experimentelle Untersuchung von Phasenuebergaengen in einem kolloidalen Modellsystem(theis) harter Kugeln.* PhD thesis, 2014.

[66] Markus Franke, Achim Lederer, and Hans Joachim Schoepe. Heterogeneous and homogeneous crystal nucleation in colloidal hard-sphere like microgels at low metastabilities. *Soft Matter*, 7:11267–11274, 2011.

[67] D. Frenkel, R. J. Vos, C. G. de Kruif, and A. Vrij. Structure factors of polydisperse systems of hard spheres: A comparison of monte carlo simulations and percus-yevick theory. *The Journal of Chemical Physics*, 84(8):4625–4630, 1986.

[68] Urs Gasser. *Phase behavior, crystal nucleation, and interactions in colloidal model systems.* 2015.

[69] Urs Gasser, Eric R Weeks, Andrew Schofield, PN Pusey, and DA Weitz. Real-space imaging of nucleation and growth in colloidal crystallization. *Science*, 292(5515):258–262, 2001.

[70] László Gránásy and Gyula I Tóth. Colloidal suspense. *Nature Physics*, 10(1):12–13, 2014.

[71] Sei Hachisu and Yoko Kobayashi. Kirkwood-alder transition in monodisperse latexes. ii. aqueous latexes of high electrolyte concentration. *Journal of Colloid and Interface Science*, 46(3):470–476, 1974.

[72] Sei Hachisu, Yoko Kobayashi, and Akira Kose. Phase separation in monodisperse latexes. *Journal of Colloid and Interface Science*, 42(2):342–348, 1973.

[73] Kenneth R. Hall. Another HardSphere Equation of State. *The Journal of Chemical Physics*, 57(6):2252–2254, 09 2003.

[74] S. Hamaguchi, R. T. Farouki, and D. H. E. Dubin. Triple point of yukawa systems. *Phys. Rev. E*, 56:4671–4682, Oct 1997.

[75] J. Hansen, P. N. Pusey, P. B. Warren, Z. Dogic, and S. Fraden. Development of model colloidal liquid crystals and the kinetics of the isotropic-smectic transition. *Philosophical Transactions of the Royal Society of London. Series A: Mathematical, Physical and Engineering Sciences*, 359(1782):997–1015, 2001.

[76] Jean-Pierre Hansen and John B. Hayter. A rescaled msa structure factor for dilute charged colloidal dispersions. *Molecular Physics*, 46(3):651–656, 1982.

[77] Jean-Pierre Hansen and Loup Verlet. Phase transitions of the lennard-jones system. *physical Review*, 184(1):151, 1969.

[78] J. L. Harland and W. van Megen. Crystallization kinetics of suspensions of hard colloidal spheres. *Phys. Rev. E*, 55:3054–3067, Mar 1997.

[79] J.L. Harland, S.I. Henderson, S.M. Underwood, and W. van Megen. Observation of Accelerated Nucleation in Dense Colloidal Fluids of Hard Sphere Particles. *prl*, 75(19):3572–3575, November 1995.

[80] Yueming He, Bruce J. Ackerson, W. van Megen, S. M. Underwood, and Klaus Schätzel. Dynamics of crystallization in hard-sphere suspensions. *Phys. Rev. E*, 54:5286–5297, Nov 1996.

[81] M. Heinen. *PhD thesis*. PhD thesis, 2011.

[82] Marco Heinen, Peter Holmqvist, Adolfo J. Banchio, and Gerhard Nagele. Pair structure of the hard-sphere Yukawa fluid: An improved analytic method versus simulations, Rogers-Young scheme, and experiment. *The Journal of Chemical Physics*, 134(4):044532, 01 2011.

[83] Martin Heni and Hartmut Löwen. Surface freezing on patterned substrates. *Phys. Rev. Lett.*, 85:3668–3671, Oct 2000.

[84] Martin Heni and Hartmut LÃűwen. Precrystallization of fluids induced by patterned substrates. *Journal of Physics: Condensed Matter*, 13(21):4675, may 2001.

[85] Dieter M Herlach, Ina Klassen, Patrick Wette, and Dirk Holland-Moritz. Colloids as model systems for metals and alloys: a case study of crystallization. *Journal of Physics: Condensed Matter*, 22(15):153101, mar 2010.

[86] M. Hermes, E. C. M. Vermolen, M. E. Leunissen, D. L. J. Vossen, P. D. J. van Oostrum, M. Dijkstra, and A. van Blaaderen. Nucleation of colloidal crystals on configurable seed structures. *Soft Matter*, 7:4623–4628, 2011.

[87] Jacob P. Hoogenboom, Didi Derks, Peter Vergeer, and Alfons van Blaaderen. Stacking faults in colloidal crystals grown by sedimentation. *The Journal of Chemical Physics*, 117(24):11320–11328, 12 2002.

[88] Jacob P. Hoogenboom, Peter Vergeer, and Alfons van Blaaderen. A real-space analysis of colloidal crystallization in a gravitational field at a flat bottom wall. *The Journal of Chemical Physics*, 119(6):3371–3383, 07 2003.

[89] William G. Hoover and Francis H. Ree. Melting transition and communal entropy for hard spheres. *The Journal of Chemical Physics*, 49(8):3609–3617, 1968.

[90] Maurice L. Huggins. Solutions of long chain compounds. *Journal of Chemical Physics*, 9:440–440, 1941.

[91] Neil Hunt, Roger Jardine, and Paul Bartlett. Superlattice formation in mixtures of hard-sphere colloids. *Phys. Rev. E*, 62:900–913, Jul 2000.

[92] Antti-Pekka Hynninen and Marjolein Dijkstra. Phase diagrams of hard-core repulsive yukawa particles. *Phys. Rev. E*, 68:021407, Aug 2003.

[93] Sara Iacopini, Thomas Palberg, and Hans Joachim Schoepe. Ripening-dominated crystallization in polydisperse hard-sphere-like colloids. *Phys. Rev. E*, 79:010601, Jan 2009.

[94] M.C. Jenkins and S.U. Egelhaaf. Confocal microscopy of colloidal particles: Towards reliable, optimum coordinates. *Advances in Colloid and Interface Science*, 136(1):65–92, 2008.

[95] G Kahl and G Pastore. Percus-yevick pair-distribution functions of a binary hard-sphere system covering the whole r-range. *Journal of Physics A: Mathematical and General*, 24(13):2995–3012, jul 1991.

[96] Sahana Kale, Achim Lederer, Martin Oettel, and Hans Joachim Schoepe. Approaching the hard sphere limit in colloids suitable for confocal microscopy-the end of a decade lasting quest. *Soft Matter*, 19:2146–2157, 2023.

[97] S. Karthika, T. K. Radhakrishnan, and P. Kalaichelvi. A review of classical and nonclassical nucleation theories. *Crystal Growth & Design*, 16(11):6663–6681, 2016.

[98] D. Kashchiev. Solution of the non-steady state problem in nucleation kinetics. *Surface Science*, 14(1):209–220, 1969.

[99] Takeshi Kawasaki and Hajime Tanaka. Formation of a crystal nucleus from liquid. *Proceedings of the National Academy of Sciences*, 107(32):14036–14041, 2010.

[100] Takeshi Kawasaki and Hajime Tanaka. Structural origin of dynamic heterogeneity in three-dimensional colloidal glass formers and its link to crystal nucleation. *Journal of Physics: Condensed Matter*, 22(23):232102, may 2010.

[101] K.F. Kelton. Crystal nucleation in liquids and glasses. volume 45 of *Solid State Physics*, pages 75–177. Academic Press, 1991.

[102] Stefania Ketzetzi, John Russo, and Daniel Bonn. Crystal nucleation in sedimenting colloidal suspensions. *The Journal of Chemical Physics*, 148(6):064901, 02 2018.

[103] C. S. Kiang, D. Stauffer, G. H. Walker, O. P. Puri, J. D. Wise, and E. M. Patterson. A reexamination of homogeneous nucleation theory. *Journal of Atmospheric Sciences*, 28(7):1222 – 1232, 1971.

[104] David A. Kofke and Peter G. Bolhuis. Freezing of polydisperse hard spheres. *Phys. Rev. E*, 59:618–622, Jan 1999.

[105] Anke Kuijk, Dmytro V. Byelov, Andrei V. Petukhov, Alfons van Blaaderen, and Arnout Imhof. Phase behavior of colloidal silica rods. *Faraday Discuss.*, 159:181–199, 2012.

[106] S. Labík and A. Malijevský. An effective Monte Carlo calculation of the radial distribution function of hard spheres on a minicomputer. *Czechoslovak Journal of Physics*, 33(2):128–134, February 1983.

[107] Stanislav Labik and Anatol Malijevsky. Monte carlo simulations of the radial distribution function of fluid hard spheres. *Molecular Physics*, 42(3):739–744, 1981.

[108] Anthony J. C. Ladd. Hydrodynamic transport coefficients of random dispersions of hard spheres. *The Journal of Chemical Physics*, 93(5):3484–3494, 09 1990.

[109] L. D. Landau, E. M. Lifschitz, and Paul Ziesche. *Quantenmechanik: Mit 11 Tabellen*, volume Bd. 3 of *Lehrbuch der theoretischen Physik : in 10 Bänden / L.D. Landau*. Deutsch, Frankfurt am Main, 9. aufl., unveränd. nachdr edition, 2007.

[110] L.Antl and et.al. The preparation of poly(methyl methacrylate) latices in non-aqueous media. *Colloids and Surfaces*, 17(1):67–78, 1928.

[111] Wolfgang Lechner and Christoph Dellago. Accurate determination of crystal structures based on averaged local bond order parameters. *The Journal of Chemical Physics*, 129(11):114707, 09 2008.

[112] Wolfgang Lechner, Christoph Dellago, and Peter G. Bolhuis. Role of the prestructured surface cloud in crystal nucleation. *Phys. Rev. Lett.*, 106:085701, Feb 2011.

[113] Wolfgang Lechner, Christoph Dellago, and Peter G Bolhuis. Role of the prestructured surface cloud in crystal nucleation. *Physical review letters*, 106(8):085701, 2011.

[114] Achim Lederer. *Konfokalmikroskopie an stabilen und metastabilen kolloidalen Hartkugel-Fluiden.* PhD thesis, 2015.

[115] Sang-Hyuk Lee, Yohai Roichman, Gi-Ra Yi, Shin-Hyun Kim, Seung-Man Yang, Alfons van Blaaderen, Peter van Oostrum, and David G. Grier. Characterizing and tracking single colloidal particles with video holographic microscopy. *Opt. Express*, 15(26):18275–18282, Dec 2007.

[116] Mathieu Leocmach and Hajime Tanaka. Roles of icosahedral and crystal-like order in the hard spheres glass transition. *Nature Communications*, 3(1), jul 2012.

[117] Mirjam Leunissen. *Manipulating Colloids with Charges and Electric Fields.* PhD thesis, 2007.

[118] Mirjam E Leunissen, Christina G Christova, Antti-Pekka Hynninen, C Patrick Royall, Andrew I Campbell, Arnout Imhof, Marjolein Dijkstra, Rene van Roij, and Alfons van Blaaderen. Ionic colloidal crystals of oppositely charged particles. *Nature*, 437(7056):235–240, September 2005.

[119] Beth A. Lindquist, Ryan B. Jadrich, and Thomas M. Truskett. Communication: From close-packed to topologically close-packed: Formation of laves phases in moderately polydisperse hard-sphere mixtures. *The Journal of Chemical Physics*, 148(19):191101, 05 2018.

[120] H. M. Lindsay and P. M. Chaikin. Elastic properties of colloidal crystals and glasses. *The Journal of Chemical Physics*, 76(7):3774–3781, 04 1982.

[121] R. A. Lionberger and W. B. Russel. High frequency modulus of hard sphere colloids. *Journal of Rheology*, 38(6):1885–1908, 11 1994.

[122] Peter J. Lu, David A Weitz, and J. S. Langer. *Colloidal particles: Crystals, glasses, and gels*, volume 4 of *Annual Review of Condensed Matter Physics*, pages 217–233. 2013.

[123] Yunzhuo Lu, Xing Lu, Zuoxiang Qin, and Jun Shen. Experimental evidence for ordered precursor foreshadowing crystal nucleation in colloidal system. *Solid State Communications*, 217:13–16, 2015.

[124] James F Lutsko. Communication: A dynamical theory of homogeneous nucleation for colloids and macromolecules. *The Journal of chemical physics*, 135(16), 2011.

[125] James F Lutsko. A dynamical theory of nucleation for colloids and macromolecules. *The Journal of chemical physics*, 136(3), 2012.

[126] James F. Lutsko and Grégoire Nicolis. Theoretical evidence for a dense fluid precursor to crystallization. *Phys. Rev. Lett.*, 96:046102, Feb 2006.

[127] G. A. Mansoori, N. F. Carnahan, K. E. Starling, and Jr. Leland, T. W. Equilibrium Thermodynamic Properties of the Mixture of Hard Spheres. *The Journal of Chemical Physics*, 54(4):1523–1525, 09 2003.

[128] Antonio López Mendoza and José Ángel Gómez. Zeta potential of molybdenite to fine sizes. 2018.

[129] Sarath Menon, Grisell Díaz Leines, Ralf Drautz, and Jutta Rogal. Role of pre-ordered liquid in the selection mechanism of crystal polymorphs during nucleation. *The Journal of Chemical Physics*, 153(10), 2020.

[130] Ralf Metzler and Joseph Klafter. The random walk's guide to anomalous diffusion: a fractional dynamics approach. *Physics Reports*, 339(1):1–77, 2000.

[131] Walter Mickel, Sebastian C. Kapfer, Gerd E. Schroeder-Turk, and Klaus Mecke. Shortcomings of the bond orientational order parameters for the analysis of disordered particulate matter. *The Journal of Chemical Physics*, 138(4):044501, 2013.

[132] Marvin Minsky. Memoir on inventing the confocal scanning microscope. scanning. *Jornal of scanning microscopy*, 1988.

[133] Yiannis Monovoukas and Alice P Gast. The experimental phase diagram of charged colloidal suspensions. *Journal of Colloid and Interface Science*, 128(2):533–548, 1989.

[134] R. Morgado, I. V. L. Costa, and F. A. Oliveira. Normal and Anomalous Diffusion: Ergodicity and Fluctuation–Dissipation Theorem. *Acta Physica Polonica B*, 35(4):1359, April 2004.

[135] Rafael Morgado, Fernando A. Oliveira, G. George Batrouni, and Alex Hansen. Relation between anomalous and normal diffusion in systems with memory. *Phys. Rev. Lett.*, 89:100601, Aug 2002.

[136] Takayuki Narumi, Scott V. Franklin, Kenneth W. Desmond, Michio Tokuyama, and Eric R. Weeks. Spatial and temporal dynamical heterogeneities approaching the binary colloidal glass transition. *Soft Matter*, 7:1472–1482, 2011.

[137] Anand Newman.Hugh D, Yethiraj. Clusters in sedimentation equilibrium for an experimental hard-sphere-plus-dipolar brownian colloidal system. *Scientific Reports*, 5:2045–2322, 2015.

[138] Ran Ni, Anjan Prasad Gantapara, Joost de Graaf, Rene van Roij, and Marjolein Dijkstra. Phase diagram of colloidal hard superballs: from cubes via spheres to octahedra. *Soft Matter*, 8:8826–8834, 2012.

[139] Brendan O Malley and Ian Snook. Structure of hard-sphere fluid and precursor structures to crystallization. *The Journal of Chemical Physics*, 123(5):054511, 08 2005.

[140] Takehiro Ohtsuka, C. Patrick Royall, and Hajime Tanaka. Local structure and dynamics in colloidal fluids and gels. *Europhysics Letters*, 84(4):46002, nov 2008.

[141] Fernando A. Oliveira, Rogelma M. S. Ferreira, Luciano C. Lapas, and Mendeli H. Vainstein. Anomalous diffusion: A basic mechanism for the evolution of inhomogeneous systems. *Frontiers in Physics*, 7, 2019.

[142] D W Oxtoby. Homogeneous nucleation: theory and experiment. *Journal of Physics: Condensed Matter*, 4(38):7627, sep 1992.

[143] O. P. Behrend P. N. Segre and P. N. Pusey. Plasmas, Fluids, Relat. Interdiscip. Top.Phys. *Phys. Rev. E: Stat*, 52:5070–5083, 1995.

[144] Stephen W. Paddock. S.w. principles and practices of laser scanning confocal microscopy. *Mol Biotechnol.*, 16(3):127–149, 2000.

[145] Thomas Palberg. Crystallization kinetics of repulsive colloidal spheres. *Journal of Physics: Condensed Matter*, 11(28):R323, jul 1999.

[146] Thomas Palberg. Crystallization kinetics of colloidal model suspensions: recent achievements and new perspectives. *Journal of Physics: Condensed Matter*, 26(33):333101, jul 2014.

[147] Elisabeth Paschinger, Albert Reiner, and Gerhard Kahl. An efficient method for calculating the pair distribution functions of a ternary hard-sphere system in r space within the percus-yevick approximation. *Molecular Physics*, 94:743–750, 1998.

[148] S. E. Paulin and Bruce J. Ackerson. Observation of a phase transition in the sedimentation velocity of hard spheres. *Phys. Rev. Lett.*, 64:2663–2666, May 1990.

[149] Ph. Pellin and Andre Broca. A Spectroscope of Fixed Deviation. *Astrophysical Journal*, 10:337, December 1899.

[150] Jerome K. Percus and George J. Yevick. Analysis of classical statistical mechanics by means of collective coordinates. *Phys. Rev.*, 110:1–13, Apr 1958.

[151] Jean Perrin. Mouvement brownien et molecules. *J. Phys. Theor. Appl.*, 01 1910.

[152] E Phan, W B Russel, Z Cheng, J H Dunsmuir J Zhu, P M Chaikin, and R H Ottewill. Plasmas,fluids,relat.interdiscip.top. *Phys.Rev.E*, 54:6633–6645, 1996.

[153] See-Eng Phan, William B. Russel, Zhengdong Cheng, Jixiang Zhu, Paul M. Chaikin, John H. Dunsmuir, and Ronald H. Ottewill. Phase transition, equation of state, and limiting shear viscosities of hard sphere dispersions. *Phys. Rev. E*, 54:6633–6645, Dec 1996.

[154] See-Eng Phan, William B. Russel, Jixiang Zhu, and Paul M. Chaikin. Effects of polydispersity on hard sphere crystals. *The Journal of Chemical Physics*, 108(23):9789–9795, 06 1998.

[155] Pawel Pieranski. Colloidal crystals. *Contemporary Physics*, 24(1):25–73, 1983.

[156] Wilson Poon. Colloids as big atoms. *Science*, 304(5672):830–831, 2004.

[157] V Prasad, D Semwogerere, and Eric R Weeks. Confocal microscopy of colloids. *Journal of Physics: Condensed Matter*, 19(11):113102, feb 2007.

[158] P. N. Pusey and W. van Megen. Observation of a glass transition in suspensions of spherical colloidal particles. *Phys. Rev. Lett.*, 59:2083–2086, Nov 1987.

[159] P. N. Pusey, E. Zaccarelli, C. Valeriani, E. Sanz, Wilson C. K. Poon, and Michael E. Cates. Hard spheres: crystallization and glass formation. *Philosophical Transactions of the Royal Society A: Mathematical, Physical and Engineering Sciences*, 367(1909):4993–5011, 2009.

[160] Peter N. Pusey. The effect of polydispersity on the crystallization of hard spherical colloids. *Journal De Physique*, 48:709–712, 1987.

[161] P.N. Pusey and W. van Megen. Phase behaviour of concentrated suspensions of nearly hard colloidal spheres. *nat*, 320(6060):340–342, March 1986.

[162] M. Radu and T. Schilling. Solvent hydrodynamics speed up crystal nucleation in suspensions of hard spheres. *Europhysics Letters*, 105(2):26001, feb 2014.

[163] Pieter Rein ten Wolde, Maria J. Ruiz-Montero, and Daan Frenkel. Numerical calculation of the rate of crystal nucleation in a lennardâĂŘjones system at moderate undercooling. *The Journal of Chemical Physics*, 104(24):9932–9947, 1996.

[164] M. D. Rintoul and S. Torquato. Computer simulations of dense hard-sphere systems. *The Journal of Chemical Physics*, 105(20):9258–9265, 1996.

[165] Margaret Robins and Annette Fillery-Travis. Colloidal dispersions. edited by w. b. russel, d. a. saville & w. r. schowalter, cambridge university press, cambridge, uk, 1989. *Journal of Chemical Technology & Biotechnology*, 54(2):201–202, 1992.

[166] Laura Rossi, Stefano Sacanna, William T. M. Irvine, Paul M. Chaikin, David J. Pine, and Albert P. Philipse. Cubic crystals from cubic colloids. *Soft Matter*, 7:4139–4142, 2011.

[167] C. Patrick Royall, Mirjam E. Leunissen, Antti-Pekka Hynninen, Marjolein Dijkstra, and Alfons van Blaaderen. Re-entrant melting and freezing in a model system of charged colloids. *The Journal of Chemical Physics*, 124(24):244706, 2006.

[168] C. Patrick Royall, Wilson C. K. Poon, and Eric R. Weeks. In search of colloidal hard spheres. *Soft Matter*, 9:17–27, 2013.

[169] John Russo, Anthony C. Maggs, Daniel Bonn, and Hajime Tanaka. The interplay of sedimentation and crystallization in hard-sphere suspensions. *Soft Matter*, 9:7369–7383, 2013.

[170] John Russo and Hajime Tanaka. The microscopic pathway to crystallization in supercooled liquids. *Scientific reports*, 2(1):505, 2012.

[171] Kirill Sandomirski, Elshad Allahyarov, Hartmut Lowen, and Stefan U. Egelhaaf. Heterogeneous crystallization of hard-sphere colloids near a wall. *Soft Matter*, 7:8050–8055, 2011.

[172] Kirill Sandomirski, Stefan Walta, Janine Dubbert, Elshad Allahyarov, Andrew B Schofield, Hartmut Lowen, Walter Richtering, and Stefan Egelhaaf. Heterogeneous crystallization of hard and soft spheres near flat and curved walls. *European Physical Journal - Special Topics*, 223(3):439–454, 2014.

[173] Andrés Santos, Santos B. Yuste, Mariano López de Haro, Gerardo Odriozola, and Vitaliy Ogarko. Simple effective rule to estimate the jamming packing fraction of polydisperse hard spheres. *Phys. Rev. E*, 89:040302, Apr 2014.

[174] N. Sator. Clusters in simple fluids. *Physics Reports*, 376(1):1–39, 2003.

[175] J. R. Savage and A. D. Dinsmore. Experimental evidence for two-step nucleation in colloidal crystallization. *Phys. Rev. Lett.*, 102:198302, May 2009.

[176] W. Schaertl and H. Sillescu. Brownian dynamics of polydisperse colloidal hard spheres: Equilibrium structures and random close packings. *Journal of Statistical Physics*, 77(5-6):1007–1025, December 1994.

[177] Klaus Schätzel and Bruce J. Ackerson. Density fluctuations during crystallization of colloids. *Phys. Rev. E*, 48:3766–3777, Nov 1993.

[178] T Schilling, S Dorosz, H J Schoepe, and G Opletal. Crystallization in suspensions of hard spheres: a monte carlo and molecular dynamics simulation study. *Journal of Physics: Condensed Matter*, 23(19):194120, apr 2011.

[179] T. Schilling, H. J. Schoepe, M. Oettel, G. Opletal, and I. Snook. Precursor-mediated crystallization process in suspensions of hard spheres. *Phys. Rev. Lett.*, 105:025701, Jul 2010.

[180] Hans Joachim Schoepe, Gary Bryant, and William van Megen. Small changes in particle-size distribution dramatically delay and enhance nucleation in hard sphere colloidal suspensions. *Phys. Rev. E*, 74:060401, Dec 2006.

[181] Hans Joachim Schoepe, Gary Bryant, and William van Megen. Effect of polydispersity on the crystallization kinetics of suspensions of colloidal hard spheres when approaching the glass transition. *The Journal of Chemical Physics*, 127(8):084505, 2007.

[182] HJ Schöpe and T Palberg. Frustration of structural fluctuations upon equilibration of shear melts. *Journal of non-crystalline solids*, 307:613–622, 2002.

[183] G. E. Schröder-Turk, W. Mickel, M. Schröter, G. W. Delaney, M. Saadatfar, T. J. Senden, K. Mecke, and T. Aste. Disordered spherical bead packs are anisotropic. *Europhysics Letters*, 90(3):34001, may 2010.

[184] R. P. Sear. Phase separation and crystallisation of polydisperse hard spheres. *Europhysics Letters*, 44(4):531, nov 1998.

[185] Richard P Sear. Nucleation: theory and applications to protein solutions and colloidal suspensions. *Journal of Physics: Condensed Matter*, 19(3):033101, jan 2007.

[186] C. J. R. Sheppard and D. M. Shotton. Confocal laser scanning microscopy. *BIOS Scientific Publishers, Oxford,*, 1997.

[187] Shimono, M. and Onodera, H. Icosahedral symmetry, fragility and stability of supercooled liquid state of metallic glasses. *Rev. Metall.*, 109(1):41–46, 2012.

[188] Ullrich Siems and Peter Nielaba. Brownian dynamics simulations of model colloids in channel geometries and external fields. *Journal of Physics: Conference Series*, 1012(1):012011, apr 2018.

[189] C.and Heymann Sinn. Solidification kinetics of hard-sphere colloidal suspensions. In *Trends in Colloid and Interface Science XV*, pages 266–275, Berlin, Heidelberg, 2001. Springer Berlin Heidelberg.

[190] E. B. Sirota, H. D. Ou-Yang, and Sinha. Complete phase diagram of a charged colloidal system: A synchro- tron x-ray scattering study. *Phys. Rev. Lett.*, 62:1524–1527, Mar 1989.

[191] I. K. Snook and J. B. Hayter. Static structure of strongly interacting colloidal particles. *Langmuir*, 8(12):2880–2884, 1992.

[192] Peter Sollich. Predicting phase equilibria in polydisperse systems. *Journal of Physics: Condensed Matter*, 14(3):R79, dec 2001.

[193] Peter Sollich and Nigel B Wilding. Polydispersity induced solid-solid transitions in model colloids. *Soft Matter*, 7:4472–4484, 2011.

[194] Ajay K. Sood. Structural ordering in colloidal suspensions. volume 45 of *Solid State Physics*, pages 1–73. Academic Press, 1991.

[195] Gabriele C. Sosso, Ji Chen, Stephen J. Cox, Martin Fitzner, Philipp Pedevilla, Andrea Zen, and Angelos Michaelides. Crystal nucleation in liquids: Open questions and future challenges in molecular dynamics simulations. *Chemical Reviews*, 116(12):7078–7116, 2016. PMID: 27228560.

[196] Todd M. Squires and Stephen R. Quake. Microfluidics: Fluid physics at the nanoliter scale. *Rev. Mod. Phys.*, 77:977–1026, Oct 2005.

[197] Paul J. Steinhardt, David R. Nelson, and Marco Ronchetti. Bond-orientational order in liquids and glasses. *Phys. Rev. B*, 28:784–805, Jul 1983.

[198] T.F. Tadros. *Formulation of Disperse Systems: Science and Technology.* Wiley, 2014.

[199] Jade Taffs, Stephen R. Williams, Hajime Tanaka, and C. Patrick Royall. Structure and kinetics in the freezing of nearly hard spheres. *Soft Matter*, 9:297–305, 2013.

[200] Peng Tan, Ning Xu, and Lei Xu. Visualizing kinetic pathways of homogeneous nucleation in colloidal crystallization. *Nature Physics*, 10:73 – 79, 2013.

[201] Pieter Rein ten Wolde, M. J. Ruiz-Montero, and Daan Frenkel. Numerical calculation of the rate of crystal nucleation in a lennardâĂŘjones system at moderate undercooling. *Journal of Chemical Physics*, 104:9932–9947, 1996.

[202] S. Torquato and F. H. Stillinger. Publisher's note: Jammed hard-particle packings: From kepler to bernal and beyond [rev. mod. phys. 82, 2633 (2010)]. *Rev. Mod. Phys.*, 82:3197–3197, Dec 2010.

[203] Thomas M. Truskett, Salvatore Torquato, Srikanth Sastry, Pablo G. Debenedetti, and Frank H. Stillinger. Structural precursor to freezing in the hard-disk and hard-sphere systems. *Phys. Rev. E*, 58:3083–3088, Sep 1998.

[204] Alfons van Blaaderen, Rene Ruel, and Pierre Wiltzius. Template-directed colloidal crystallization. *nat*, 385(6614):321–324, January 1997.

[205] W. van Megen. Crystallisation and the glass transition in suspensions of hard colloidal spheres. *Transport Theory and Statistical Physics*, 24(6-8):1017–1051, 1995.

[206] W. van Megen. Comparison of dynamic light scattering measurements and mode-coupling theory for the tagged particle dynamics of a hard-sphere suspension. *Phys. Rev. E*, 76:061401, Dec 2007.

[207] William van Megen. Ordered states in systems of macroscopic particles. *Nature*, 262:1476–4687, 1976.

[208] Peter G Vekilov and Oleg Galkin. On the methods of determination of homogeneous nucleation rates of protein crystals. *Colloids and Surfaces A: Physicochemical and Engineering Aspects*, 215(1):125–130, 2003.

[209] Loup Verlet and Jean-Jacques Weis. Equilibrium theory of simple liquids. *Phys. Rev. A*, 5:939–952, Feb 1972.

[210] Teun Vissers. *Oppositely Charged Colloids Out of Equilibrium.* PhD thesis, 2010.

[211] D. J. Walbridge and J. A. Waters. Rheology of sterically stabilized dispersions of poly(methyl methacrylate) in aliphatic hydrocarbons. *Discuss. Faraday Soc.*, 42:294–300, 1966.

[212] Robert H Webb. Confocal optical microscopy. *Reports on Progress in Physics*, 59(3):427–471, mar 1996.

[213] Eric R. Weeks, J. C. Crocker, Andrew C. Levitt, Andrew Schofield, and D. A. Weitz. Three-dimensional direct imaging of structural relaxation near the colloidal glass transition. *Science*, 287(5453):627–631, 2000.

[214] John D. Weeks, David Chandler, and Hans C. Andersen. Role of Repulsive Forces in Determining the Equilibrium Structure of Simple Liquids. *The Journal of Chemical Physics*, 54(12):5237–5247, 09 2003.

[215] M. S. Wertheim. Analytic solution of the percus-yevick equation. *Journal of Mathematical Physics*, 5(5):643–651, 1964.

[216] Patrick Wette, Andreas Engelbrecht, Roushdey Salh, Ina Klassen, Dirk Menke, Dieter M Herlach, Stephan V Roth, and Hans Joachim SchÃűpe. Competition between heterogeneous and homogeneous nucleation near a flat wall. *Journal of Physics: Condensed Matter*, 21(46):464115, oct 2009.

[217] Patrick Wette and Hans Joachim Schoepe. Nucleation kinetics in deionized charged colloidal model systems: A quantitative study by means of classical nucleation theory. *Phys. Rev. E*, 75:051405, May 2007.

[218] Patrick Wette, Hans Joachim Schoepe, and Thomas Palberg. Crystallization in charged two-component suspensions. *The Journal of Chemical Physics*, 122(14):144901, 04 2005.

[219] Nigel B. Wilding and Peter Sollich. Phase behavior of polydisperse spheres: Simulation strategies and an application to the freezing transition. *The Journal of Chemical Physics*, 133(22):224102, 2010.

[220] Tony Wilson and Simon J. Hewlett. Imaging strategies in three-dimensional confocal microscopy. In Alan Conrad Bovik and William E. Higgins, editors, *Biomedical Image Processing*, volume 1245, pages 35 – 45. International Society for Optics and Photonics, SPIE, 1990.

[221] Nicholas Wood, John Russo, Francesco Turci, and C. Patrick Royall. Coupling of sedimentation and liquid structure: Influence on hard sphere nucleation. *The Journal of Chemical Physics*, 149(20):204506, 11 2018.

[222] Nicholas Wood, John Russo, Francesco Turci, and C. Patrick Royall. Coupling of sedimentation and liquid structure: Influence on hard sphere nucleation. *The Journal of Chemical Physics*, 149(20):204506, 11 2018.

[223] Shenghua Xu, Hongwei Zhou, Zhiwei Sun, and Jingchang Xie. Formation of an fcc phase through a bcc metastable state in crystallization of charged colloidal particles. *Phys. Rev. E*, 82:010401, Jul 2010.

[224] Seung Yun Yang, Jeong-A Yang, Eung-Sam Kim, Gumhye Jeon, Eun Ju Oh, Kwan Yong Choi, Sei Kwang Hahn, and Jin Kon Kim. Single-file diffusion of protein drugs through cylindrical nanochannels. *ACS nano*, 4(7):3817–3822, 2010.

[225] van Blaaderen Yethiraj, A. A colloidal model system with an interaction tunable from hard sphere to soft and dipolar. *Nature*, 421:513–517, 2003.

[226] Yuste, Haro, and Santos. Structure of hard-sphere metastable fluids. *Physical review. E, Statistical physics, plasmas, fluids, and related interdisciplinary topics*, 53 5:4820–4826, 1996.

[227] E. Zaccarelli, C. Valeriani, E. Sanz, W. C. K. Poon, M. E. Cates, and P. N. Pusey. Crystallization of hard-sphere glasses. *Phys. Rev. Lett.*, 103:135704, Sep 2009.

[228] K. Zahn, J. M. Méndez-Alcaraz, and G. Maret. Hydrodynamic interactions may enhance the self-diffusion of colloidal particles. *Phys. Rev. Lett.*, 79:175–178, Jul 1997.

[229] Qi Zhang, Jincheng Wang, Sai Tang, Yujian Wang, Junjie Li, Wenquan Zhou, and Zhijun Wang. Molecular dynamics investigation of the local structure in iron melts and its role in crystal nucleation during rapid solidification. *Physical Chemistry Chemical Physics*, 21(8):4122–4135, 2019.

[230] Tian Hui Zhang and Xiang Yang Liu. How does a transient amorphous precursor template crystallization. *Journal of the American Chemical Society*, 129(44):13520–13526, 2007.

[231] Jixiang Zhu, Min Li, R. Rogers, W. Meyer, R.H. Ottewill, Sts-73 Space Shuttle Crew, W.B. Russel, and P.M. Chaikin. Crystallization of hard-sphere colloids in microgravity. *Nature*, 387(6636):883–885, June 1997.

[232] C.F. Zukoski, A.M. Kulkarni, and N.M. Dixit. Response to: On methods of determination of homogeneous nucleation rates of protein crystals. *Colloids and Surfaces A: Physicochemical and Engineering Aspects*, 215(1):137–140, 2003.

Appendices

Appendix A

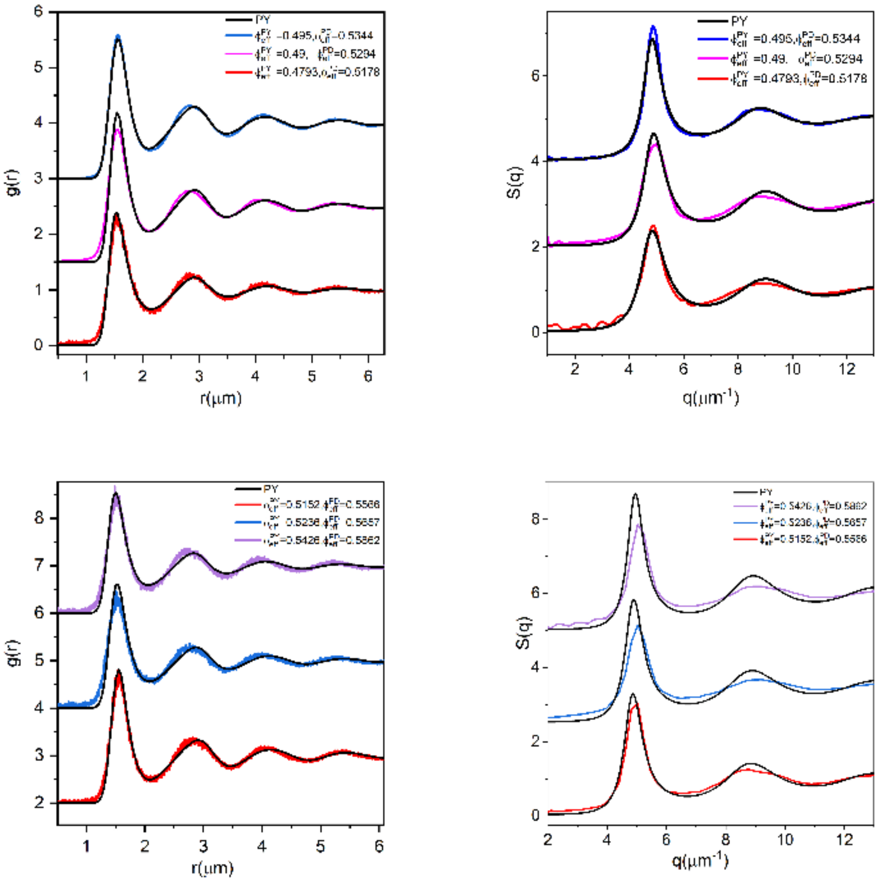

Figure 1: Left:Overview of the measured g(r) for CDL+TCE for ϕ_{eff}^{PD} = 0.449-0.529 . The graph contains error-enhanced, polydisperse PY-g (r) with scaling factor S = 1.042 and position error $\Delta\xi = 5.0\%$. These refer to the PY-g(r). Right: Overview of the corresponding structure factors in the same volume fracture range. For a better overview, the data points in both Graphs shifted upward.

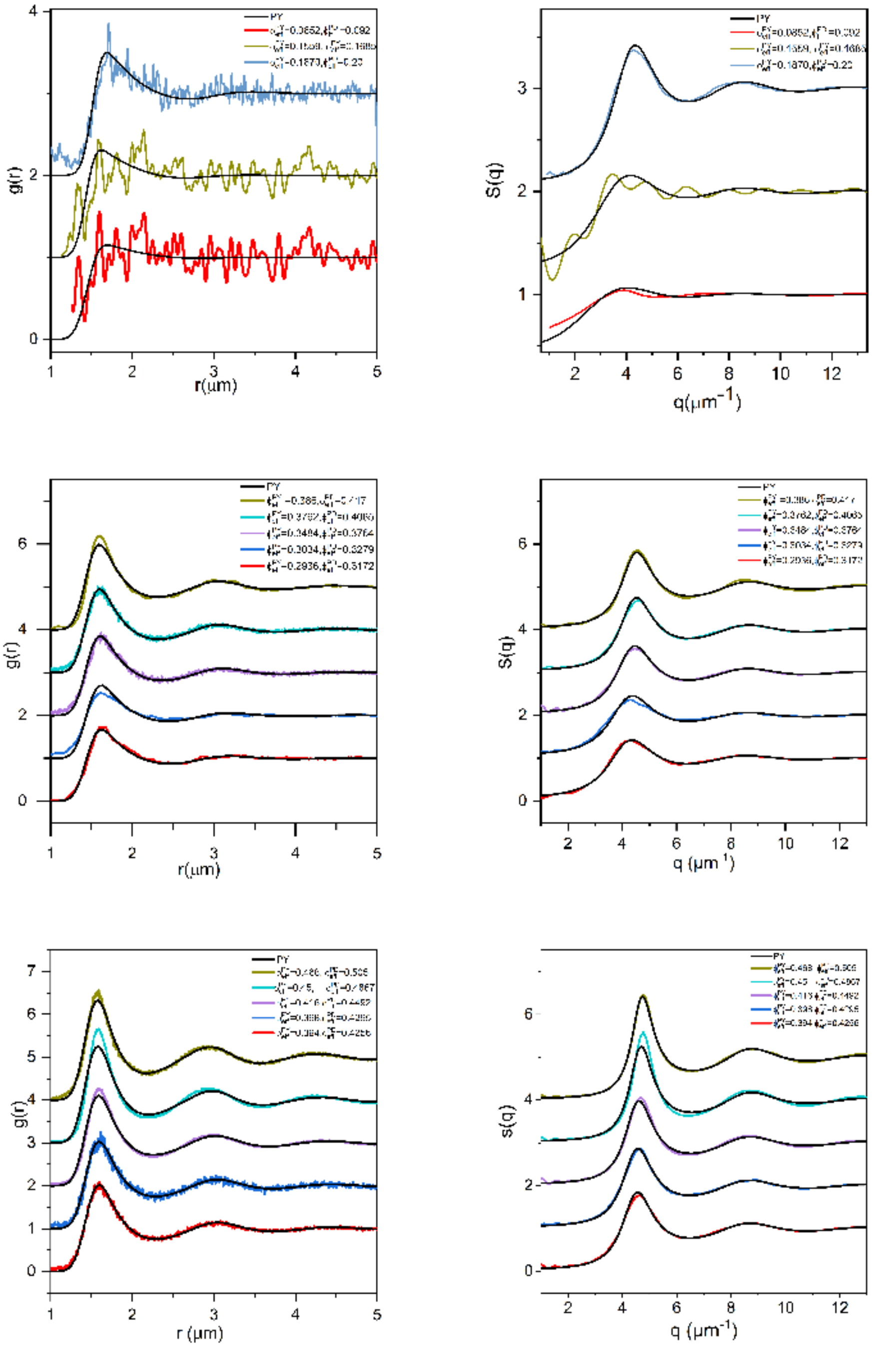

Figure 2: Left: Overview of the measured pair distribution functions for particles in TCE+CDL, for ϕ_{eff}^{PD} = 0.092-0.505. The plot also contains error-broadened, poly-disperse PY theory curves with scaling factor S = 1.042 and position error $\Delta\xi = 5.0\%$. The brackets' legend gives the volume fractions ϕ_{eff}^{PD} calculated using the scaling factor S = 1.042. Right: Overview of the corresponding structure factors in the same volume fraction range. For a better overview, successive curves are given with y-offsets.

Appendix B

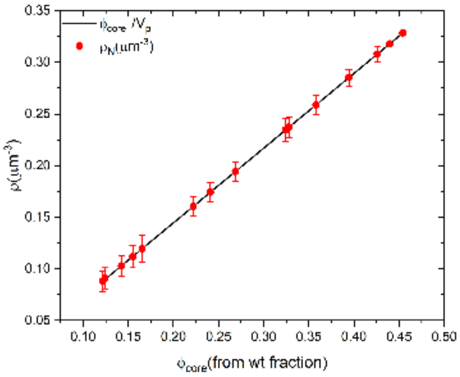

Figure 3: Plot of number density measured from confocal microscopy versus prepared core volume fraction from weight fraction for CHB in CDL. The line represents the expected relationship between core volume fraction and particle number density.

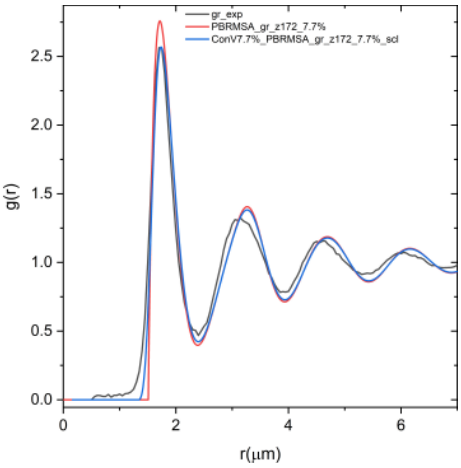

Figure 4: Experimental g(r)(black) for CHB+CDL having $\rho = 0.2372\mu m^{-3}$ is given with a comparison with PBRMSA data(red) obtained from Marco Heinen software and corresponding convoluted data(blue).

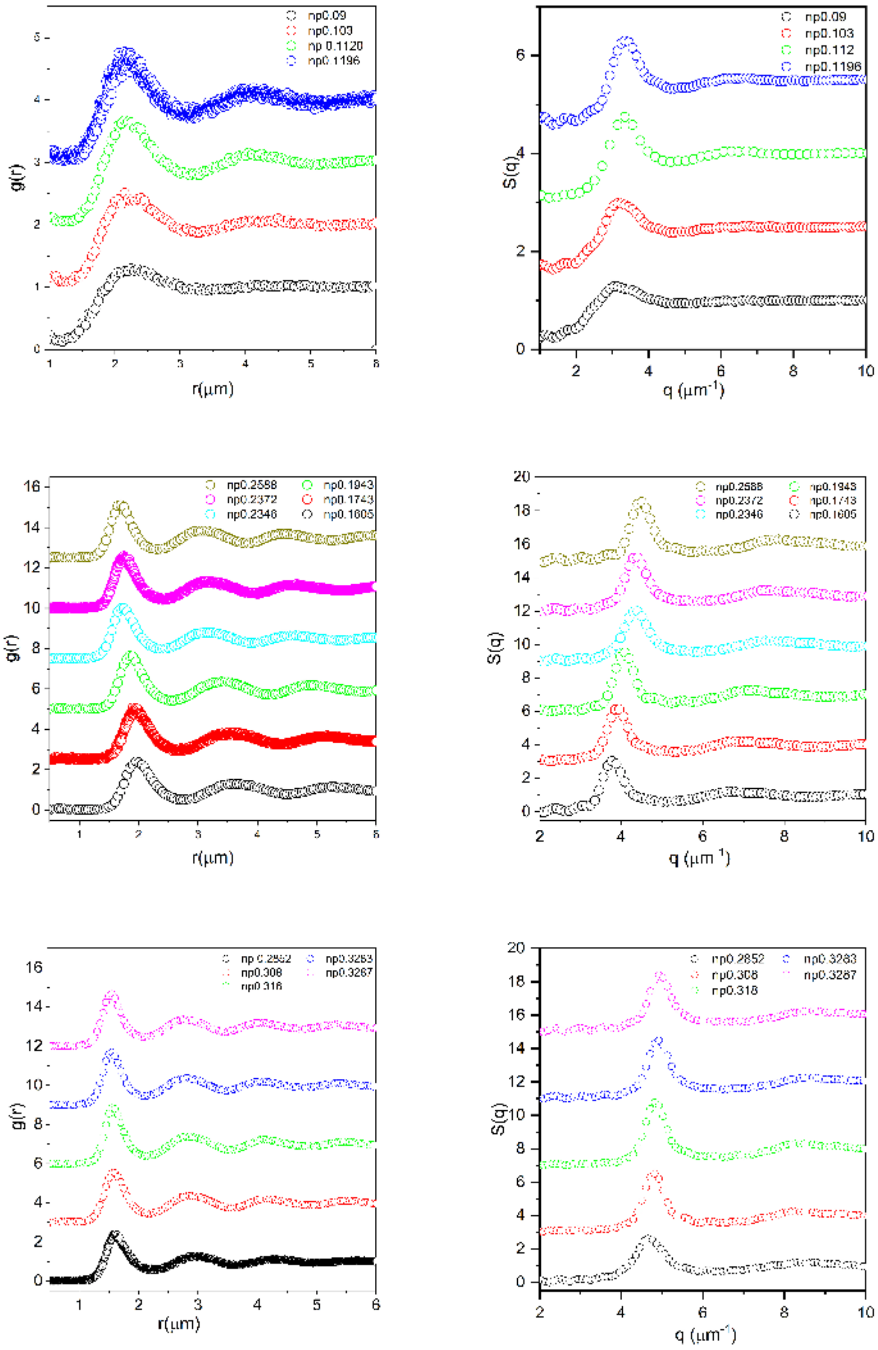

Figure 5: Left: Overview of the measured g(r) for CHB+CDL in the range of ρ=0.09 to 0.2588. Right: Overview of the corresponding structure factors in the same range. For a better overview, the data histories in both Graphs shifted upward.

Appendix C

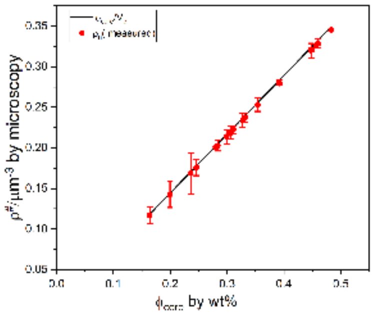

Figure 6: Experimental g(r)(black) for CHB+CDL+TBAB having ρ= 0.2340 µm^{-3} is given with a comparison with PBRMSA data(red) obtained from Marco Heinen software and corresponding convoluted data(blue).

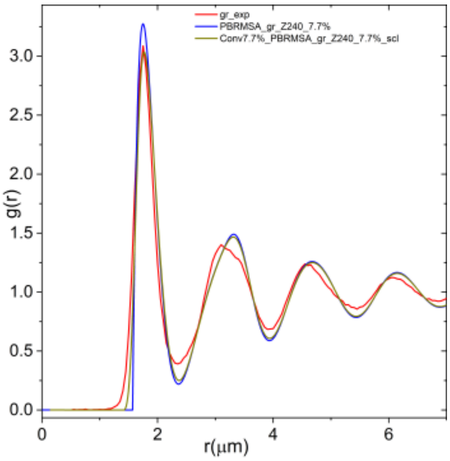

Figure 7: Experimental g(r)(black) for ρ =0.2340 for CHB+TBAB+CDL is given with a comparison with PBRMSA data(red) obtained from Marco Heinen software and corresponding convoluted data(blue).

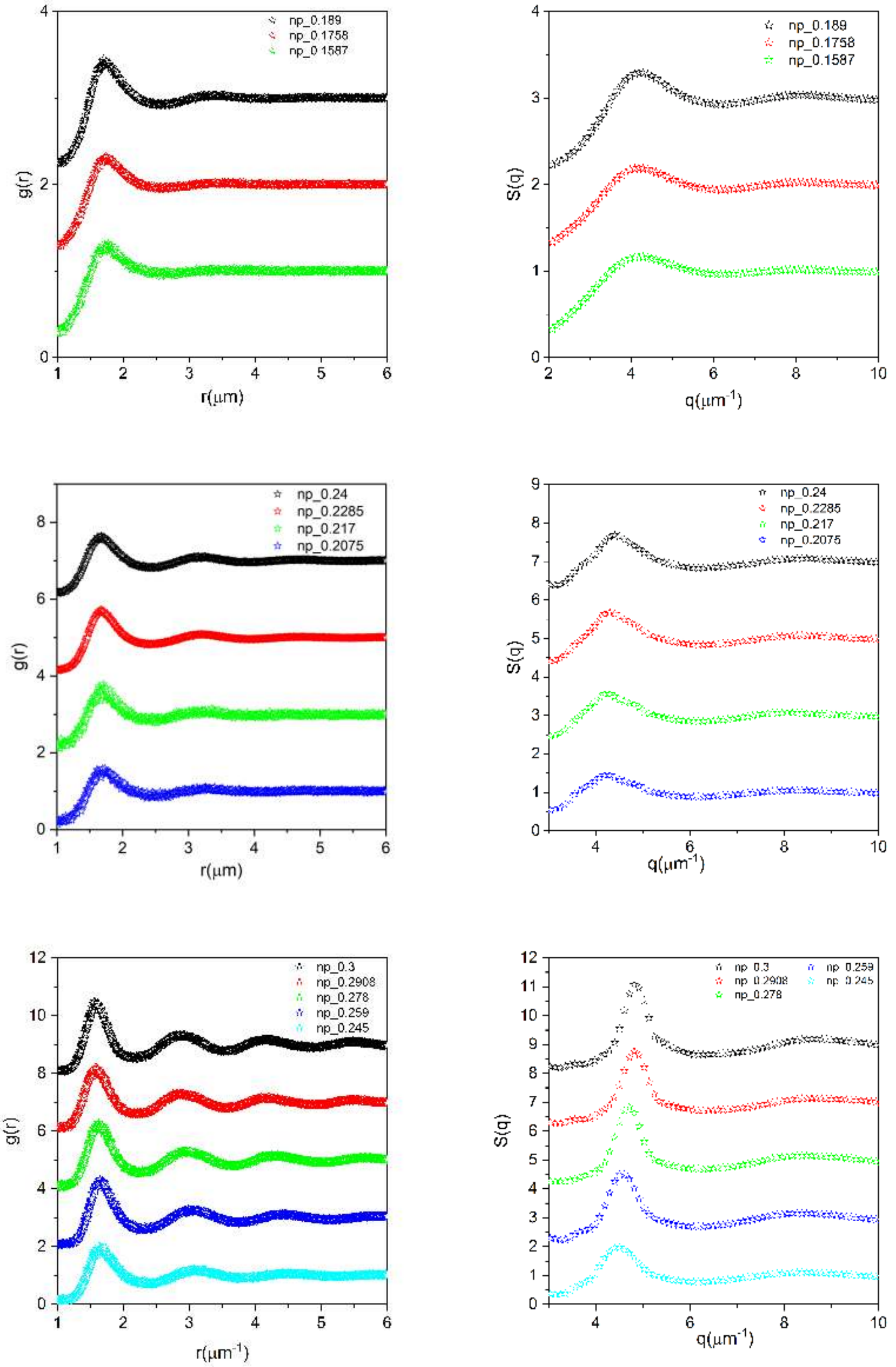

Figure 8: Left: Overview of the measured pair distribution functions for samples in CHB+CDL+3.8mM TBAB for ρ=0.09 to 0.2588. Right: Overview of the corresponding structure factors in the same range. For a better overview, the data points in both Graphs shifted upward.

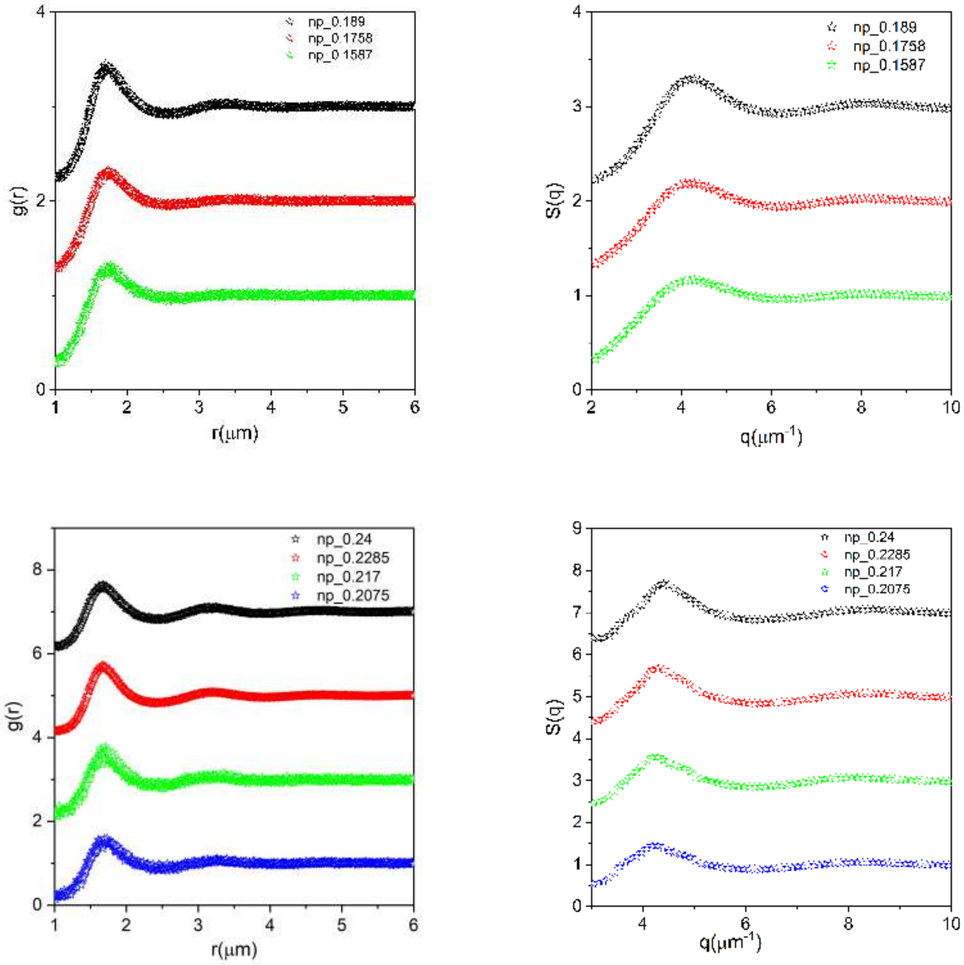

Figure 9: Overview of the measured pair distribution functions for samples in CHB+CDL+1mM TBAB for respective densities. Right: Overview of the corresponding structure factors in the same range. For a better overview, the data points in both Graphs shifted upward.

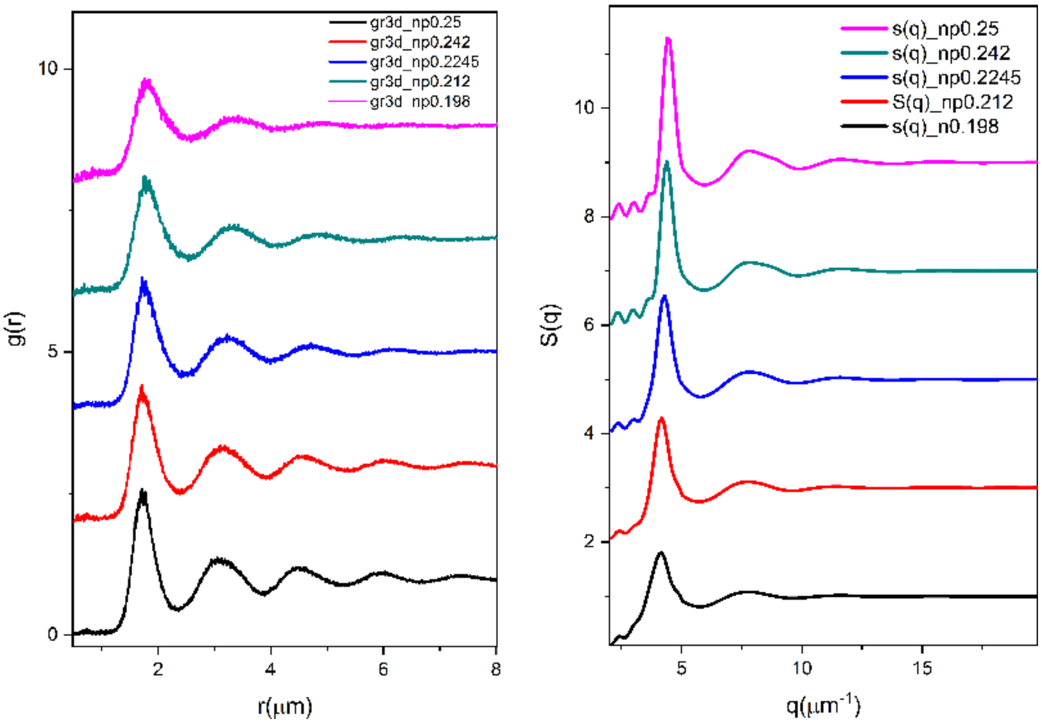

Figure 10: Left: Overview of the measured pair distribution functions for samples in CHB+CDL+ 1 µ M TBAB respective densities. Right: Overview of the corresponding structure factors in the same range. For a better overview, the data histories in both Graphs shifted upward.

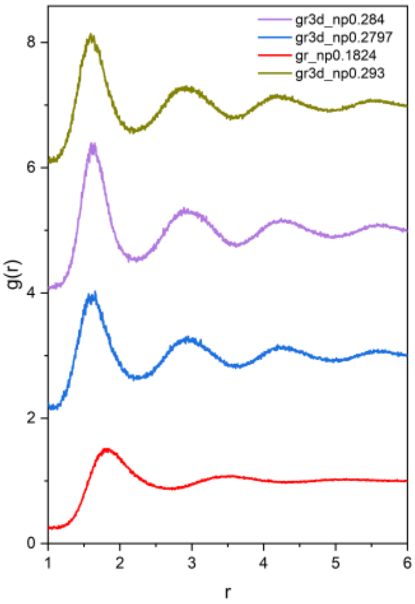

Figure 11: Few measured g(r) data for samples prepared from 4mM TBAC in CHB+CDL

Appendix D

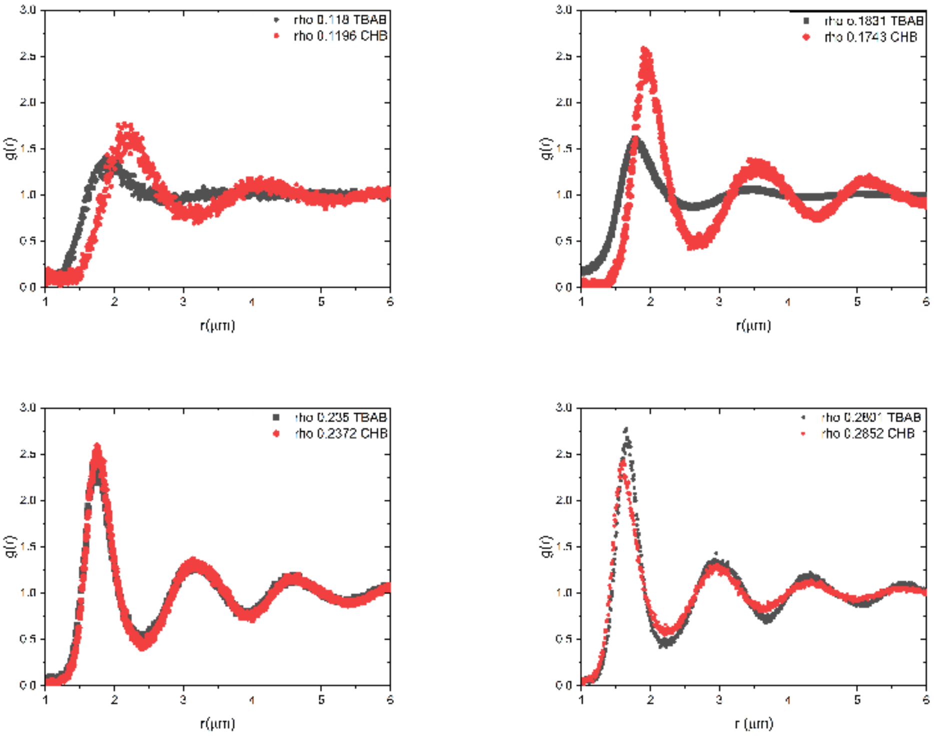

Figure 12: Overview of the measured pair distribution functions for samples with CHB and TBAB for nearly same densities.

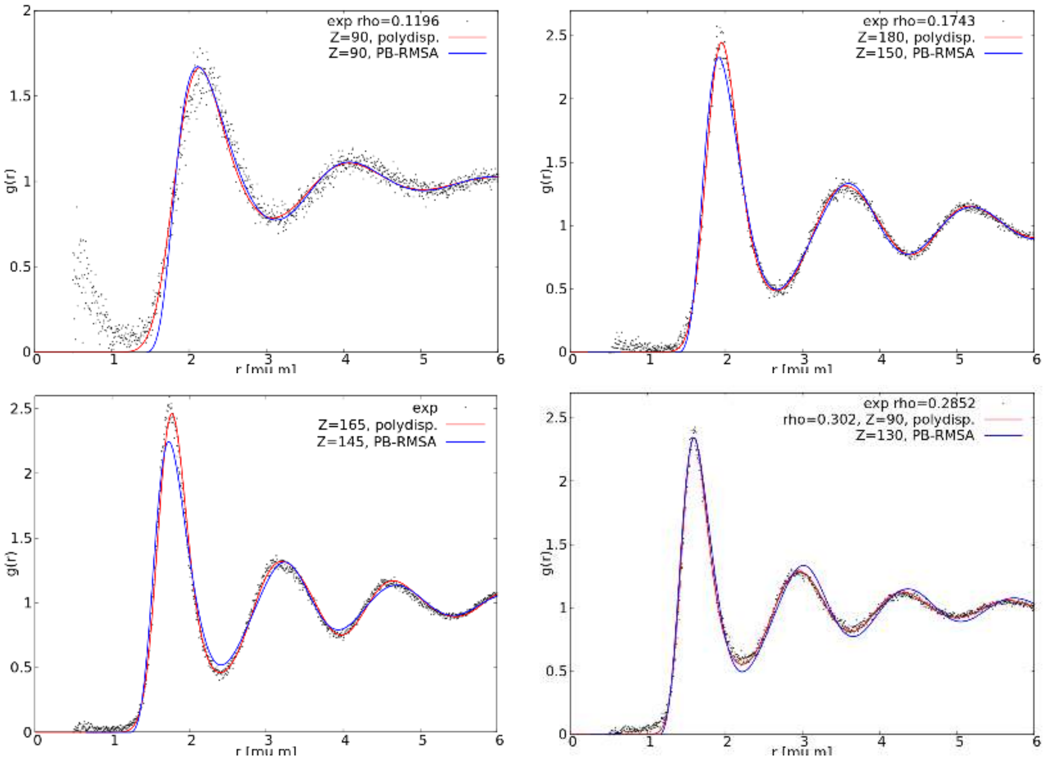

Figure 13: g(r) from experiment, PB-RMSA and polydisperse simulations (overall fit) for four densities. Results from PB-RMSA and simulations have been smeared.

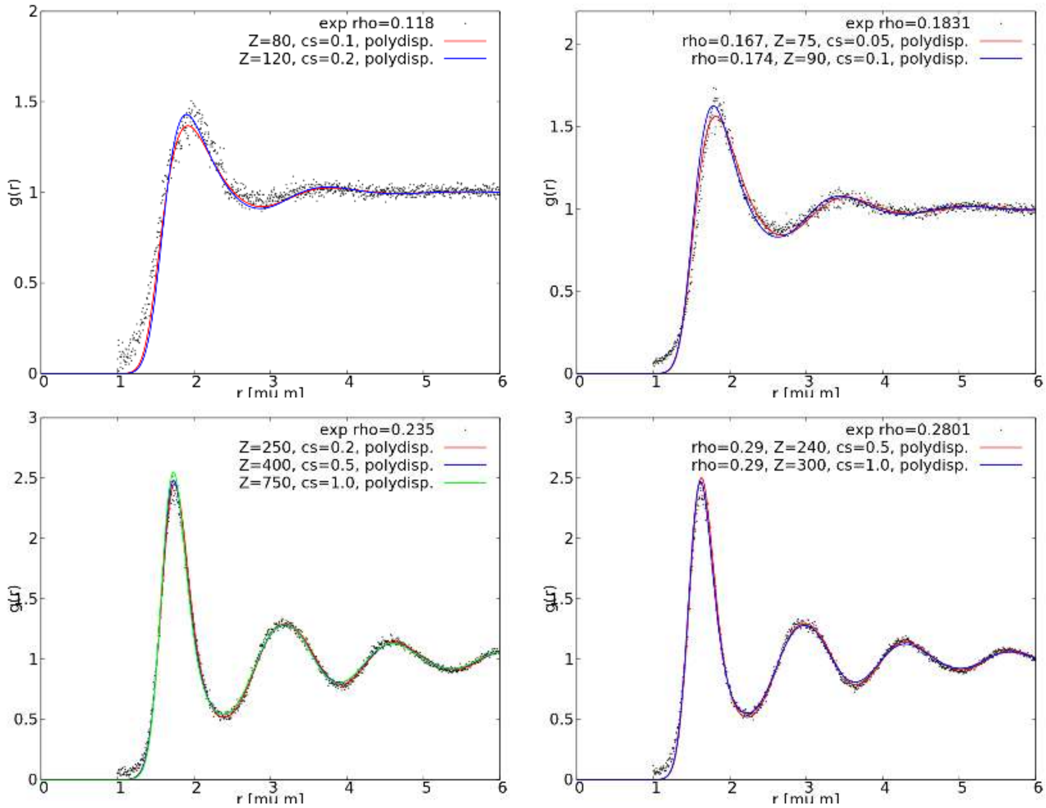

Figure 14: g(r) from experiment and polydisperse simulations (overall fit) for four densities. Results from simulations have been smeared.